[redacted]

CENTRAL RESEARCH LIBRARY
DOCUMENT COLLECTION

~~AEC RESEARCH AND DEVELOPMENT REPORT~~

ORNL-1911
Progress

MARTIN MARIETTA ENERGY SYSTEMS LIBRARIES
3 4456 0349852 4

6A

DECLASSIFIED
CLASSIFICATION CHANGED TO:
BY AUTHORITY OF: AEC - 6-8-62
BY: N. Bowman 8-14-62

AEC RESEARCH AND DEVELOPMENT REPORT

METALLURGY DIVISION

SEMIANNUAL PROGRESS REPORT

FOR PERIOD ENDING APRIL 10, 1955

CENTRAL RESEARCH LIBRARY
DOCUMENT COLLECTION
LIBRARY LOAN COPY
DO NOT TRANSFER TO ANOTHER PERSON
If you wish someone else to see this document, send in name with document and the library will arrange a loan.

OAK RIDGE NATIONAL LABORATORY
OPERATED BY
UNION CARBIDE NUCLEAR COMPANY
A Division of Union Carbide and Carbon Corporation
UCC
POST OFFICE BOX P · OAK RIDGE, TENNESSEE

[redacted]

[redacted]

[redacted]

ORNL-1911

This document consists of 144 pages.
Copy 6 of 149 copies. Series A.

Contract No. W-7405-eng-26

METALLURGY DIVISION
SEMIANNUAL PROGRESS REPORT
for Period Ending April 10, 1955

DATE ISSUED

OCT 14 1955

OAK RIDGE NATIONAL LABORATORY
Operated by
UNION CARBIDE NUCLEAR COMPANY
A Division of Union Carbide and Carbon Corporation
Post Office Box P
Oak Ridge, Tennessee

[redacted]

MARTIN MARIETTA ENERGY SYSTEMS LIBRARIES

3 4456 0349852 4

[redacted]

INTERNAL DISTRIBUTION

1. C. E. Center
2. Biology Library
3. Health Physics Library
4. Metallurgy Library
5-7. Central Research Library
8. Reactor Experimental Engineering Library
9-13. Laboratory Records Department
14. Laboratory Records, ORNL RC
15. A. M. Weinberg
16. L. B. Emlet (K-25)
17. J. P. Murray (Y-12)
18. J. A. Swartout
19. E. H. Taylor
20. E. J. Murphy
21. E. D. Shipley
22. J. H. Frye, Jr.
23. F. C. VonderLage
24. W. H. Jordan
25. R. A. Charpie
26. S. C. Lind
27. F. L. Culler
28. A. H. Snell
29. A. Hollaender
30. M. T. Kelley
31. K. Z. Morgan
32. T. A. Lincoln
33. A. S. Householder
34. C. S. Harrill
35. C. E. Winters
36. D. S. Billington
37. D. W. Cardwell
38. E. M. King
39. A. J. Miller
40. D. D. Cowen
41. P. M. Reyling
42. W. H. Bridges
43. G. C. Williams
44. S. Cromer
45. L. K. Jetter
46. R. R. Dickison
47. W. D. Manly
48. C. D. Susano
49. W. W. Parkinson
50. R. J. Gray
51. H. L. Yakel
52. P. Patriarca
53. E. E. Stansbury
54. G. P. Smith
55. J. E. Cunningham
56. R. S. Crouse
57. R. E. Adams
58. J. H. Erwin
59. J. O. Betterton, Jr.
60. W. O. Harms (consultant)
61. G. M. Adamson
62. E. S. Bomar
63. R. J. Beaver
64. T. W. Fulton
65. W. J. Fretague
66. R. B. Oliver
67. J. T. Howe
68. T. H. Blewitt
69. C. R. Boston
70. J. H. Crawford, Jr.
71. J. C. Wilson
72. H. W. Savage
73. E. E. Hoffman
74. W. J. Leonard
75. J. A. Milko
76. J. M. Warde
77. H. G. MacPherson (consultant)
78. E. C. Cruetz (consultant)
79. E. P. Wigner (consultant)
80. W. W. Grigorieff (consultant)
81. H. J. Grant (consultant)
82. T. S. Shevlin (consultant)
83. R. W. Johnson
84. J. A. Lane
85. G. E. Boyd
86. ORNL Document Reference Library, Y-12 Branch

[redacted]

[redacted]

[redacted]

EXTERNAL DISTRIBUTION

87-94. Argonne National Laboratory
95-102. Atomic Energy Commission, Washington
103. Battelle Memorial Institute
104-107. Brookhaven National Laboratory
108. Brush Beryllium Company (N. W. Bass)
109-110. Knolls Atomic Power Laboratory
111-112. General Electric Company, Richland
113-115. General Electric Company (ANPD)
116. Hanford Operations Office
117. Phillips Petroleum Company (NRTS)
118-121. Los Alamos Scientific Laboratory
122. Nuclear Metals, Inc.
123-124. New York Operations Office
125. Patent Branch, Washington
126. duPont Company, Wilmington
127-141. Technical Information Service, Oak Ridge
142-145. University of California Radiation Laboratory, Berkeley
146. Bettis Plant (WAPD)
147. Atomic Energy Commission, Pittsburgh Area Office
148. Atomic Energy Commission, Schenectady Operations Office
149. Division of Research and Medicine, AEC, ORO

[redacted]

[redacted]

Reports previously issued in this series are as follows:

ORNL-28	Period Ending March 1, 1948
ORNL-69	Period Ending May 31, 1948
ORNL-407	Period Ending July 31, 1949
ORNL-511	Period Ending October 31, 1949
ORNL-583	Period Ending January 31, 1950
ORNL-754	Period Ending April 30, 1950
ORNL-827	Period Ending July 31, 1950
ORNL-910	Period Ending October 31, 1950
ORNL-987	Period Ending January 31, 1951
ORNL-1033	Period Ending April 30, 1951
ORNL-1108	Period Ending July 31, 1951
ORNL-1161	Period Ending October 31, 1951
ORNL-1267	Period Ending January 31, 1952
ORNL-1302	Period Ending April 30, 1952
ORNL-1366	Period Ending July 31, 1952
ORNL-1437	Period Ending October 31, 1952
ORNL-1503	Period Ending January 31, 1953
ORNL-1551	Period Ending April 10, 1953
ORNL-1625	Period Ending October 10, 1953
ORNL-1727	Period Ending April 10, 1954
ORNL-1875	Period Ending October 10, 1954

[redacted]

[redacted]

CONTENTS

SUMMARY vii

METALLURGICAL MATERIALS AND PROCESSING 1

Thorium – The Metallex Process 1
Pressing 1
Retorting 2
Pickling 3
Storage 3
Experimental Results 4
Future Work 5

Preparation of Aluminum-Uranium Alloys 5

Growth of ORNL Graphite Reactor Slugs 5

FUNDAMENTAL PHYSICO-METALLURGICAL RESEARCH 7

Preferred Orientation in Annealed Aluminum Rod 7

Preferred Orientation in Extruded Thorium Rod 11

Fundamental Studies of Alloying 16
The Silver-Zirconium System 16
The Indium-Zirconium System 19
Zirconium-Lead Phase Diagram 21

Floating-Zone Purification of Zirconium 23

HRP METALLURGY 25

Physical Metallurgy of Titanium and of Zirconium Alloys 25
Commercial Titanium 25
Zirconium Alloys 25

Welding of Stainless Steels 33
Welding Development on 1-in. Carbon-Steel Plates Clad with Type 347 Stainless Steel 33

Metallurgical Engineering Service 37
Fabrication of HRT Zircaloy-2 Core Vessel 37

HRP Physical Metallurgy 49
Metallurgy of Corrosion 49
Zirconium and Titanium Metals and Alloys 52

HIGH-TEMPERATURE METALLURGY 54

Dynamic Corrosion 54
Sodium Corrosion 54

General Corrosion 55
Single-Crystal MgO Specimens in Static Lithium and Lead 55
Dissimilar-Metal Mass-Transfer Study on the Zirconium–Type 304 Stainless Steel–Sodium System 55
Magnesium-Lithium Alloys in Water 56

Mechanical Testing 56

Welding and Brazing 65
Brazing Alloy Development 65
High-Conductivity Fin-Radiator Fabrication 68

[redacted]

[redacted]

Cermet-to-Metal Brazing 71
Fabrication of Hastelloy B Reactor Components 72
ORR Project 83

Physical Chemistry of Corrosion 83
Mass Transfer in Liquid Lead 83
Mass Transfer and Corrosion in Fused Hydroxides 84
Spectrophotometry of Fused Hydroxides 86
Fused Hydroxides as Acid-Base Analog Systems 86
Film Formation on Metals 97

PACKAGE POWER REACTOR PROGRAM 103

Fishtailing in APPR Fuel Plates 103

APPR Component Assembling by Brazing 103

Preparation of Component for Irradiation Testing in the STR 105

Preparation of Test Component for Irradiation Testing in the MTR 106

CERAMICS RESEARCH 108

Production of Large Particles of UO_2 from UO_3 Hydrates 108

UO_2 Volatilization in Firing 112

BeO Slip Casting 112

Thoria Densification 112

Conversion and Radiation Effects on ThO_2 112

SiC-Si Fuel Element 114

Rare-Earth Ceramics 117

Sm_2O_3-Gd_2O_3 Ceramic Control Rods 118

Graphite-Hydrogen Reaction and Erosion Investigation 118

Hafnium Carbide Investigations 118

Specific Heat Measurements 120

High-Temperature X-Ray Studies 120

Ceramic Aspects of Waste Disposal 122
Fixation of Radioisotopes 122
Concrete for Retaining Hope Solution 122
Waste Disposal Heat Experiment No. 1 123
Viscosity Studies of Selected Clays for Use in Lining Waste-Disposal Pits 124

METALLOGRAPHIC RESEARCH 128

Techniques for the Metallography of High-Purity Aluminum 128

Inclusions in High-Purity and Commercial-Grade Uranium-Iron Alloys 131

[redacted]

[redacted]

METALLURGY DIVISION
SEMIANNUAL PROGRESS REPORT

SUMMARY

METALLURGICAL MATERIALS AND PROCESSING

Impetus to the thorium recovery program was given by developing the metallurgical phases of the Metallex process. The process consists in reducing thorium tetrachloride either as the dry salt or in a solution of propylenediamene. Reduction is accomplished at a moderate temperature with sodium amalgam; an amalgam containing 3% thorium results. The mercury is removed by pressing followed by vacuum distillation; the mercury is reduced to a level of a few ppm. The resulting thorium is stable in contact with air.

FUNDAMENTAL PHYSICO-METALLURGICAL RESEARCH

In order to determine the origin of preferred orientations in recrystallized metals, a study was made of the fiber-axis distributions in some extruded and annealed aluminum rod. Annealing at 1000°F produced a duplex <111> - <118> texture in a specimen which had a duplex <111> - <001> "as-extruded" texture. The components of the recrystallized texture can be related to those of the deformed texture by (1) a rotation of 30 to 40 deg about a <111> axis and (2) a rotation of 45 deg about a <011> axis.

The fiber-axis distributions were found for some extruded thorium rod. In a rod extruded so as to prevent recrystallization, a duplex <111> - <001> texture was observed [93% <111>]; and in one extruded so as to cause complete recrystallization, a <114> texture was found.

In the fundamental research program on the study of alloys the refinements in the phase diagrams, silver-zirconium and indium-zirconium, which resulted from the use of alloys of greater purity, are of the following nature: first, in the Ag-Zr system the alpha-phase solid solubility was increased from approximately 0.1 to 0.8% Ag; second, in the In-Zr system the α/β boundaries were found to be closer together. In both cases these results are in better agreement with the results which might be expected from a thermodynamic treatment of these boundaries.

Floating-zone purification experiments with zirconium have now proceeded to the point where multiple passes are practical. Experiments are now under way to determine the optimum condition for the purification of minor impurities.

HRP METALLURGY

Investigation of the impact properties of a titanium corrosion-specimen holder continued. Impact tests on samples machined from the holder show an increase in the brittle transition temperature over that occurring with unexposed stock. Metallographic and x-ray diffraction studies indicate an unidentified phase in the exposed specimens, which does not appear to be a hydride. Specially heat-treated specimens from the same lot of commercial-purity titanium also show this second phase.

Elevated-temperature tensile tests of Zircaloy-2 plate and weldments were performed to determine the properties obtained with these materials and under the fabrication conditions used to make the HRT core tank. Elevated-temperature tensile tests were performed on specimens obtained from a Zircaloy-2 test block forging. The results obtained emphasize the anisotropy which can be expected from heavy forged sections of Zircaloy-2.

Impact tests on Zircaloy-2 specimens from the first in-pile loop run were completed, and the results were compared with those obtained with specimens exposed to similar conditions out-of-pile and with unexposed control specimens. No apparent change in transition temperature resulted from the in-pile exposure.

Four basic techniques, proposed by the subcontractor for the closure weld of the HRT pressure-vessel shell, were evaluated. Carbon-steel plates, 1 in. thick, and clad with a 20% thickness of type 347 stainless steel, were welded into test coupons for later evaluation by nondestructive testing, mechanical testing, and metallographic study. The most desirable technique, based on the results of the limited number of tests in this program, appeared to be as follows:

1. The groove is filled with type 347 stainless

[redacted]

[redacted]

steel weld metal to a point $\frac{1}{16}$ in. below the carbon steel–stainless steel base-plate interface; two layers of type 308L stainless steel weld metal are placed over the type 347 weld metal, which brings the deposit to a level approximately $\frac{1}{8}$ in. above the interface between the carbon-steel base plate and the stainless steel cladding. One layer of ingot-iron weld metal is then placed over the type 308L deposit, and the rest of the groove is then filled by means of low-hydrogen-type carbon-steel coated electrodes.

2. An alternative method consists in following the same welding sequence as above, except that type 308L weld metal is substituted for the ingot iron. This results in two layers of type 308L weld metal, with the carbon-steel weld metal deposited directly on the type 308L weld metal and with no intermediate layer of ingot iron.

The HRP Metallurgy Section has furnished assistance to the subcontractor in the fabrication of a Zircaloy-2 core tank for the HRT. The vessel has been completed and has been pressure tested successfully.

Initial work on the study of some aspects of the stress-corrosion cracking of austenitic stainless steels has been directed toward determining an acceptable testing procedure. Equipment has been completed and tested and now appears to be satisfactory for the experimental program.

Studies of the relation of metallurgical factors to corrosion behavior in dynamic-corrosion tests have included the investigation of stainless steel weld deposits, the preparation of specimens for the evaluation of potential grain-size differences in wrought stainless steels, and the behavior of specially melted specimens intended to produce a completely sigma-phase structure. Equipment has been practically completed to study the effect of hydrogen on the properties of zirconium and its alloys and to study the effect of oxide films on the rate of hydrogen absorption by zirconium and its alloys.

HIGH-TEMPERATURE METALLURGY

The program to investigate the mass transfer of container materials in liquid sodium has continued. The mechanical testing facilities have been expanded. The level of rupture strength for a given rupture life at 1500 and 1650°F was found to be greater for Hastelloy B than for Inconel or type 316 stainless steel.

The development of brazing alloys with improved oxidation resistance has continued. Most of the nickel and nickel-chromium base alloys tested were suitable for service in an oxidizing atmosphere at 1500°F. Methods for placing brazing alloy on fins have been devised so that during the furnace-brazing operation there is no excess that will "puddle."

Methods for the successful fabrication of components from Hastelloy B have been under study. Indications are that the degree of precipitation in weld deposits and heat-affected zones might be different from that found in wrought structures. An investigation has been started to determine the function of several variables on the type and quantity of precipitate.

Type 310 stainless steel was tested for mass transfer in a quartz thermal-convection loop containing lead at 805°C. Mass transfer occurred at a relatively rapid rate. A summary chart is given for all liquid-lead mass-transfer tests conducted by the Physical Chemistry Group.

Preliminary measurements show that the absorption spectrum of fused sodium hydroxide changes with temperature. When the temperature has increased to 700°C, a sharp absorption peak appears at 440 mμ.

The self-decomposition of fused hydroxides has been examined thermodynamically in terms of Temkins rules. Expressions were obtained which show the effect of the composition of the melt on the self-decomposition constant. The way in which the self-decomposition controls certain classes of reactions in a hydroxide melt is qualitatively shown in terms of an acid-base analog theory.

Studies of the oxidation of solid sodium were extended down to –79°C. At the lower temperatures the protective character of the oxide film was found to be particularly marked. After 1000 min of oxidation at –79°C the thickness of the oxide film was only 30 Å.

PACKAGE POWER REACTOR PROGRAM

Development work is well advanced on the stainless steel–uranium dioxide fuel components proposed for service in the Army Package Power Reactor. Material and dimensional specifications on the flat-plate type of fuel component are essentially complete. Sufficient fabrication technology is available to proceed with the construction of

[redacted]

full-scale enriched-fuel assemblies for irradiation test purposes.

Numerous refinements have been incorporated into the fabrication techniques developed for manufacturing the fuel element. The rolling schedule employed in the preparation of the stainless-steel-clad fuel plates has been adjusted to minimize "fishtailing" of the core section, which consists of a sintered powder of UO_2, B_4C, and stainless steel. The rolling temperature has been lowered to 1150°C to avoid partial reduction or dissociation of the B_4C compound, which was encountered at higher hot-working temperatures.

Analytical chemical results on six samples taken from a finished enriched-fuel plate indicated the presence of a uniform dispersion of UO_2 throughout the core or fuel-bearing section. The maximum deviation from the average content (15.77% metallic uranium in the core) was found to be 1.2%; whereas the average deviation was only 0.76%.

Several full-scale APPR fuel assemblies containing normal UO_2 have been successfully brazed. Inspection revealed that sound brazed joints were achieved over the entire length of the 18 fuel-bearing plates and that the brazed units were dimensionally within tolerance.

It was found that when dry brazing-alloy powder was applied a more uniform fillet and less runout of the brazing alloy onto the fuel plate resulted. An average ultimate tensile value of 28,800 psi was obtained by pulling several composite 304L stainless steel bars brazed with Coast Metals NP brazing alloy at room temperature. Metallographic examination and a hardness traverse across the brazed joint revealed that the alloy contains extremely brittle phases in a rather ductile matrix.

With the cooperation of WAPD, a modified stainless steel enriched-fuel subassembly has been designed, constructed, and pretreated and has been inserted in core 1 of the STR at the NRTS. The test element will be exposed under the combined hydraulic, thermal, pressure, and irradiation conditions present for 400 hr of full-power operation.

CERAMICS

A technique has been developed for the production of large particles of UO_2 by growing crystals from UO_3 hydrate in an autoclave and reducing them to UO_2 in hydrogen.

A method was developed for slip-casting BeO ceramics in the presence of a basic deflocculant.

Densification of ThO_2 by CaO is most effective if the CaO (0.5 wt %) is added to ThO_2 after it has been calcined at 900°C; the mixture is then pressed into shapes and sintered at 1600 or 1800°C. The oxidation characteristics of uranium disilicide have been determined from differential thermal analysis and weight-loss data. The use of large particles (greater than 140 mesh) of UO_2 was found to reduce the reaction rate between fuel and silicon and thereby reduce the bursting tendency of the compact.

Physical properties of Sm_2O_3 and Gd_2O_3 sintered at 1300 and 1500°C are reported. Both oxides formed compounds with Al_2O_3, Fe_2O_3, SiO_2, and SrO; the Sm_2O_3 and Gd_2O_3 compounds with Al_2O_3 and Fe_2O_3 apparently had the perovskite structure similar to barium titanate. Both Sm_2O_3 and Gd_2O_3 formed solid solutions with CaO, HfO_2, MgO, ThO_2, and ZrO_2. Specimens of a mixture of Sm_2O_3 and Gd_2O_3 were made for measurement of their value as reactor poisons. Enthalpy determinations, from three different temperatures to 0°C, are reported on Gd_2O_3 and Sm_2O_3. High-temperature (up to 1050°C) x-ray examination of Sm_2O_3 showed no inversion.

Little, if any, reaction was noted when graphite was exposed to static H_2 at 1800°C for 2 min and 2300°C for 30 sec.

Hafnium carbide was found to have microhardness values from 1939 to 2305, which is of the same order as boron carbide.

Low-cost ceramic mixes have been developed into which radioactive wastes will be incorporated, and the body will be fused and subjected to leaching tests.

METALLOGRAPHIC RESEARCH

In order to aid in the study of preferred orientation in high-purity aluminum, a metallographic technique has been developed which reveals some conception of the preferred orientation. By the use of proper polishing and anodizing techniques it is possible to determine whether the specimen is deformed or partly or fully recrystallized. When etch pits are developed on the surface, the approximate relative orientations of deformed and recrystallized aluminum can be determined because the pits in the vicinity of (111) are triangular and those near (100) are square.

The effort to identify inclusions in uranium has continued. The microstructures of uranium containing iron additions of 12.0, 2.93, and 0.4 wt % have been studied in detail.

[redacted]

METALLURGICAL MATERIALS AND PROCESSING

J. L. Gregg

THORIUM – THE METALLEX PROCESS

E. S. Bomar

The Metallex process, being developed by the Chemical Technology Division for the reduction of thorium tetrachloride to the metal, produces a dilute thorium amalgam. The amalgam has been produced by dissolving the tetrachloride in propylenediamine and contacting the solution with sodium amalgam. It has also been produced by simply mixing dry thorium tetrachloride with sodium amalgam. Amalgam produced by either route is freed from unreacted sodium, thorium tetrachloride, and sodium chloride by washing it in a dilute solution of hydrochloric acid. The resulting thorium amalgam contains approximately 3% thorium. It is a semiliquid at room temperature and is believed to consist of a liquid phase of substantially pure mercury and a finely dispersed phase of an intermetallic compound of thorium and mercury.

From 70 to 80% of the mercury in the amalgam containing 3% thorium can be eliminated mechanically to yield an amalgam containing between 10 and 15% thorium. This quantity of mercury has been extracted from the amalgam by pressing it in a conventional punch and die used for making powder compacts. In this operation the free mercury is forced through the space between the punch and die so that the operation is, in effect, filtering with a high pressure on the filter cake. Actual pressures on the compact have varied from 2½ to 45 tsi, but variations in pressure within this range have little effect on the quantity of mercury eliminated or on the properties of the filter cake. Mercury has also been removed to the same extent by pressing the amalgam against a stainless steel filter so that mercury is forced through the pores of the filter. Substantially, the same results were obtained as with the simple punch and die. The pressed amalgam, containing 10 to 15% thorium, is a solid at room temperature; and only the surface seems to oxidize on exposure to a moderately oxidizing environment. Compacts having diameters of ½ and 2 in. have been used for the experimental work.

Two rather obvious procedures for producing metallic thorium in usable form by eliminating the mercury from amalgam containing between 10 and 15% thorium are (1) to heat the amalgam to the melting temperature of thorium in a refractory crucible in a vacuum and cast the thorium into the desired shape, or (2) to heat it in a retort (equipped with a condenser for recovery of the mercury) until the thorium sinters. The first method has serious disadvantages, namely, the mercury vapor in the vacuum chamber and the great decrease in volume on elimination of mercury. Consequently, much of the experimental work has been directed toward developing a satisfactory retorting procedure.

Figure 1 shows Metallex material at different stages of processing, beginning with the 3% thorium amalgam and ending with either metal pressed after retorting or metal melted after retorting. Details of the various operations are discussed below.

Pressing

Experiments on removal of mercury from the amalgam were first performed with a ½-in.-dia die. Compacts were subsequently pressed into several sizes with diameters varying up to 2 in. No differences in the pressing behavior of the amalgam were detected as the size of the die was changed.

The tendency for the solids to extrude into the die-punch clearance varied with the different batches processed. The majority of the materials pressed, however, did not display this tendency. Attempts to correlate extrusion with a chemical variable were not successful, nor could a connection between the thixotropic properties of the amalgam and the extrusion be found. In those instances in which extrusion did occur, an appreciable push-out pressure was required to remove the compact from the die. The use of stearic acid as a die-wall lubricant helped to minimize the ejection pressure required. In the worst case encountered, a pressure of 15 tsi was required as contrasted to a value of a few hundred psi in most instances. Galling of the die wall and punch occurred in this pressing.

The contribution of the stearic acid lubricant to the carbon content of the retorted thorium could not be ascertained because the amalgam, as supplied, has an appreciable carbon content which possibly originates from residual propylenediamine.

[redacted]

UNCLASSIFIED
Y-14037

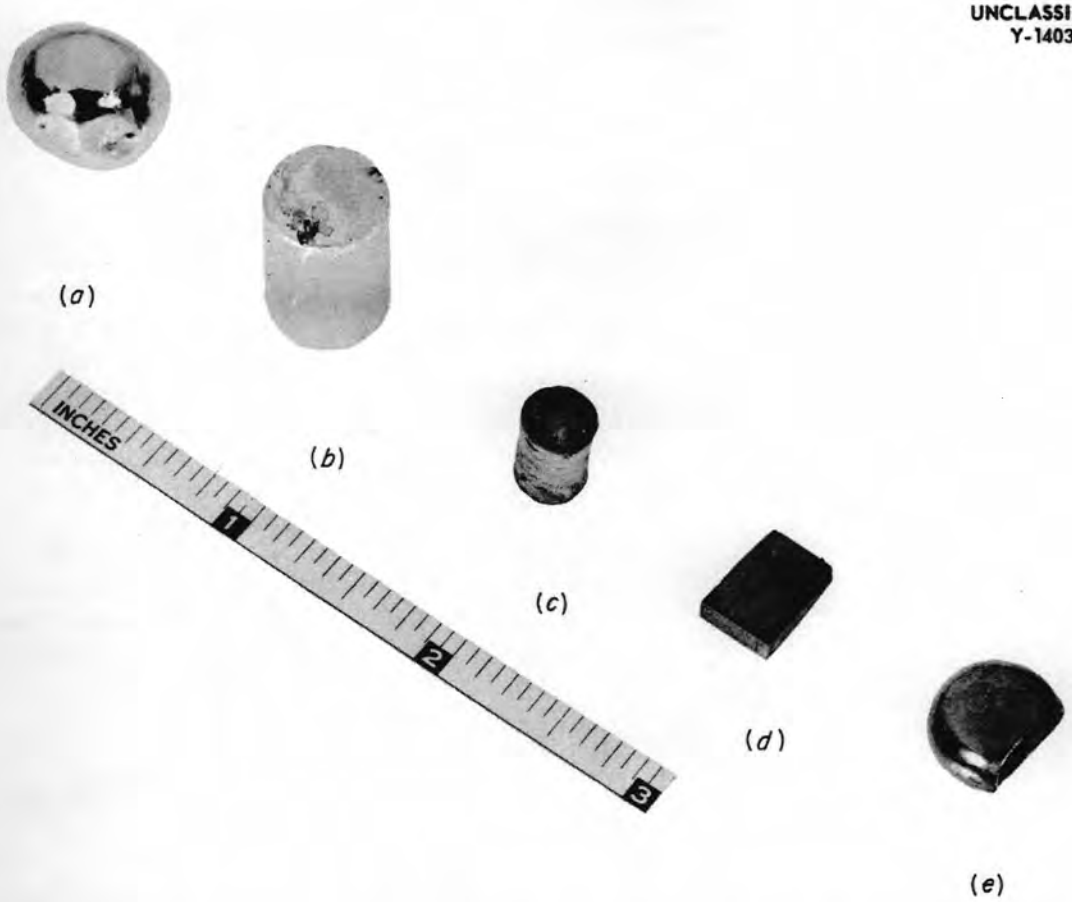

Fig. 1. Process Sequence for Metallex Amalgam. (*a*) Quasi. (*b*) Cold-pressed quasi, 10 tsi. (*c*) Sintered compact. (*d*) Cold-upset compact. (*e*) Arc-melted button.

To speed up the elimination of mercury during pressing, an arrangement was set up with a sintered stainless steel frit replacing the bottom punch. Prior to loading with amalgam, the 2-in. die was pressed down onto the frit with a pressure of 15 tsi to form a smooth seat between the die bottom and the frit. A metal block with a grooved surface was placed beneath the frit to permit the mercury to flow through the frit and out of the grooves into a collecting pan. As much as 3500 g of amalgam was loaded into the die and pressure applied to the punch. The mercury was readily forced through "G" grade filter stock manufactured by the Micro Metallic Corporation. The "G" frit is stated to have an average pore size of 10 μ. The time for the pressing operation was reduced from about 15 to 5 min by this arrangement. Fifteen 2-in.-dia compacts have been pressed on one frit without any appreciable decrease in the rate of mercury elimination.

Retorting

Two pieces of apparatus were assembled for retorting experiments. Preliminary work was performed in a system containing a mullite refractory tube with an inside diameter of $1\frac{1}{2}$ in. Evacuation was effected with an oil diffusion pump and a mechanical fore pump plus a liquid-nitrogen cold trap. Pressures of less than 0.1 μ Hg could be obtained in the refractory tube at 1100° C.

When work with small samples in the above equipment indicated that the residual mercury could be removed by a thermal treatment, an all-metal system was built. This equipment can accommodate compacts made in the 2-in. die. Also, the behavior of an all-metal system under

the retorting conditions is of interest if appreciable quantities of thorium are to be prepared by this method.

The retort for the all-metal system was made of type 347 stainless steel. The vacuum system was a duplication of that used on the first retorting setup. A water-cooled receiver was placed between the retort and the liquid-nitrogen cold trap which removed the bulk of the distilled mercury. The best vacuum obtained in this system was about 0.1 μ at 1100°C. Most of the runs were made at pressures not exceeding 0.8 μ.

In order to avoid the possibility of forming a low-melting alloy (eutectics: Th-Cr, 1230°C; Th-Ni, 1000°C) with the constituents of stainless steel, a boat of 0.015-in.-thick tantalum was used to hold the compacts during retorting.

Pickling

Even at the pressure levels of the retort atmosphere employed in these experiments, the chemical activity of thorium was sufficient to form a film of thorium oxide on the surface of the compacts. This film was later removed by pickling with an aqueous solution of 42% nitric acid and 6% hydrofluosilicic acid by weight. Surface texture before and after pickling is shown in Fig. 2.

Storage

The amalgam, as received from the Chemical Technology Division, was in containers flooded with petroleum ether. Even under this protective fluid there was a gradual buildup of a gelatinous material, probably hydrated thorium oxide. Elimination of mercury resulted in an increased reactivity; the solid material and compacts stored under petroleum ether rapidly acquired a dark surface film. This film, in turn, tended to scale off, thereby exposing additional surface for reaction. There was apparently less reaction when amalgam was stored under a tank-helium atmosphere than when it was stored in ether. Alternate storage environments are of interest because of the flammable nature of ether.

UNCLASSIFIED
Y-14298

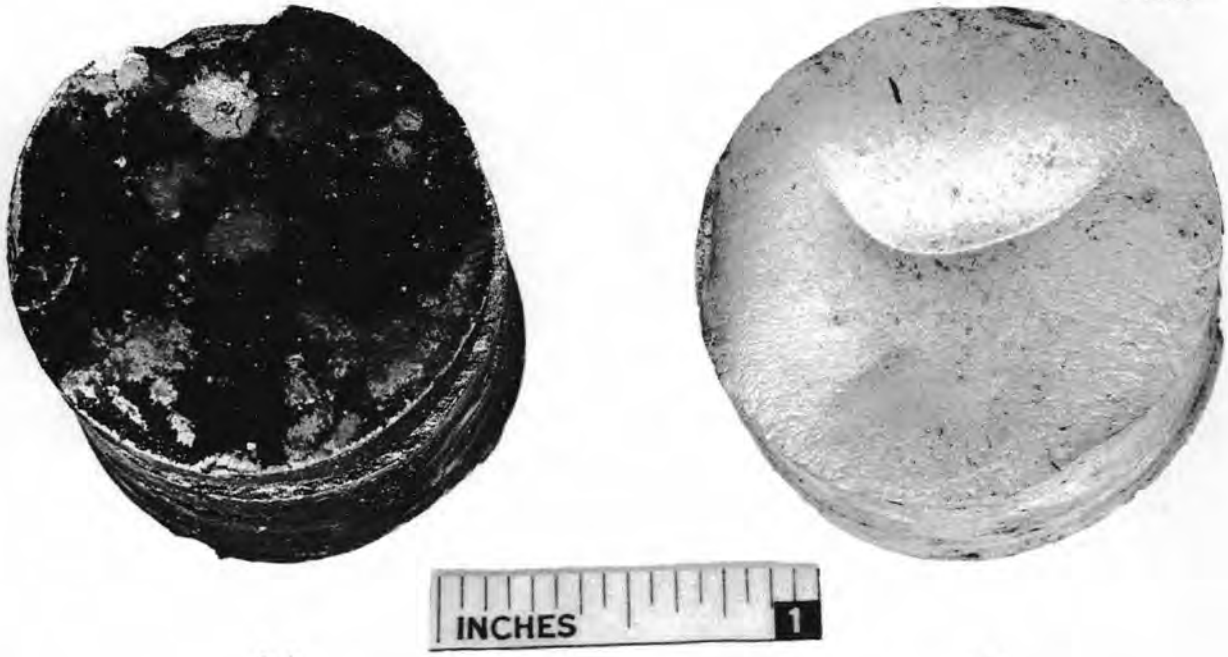

(*a*) (*b*)

Fig. 2. Retorted Thorium from Pressed Metallex Amalgam. (*a*) As-retorted, 1 hr at 1100°C. (*b*) Pickled in HNO_3-H_2SiF_6 mixture.

Experimental Results

A study was made to examine the effect of several experimental variables in the pressing and retorting operations. Retorted bulk density and the ratio of mercury removed to the weight of the compact were determined and were compared with the consolidating pressure for 2-in.-dia samples. Pressures of 5 to 24 tsi were used to press the amalgam, and bulk densities of retorted material ranging from 8.56 to 11.37 g/cc were obtained, but no correlation could be obtained. The same consolidating pressures resulted in values of 2.18 to 4.31 for the ratio of the weight of mercury ejected to the weight of the resulting compacts, but again without any relationship between the variables.

Variation in bulk density is due principally to the extent of internal-void formation in the retorting step. A cross section from a retorted sample is shown in Fig. 3. The surfaces of these voids were bright, which indicated the absence of an oxidizing atmosphere.

The bulk of mercury removable by pressing appears to have been pressed out at 15 tsi. Actually, pressing the samples on the stainless steel frit eliminates mercury to a considerable extent even at 2½ tsi.

Retorting temperatures were varied from 800 to 1100°C. The texture of the retorted compacts and analyses of residual mercury indicated that the higher temperature is more desirable. One sample, retorted at 800°C, ignited at room temperature on exposure to air. All the samples treated at higher temperatures behaved as does massive thorium upon exposure to air. Retorting times of ½ to 2 hr were used, but a value of 1 hr is presently being used until some of the other variables have been evaluated.

The results of chemical analyses of several samples are given in Table 1.

Fig. 3. Cross Section of Retorted Thorium from Metallex-Amalgam, Showing Retorting Shrinkage.

TABLE 1. ANALYSES OF THORIUM RETORTED AT A PRESSURE OF LESS THAN 0.1 μ

Test Conditions		Analyses					
Retorting Temperature (°C)	Total Heating Time (hr)	Density (g/cc)	Hg (ppm)	C (ppm)	N_2 (ppm)	Na (ppm)	Vickers Hardness
800	0.5		650				
900	0.5	7.55	400	330	190		
1050	0.5	10.25	175	110	385		
1000	0.5	7.68	210	210	160		
1000	2.0	11.2		280			30*
1100	0.5	9.40	13	1540	140	45	
1100	1.0	9.57	20	530	560		
1100	1.0	11.1	155	520	245		
1100	2.0	9.05	45	156	200		

*Cold rolled 50% and annealed for ½ hr at 800°C.

Future Work

Since a procedure has been established for recovering metallic thorium from the amalgam, methods for forming usable shapes will be investigated. These will include canning the retorted compacts; extruding, in an attempt to form rod stock; and arc melting of compacts, followed by extrusion. Contingent on the development of a satisfactory extrusion method, the physical properties of the amalgam will be determined.

In cooperation with the Chemical Technology Division, efforts to define more completely the several process variables will be continued.

PREPARATION OF ALUMINUM-URANIUM ALLOYS

J. L. Gregg J. A. Milko

Aluminum-uranium alloys, used for fuel elements in reactors, are generally dilute alloys of uranium in aluminum; a $7\frac{1}{2}$ wt % uranium alloy has only 1 at. % uranium. It is, therefore, possible to prepare such alloys by using molten aluminum to reduce uranium from the fluoride. This method of preparing alloys would seem to have some advantages over the method of first reducing uranium tetrafluoride in a bomb and subsequently alloying the uranium with aluminum. Work is, therefore, being carried out on the direct reduction of uranium tetrafluoride with aluminum to produce a master alloy that later can be diluted to the desired concentration.

For a study of the reduction of uranium tetrafluoride by aluminum, quantities of materials were used so that the yield would be approximately 500 g of an alloy containing 20% uranium. The melts were made in a graphite crucible. In addition, a variable quantity of sodium fluoride was used to produce a liquid fluoride phase at the reaction temperature.

If uranium fluoride is reduced by aluminum in accordance with the reaction

$$3UF_4 + 4Al = 4AlF_3 + 3U$$

133 g of UF_4 and 416 g of aluminum should yield an alloy containing 100 g of uranium and 400 g of aluminum. These quantities of starting materials were used in most of the experiments. The quantity of sodium fluoride varied from zero to 213 g. In the experiments the reactants were held at a temperature of 1150°C for 10 min. The molten metal and salt were poured on a steel plate, collected, weighed, and analyzed.

Chemical analyses are not available for all the experiments, but those that are available indicate that approximately 3% of the uranium remained in the fluoride phase. A considerable quantity of the sodium from the sodium fluoride was volatilized from each of the melts containing this compound. Further work is needed to determine the most expeditious method of carrying out the reduction and to determine what problems are involved in recovering unreduced uranium in the fluoride phase.

GROWTH OF ORNL GRAPHITE REACTOR SLUGS

R. E. Adams

Early in April 1952 the ORNL Graphite Reactor was recharged with aluminum-silicon-bonded uranium slugs. Since that time the lengths of the discharged slugs have been measured. Prior to about September 1, 1953, 17 slugs had ruptured. Data on such slugs, exposed for a maximum of 464 days, have been reported previously.[1]

Between September 1, 1953, and March 8, 1955, seven more slugs ruptured. A change in reactor operation procedure, in which the reactor is brought to full power more slowly, is believed to account for the decrease in frequency of slug rupture. In addition to the 7 ruptured slugs, 207 additional slugs have been discharged. These slugs, exposed for a maximum of 1016 days, have been examined and measured.

Little additional information has been obtained from examination of the discharged slugs. It is still believed that the ruptures are caused by air which somehow enters the cans and subsequently oxidizes the uranium, which causes the cans to swell and rupture.

A summary of the data obtained from length measurements of the discharged slugs is given in Table 2, which also includes the results of measurements previously reported. The new data (for irradiation times in excess of 464 days) verify the earlier results. Slugs which have been beta-transformed grow very slowly and have maximum growth rates of less than 0.040 in./year and average growth rates of about 0.010 in./year. Slugs which were not beta-transformed grew much more; the growth rates ranged from an average of about 0.050 in./year to a maximum of 0.214 in./year.

[1] R. E. Adams, *Met. Semiann. Prog. Rep. Oct. 10, 1953*, ORNL-1625, p 7.

TABLE 2. GROWTH OF ORNL GRAPHITE REACTOR FUEL SLUGS

Slug Identification Number	Per Cent of Sample Lot Showing Beta Transformation	Time in Reactor (days)	Number of Slugs Measured	Growth (in.)			Growth Rate (in./year)	
				Minimum	Maximum	Average	Maximum	Average
4	0	195	10	0.010	0.043	0.024	0.080	0.045
8	0	419	15	0.013	0.099	0.045	0.086	0.039
13	0	464	40	−0.002	0.183	0.063	0.144	0.050
19	0	559	23	0.038	0.159	0.084	0.104	0.055
22	0	935	40	0.007	0.547	0.151	0.214	0.059
7	25	363	16	0.013	0.085	0.043	0.086	0.043
23	27	931	50	0.001	0.207	0.056	0.081	0.022
24	70	1016	16	0.003	0.057	0.014	0.021	0.005
3	87	189	10	0.000	0.022	0.011	0.042	0.021
5	100	203	34	0.001	0.021	0.008	0.037	0.014
14	100	245	34	−0.006	0.009	0.002	0.015	0.003
9	100	385	52	−0.002	0.014	0.006	0.012	0.005
15	100	455	10	0.004	0.043	0.012	0.034	0.009
18	100	490	8	0.004	0.015	0.010	0.011	0.007
20	100	826	18	0.005	0.013	0.009	0.006	0.004
21	100	819	52	−0.001	0.040	0.011	0.018	0.005

One of the slugs grew a total of 0.547 in. without rupturing. However, in some thermal-cycling experiments, cans ruptured when approximately this amount of growth occurred.

Thus, in slugs which were not beta-transformed, growth may be expected to cause some ruptures in the near future. On the other hand, it seems unlikely that growth of beta-transformed slugs will be an important factor in causing slug rupture.

FUNDAMENTAL PHYSICO-METALLURGICAL RESEARCH

L. K. Jetter

PREFERRED ORIENTATION IN ANNEALED ALUMINUM ROD

L. K. Jetter C. J. McHargue

In an attempt to study the conversion of the deformation texture to the recrystallization texture, a 0.89-in.-dia aluminum rod was extruded from a 3.125-in.-dia ingot (extrusion ratio 12.3) at a temperature of 450°F and at a speed of 615 fpm. The rod was water-quenched at the die to retain, insofar as possible, the as-extruded structure. A specimen from the front of this rod was annealed in a salt bath at 1000°F for 4.5 min.

On a 0.19-in. spherical x-ray diffraction specimen, pole distribution data were obtained by the spectrometric method described previously.[1] These data for the as-extruded rod are given in an earlier report.[2]

The pole-distribution charts (R vs ϕ) for the {004}, {222}, and {022} planes of the annealed specimen are given in Fig. 4. These charts were obtained by normalizing the x-ray diffraction data (I vs ϕ). The axis-distribution chart (T vs ϕ,β) deduced from these pole distributions is given in Fig. 5. On this chart the contours indicate angular locations of equal normalized axis density, T. The pole distributions calculated from the assumed axis distribution are compared with the experimental curves in Fig. 4.

The axis-distribution chart shows the texture to be duplex, the <111> and a direction 2 deg from the <118> being the preferred crystallographic directions of the fiber axis. The axis density first falls off symmetrically from the peaks at these locations but then falls off asymmetrically to form a saddle along the <$\bar{1}$10> zone and a region of relatively high density at <001>.

The volume fraction of material associated with each of the <111> and <118> components was computed from the pole-distribution charts of Fig.

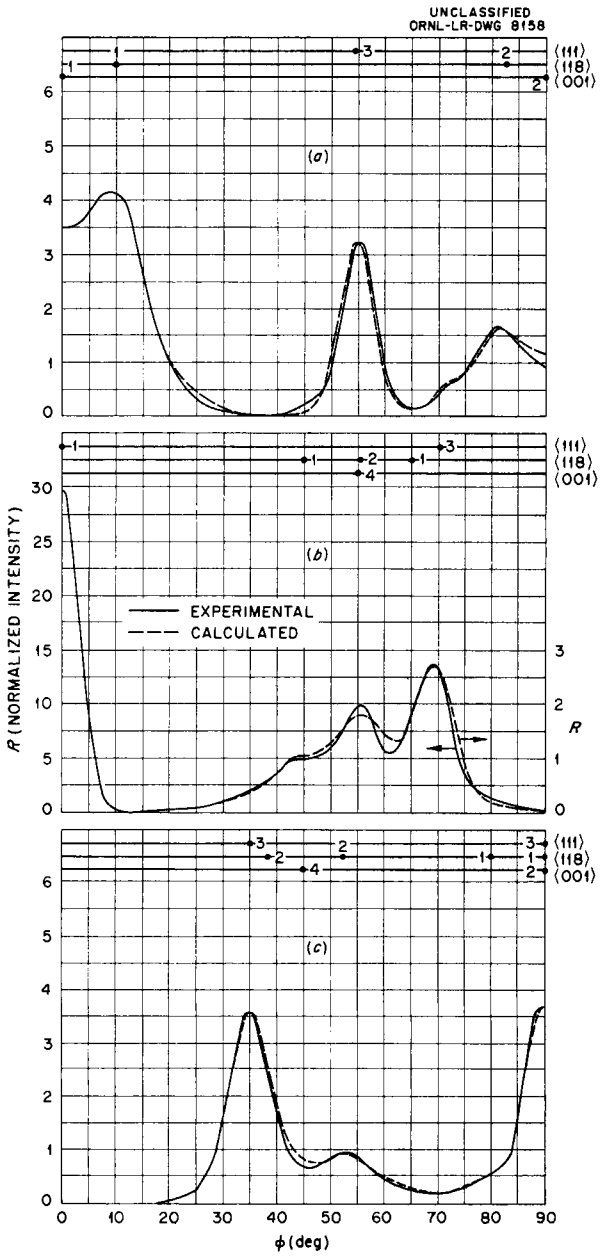

Fig. 4. Pole-Distribution Charts for Aluminum Rod Extruded at 450°F and 615 fpm and Annealed at 1000°F. (*a*) {004}. (*b*) {222}. (*c*) {022}.

[1] L. K. Jetter and B. S. Borie, Jr., *Proceedings of the Spring Metallurgy Conference, March 24–26, 1952*, vol. 2, TID-5084 (June 1952), p 529.

[2] C. J. McHargue and L. K. Jetter, *Met. Semiann. Prog. Rep. Oct. 10, 1954*, ORNL-1875, p 1.

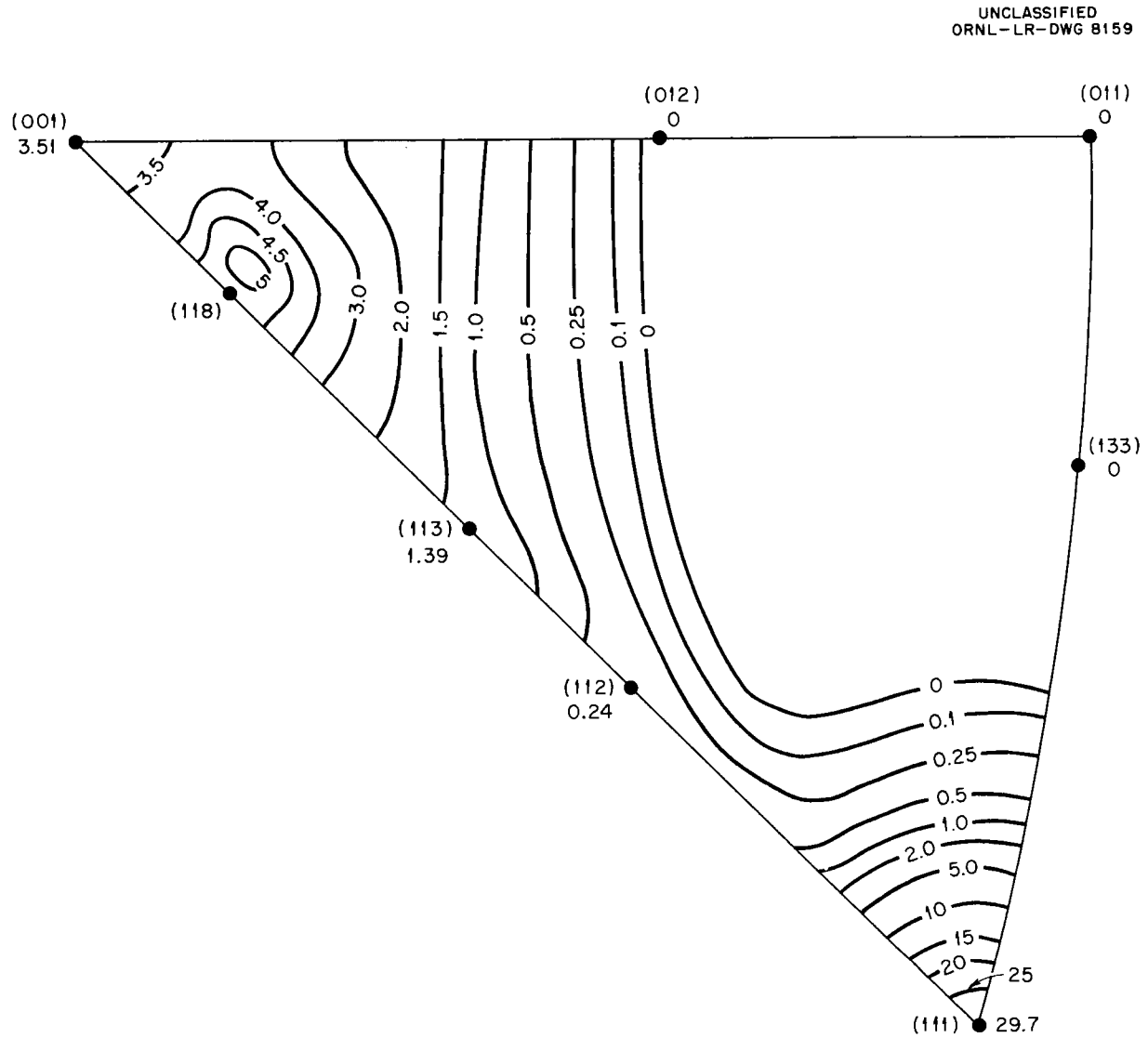

Fig. 5. Fiber-Axis Distribution Chart Representing the Preferred Orientation in the Same Specimen Shown in Fig. 4.

4. Thirty-four per cent of the material had the <111> component as the fiber axis and 66% the <118> component.

In order that the effect of annealing on the fiber texture can be noted, the axis-distribution chart for the as-extruded rod is shown in Fig. 6. A duplex, <111> - <001>, texture was present; 88% of the material was associated with the <111> fiber axis and 12% with the <001>.

An etch-pit technique was developed to supplement the x-ray method of preferred-orientation determination. By this method triangular pits are formed in grains having {111} planes parallel to a transverse surface, and square pits are formed in those grains having {001} planes parallel to the surface. Photomicrographs of the pits on transverse sections of the as-extruded and the annealed rod are reproduced in Figs. 7 and 8. In the as-extruded condition the <001> component was present only in those grains which recrystallized during the extruding process, and the <111> component was present only in the deformed material. The micro-

UNCLASSIFIED
ORNL-LR-DWG 8160

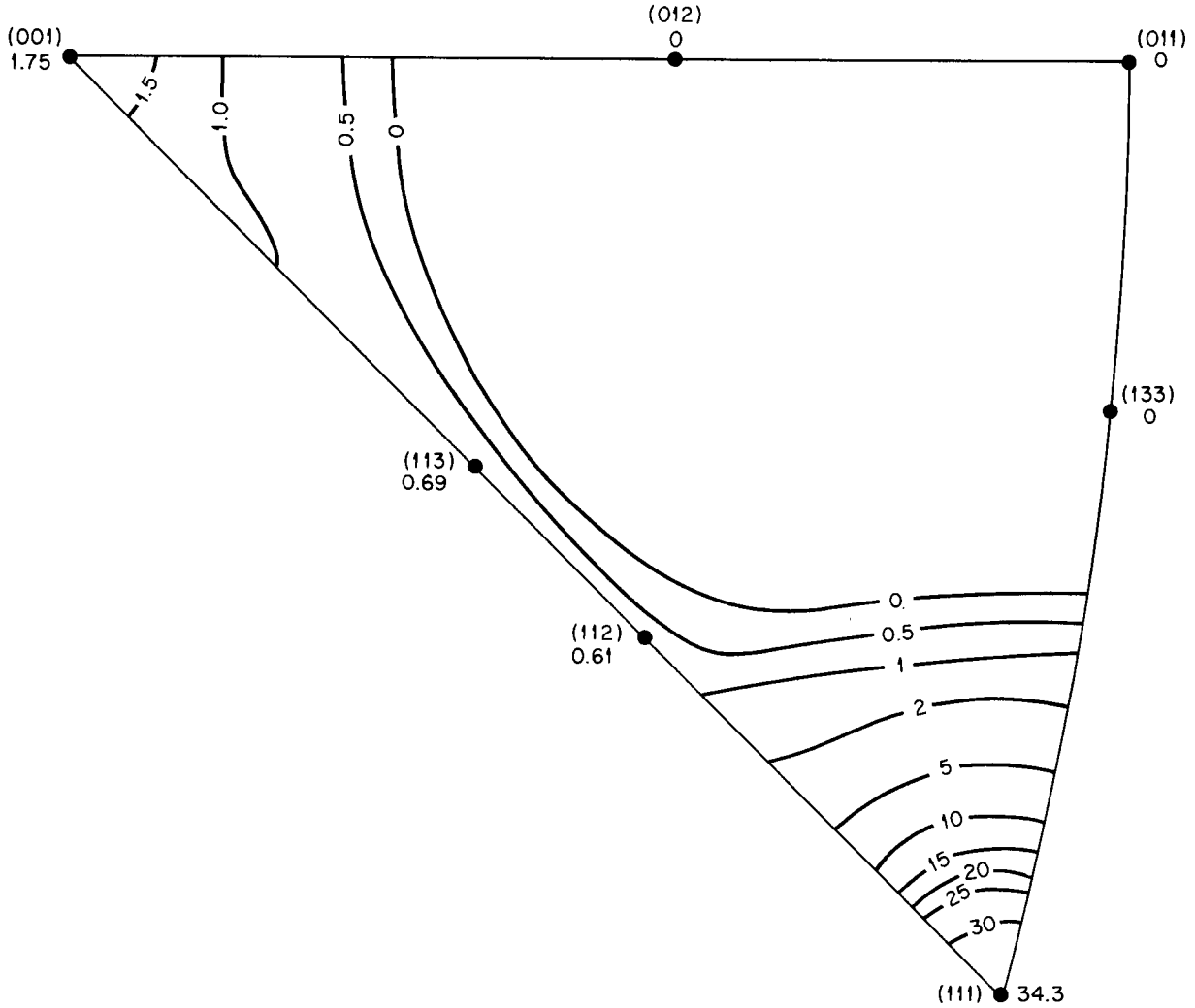

Fig. 6. Fiber-Axis Distribution Chart Representing the Preferred Orientation in Aluminum Rod Extruded at 450°F and 615 fpm.

structure of the annealed specimen indicates complete recrystallization, and Fig. 8 contains both triangular and square pits.

Both current theories of recrystallization texture formation – oriented growth or oriented nucleation – propose an orientation relationship between the new grains and the matrix. The relationship most frequently cited is a rotation of 25 to 45 deg around some <111> direction, with rotations around <001> and <011> being proposed in a few cases.[3] Liu and Hibbard[4] have suggested that components of the recrystallized texture of cold-rolled single crystals of aluminum are related to the deformation texture by 40-deg rotations about <111> and by 30-deg rotations about <001>.

Various rotational relationships between the fiber textures of the as-extruded aluminum rod and the annealed rod are shown in Fig. 9. The <111> component of the annealed rod can be derived from the <111> component of the deformed material by

[3] C. S. Barrett, *Structure of Metals*, 2d ed., McGraw-Hill, New York, 1952.

[4] Y. C. Liu and W. R. Hibbard, Jr., to be published in *Trans. Am. Inst. Mining Met. Engrs.*

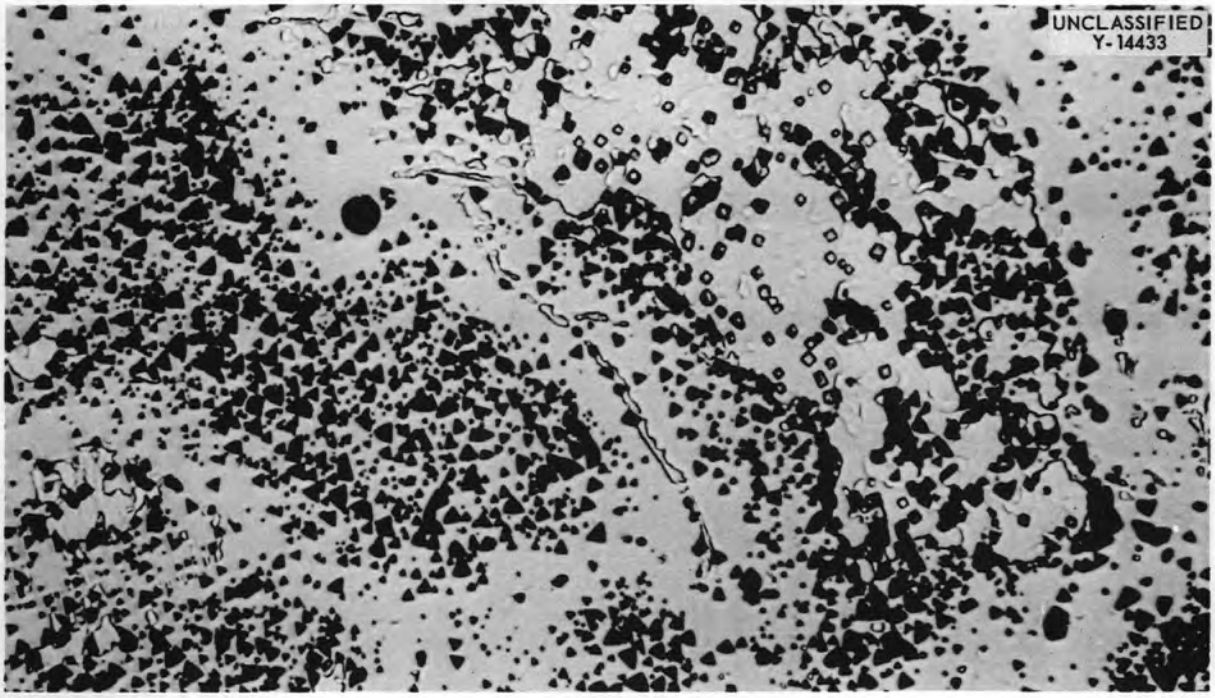

Fig. 7. Transverse Section of Aluminum Rod Extruded at 450°F and 615 fpm. Triangular etch pits indicate {111} and square pits indicate {001}. 500X.

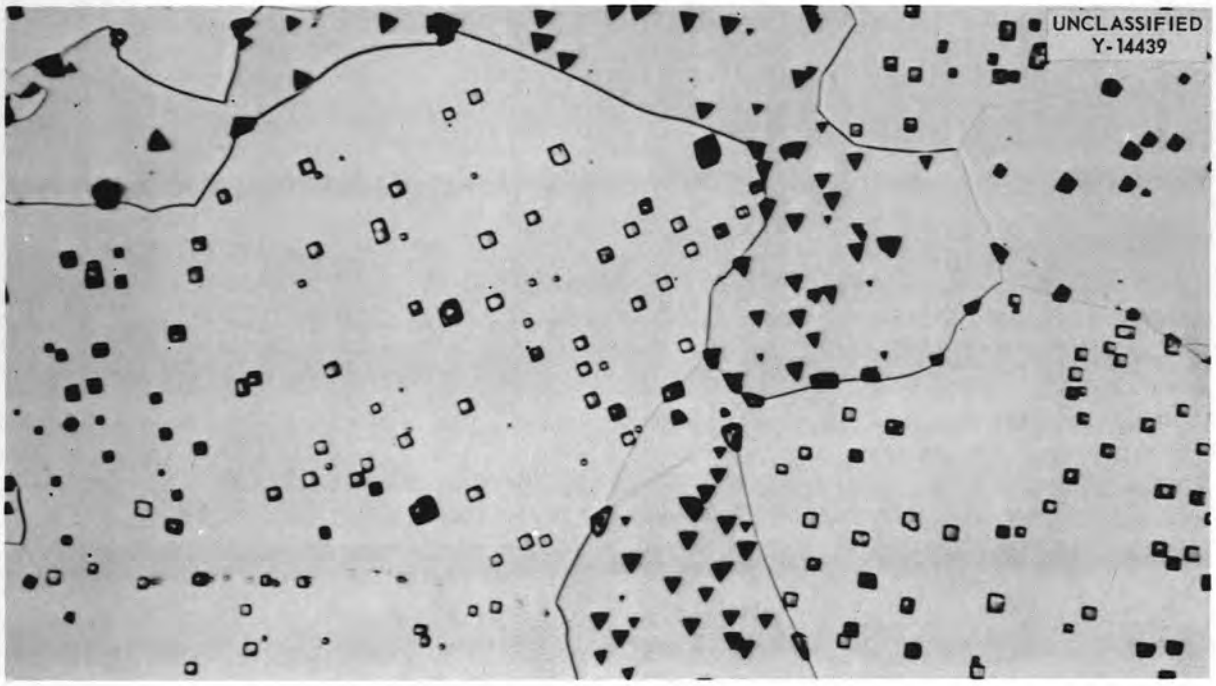

Fig. 8. Transverse Section of Aluminum Rod Extruded at 450°F and 615 fpm and Annealed at 1000°F. 500X.

UNCLASSIFIED
ORNL-LR-DWG 8161

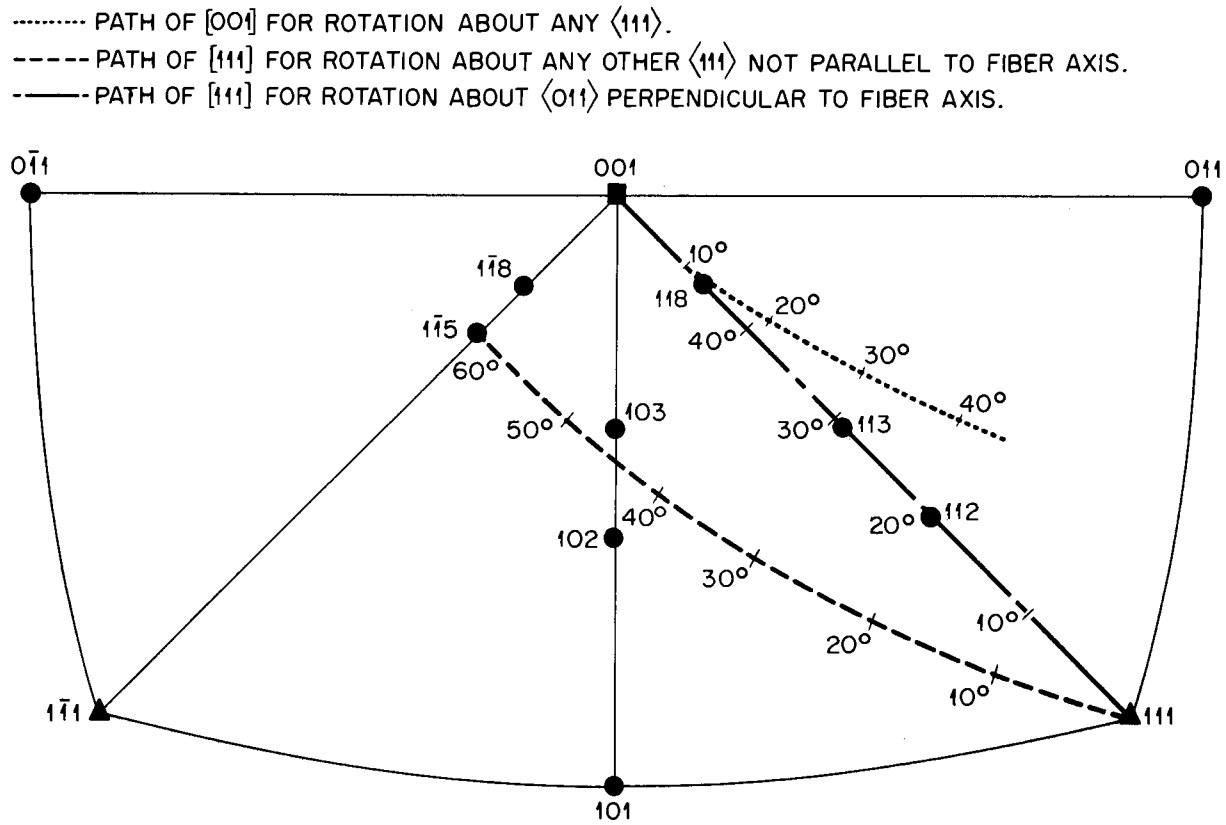

Fig. 9. Recrystallization Reorientations for Fiber-Texture Components in Face-centered Cubic Metals.

a rotation of any amount by using that <111> direction parallel to the extrusion direction as the axis of rotation. It has been shown[3] that high boundary mobility is associated with boundaries where there is a rotation of 30 to 40 deg around <111>.

The <118> component cannot be derived from the <111> matrix by any simple rotation if the <111> directions are used as axes of rotation. A rotation of 12 deg about any <111> not parallel to the extrusion direction will produce the <118> orientation from the <001> position. However, grain boundaries between regions having orientation differences of this magnitude have been found to be fairly immobile. Furthermore, a grain size much larger than that seen in Fig. 8 would be required in order that the 12% of material having the <001> texture in the as-extruded rod could grow to 66% of the volume of the recrystallized rod.

A rotation of 45 deg about a <011> direction 90 deg from the <111> parallel to the fiber axis will bring the <111> to a position within 2 deg of the <118> component of the annealed texture.

It appears that the <111> and <118> recrystallized grains may originate in the deformed <111> matrix and that annealing does not further reorient the <001> recrystallized grains formed during the deformation process.

PREFERRED ORIENTATION IN EXTRUDED THORIUM ROD

L. K. Jetter C. J. McHargue

With the use of methods for obtaining the distribution of the fiber axis with respect to the crystallographic axes, a study was made of the fiber-texture type of preferred orientation which develops in some thorium rod.

Two 1-in.-dia thorium rods were extruded from a 3-in.-dia billet (extrusion ratio 9) at a billet

temperature of 850°C. One rod was extruded at 600 fpm and the other at 1 fpm. Pole-distribution data were obtained on 0.19-in. spherical x-ray diffraction specimens by the spectrometric method.

The pole-distribution charts (R vs ϕ) for the {111}, {002}, and {022} planes for the specimen taken from the rod extruded at the slower speed are given in Fig. 10; the charts for the rod extruded at the faster speed are given in Fig. 11. These

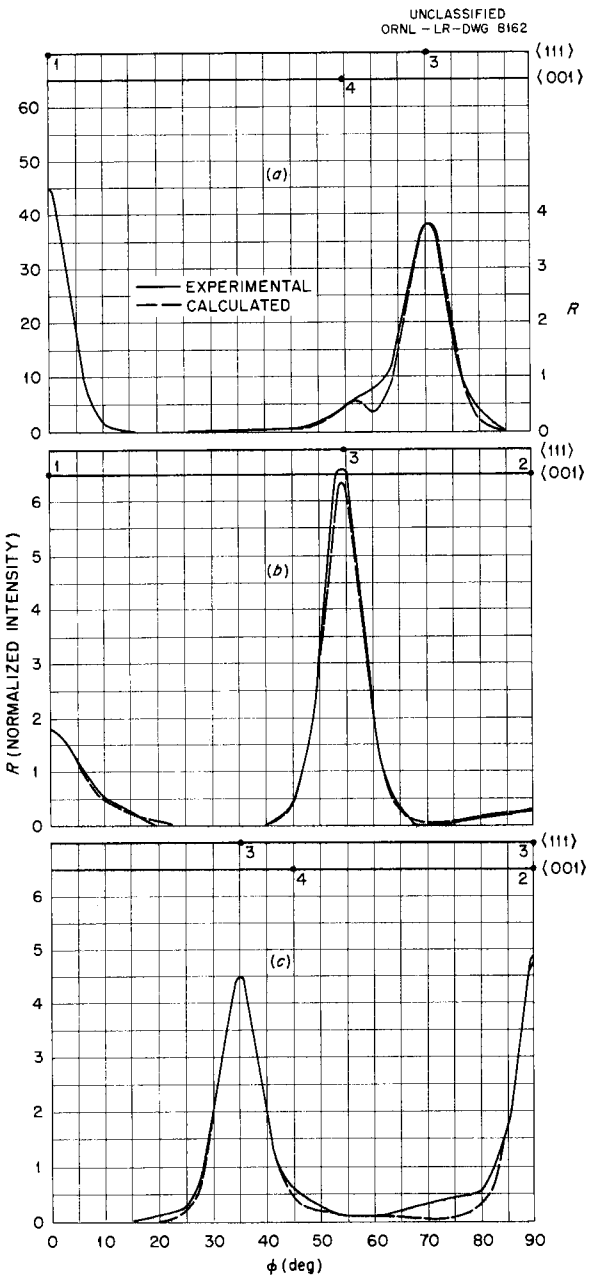

Fig. 10. Pole-Distribution Charts for Thorium Rod Extruded at 850°C and 1 fpm. (*a*) {111}. (*b*) {002}. (*c*) {022}.

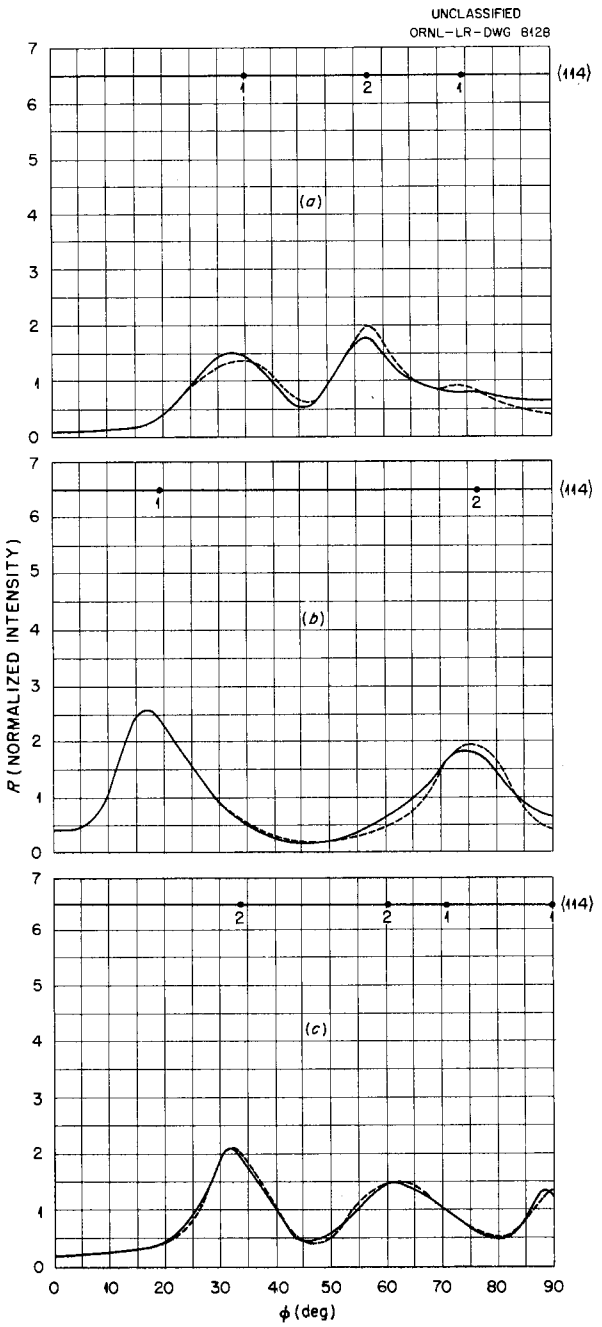

Fig. 11. Pole-Distribution Charts for Thorium Rod Extruded at 850°C and 600 fpm. (*a*) {111}. (*b*) {002}. (*c*) {022}.

UNCLASSIFIED
ORNL-LR-DWG 8129

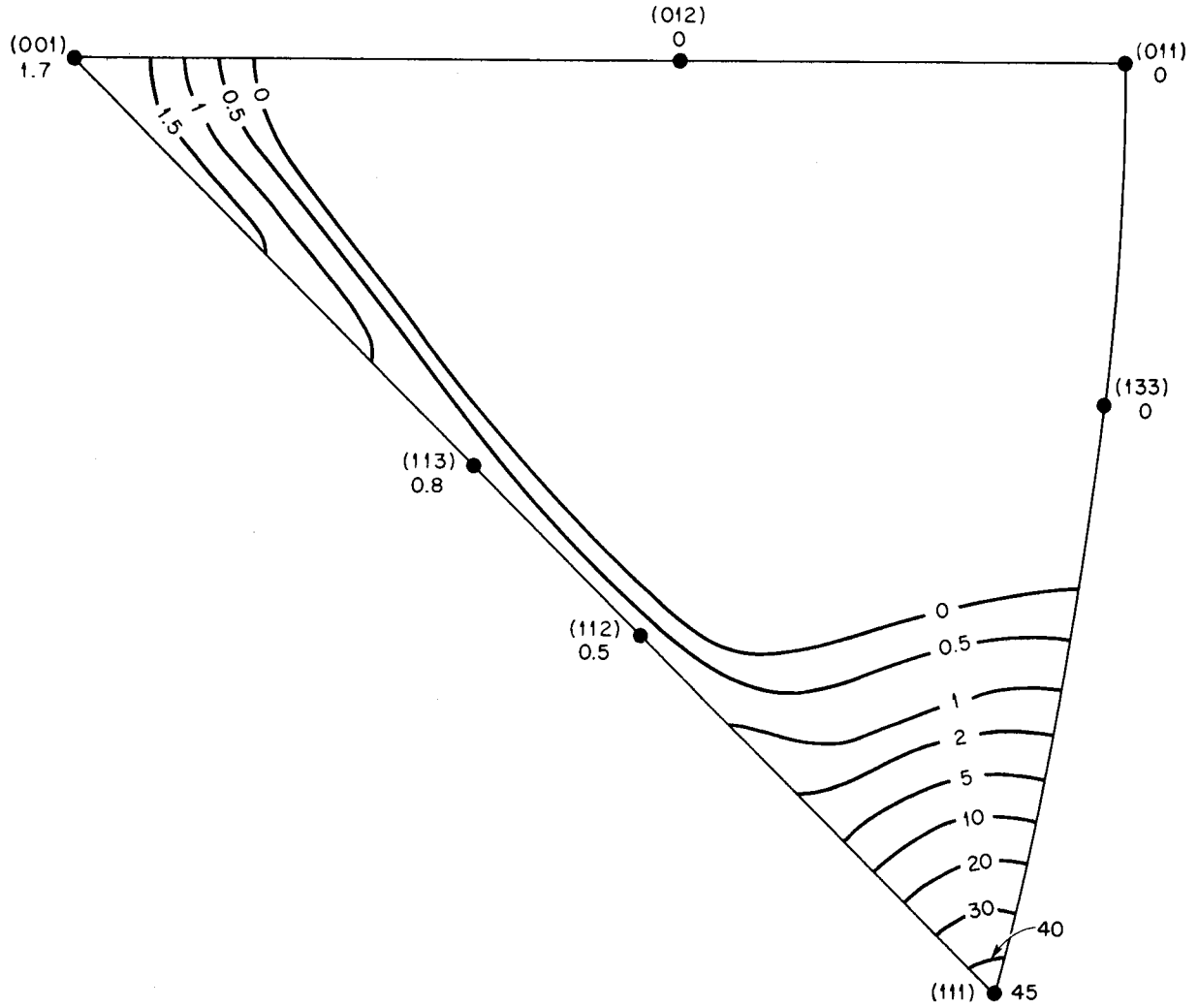

Fig. 12. Fiber-Axis Distribution Chart Representing the Preferred Orientation in Thorium Rod Extruded at 850°C and 1 fpm.

curves were obtained by normalizing the x-ray diffraction data (I vs ϕ).

The axis-distribution charts (T vs ϕ,β), deduced from the pole distributions, are given in Figs. 12 and 13. The pole distributions calculated from these assumed axis distributions and their comparisons with the experimental curves are shown in Figs. 10 and 11.

The axis-distribution chart for the specimen taken from the rod extruded at the slower speed shows the texture to be duplex, the <111> and <001> being the preferred crystallographic directions of the fiber axis. The axis density at first falls off symmetrically from the peak at <111> but later falls off asymmetrically from this peak and from that at <001> and forms a saddle along the <$\bar{1}$10> zone. The ratio of the volume fraction of the material with the <111> component to the volume fraction with the <001> component was computed from the pole distribution charts of Fig. 10 and was found to be 13.2. This means that 93% of the volume had a <111> fiber axis and that 7% had a <001> fiber axis.

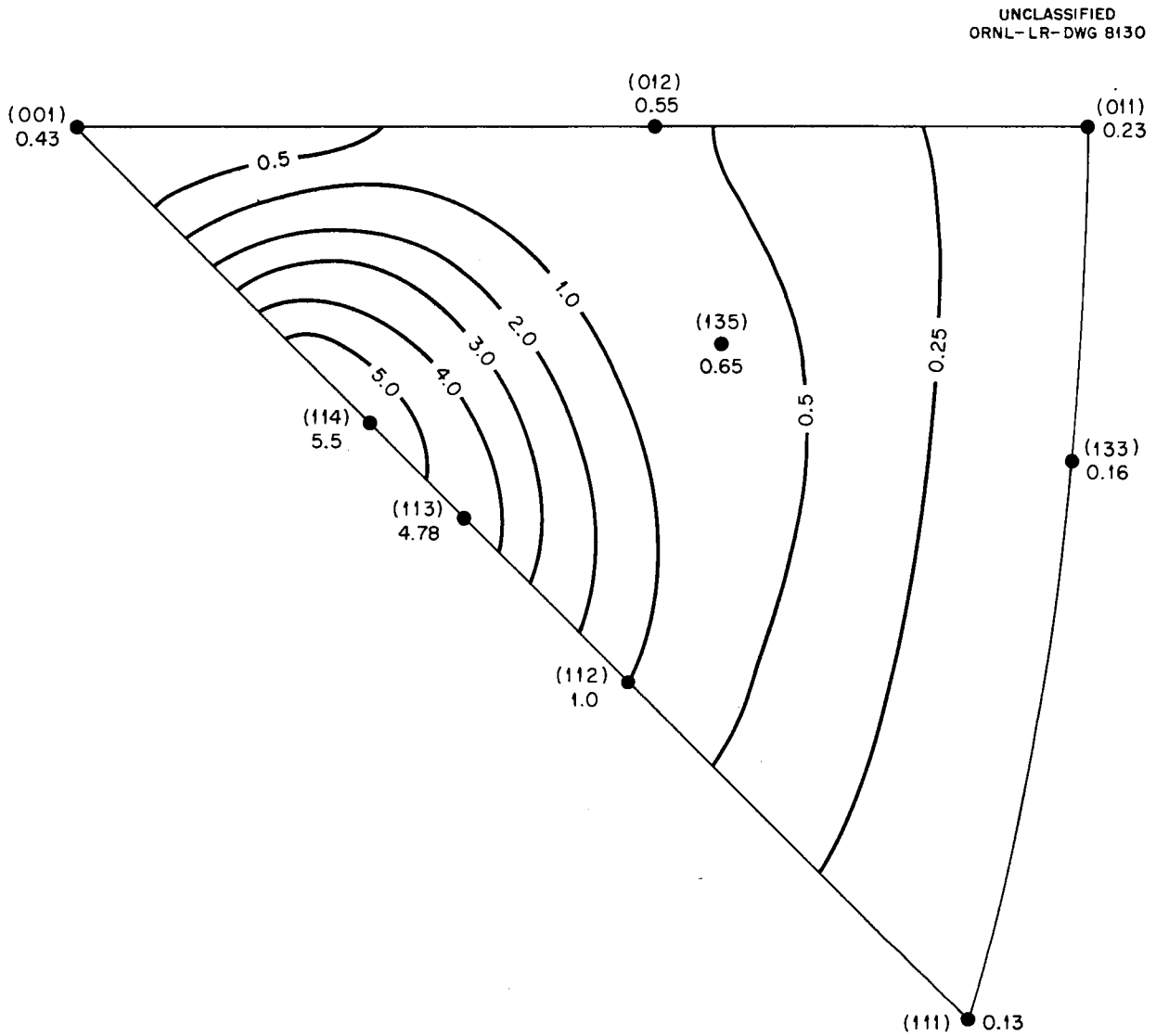

Fig. 13. Fiber-Axis Distribution Chart Representing the Preferred Orientation in Thorium Rod Extruded at 850°C and 600 fpm.

The axis-distribution chart for the specimen taken from the rod extruded at the faster speed is given in Fig. 13 and shows a single <114> fiber axis. The axis density falls off symmetrically from the peak at this position.

The photomicrographs of Figs. 14 and 15 and the x-ray transmission photograms of Fig. 16 show that the rod extruded at the slower speed contains very little, if any, recrystallized material, whereas the rod extruded at the faster rate was completely recrystallized.

The behavior of thorium with respect to deformation-fiber-texture formation is similar to that of aluminum. In rods extruded so that little recrystallization occurs, a strong <111> fiber texture is present in all deformed grains, and a weak <001> fiber component is present in any recrystallized grains. Thus, it would appear that a single <111> fiber texture would be developed in aluminum and thorium rods extruded in such a manner that no recrystallization occurred.

Thorium rod which completely recrystallized during the fabrication process contained a single <114> fiber texture. Increasing the amount of

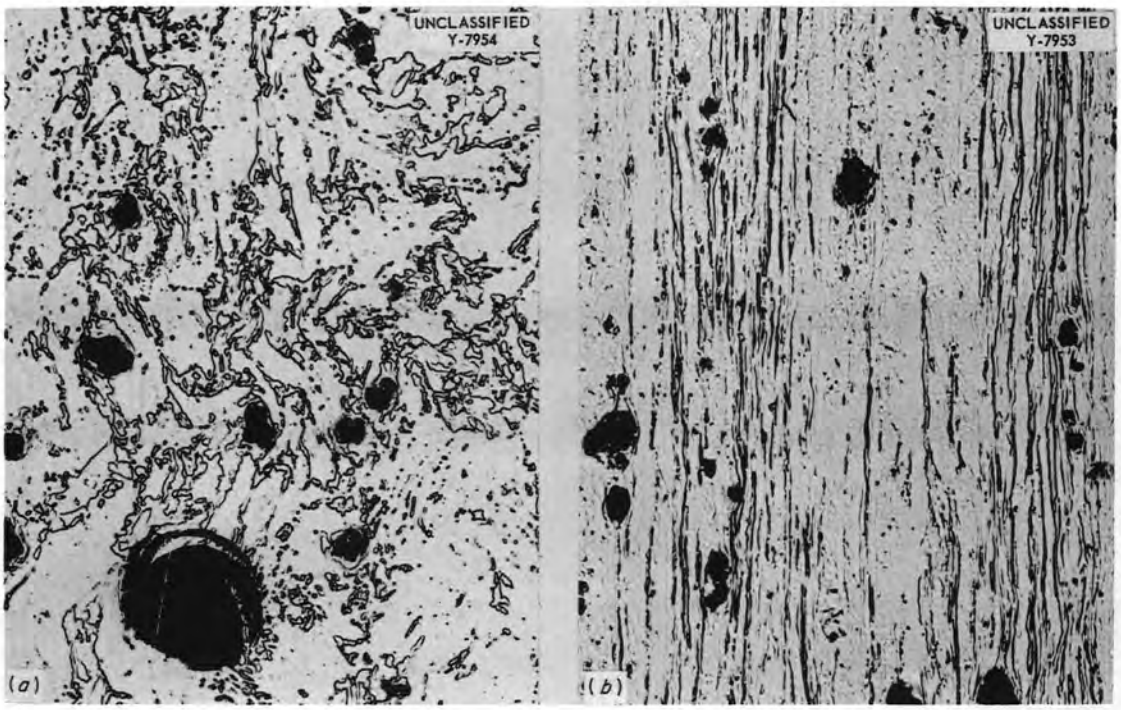

Fig. 14. Thorium Rod Extruded at 850°C and 1 fpm. (*a*) Transverse. (*b*) Longitudinal. 250X. Reduced 21%.

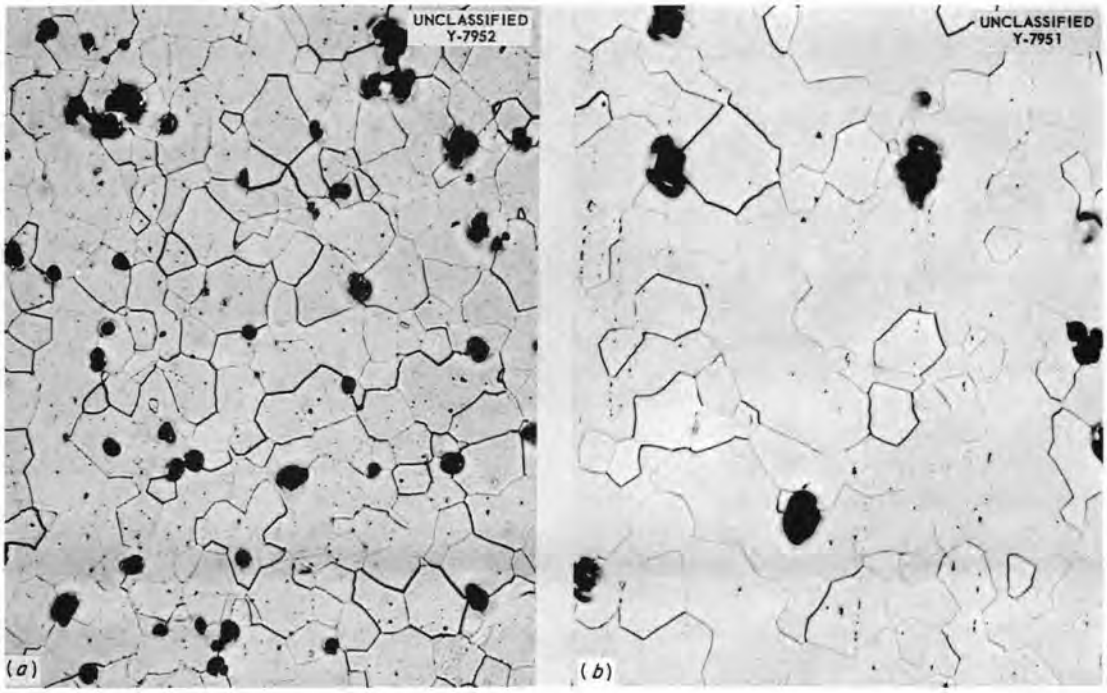

Fig. 15. Thorium Rod Extruded at 850°C and 600 fpm. (*a*) Transverse. (*b*) Longitudinal. 250X. Reduced 22%.

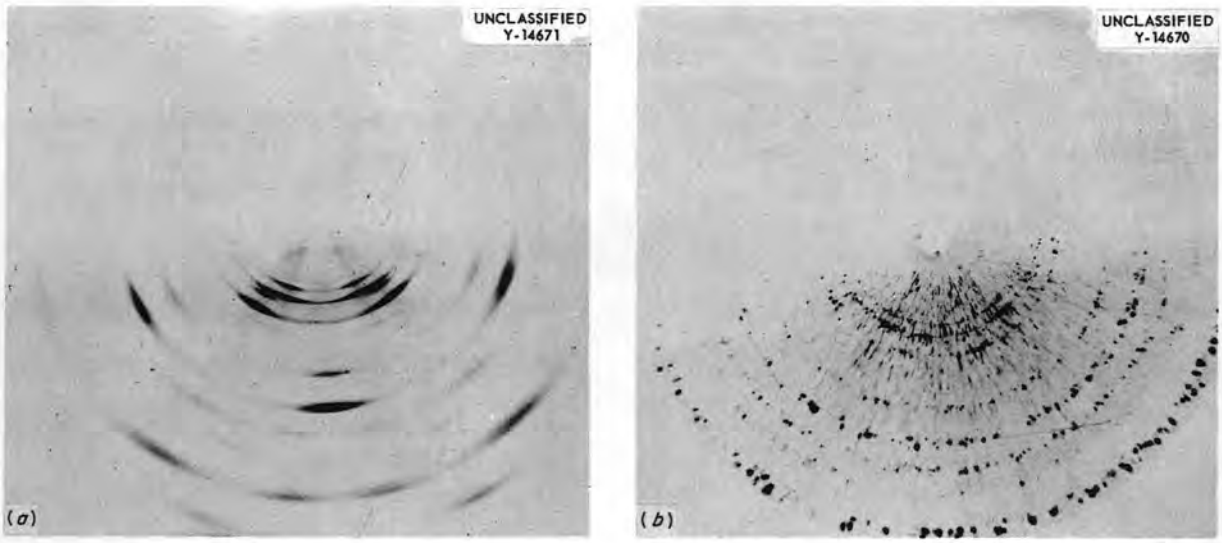

Fig. 16. Reflection X-Ray Diffraction Patterns for Thorium Rods Extruded at (*a*) 850°C, 1 fpm, (*b*) 850°C, 600 fpm.

recrystallization during fabrication of aluminum rods was accompanied by a corresponding increase in the <001> component of the fiber texture. The reasons for this difference in the behavior of these two face-centered cubic metals are not apparent at the present time.

It can be seen in Fig. 9 that a 36-deg rotation of the <111> fiber-texture component about a <011> direction perpendicular to the fiber axis gives the <114> fiber texture.

Thorium rod extruded so as to minimize the degree of recrystallization developed a duplex fiber texture – 93% <111> and 7% <001>. The minor <001> component is attributed to a small amount of recrystallized material. On extruding under conditions which cause complete recrystallization, a single <114> fiber texture developed from the <111> deformed matrix.

FUNDAMENTAL STUDIES OF ALLOYING

The Silver-Zirconium System

D. S. Easton J. O. Betterton, Jr.

Silver is the first element in the solute series (silver, cadmium, indium, tin, and antimony) which is being added to zirconium in a general program of zirconium-phase-diagram determinations. Study of these solutes has been undertaken to determine the effects of elements of known valency in zirconium.

The general nature of the silver-zirconium phase diagram has been reported previously[5] and is shown in Fig. 17. In the earlier report reference was made to possible effects of minor impurities, such as iron and nickel, upon the constitution of zirconium-rich alloys. In particular it was supposed that the alpha solid-solubility limit would be considerably greater than the <0.12 at. % silver determined at that time, providing that alloys could be prepared with zirconium of greater purity.

Recent experiments with zirconium of improved purity have shown that this is indeed true. The results are shown in Fig. 18, which is an enlarged section of the phase diagram in the eutectoid region. The alpha-solubility limit has been increased to 0.7 to 0.8 at. % silver by the use of zirconium containing 63 ppm iron and 7 ppm nickel.[6] The former results along the $\alpha/(\alpha + \gamma)$ boundary, which indicated lower solubility, have now been discarded on the basis of an analysis performed on a typical alloy, 0.2 at. % Ag, which contained 233 ppm Fe, 11 ppm Ni, 20 ppm Cu, 10 ppm Mo, and 31 ppm Si.

[5] J. O. Betterton, Jr., G. W. Cunningham, and D. S. Easton, *Met. Semiann. Prog. Rep. April 10, 1954*, ORNL-1727, p 125.

[6] All analyses for iron, nickel, copper, molybdenum, and silicon mentioned in this discussion were obtained by G. W. Leddicotte with the use of the activation-analysis method.

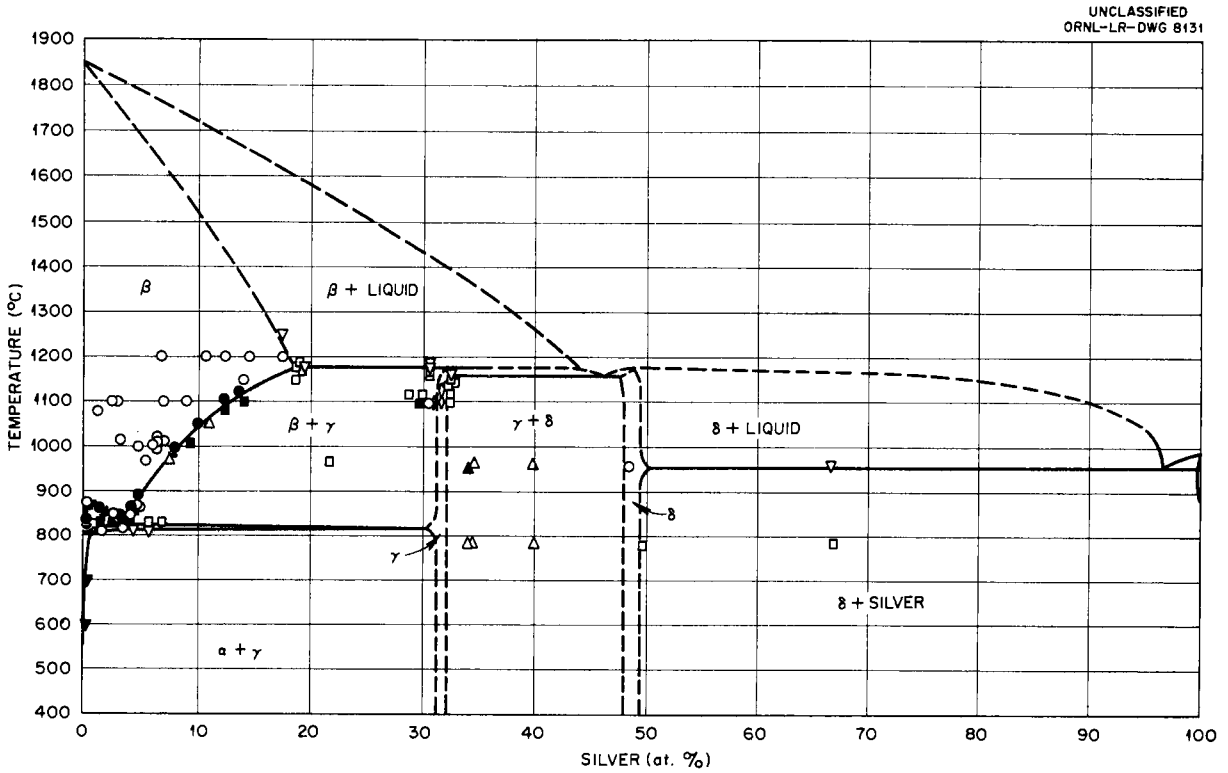

Fig. 17. Silver-Zirconium Phase Diagram.

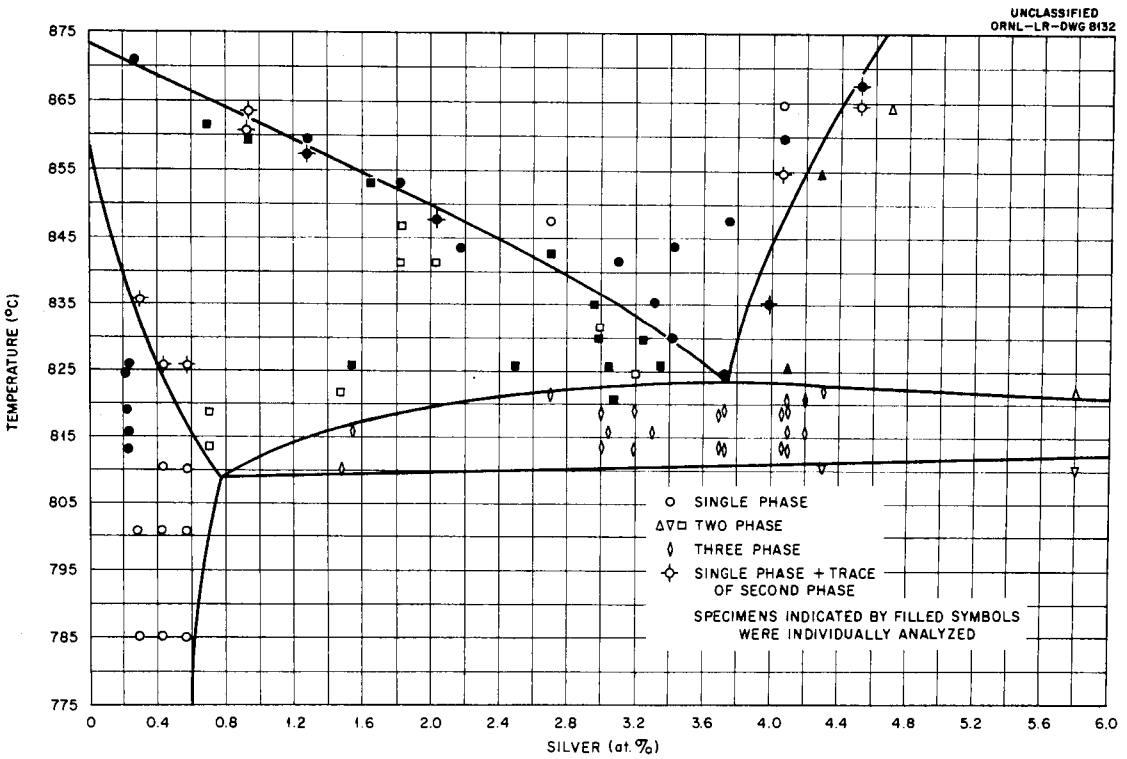

Fig. 18. Eutectoid Region of the Silver-Zirconium System.

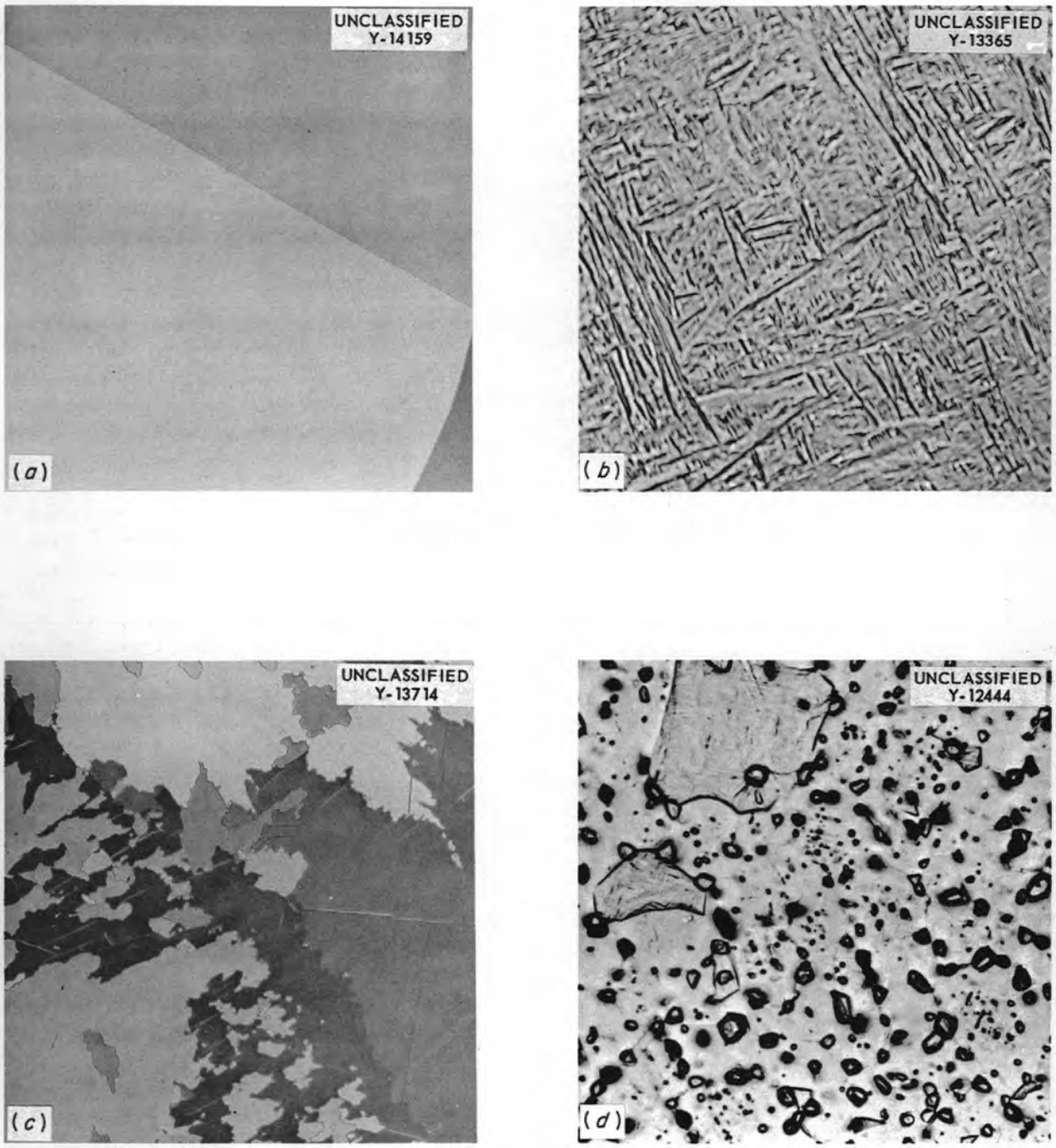

Fig. 19. Microstructures of Silver-Zirconium Alloys. (*a*) 0.6 at. % Ag, 810.4°C; homogeneous alpha solid solution; 100X. (*b*) 3.7 at. % Ag, 825°C; beta phase of eutectoid composition; 100X. (*c*) 0.3 at. % Ag, 871°C; homogeneous beta phase just above the ($\alpha + \beta$) region; 100X. (*d*) 4.1 at. % Ag, 813.5°C; example of a microstructure observed in the ($\alpha + \beta + \gamma$) region; 500X.

No attempt has been made to idealize the diagram of Fig. 18 to conditions of true binary equilibrium, as has been done in some earlier zirconium diagrams.[7] Rather, the results of a detailed investigation of the three-phase region ($\alpha + \beta + \gamma$) have been shown. This part of the investigation was made with three different batches of zirconium with iron ranging from 63 to 114 ppm and nickel from 7 to 23 ppm, and with essentially constant other impurities: 200 ppm carbon, 100 ppm hafnium, 5 to 10 ppm hydrogen, and 100 to 200 ppm oxygen.[8] Presumably, the three-phase effect is due to these impurities; and, since there was no immediate prospect of obtaining purer zirconium, the data are presented in this fashion.

The specimens which determine the $\beta/(\alpha + \beta)$ and the $\beta/(\beta + \gamma)$ boundaries include some of the former alloys made with zirconium containing 400 ppm iron and 270 ppm nickel. These data have been retained since recheck specimens, made with zirconium of low iron and nickel content, have agreed very well with the earlier work. New $\beta/(\alpha + \beta)$ and $\beta/(\beta + \gamma)$ boundaries, determined near the eutectoid composition in the temperature range 823 to 835°C, connect smoothly with the former boundaries. Also, determinations of the $\beta/(\beta + \gamma)$ boundary above 900°C had been done on zirconium containing 113 ppm iron and 20 ppm nickel, and this work smoothly fits the results in the range 840 to 900°C from alloys containing greater amounts of iron and nickel.

The microstructures of some of the silver-zirconium alloys are shown in Fig. 19. Figure 19*a* shows an alloy of 0.6 at. % silver which is entirely free of any $AgZr_2$ phase particles and illustrates the increased alpha solubility with the use of purer zirconium. Figure 19*b* shows an alloy which was very close to the eutectoid composition and which was annealed only several degrees above the temperature of the decomposition of the beta phase. Figure 19*c* illustrates the appearance of a homogeneous beta-phase alloy which has been transformed by quenching into a typical serrated grain structure. This alloy would surely be in the ($\alpha + \beta$) region if an appreciable increase in the oxygen content had occurred in casting. Finally, Fig. 19*d* illustrates the type of microstructure observed in the three-phase region – in this case, after 67 days of isothermal annealing.

[7] *Phase Diagrams of Zirconium-Base Binary Alloys; A Study of the Systems of Zirconium with Tin, Molybdenum, Copper, Wolfram, Chromium, Silicon, Aluminum, and Magnesium; Final Report, January 1, 1951–May 31, 1952,* COO-89, p 33 (April 14, 1952).

[8] The variation in oxygen is not between batches but represents differences between two different methods of analysis.

The Indium-Zirconium System

W. K. Noyce J. O. Betterton, Jr.

The general form of the zirconium-rich portion of the indium-zirconium system was found earlier[9] to consist of extended solid solutions of indium in both alpha and beta zirconium. The alpha- and beta-solid solutions were in equilibrium with a face-centered-cubic intermediate phase whose composition was approximately Zr_3In. The phase boundaries between the alpha and beta regions rose with indium addition, and eventually these phase boundaries terminated at the peritectoid reaction,

$$\alpha \rightleftharpoons \beta + Zr_3In$$

Refinements have now been made in the location of the boundaries of the ($\alpha + \beta$) region. Formerly, these boundaries were separated quite widely; and, when a lineal analysis of the volume proportion of the two phases was done on a series of alloys at the same temperature, this proportion did not obey the usual lever rule. This is shown by the dotted curve of Fig. 20. It is an effect which

[9] G. W. Boyd and J. O. Betterton, Jr., *Met. Semiann. Prog. Rep. April 10, 1954,* ORNL-1727, p 131.

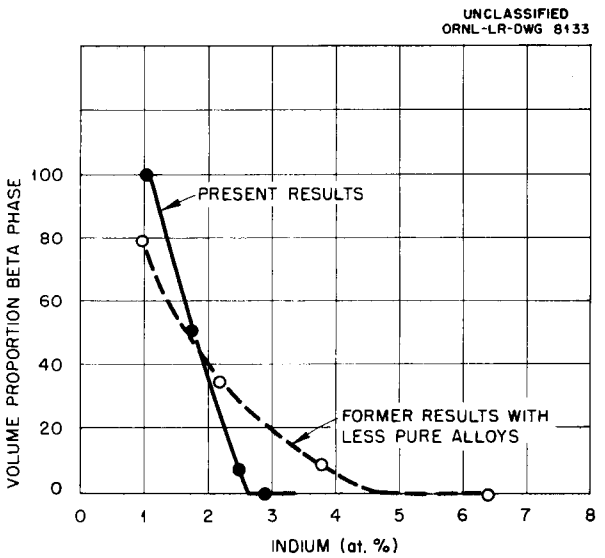

Fig. 20. Effect of Impurities on the Variation of the Volume Proportion of Alpha and Beta Phases in the ($\alpha + \beta$) Regions at 900°C.

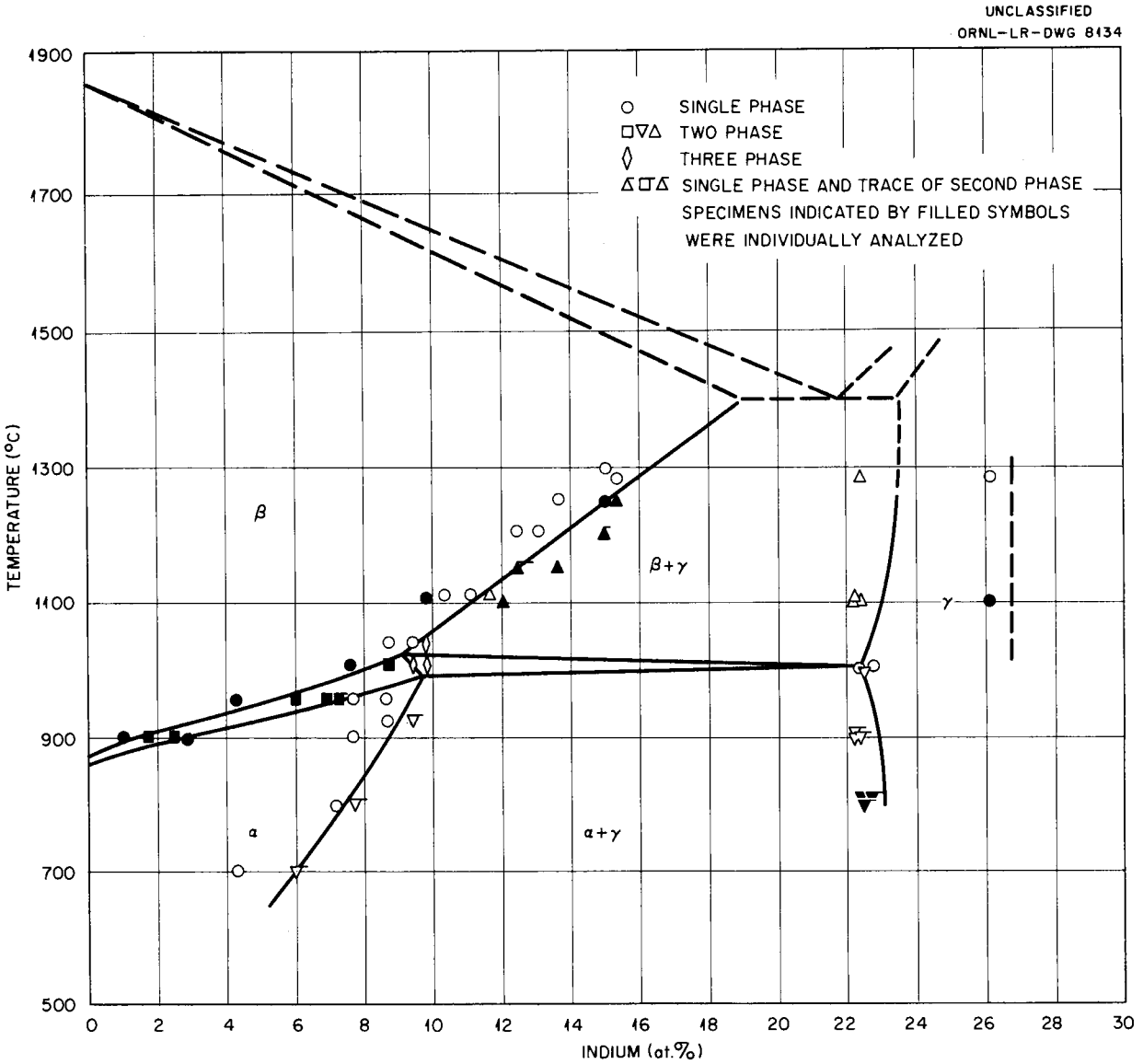

Fig. 21. Indium-Zirconium Phase Diagram.

might reasonably be expected from an impurity of low solubility in the alpha phase. The whole of the ($\alpha + \beta$) region has been reinvestigated with some of the purer zirconium used in the silver-zirconium case described above. The experimental points are shown in Fig. 21, and the new boundaries (solid lines) are compared with the former boundaries (dotted lines) in Fig. 22.

The α/β boundaries are seen to be closer together, and on Fig. 20 the solid line shows that these alloys give an approximate linear relationship between volume proportion and composition in the ($\alpha + \beta$) region. This, together with the Vickers hardness values of the new alloys, which extrapolate to a range of 70 ± 10 VPN compared with 95 ± 10 VPN for earlier alloys, indicates that the present results are certainly to be preferred. The peritectoid temperature was found to be lower, but the need for a purer zirconium is indicated by the presence of a three-phase region in the vicinity of the peritectoid reaction. The impurities are somewhat lower (60–170 ppm C, 50–100 ppm O, 100 ppm Hf, 63 ppm Fe, 10–40 ppm N, 8 ppm Si, 7 ppm Ni, 5 ppm H) in a third type of zirconium now

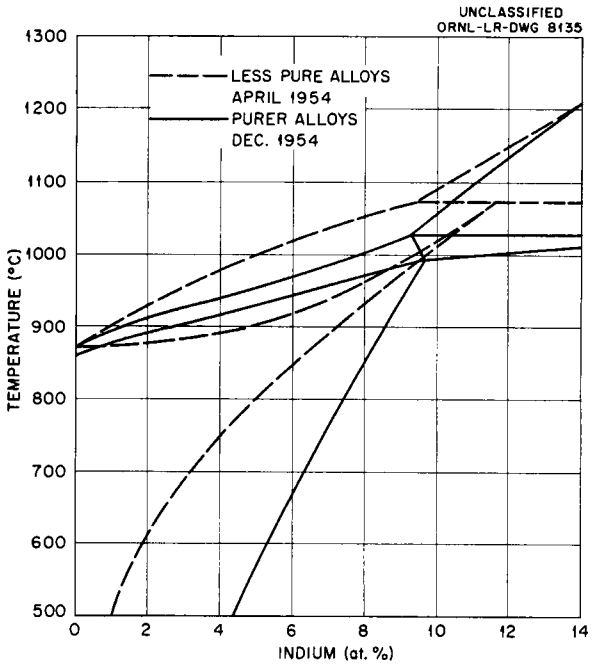

Fig. 22. Effect of Increased Purity of Indium-Zirconium Alloys.

being used to investigate the peritectoid region more fully, and it is hoped that, in the absence of a single temperature for the reaction, the boundaries of only a narrow three-phase region will be determined.

The investigation of the $\beta/(\beta + \gamma)$ boundary with the new zirconium has shown agreement with the former results so that the results above 12% indium have been retained and are included in Fig. 21. Similarily, the limited older results which were available on the boundaries of the gamma phase have been retained and are shown in Fig. 21. In the case of the $\alpha/(\alpha + \gamma)$ boundary, only critical specimens of the newer type zirconium have been used to plot the boundary, although both the noncritical alloys and the older alloys agree with the position of this boundary.

The location of the $\alpha/(\alpha + \gamma)$ boundary was confused by the presence of an impurity phase which occurred as very thin ledges after etching. This phase is illustrated in Figs. 23*a*, *b*, and *c*. The alloy, 8.6 at. % indium, is shown after (*a*) annealing the $(\alpha + \beta)$ region at 1007°C, and (*b*) in the alpha region at 957°C and (*c*) at 925°C. In the first case the minute particles were observed in the beta grains of the two-phase alloy, whereas in Figs. 23*d* and *e* similar material appeared in the otherwise homogeneous alpha phase. These effects were not influenced appreciably by temperature, and other specimens in the alpha region showed that they were apparently independent of indium content. Attempts to identify this material by x-ray diffraction were not successful, apparently because of the minute quantity present, and attempts to resolve the particles at higher magnifications with electron microscopy were unsuccessful because of the adverse etching character of the particles.

In Figs. 23*c*, *d*, and *e*, the temperature of annealing is kept constant at 925°C, while the indium content is increased. Here the increase in indium content is accompanied by the appearance of gamma-phase particles, which in most cases can be resolved and identified and which increase with indium content sharply. The $\alpha/(\alpha + \gamma)$ boundary is based on the appearance of second-phase particles, as shown in Fig. 23*d*, and the traces of minute particles, as shown in Fig. 23*c*, have been disregarded in Fig. 22.

The difference in the effect of trivalent indium and that of univalent silver on the allotropic transition temperature of zirconium may be observed by comparing Fig. 22 with Fig. 18. This difference has been taken as the basis for regarding zirconium as being approximately divalent, for in this case the indium is considered to add electrons to the average number in the alloy, and the silver is considered to reduce this number. Hence, the observed effects would result if the phase boundaries are assumed to be functions of electron concentration.

Zirconium-Lead Phase Diagram

G. D. Kneip, Jr. J. O. Betterton, Jr.

A redetermination of the previously determined phase boundaries in the region of the zirconium α,β transition has been undertaken with higher-purity zirconium used as the base material. The general form of the diagram showing a peritectoid formation of the α phase, as previously reported, has been confirmed. Preliminary results indicate the initial slope of the $\beta/(\alpha + \beta)$ boundary to be approximately 20°C per atomic per cent lead.

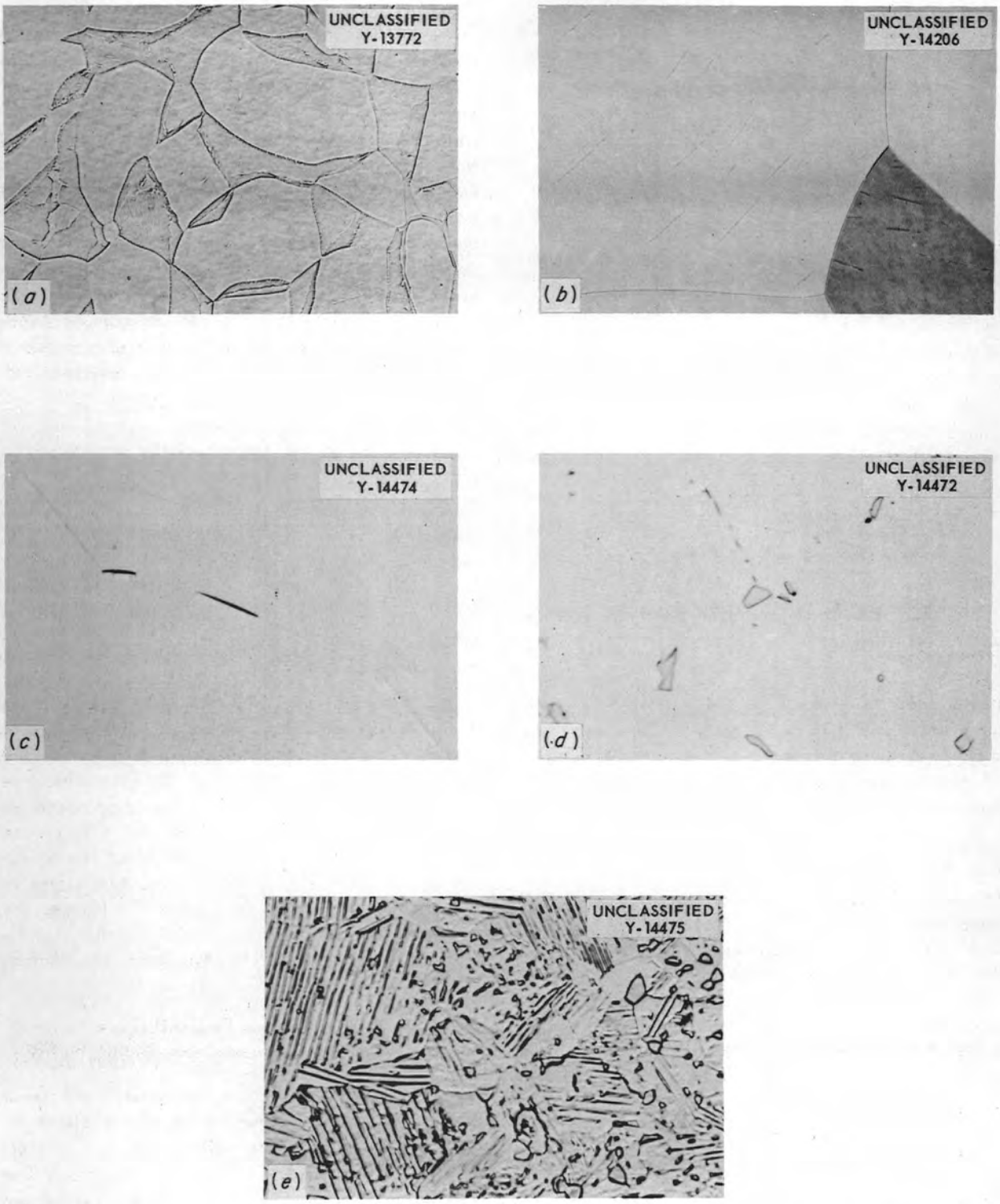

Fig. 23. Microstructures Illustrating the Difference Between Gamma Phase and Impurity Particles in Indium-Zirconium Alloys. (*a*) 8.6 at. % In, 1007°C; ($\alpha + \beta$) region, small particles in β; 100X. (*b*) 8.6 at. % In, 957°C; alpha phase + small particles; polarized light; 100X. (*c*) 8.6 at. % In, 925°C; alpha phase + small particles; 1200X. (*d*) 9.4 at. % In, 925°C; ($\alpha + \gamma$) region; 500X. (*e*) 9.8 at. % In, 925°C; ($\alpha + \gamma$) region; 500X.

FLOATING-ZONE PURIFICATION OF ZIRCONIUM

G. D. Kneip, Jr. J. O. Betterton, Jr.

Zirconium with a lower impurity content than grade 1 crystal bar is needed to undertake the study of the binary alloy systems of zirconium which exhibit very limited solubility of the alloying element in zirconium or which have eutectoid or peritectoid temperatures near the transition temperature of zirconium. For this reason the investigation of molten-zone refining has been continued.

Previous work indicated that the instability of the floating zone was sufficiently great for large undulations to occur in the surface of the zirconium rod (5-mm dia) during the first pass of the molten zone. These undulations adversely affected the stability of the molten zone so that further passes were impractical.

Since, theoretically, the floating zone should be more stable for smaller diameters, several quartz capsules containing lengths of 3-mm-dia zirconium rod were evacuated, sealed, and tested. Little improvement in the stability of the zone was found; apparently, this was due to the increased ratio of the length of the zone to the diameter of the rod. A further experimental difficulty found in the case of the smaller diameter rod was the increased tendency for the rod to bow out during heating because of the thermal expansion of the zirconium.

The original apparatus with the dynamic vacuum system was then modified to permit nearly unrestrained thermal expansion of the zirconium rod during heating and to get an improved vacuum in the melting chamber. Figure 24 shows the results of making a single pass on 6.4-mm-dia zirconium rod and with the molten zone moving upward at a speed of 12.5 mm/min. The surface in this case is very nearly smooth, with few undulations. The analytical results for this bar are not yet available, and therefore the efficiency of the purification for a single pass cannot yet be assessed. Figure 25 shows the results of a second pass over a surface similar to that shown in Fig. 24. The irregularities on the surface of the bar caused by the first pass are so large as to make the second-pass molten zone fairly unstable for the power input and traverse speed conditions used. The large undulations which occurred on the second pass, as shown in Fig. 25, are presumably, the result of the stepwise power control of the high frequency power source. A power source with a continuously variable power output was next used, with the result that three passes were successfully made, and a relatively smooth surface resulted, as shown in Fig. 26. This specimen is being analyzed for variations in the impurity content.

UNCLASSIFIED
Y-14673

Fig. 24. Zirconium Rod After Single Pass of the Molten Zone.

UNCLASSIFIED
Y-14616

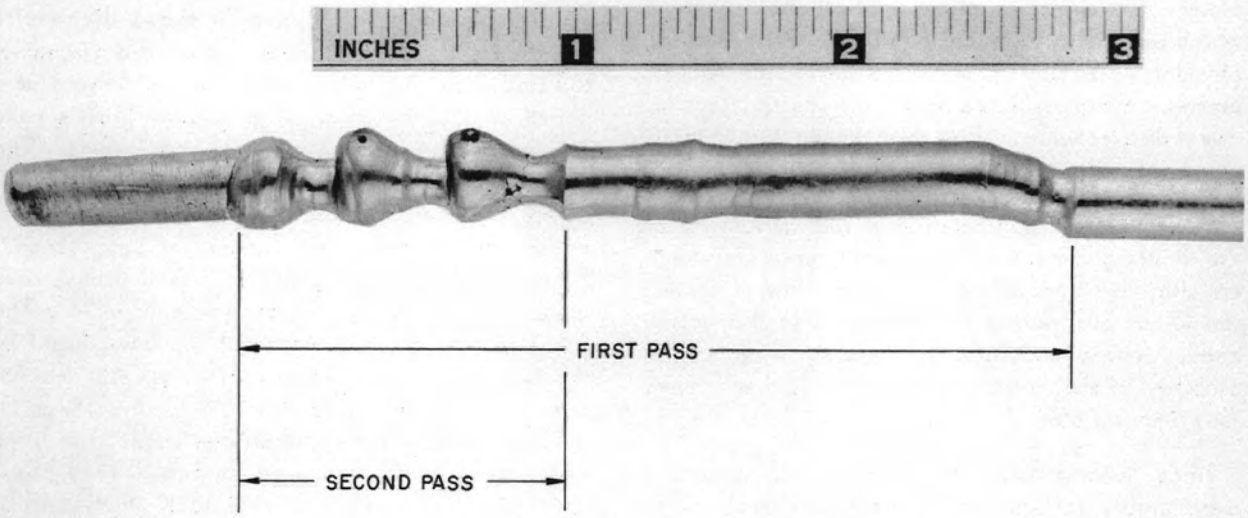

Fig. 25. Zirconium Rod After One and Two Passes of the Molten Zone.

UNCLASSIFIED
Y-15012

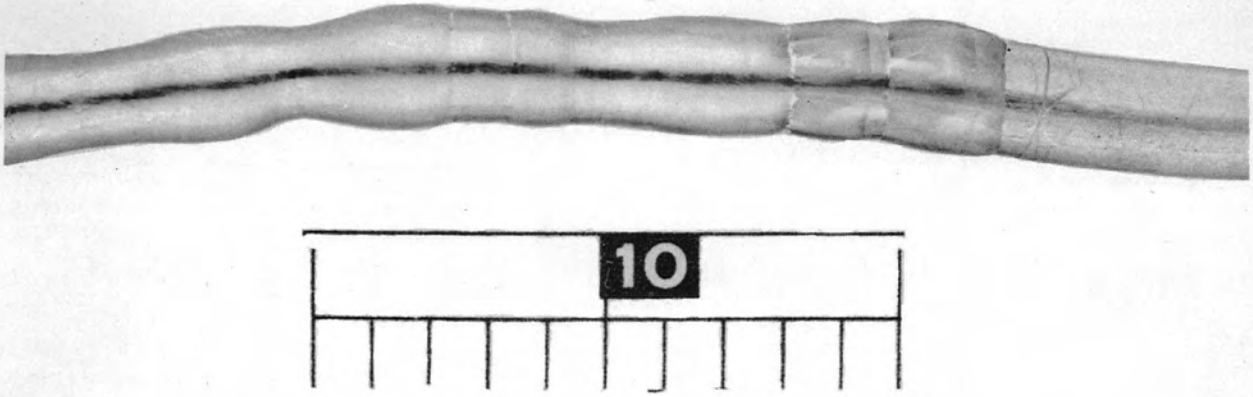

Fig. 26. Zirconium Rod After Three Passes of the Molten Zone. A continuously variable power source was used.

HRP METALLURGY

E. C. Miller

G. E. Elder
J. I. Federer
W. J. Fretague
T. W. Fulton
W. O. Harms
W. J. Leonard
G. B. Wadsworth
C. H. Wodtke
J. J. Woodhouse

PHYSICAL METALLURGY OF TITANIUM AND OF ZIRCONIUM ALLOYS

W. J. Fretague

Commercial Titanium

Investigations were continued to determine the cause of the embrittlement of commercial titanium.[1] Laue and Debye films, obtained with specimens prepared from the exposed corrosion specimen holder, exhibited extraneous reflections which could not be attributed to any of the known compounds of titanium. Metallographic examination of samples from the specimen holder revealed an as-yet-unidentified microconstituent. Examination of these microstructures under polarized light did not reveal the strong birefringence normally associated with the hydride phase. Vacuum fusion analysis for hydrogen did not reveal any increase in hydrogen content in the exposed specimen.

Three specimens of RC-70 titanium were sealed individually in evacuated Vycor capsules under a partial pressure of purified argon, heated at 250°C for periods of 500, 1000, and 2000 hr, respectively, and then water quenched to room temperature. These experiments were performed to determine whether embrittlement, as determined by impact testing the material from the exposed specimen holder, was due to the temperature of exposure alone or whether environment and temperature are both critical factors. Figures 27 through 34 illustrate typical microstructures obtained for the specimens. The metallographic evidence indicated that the unidentified microconstituent was present in all the thermally treated specimens, as well as in the sample from the exposed specimen holder, and, thus, that exposure at temperature, even in the absence of a corrosive environment, will cause the appearance of the unidentified constituent.

[1] W. J. Fretague, *Met. Semiann. Prog. Rep. Oct. 10, 1954*, ORNL-1875, p 52.

Zirconium Alloys

Zircaloy-2. – Room-temperature notched slow-bend tests (loading rate, 1 in./min) were performed on four Zircaloy-2 specimens from plate that was rolled from ingot 610D441RFB 4/5 BK. The specimen dimensions were $\frac{5}{16} \times \frac{1}{2} \times 1\frac{3}{8}$ in. with a 45-deg notch (0.040 in. deep, 0.005-in. root radius). The notch was located centrally in the $1\frac{3}{8}$-in. dimension and was parallel to the $\frac{1}{2}$-in. dimension. Load-deflection curves were obtained for each specimen, and the area under each curve from zero to maximum load was calculated. These values are recorded under each specimen number in Fig. 35. Specimens Z2A1 and Z2B1 had their $1\frac{3}{8}$-in. dimension perpendicular to the rolling direction of the plate, and specimens Z2A2 and Z2B2 were prepared with the $1\frac{3}{8}$-in. dimension parallel to the rolling direction of the plate. Figure 35 shows the appearance of the fractures obtained. Side-bend specimens ($\frac{5}{16} \times \frac{5}{16} \times 1\frac{3}{8}$ in.) were prepared and will be tested to check the high ductility that has been reported.[2]

Elevated-temperature (600°F) tensile tests were performed on two 0.505-in. specimens cut from a forging test block; the data are given in Table 3. Specimen LO-1 was taken parallel to the axis of the forging and represents the direction of the elongation. Specimen DT-1 was cut in the plane transverse to the longitudinal axis and represents the direction of elongation of the forging. Specimen DT-1 exhibits a decided anisotropy with very little reduction in thickness in the direction of the longitudinal axis. Considerably less anisotropy occurs in specimen LO-1 (see Figs. 36 and 37).

Elevated-temperature tensile tests were performed on a variety of Zircaloy-2 plate and welded-plate specimens obtained from scraps of plate

[2] Letter from Newport News Shipbuilding & Dry Dock Co., "Report on Physical Behavior of Zircaloy-2 Plate . . . ," dated April 8, 1954.

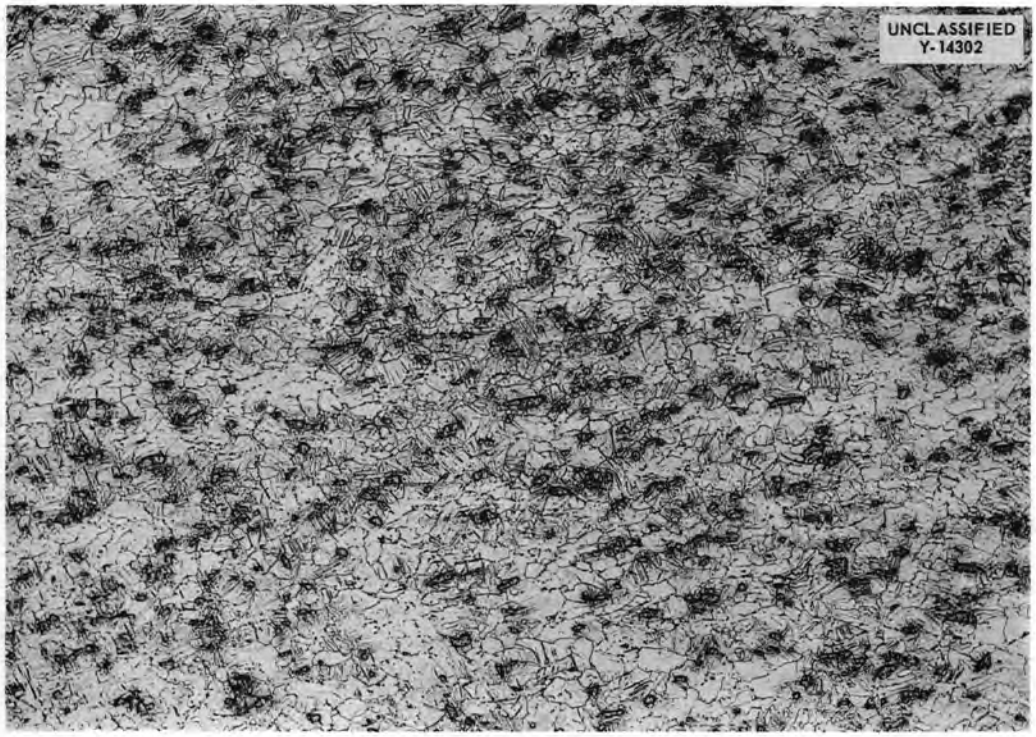

Fig. 27. Unalloyed Titanium Machined from Corrosion-Specimen Holder Exposed (~2000 hr) to a Variety of HRP Unirradiated Loop Environments. Etchant: 3 parts HF, 8 parts HNO_3, 8 parts H_2O. 100X. Reduced 14%.

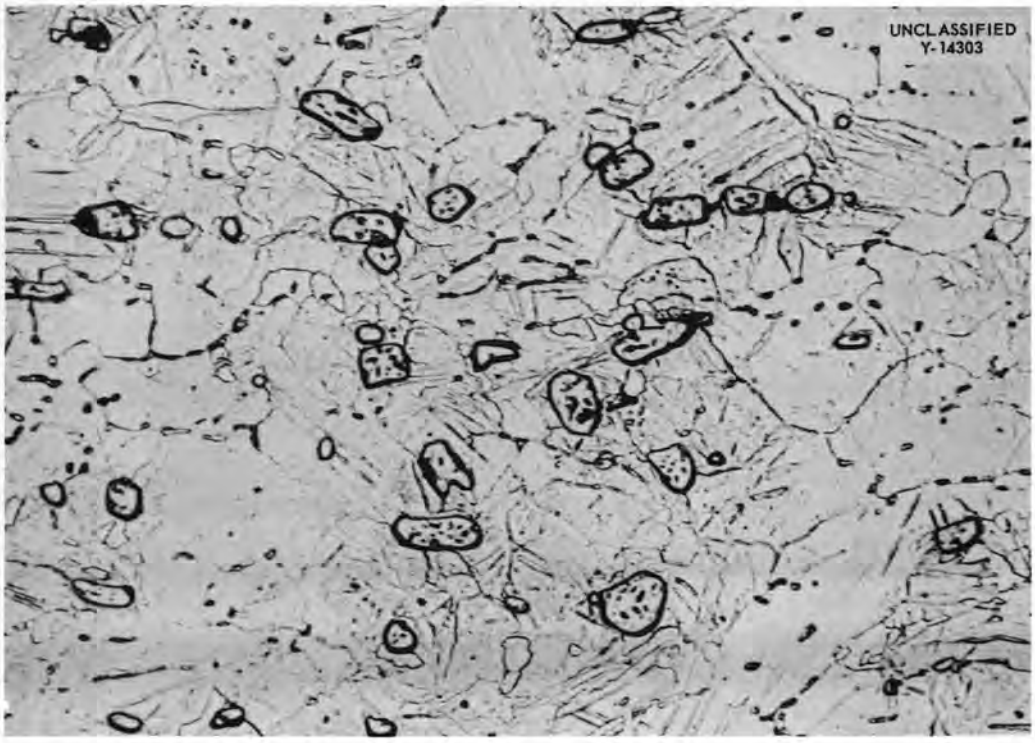

Fig. 28. Titanium Machined from Corrosion-Specimen Holder Exposed (~2000 hr) to a Variety of HRP Unirradiated Loop Environments. Etchant: 3 parts HF, 8 parts HNO_3, 8 parts H_2O. 500X. Reduced 14%.

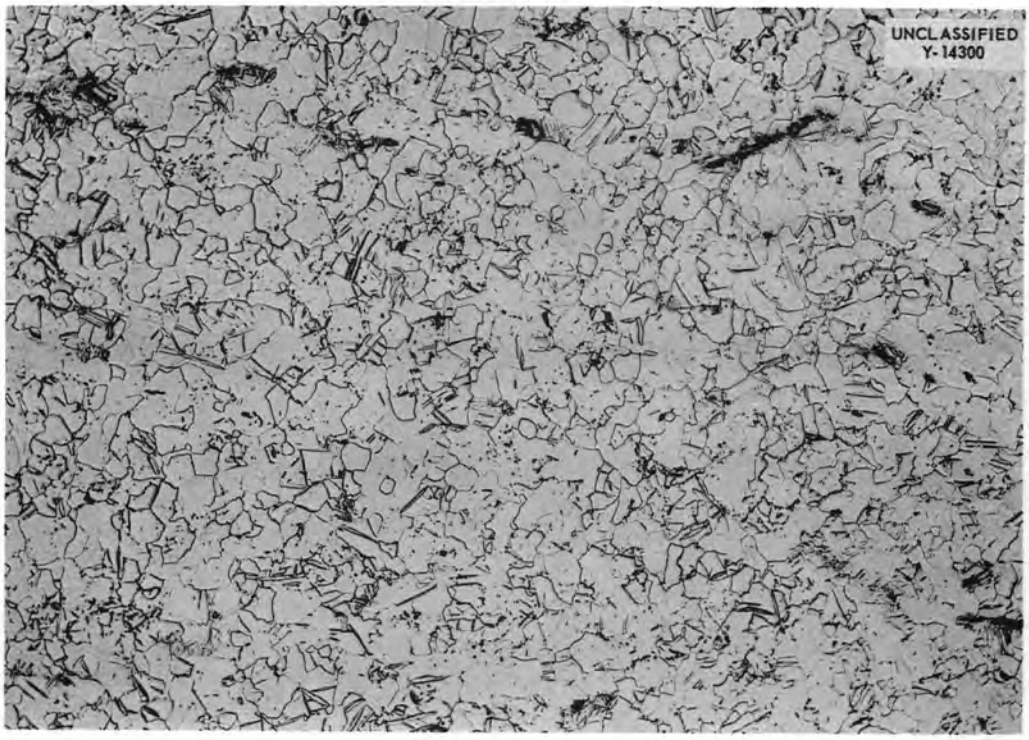

Fig. 29. Unexposed Titanium Bar Stock from Which Titanium Corrosion-Specimen Holder Was Machined. Etchant: 3 parts HF, 8 parts HNO_3, 8 parts H_2O. 100X. Reduced 14%.

Fig. 30. Unexposed Titanium Bar Stock from Which Titanium Corrosion-Specimen Holder Was Machined. Etchant: 3 parts HF, 8 parts HNO_3, 8 parts H_2O. 500X. Reduced 14%.

Fig. 31. Unalloyed Titanium Heated in Purified Argon at 250°C for 500 hr and Water-Quenched. Etchant: 3 parts HF, 8 parts HNO_3, 8 parts H_2O. 100X. Reduced 14%.

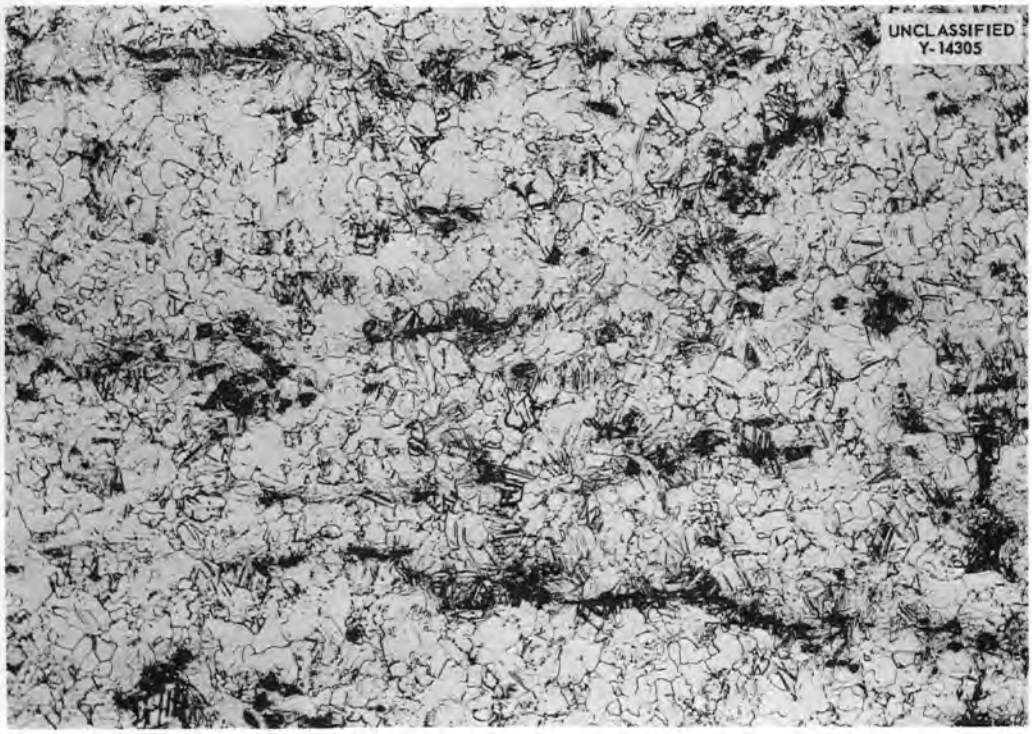

Fig. 32. Unalloyed Titanium Heated in Purified Argon at 250°C for 1000 hr and Water-Quenched. Etchant: 3 parts HF, 8 parts HNO_3, 8 parts H_2O. 100X. Reduced 14%.

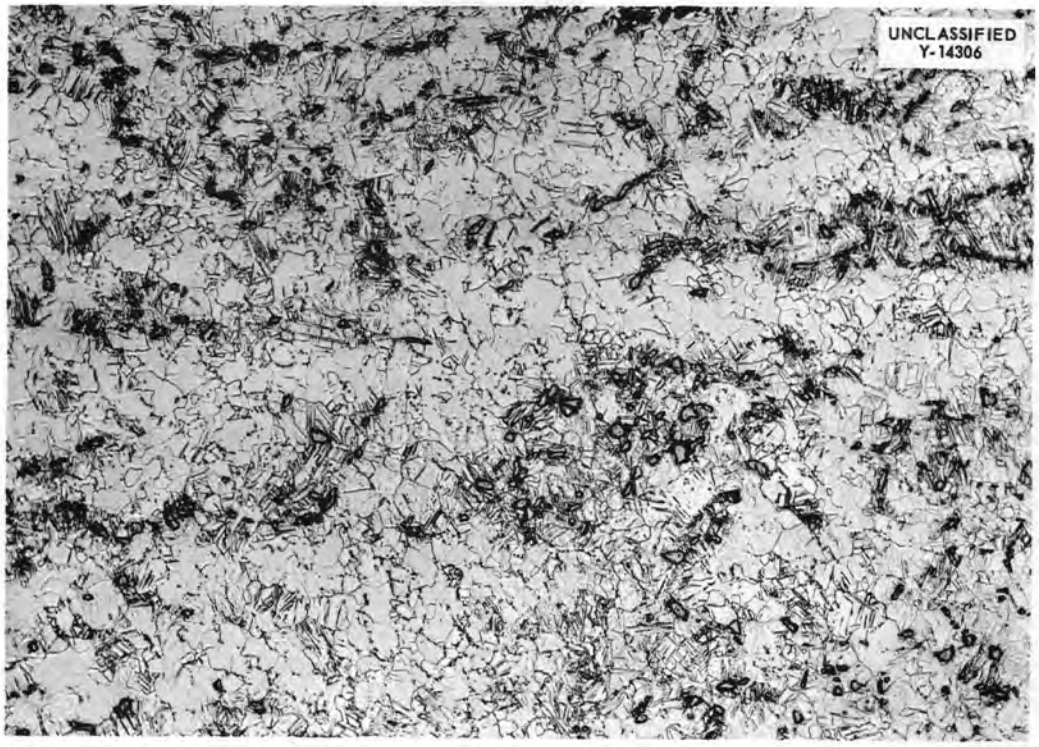

Fig. 33. Unalloyed Titanium Heated in Purified Argon at 250°C for 2000 hr and Water-Quenched. Etchant: 3 parts HF, 8 parts HNO_3, 8 parts H_2O. 100X. Reduced 14%.

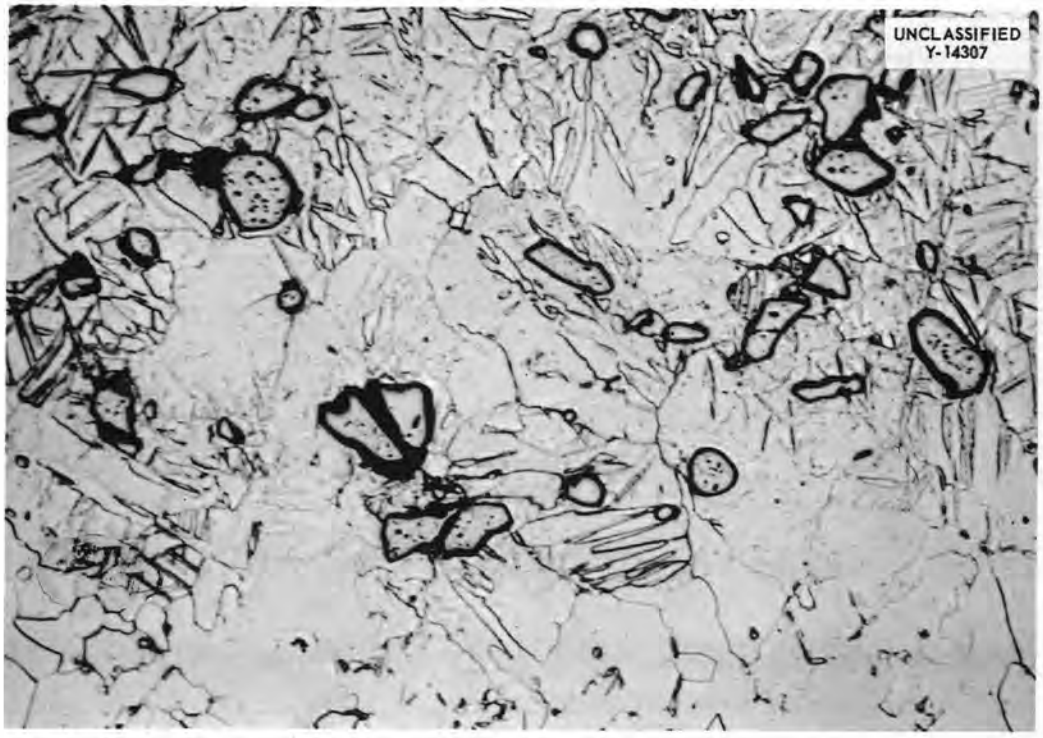

Fig. 34. Unalloyed Titanium Heated in Purified Argon at 250°C for 2000 hr and Water-Quenched. Etchant: 3 parts HF, 8 parts HNO_3, 8 parts H_2O. 500X. Reduced 14%.

UNCLASSIFIED
Y-12502

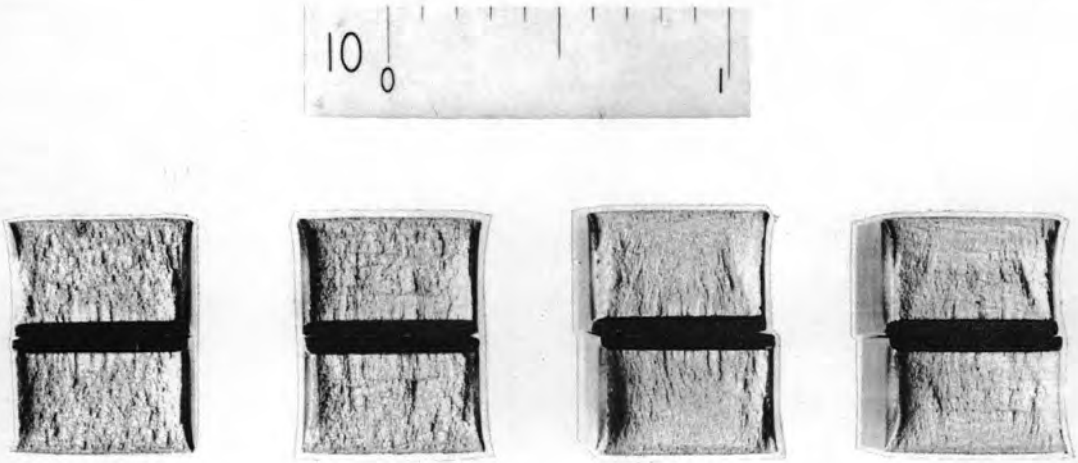

	Z2A1	Z2A2	Z2B1	Z2B2
ENERGY TO MAX. LOAD	27.30 in.-lb	22.80 in.-lb	25.80 in.-lb	28.05 in.-lb

Fig. 35. Notched, Slow-Bend-Test Specimens of Zircaloy-2.

TABLE 3. TENSILE DATA OBTAINED FROM ZIRCALOY-2 SPECIMENS TESTED AT 600°F

Specimen No.	Yield Strength, 0.2% Offset (psi)	Tensile Strength (psi)	Elongation, 2-in. Gage Length (%)	Reduction in Area (%)
DT-1	15,400	25,300	41.5	73.8
LO-1	24,200	32,900	36.0	66.2

which remained from the fabrication of the HRT Zircaloy-2 core tank. After the specimens were machined to final size, they were annealed in air at 1200°F for 30 min and air-cooled. The scale formed by this annealing treatment was removed by sandblasting. This annealing and sandblasting treatment approximates a similar postwelding treatment given to the core tank. The results obtained are reported in Table 4. Specimens 1, 2, 3, ZR3/8, and ZR1/4 were machined from plate. Specimens ZRG1, ZRFB, and ZR2 were machined from welded specimens made under various conditions.

Zircaloy-2 multiple-break impact specimens from the first in-pile loop (run DD) were impact-tested over the temperature range −196°C to 280°C. Similar specimens from in-pile loop mockup (run CC) were tested. The results of these tests are plotted in Figs. 38 and 39. The results reported previously for vacuum-annealed Zircaloy-2 control specimens are presented again in Fig. 40 for purposes of comparison. A comparison of

TABLE 4. MECHANICAL PROPERTIES OF ZIRCALOY-2 PLATE AND WELDMENTS TESTED IN AIR AT 600°F

Specimen No.	Yield Strength (psi)		Tensile Strength (psi)	Elongation, 2-in. Gage Length (%)	Reduction in Area (%)
	0.1% Offset	0.2% Offset			
1[a]	13,500	14,700	27,500	46.0	66.8
2[b]	16,700	17,500	25,000	46.0	74.3
3[b]	17,100	17,700	24,600	47.5	71.7
ZR3/8[c]	15,600	16,200	24,900	48.0	72.3
ZR1/4[d]	13,500	14,400	21,400	40.0	71.5
ZRG1[e]	14,900	16,000	22,600	f	73.6
ZRFB[e]	14,600	15,600	21,900	27.5	71.1
ZR2[e]	15,100	16,100	22,900	25.0	65.0

[a]Specimen axis parallel to rolling direction of plate.
[b]Specimen axis perpendicular to rolling direction of plate.
[c]Specimen taken from plate used in conical section of core tank.
[d]Specimen from plate used in making test welds.
[e]Specimens machined from weldments made under a variety of conditions.
[f]Specimen broke outside gage marks; 17.2% elongation between shoulders; 11.5% between gage marks.

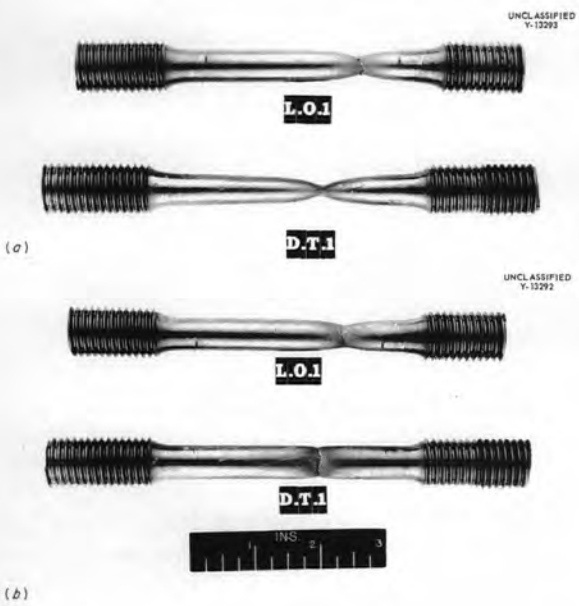

Fig. 36. Tensile Specimens Cut from Zircaloy-2 Forging. (*a*) Plane of photograph is parallel to the top of specimen DT-1 and perpendicular to the top of specimen LO-1. (*b*) Plane of photograph is parallel to the top of specimen LO-1 and perpendicular to the top of specimen DT-1.

Fig. 37. Fractures Occurring in Tensile Specimens Cut from Zircaloy-2 Forging.

Figs. 38, 39, and 40 indicates no change in transition temperature either from the in-pile exposure in UO_2SO_4 (Fig. 38, run DD) or from the out-of-pile exposure in UO_2SO_4 (Fig. 39, run CC).

A second series of Zircaloy-2 specimens from in-pile loop run FF has been received from the HRP Corrosion Group and is being tested in the Solid State Division where use is being made of their facilities for handling irradiated samples.

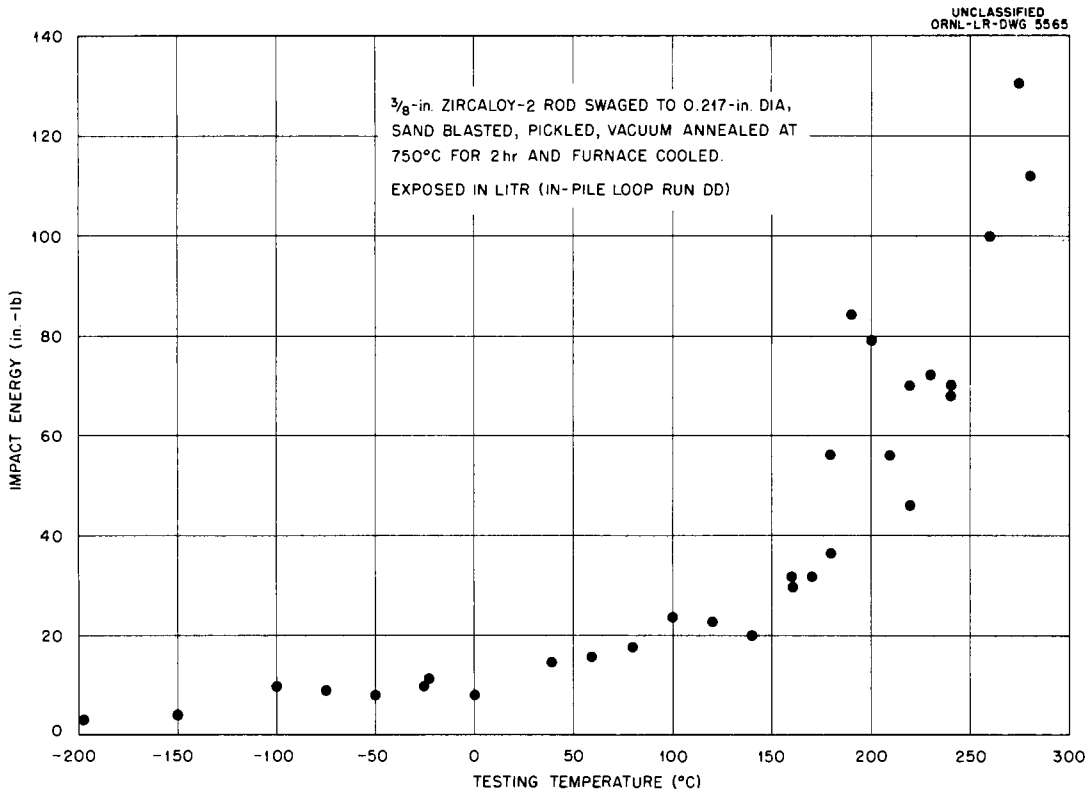

Fig. 38. Impact Energy vs Testing Temperature for Zircaloy-2 Exposed in LITR.

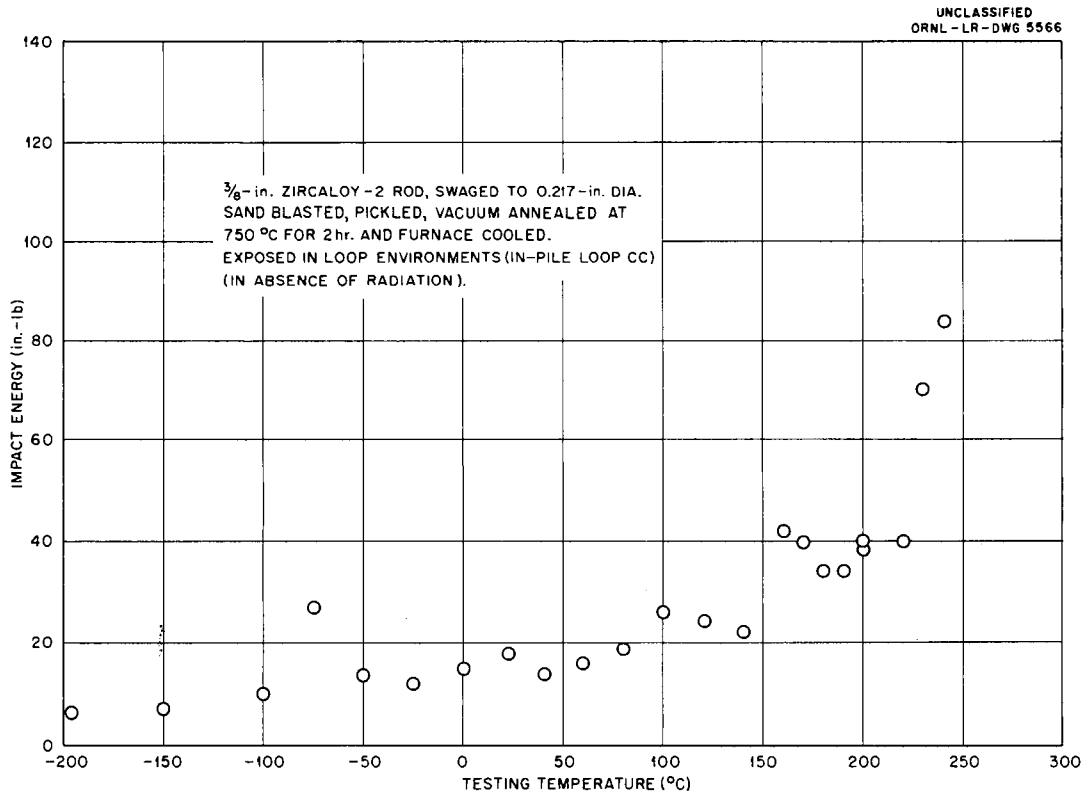

Fig. 39. Impact Energy vs Testing Temperature for Zircaloy-2 Exposed in Loop Environments Without Irradiation.

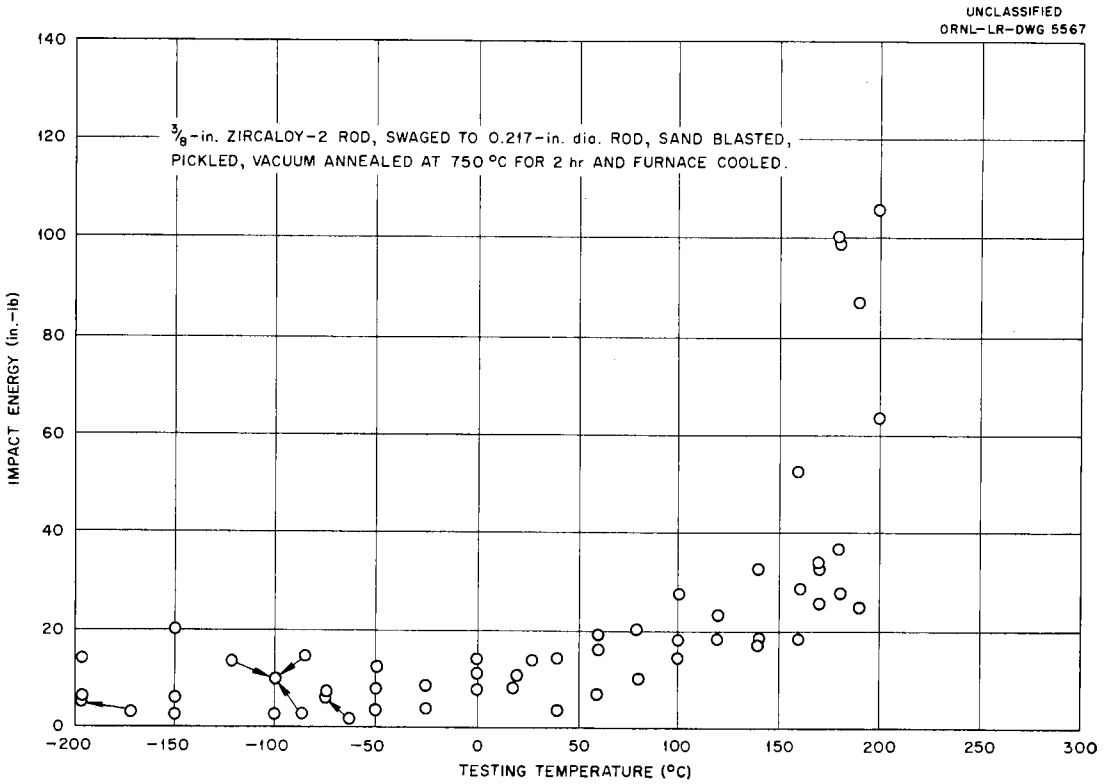

Fig. 40. Impact Energy vs Testing Temperature for Zircaloy-2 Unirradiated Control Specimens.

WELDING OF STAINLESS STEELS

W. J. Leonard

Welding Development on 1-in. Carbon-Steel Plates Clad with Type 347 Stainless Steel

Several variations have been proposed in the welding sequence for fabricating the spherical outer pressure shell of the HRT, and these received a preliminary evaluation.[3]

Welds were made in 1-in. composite plates of carbon steel (ASTM A-201 Grade A) clad with a 20% thickness of type 347 stainless steel. Four plates were welded to completion according to the basic designs proposed by Newport News Shipbuilding & Dry Dock Co., the subcontractor fabricating the vessel.

In the first method, type 347 stainless steel filler metal joined the stainless-steel-clad portion of the plate, filling the groove to the carbon steel–stainless steel interface. The face of this weld deposit was then machined flat and flush with the interface and covered with an ingot-iron strip approximately $\frac{1}{16}$ in. thick. The edges of the ingot-iron strip were welded to the adjacent carbon-steel base metal but not bonded to the underlying stainless steel weld deposit. The weld was completed by using a low-hydrogen-type carbon-steel electrode.

The second method was identical with the first up to the welding of the carbon steel–stainless steel interface. At this stage a layer of type 310 stainless steel weld metal was deposited over the type 347 stainless steel, followed by one layer of ingot-iron weld metal deposited over the type 310 layer. The weld was then completed with the same carbon-steel electrode as in the first method.

The third method consisted in welding with type 347 filler metal to a point about $\frac{1}{16}$ in. below the carbon steel–stainless steel interface, followed by two layers of type 308L stainless steel weld metal over the type 347 weld metal, bringing the level of the weld deposit approximately $\frac{1}{8}$ in. above the carbon steel–stainless steel interface.

[3] W. J. Leonard, *Met. Semiann. Prog. Rep. Oct. 10, 1954*, ORNL-1875, p 56.

One layer of ingot-iron weld metal was placed over the 308L weld metal, and the groove was then filled by carbon-steel electrodes.

In the fourth method the same procedure was used as in the third except that the ingot-iron weld metal was omitted. This resulted in the carbon-steel weld metal being placed directly on the 308L weld deposit. The weld was then completed with the carbon-steel electrodes as in the previous joints.

Figures 41, 42, 43, and 44 are macrophotographs of sections from these welded plates. All except welds obtained by the first method appear to be sound as welded. Macroscopic examination of the apparently sound weldments revealed no cracks or fissures in the joint. Side-bend tests made on specimens cut from each of the four plates are shown in Figs. 45, 46, 47, and 48. In the specimen cut from the plate made by the second method (Fig. 46), considerable dilution of the carbon-steel base metal and ingot-iron weld metal and overlying carbon-steel weld metal occurred, and the diluted weld metal tended to pull away from the base metal on bending. This same effect, but not so extensive, of ingot-iron weld metal on carbon steel was noted in the specimen representing the third welding method. The iron-to-stainless-steel interfaces did not show this effect in the bend test.

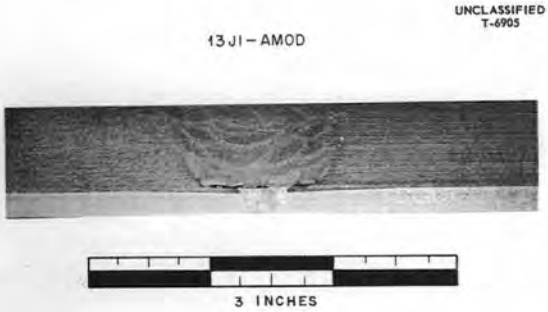

Fig. 41. Weld Obtained by Method 1. Order of metal placement: type 347 filler metal, ingot iron strip, low-hydrogen-type carbon steel.

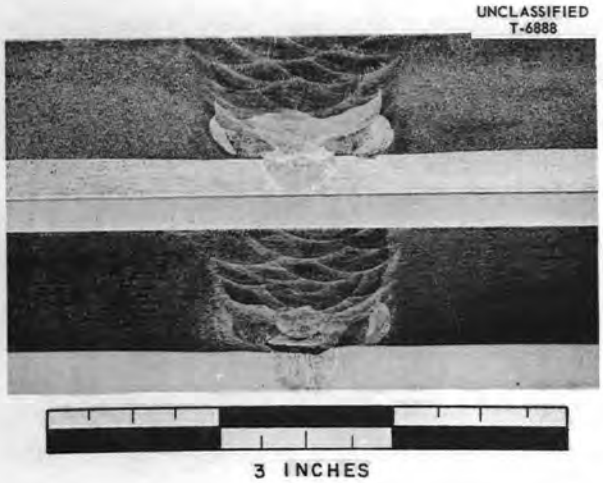

Fig. 42. Weld Obtained by Method 2. Order of weld-metal placement: type 347, type 310, ingot iron, low-hydrogen-type carbon steel.

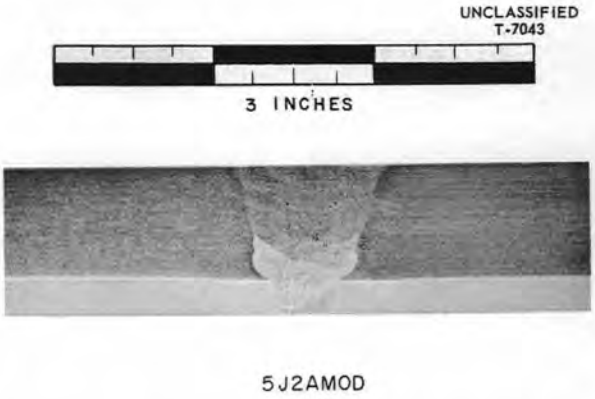

Fig. 43. Weld Obtained by Method 3. Order of weld-metal placement: type 347, type 308L, ingot iron, low-hydrogen-type carbon steel.

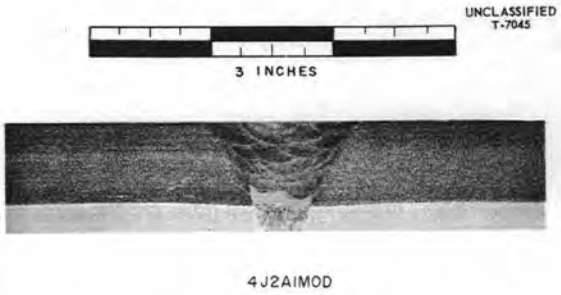

Fig. 44. Weld Obtained by Method 4. Order of weld-metal placement: type 347, type 308L, low-hydrogen-type carbon steel.

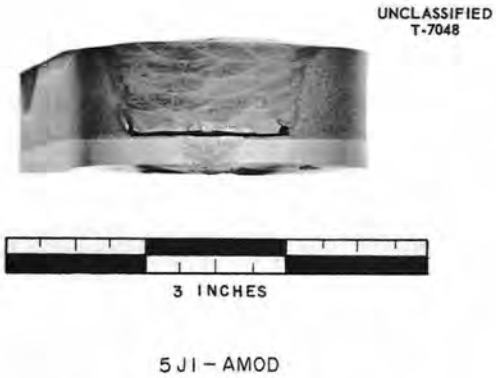

Fig. 45. Side Bend Test of Method 1 Weld.

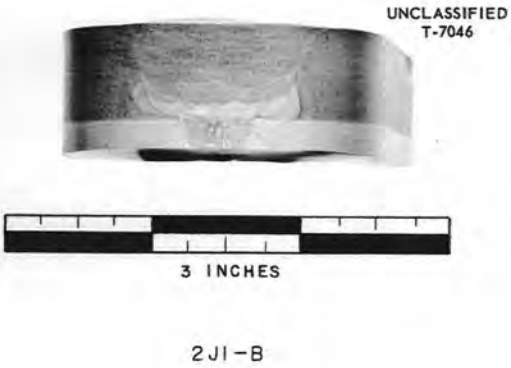

Fig. 46. Side Bend Test of Method 2 Weld.

Tensile specimens transverse to the weld were made from each of the four weldments. Dimensions used for the specimens were those recommended for standard tensile-test bars in the *Welding Handbook* of the American Welding Society. These test coupons were modified to lessen the width and thickness of the cross section of the weld in an effort to ensure that the smaller cross section of the all-weld-metal portion of the specimens would break. However, all the specimens broke in the heat-affected zone of the base metal at a position outside the weld approximately $\frac{1}{4}$ in. from the edge of the weld metal. This would indicate a higher strength for the deposited metal than indicated by the values in Table 5, which are considered adequate for this type of joint.

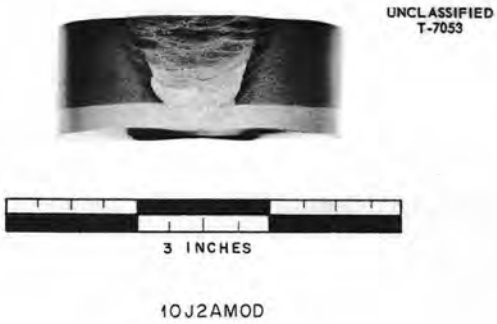

Fig. 47. Side Bend Test of Method 3 Weld.

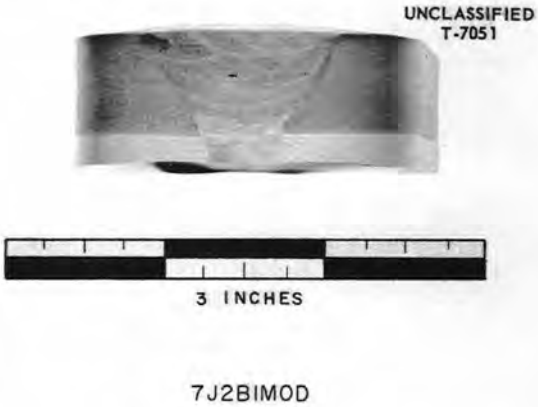

Fig. 48. Side Bend Test of Method 4 Weld.

Metallographic examination of specimens taken from the four welded plates indicated that dilution was what would be expected in welding between high-alloy and carbon-steel materials.

In the method 1 weld sample (Fig. 41) the strip barrier prevented dilution of the dissimilar metals except where the carbon-steel weld metal inadvertently burned through the ingot-iron strip and alloyed to some extent with the underlying stainless steel. As this method was obviously unsatisfactory, no detailed examination was performed. Microhardness surveys of the weld and adjacent area were made on the other three specimens.

In the method 2 weld sample (Fig. 42) the type 347 weld metal had an average hardness of 210 VPN; the type 310, 225 VPN; the carbon steel, 195 VPN. A traverse, made at the center line of

TABLE 5. PHYSICAL PROPERTIES OF TEST COUPONS TAKEN FROM WELDED CARBON STEEL–STAINLESS STEEL CLAD PLATE

Specimen	Tensile Strength of Composite (psi)	Elongation, $1\frac{1}{4}$-in. Gage Length (%)	
		Carbon Steel	Stainless Steel
Method 1	83,900		17
	83,400		17
Method 2	79,200	12.5	20
	80,100	10	20
Method 3	78,900	8.7	21
	79,500	15	20
Method 4	85,700	20*	25*

*$\frac{3}{4}$-in. gage length.

the weld metal from the underlying type 310 weld metal into the ingot-iron weld metal, gave a hardness of 240 VPN on the undiluted type 310 weld metal and a hardness of 375 VPN (average) in the ingot iron diluted with type 310 metal. A traverse from type 310 weld metal to carbon-steel base metal showed no particularly hard layer at the juncture – VPN 230 on type 310 at this position and 160 VPN on base-metal side. A similar traverse from carbon-steel weld metal to the carbon-steel base metal gave weld-metal hardness of 210 VPN at the juncture, 171 VPN in heat-affected zone of base metal, and 160 VPN in unaffected base metal. The ingot-iron weld metal diluted with type 310 stainless steel has an average hardness of 375 VPN, and its microstructure appears to be a martensitic-type stainless steel very similar to a 14% chromium or 15% chromium–2% nickel stainless steel.

In the method 3 weld sample (Fig. 43) the type 308L weld metal had an average hardness of 240 VPN. Moving upward toward the overlying ingot-iron weld metal, the hardness was 240 VPN at juncture; in the iron diluted with 308L weld metal, the average hardness was 390 VPN. The weld metal overlying this layer was further diluted by carbon-steel weld metal and had an average hardness of 370 VPN. A traverse, made from this layer into the carbon-steel base metal, gave a hardness of 385 VPN on the weld-metal side, 175 VPN in the heat-affected zone of the base metal, and 160 VPN in the base metal. A similar traverse, across the weld-metal layer consisting of diluted ingot iron and 308L weld metal (average VPN 390), indicated a very narrow, martensitic constituent at the juncture with a hardness of 413 VPN; the heat-affected zone of the carbon-steel base metal had an average hardness of 165 VPN, and the base metal had a hardness of 155 VPN.

Another traverse was made at a position where the diluted ingot-iron–308L weld metals penetrated into the stainless portion of the base plate. At the juncture of the weld metal and the base metal a hardness of 240 VPN was observed on unmelted stainless-steel base metal; the hardness in the edge of weld metal was 272 VPN and rapidly increased to 405 VPN; the balance of the weld metal averaged 427 VPN. The microstructure of this portion of the weld metal appeared to be martensitic.

In the method 4 sample (Fig. 44) a traverse was made from the type 308L weld metal, through the diluted layer of 308L and carbon-steel weld metal, to the carbon-steel weld metal. Hardness was 274 VPN in the extreme top of undiluted 308L weld metal, 375 VPN in the diluted zone, and 190 VPN in the bottom of undiluted carbon-steel weld metal. The microstructure of the diluted zone was martensitic. A traverse from the diluted

layer into the carbon-steel base metal indicated an increase in the carbon content at the juncture. The hardness increased to 400 VPN in the weld metal adjacent to the base metal; it was 170 VPN in the heat-affected zone of the base metal and was 154 VPN in base metal.

The same effect was noted in a traverse from the type 308L weld metal into the carbon-steel base metal. The hardness of the weld metal progressively increased until it was 295 VPN adjacent to the juncture. A narrow, martensitic band of weld metal occurred at the juncture with a hardness of 401 VPN. The hardness of the carbon-steel heat-affected zone was 176 VPN, the base metal's hardness was 155 VPN.

A place was found in one microspecimen where very little penetration of the carbon-steel weld metal into the 308L weld metal occurred. The dilution was so limited that no martensitic structure was observed. The hardness of the carbon-steel weld metal was 206 VPN adjacent to the juncture, whereas the 308L had a hardness of 258 VPN at the same position.

The microscopic examination of the specimens represented by Figs. 42, 43, and 44 revealed no microfissures or unsoundness even in the diluted areas, which appeared to be martensitic.

METALLURGICAL ENGINEERING SERVICE

G. E. Elder

Fabrication of HRT Zircaloy-2 Core Vessel

A considerable amount of developmental research has been required in forming and fabricating the Zircaloy-2 core vessel. This is being carried out under subcontract by the Newport News Shipbuilding & Dry Dock Co. The geometry of the component parts of the vessel is such that relatively complex jigs and fixtures are required.

Forming. – The component parts of the sphere were hot-formed from $^5/_{16}$-in. plate, with the dies and press shown in Fig. 49. The formed quadrants were clamped to the male die, as shown in Fig. 50, and machined to obtain the fitup required for the Electric Boat preplaced consumable-type insert used for the root weld. The halves of the 30- and the 90-deg cones were hot-formed from $^3/_8$-in. plate. Some reworking of the dies was necessary to make allowance for spring-back of the Zircaloy-2. After assembling and welding, the cones and the sphere halves were reformed, as illustrated in Fig. 51.

Welding. – Producing a sound weldment with Zircaloy-2 requires complete blanketing of the weld area with helium or argon. An individual shield was designed and constructed to conform with each weld geometry, as shown in Fig. 52. Inert gas was supplied to the shield, both at the Heliarc torch and behind the torch, through holes in the center copper tubing of the shield. Small notches at the contact edge of the shield permitted flow of the gas out of the shielded area and prevented contact with the outside atmosphere. Figure 53 is a close-up of the welding head, illustrating the conformation of the shield to the work surface. A hollow copper bar, Fig. 54, conforming to the inner surface, served as a backing shield for the welds on the sphere. A positive pressure of inert gas was maintained inside the bar, with the gas flowing over the weld area from regularly spaced holes. The back of the weld on the two cones and the pipes was shielded by plugging both ends of the piece and then maintaining an inert atmosphere in the piece.

The consumable insert was used as the root pass on all welds. After fitup of the parts, the insert was tack-welded in place by using a Heliarc hand torch. In all cases the welding head was held stationary, and the work was moved by an automatic positioner. Figure 55 shows the 30-deg cone in welding position. Tabs of Zircaloy-2 were tack-welded at both ends of the weld pass to assure a sound weld at the start and finish of the pass. Figure 56 shows the sphere in welding position. The jig used was the one that was designed and used for constructing the aluminum prototype vessel. Figure 57 is a photograph of the completed weld on the 90-deg cone. Figure 58 shows the setup used to weld the 30-deg cone to a pipe section. There are two knobs on the left of the shield. One was used to adjust the arc length and the other to center the head on the weld bead. One operator manipulated the knob to maintain a constant arc length, as indicated by the voltmeter mounted above the head. The other operator positioned the arc laterally and fed the weld rod, used for the cover passes, through the hole in the lower right corner of the glass front on the shield. The weld speed was controlled by the welding positioner which supported the jig. Figure 59 shows two of the diffuser plates welded in the 30-deg cone. The welding was done with a Heliarc hand torch. Shielding was accomplished

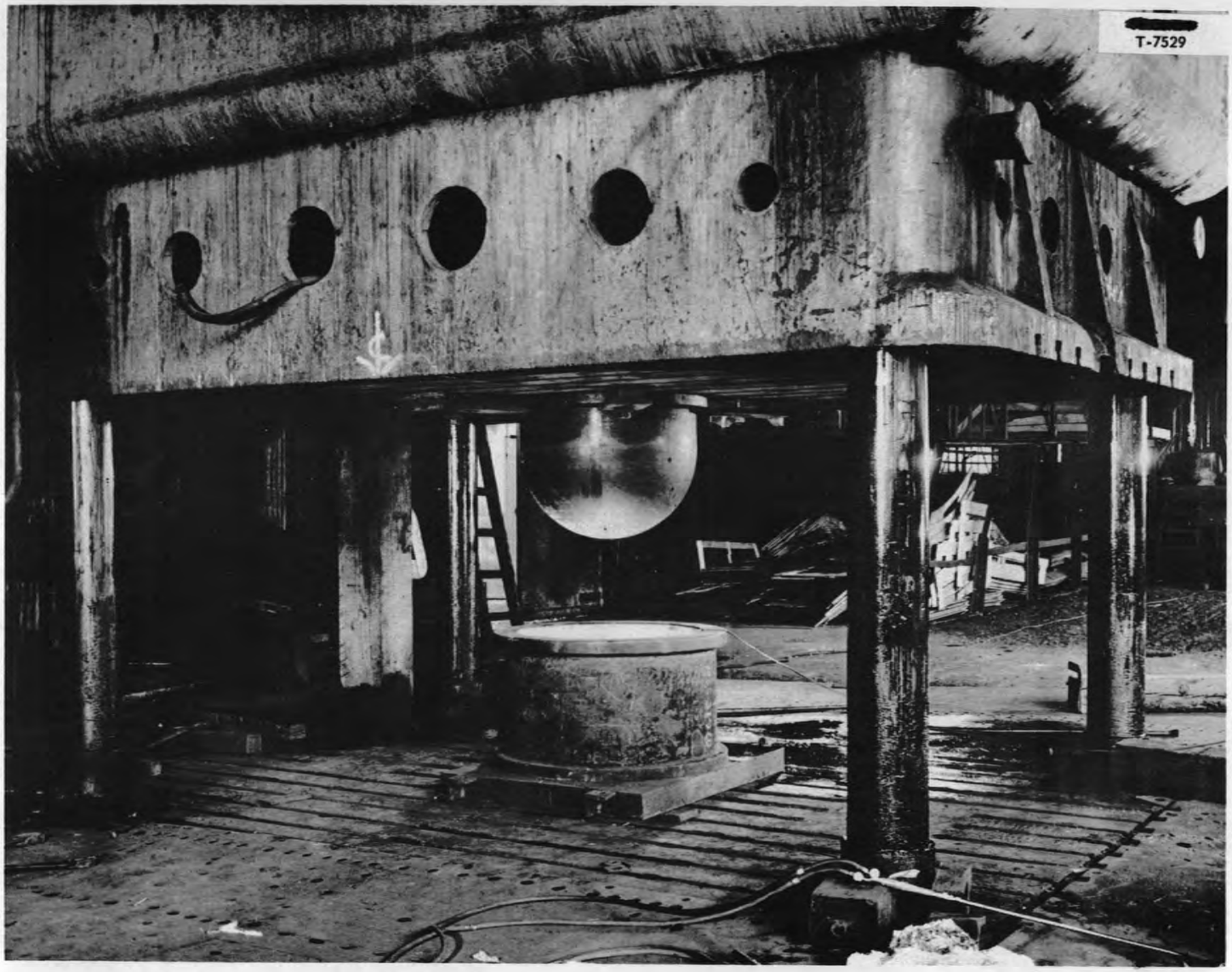

Fig. 49. Hydraulic Press with Male and Female Dies in Place and Ready for Forming Sphere Sections of Core Tank.

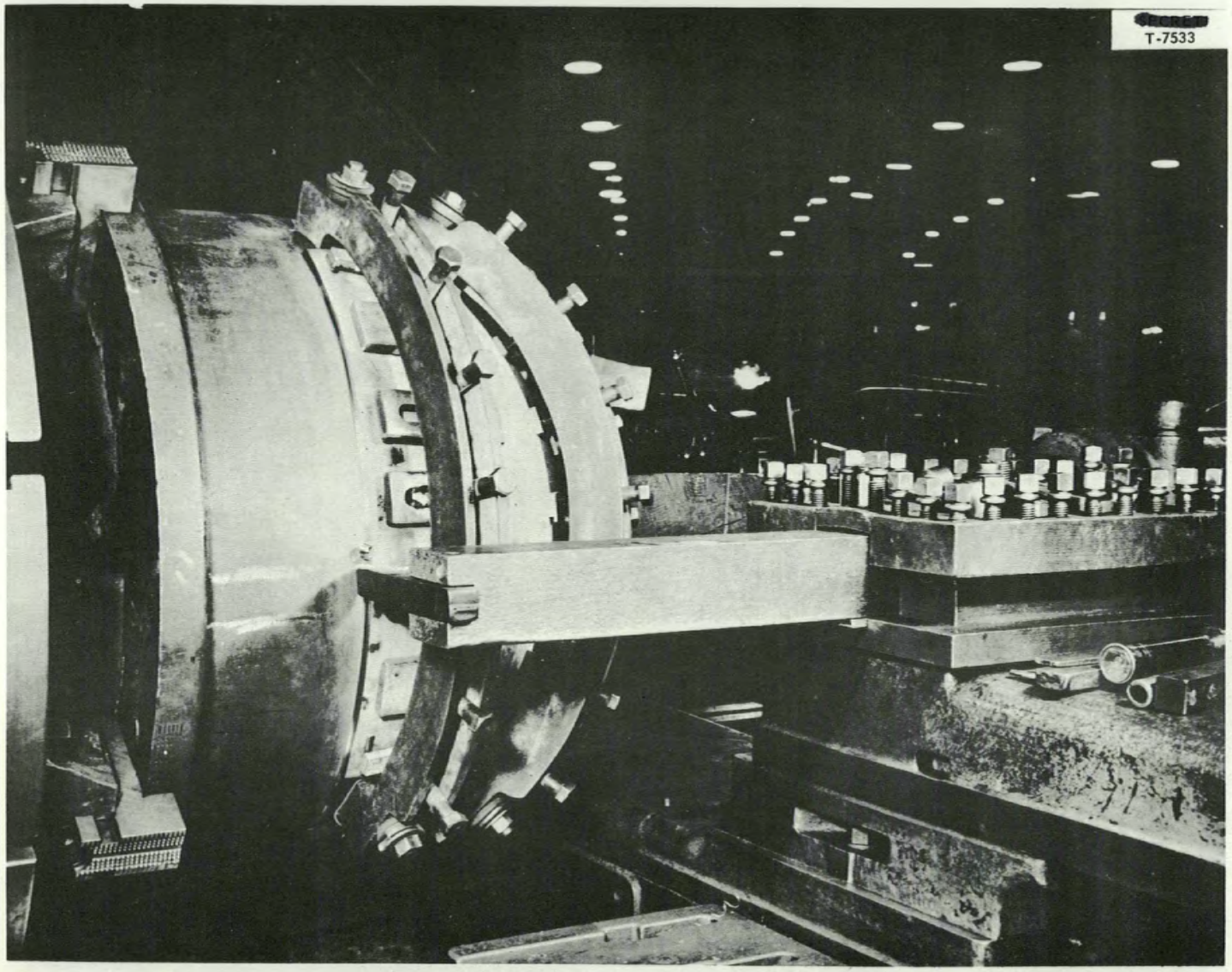

Fig. 50. Close-up Side View Showing Method of Holding and Machining Spherical Sections of Core Tank on a Large Lathe.

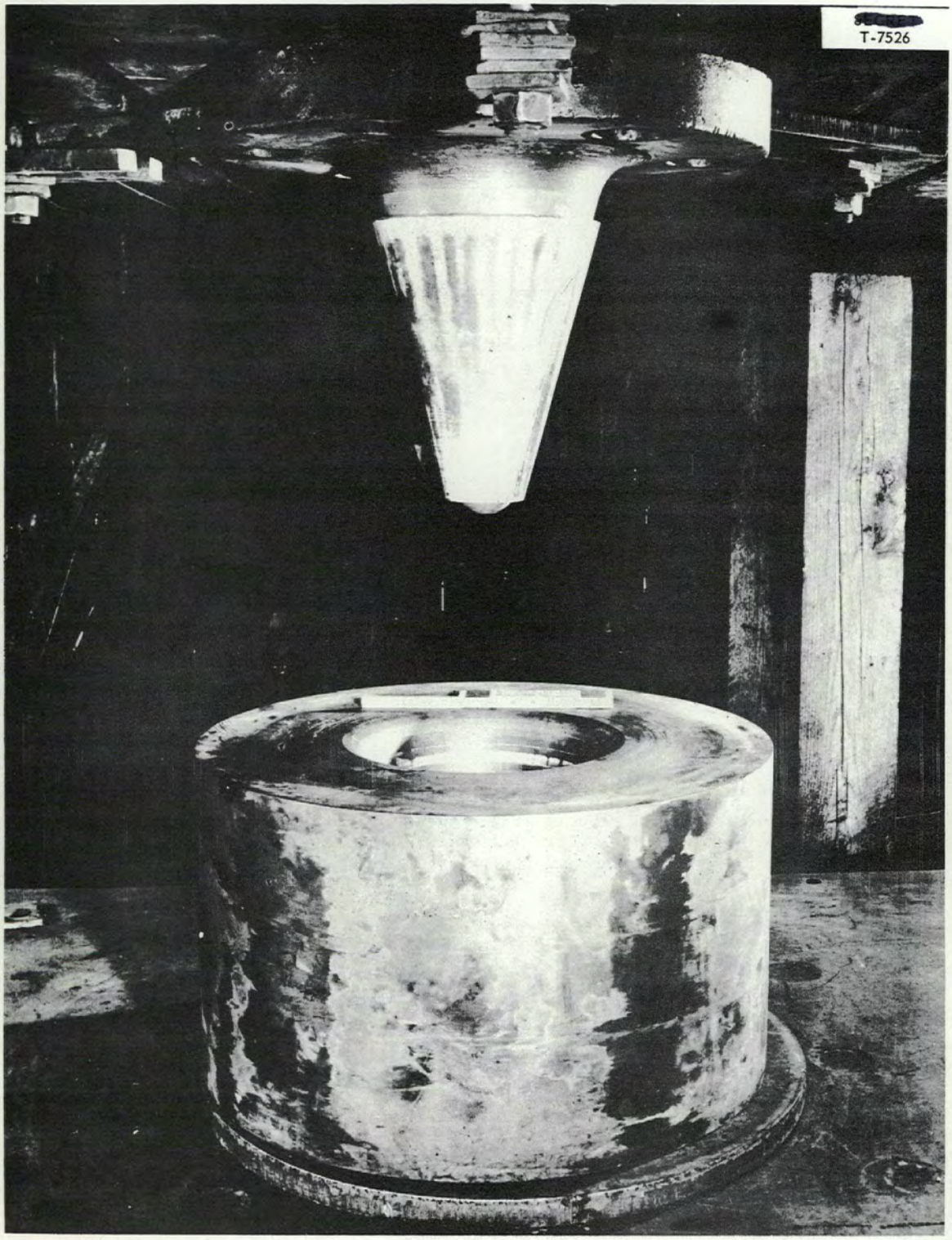

Fig. 51. Close-up View of Male and Female Dies Used for Final Forming Operation of 30-deg Cone Section of Core Tank.

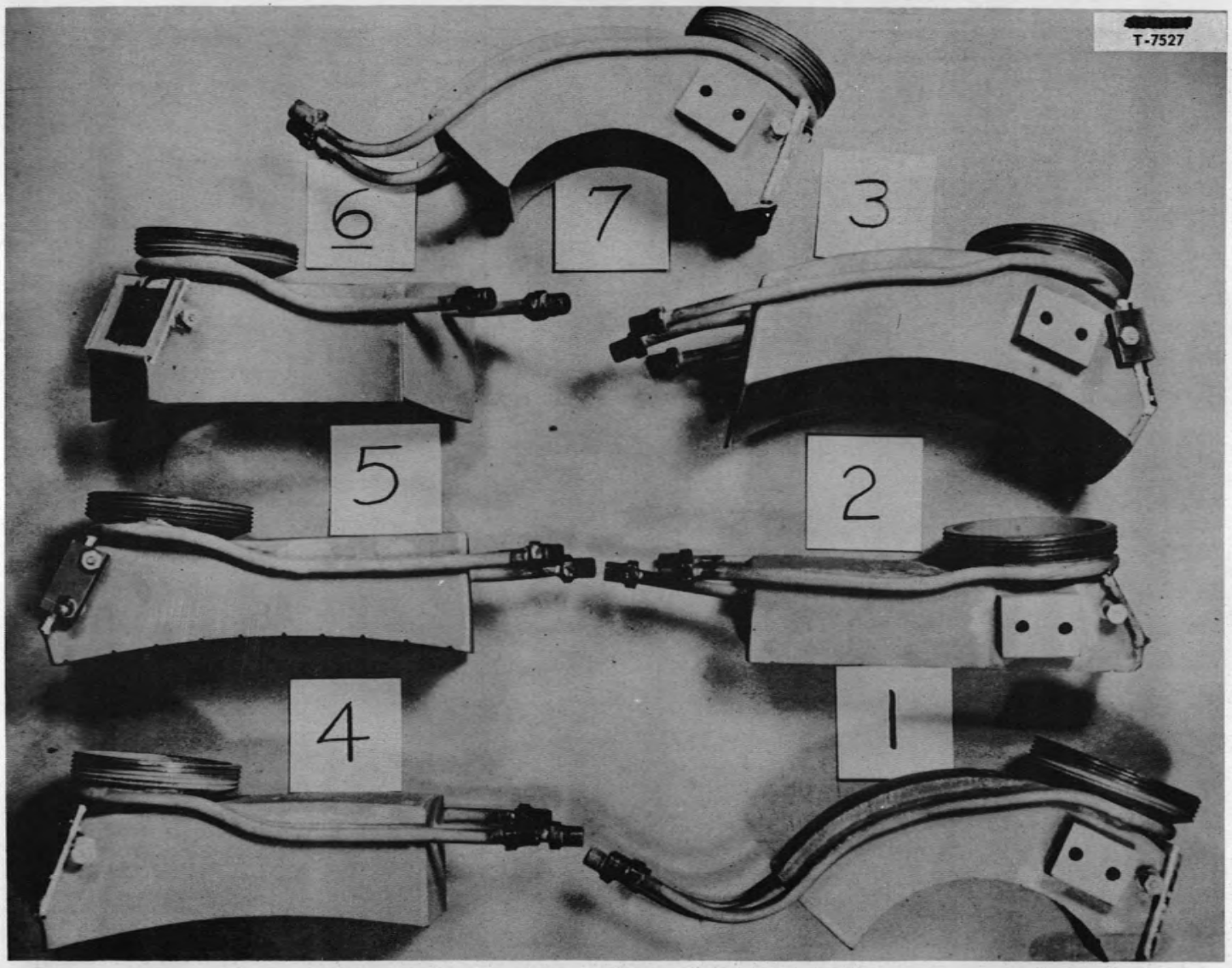

Fig. 52. Side Views of the Seven Welding Shields Used to Perform Welding Operations on Core-Tank Joints.

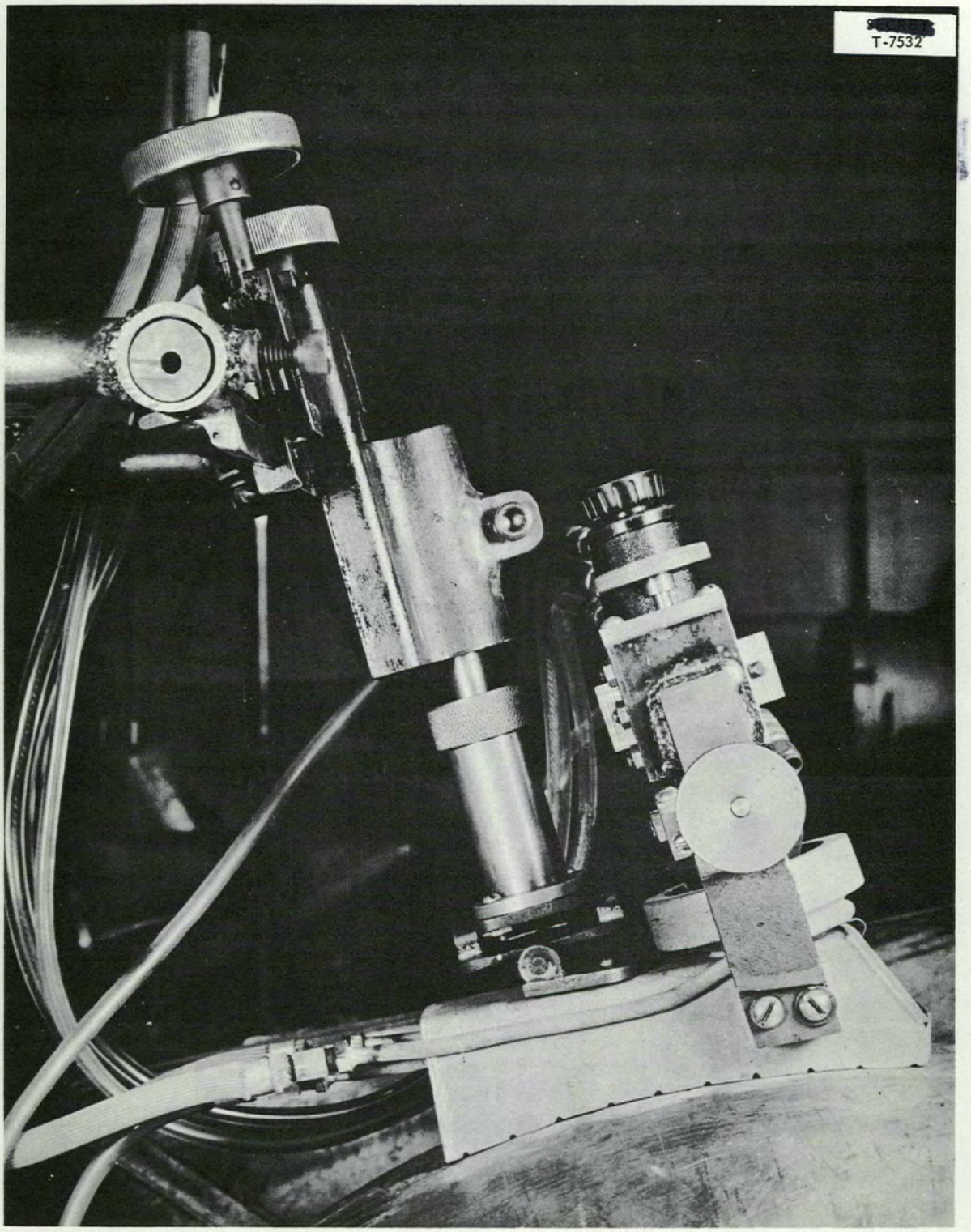

Fig. 53. Close-up Side View Showing Details of the Welding Torch and the Shield Positioning and Manipulating Fixtures.

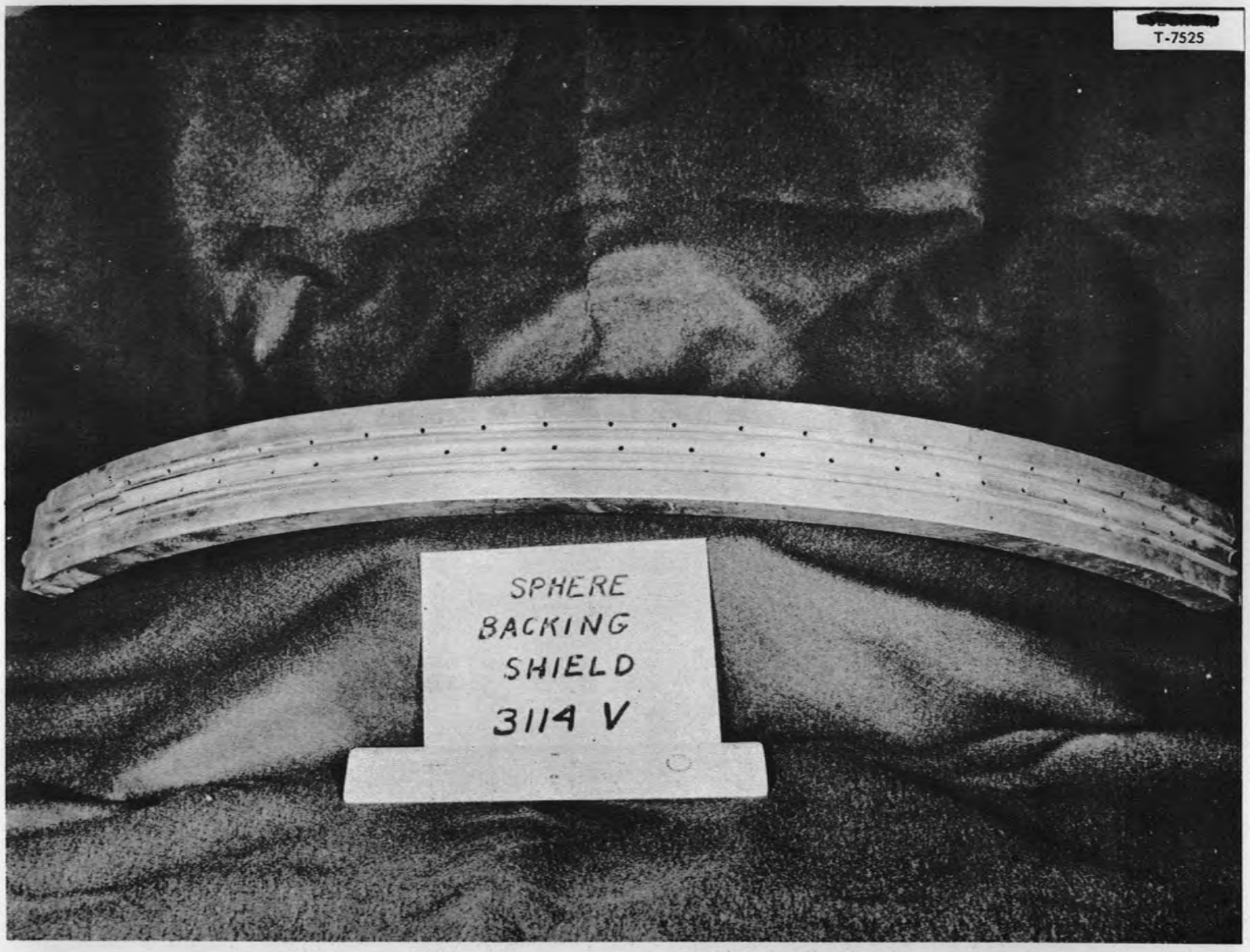

Fig. 54. Copper Bar Used for Gas Shielding on Back Side of Mid-Body Joints of Core Tank.

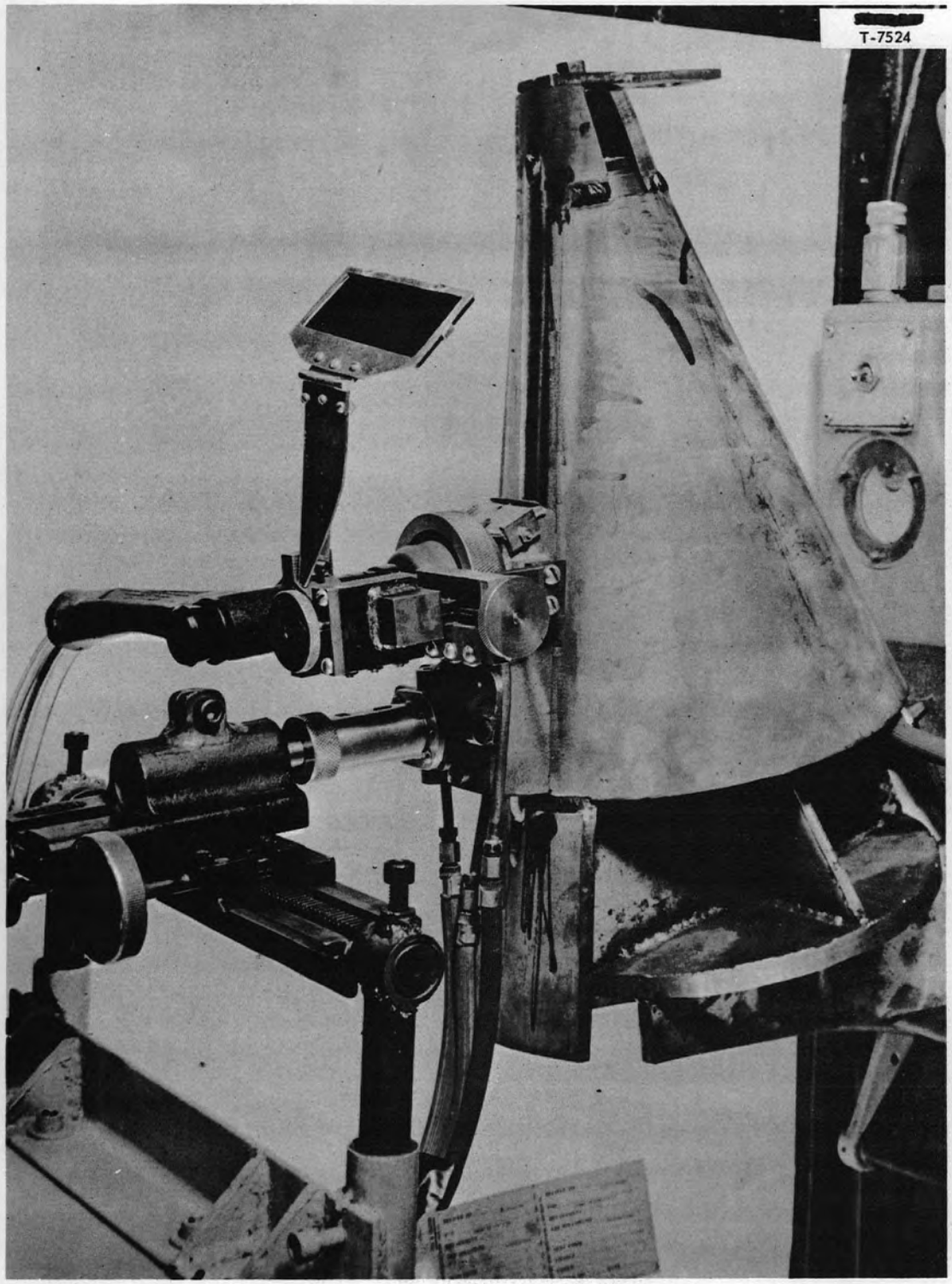

Fig. 55. Side-Top View Showing Arrangement for Making Seam Welds of 30-deg Cone Section of Core Tank.

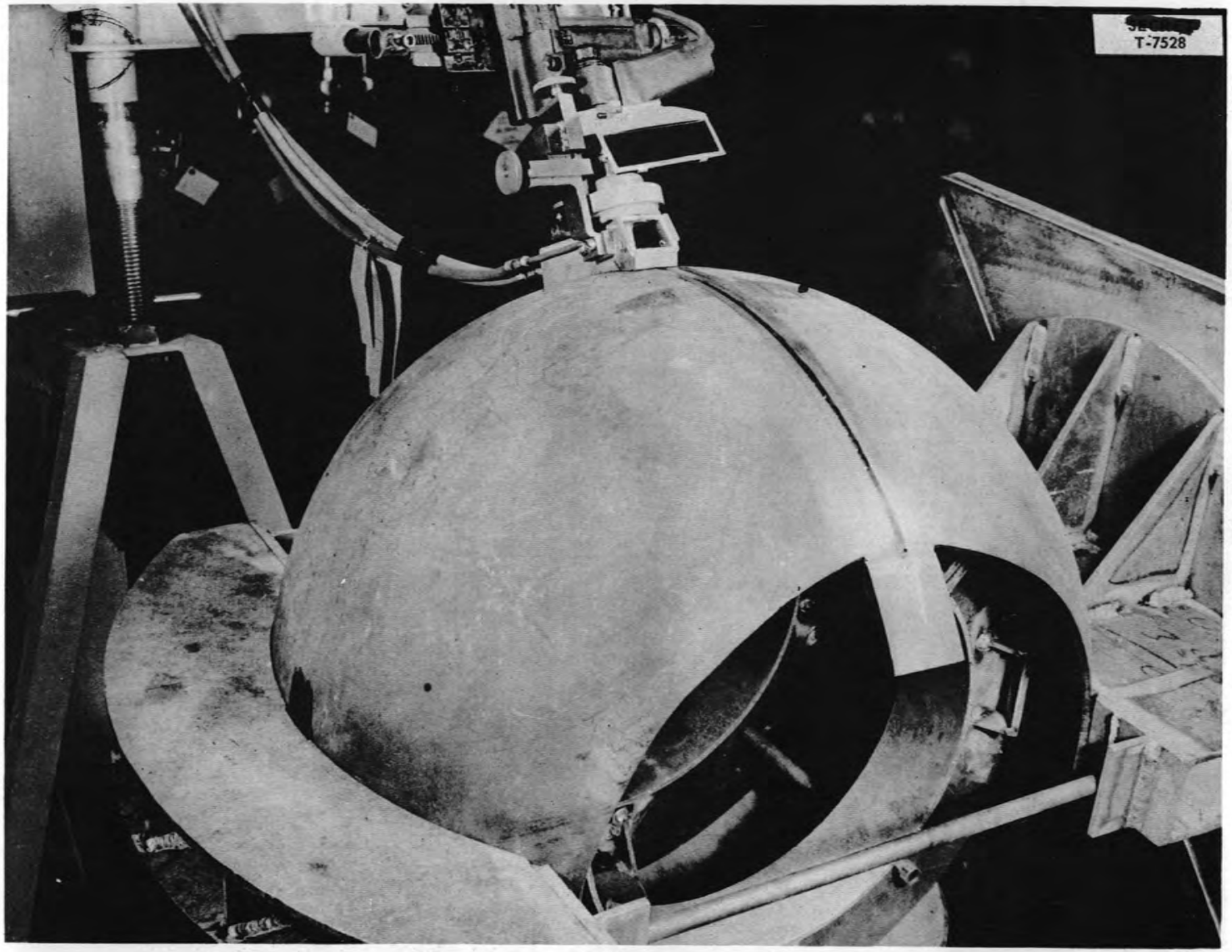

Fig. 56. Arrangement Used for Making a Weld Joining Spherical Pieces of Mid-Body Section of Core Tank.

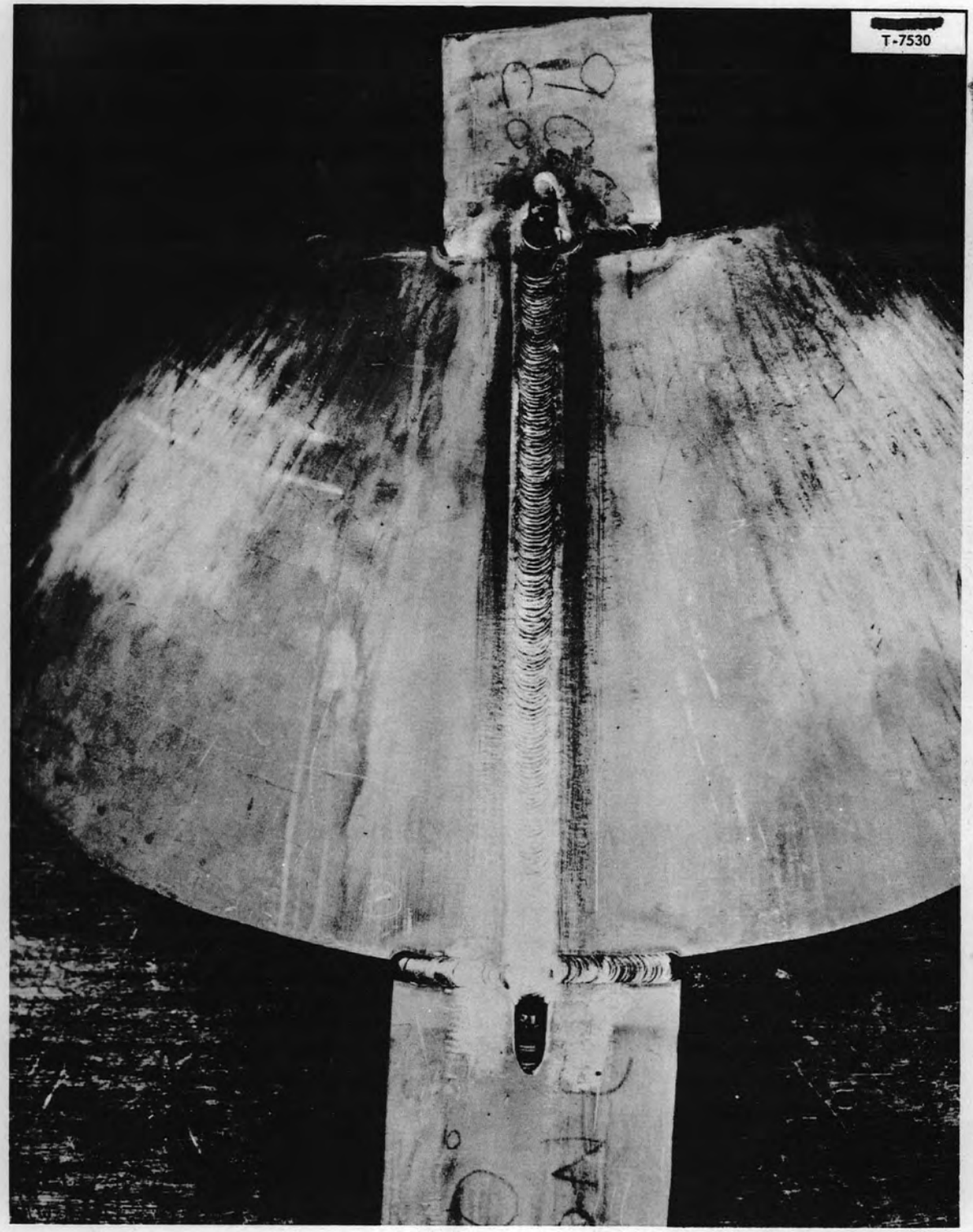

Fig. 57. Butt Side of Completed Seam Weld in 90-deg Cone Section of Core Tank.

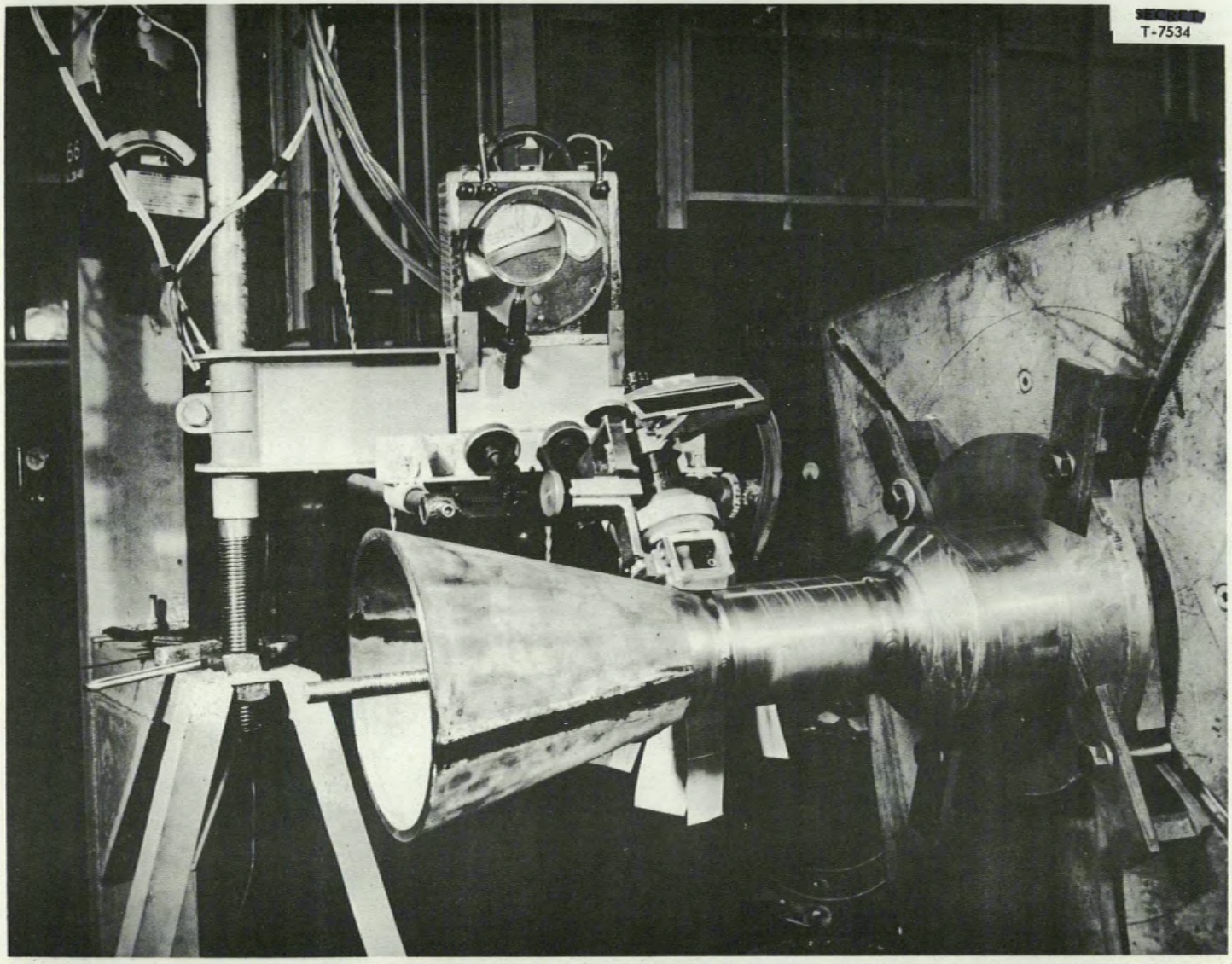

Fig. 58. Side-Front View of Arrangement for Welding Inlet Cylinder and Flange to 30-deg Cone Section of Core Tank.

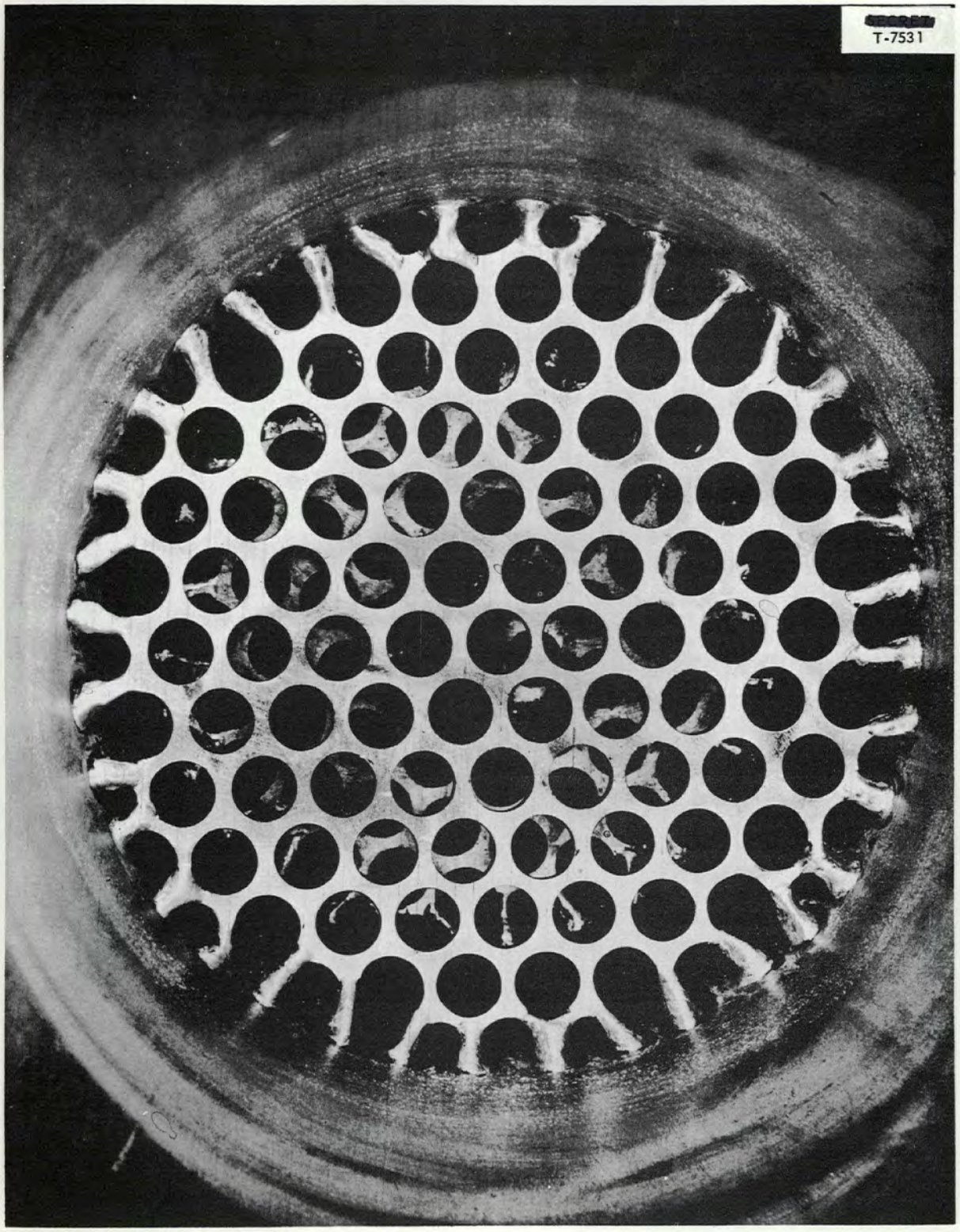

Fig. 59. Interior View of Core Tank 30-deg Cone Section Showing Welds Attaching Diffuser Plate No. 2 to Side Walls of Cone.

by capping the small end of the cone; by covering all the diffuser plate, except for a small area around the ligament being welded; and then maintaining a helium atmosphere in the cone by injecting the gas through a fitting in the end plug.

HRP PHYSICAL METALLURGY

W. O. Harms J. I. Federer
G. B. Wadsworth

Metallurgy of Corrosion

Stress-Corrosion Cracking of Austenitic Stainless Steels. – An experimental program has been initiated to evaluate the transgranular stress-corrosion cracking susceptibility of austenitic stainless steels and to study systematically the various factors that may influence this susceptibility. The purpose of this work is to obtain information regarding the mechanism of stress cracking in homogeneous reactor systems.[4] This information might be used in the future as a basis for modification of HRP materials specifications so that the probability of failure due to stress-corrosion cracking will be minimized. Initial work has consisted of determining an acceptable testing procedure.

The stress distribution on loaded specimens, the design of which was based on a modification of one introduced by Waber and McDonald,[5,6] was determined by means of strain gages and found to be neither uniform nor reproducible. The geometry of this type of specimen is such that when the specimen is loaded the outer fiber stresses on a large area would be expected to be constant. It was observed, however, that the stress varied as much as 30%. Moreover, when exposed to boiling 42 wt % magnesium chloride, the tie rods and nuts had to be coated with Teflon to prevent cracking; no cracks were observed on the specimens themselves after as long as a 30-hr exposure. In view of these difficulties the evaluation of a direct-loading-type specimen was undertaken.

The apparatus currently in use is shown in Fig. 60. The wire specimen, which is approximately 0.050 in. in diameter, is stressed by weights as shown. When failure occurs, the falling weights actuate a microswitch which stops an electric timer, indicating the moment of failure. Air is forced through a glass tube which encloses the specimen at a point just below the liquid level. This arrangement prevents contact between the specimen and the solution vapors. A second opening has been provided for the insertion of electrodes in subsequent experiments to study the effects on corrosion potentials. The position of the heater can be adjusted to control the size of the solid plug of magnesium chloride at the bottom of the glass container.

Rods of commercial alloys of types 304L, 347, 309SCb, 310, 316L, and 321 have been swaged to size and both stress–strain relationships and chemical analyses have been obtained for these materials. Based on an empirical formula developed by Eichelman and Hull,[7] these alloys represent a large range of martensite-forming susceptibilities, and the results of the tests should indicate whether any relationship exists between this tendency and the resistance to transgranular stress-corrosion cracking. The M_d temperatures for these steels were determined by adding 600°F to the M_s temperatures[7] given by the Eichelman and Hull equation and are as follows:

AISI Type	M_d (°F)
304L	369
347	181
321	141
316L	−17
309SCb	<−452
310	<−452

Thus, if transgranular stress cracks propagate along martensite plates during local yielding under applied stress, the type 304L steel would be expected to be the least resistant to this type of stress corrosion. It should be emphasized that the chemical compositions of some of the steels are somewhat different from those used in the derivation of the equation, and, therefore, the M_d temperatures as such are not to be regarded in an absolute sense but only as an approximate relative

[4] E. C. Miller *et al.*, *HRP Quar. Prog. Rep. April 30, 1954*, ORNL-1753, pp 117–122.

[5] J. T. Waber and H. J. McDonald, *Corrosion and Material Protection* 3, 13 (1946).

[6] W. O. Harms and E. C. Miller, *Met. Semiann. Prog. Rep. April 10, 1954*, ORNL-1727, p 20.

[7] G. H. Eichelman, Jr., and F. C. Hull, *Trans. Am. Soc. Metals* 45, 77 (1953).

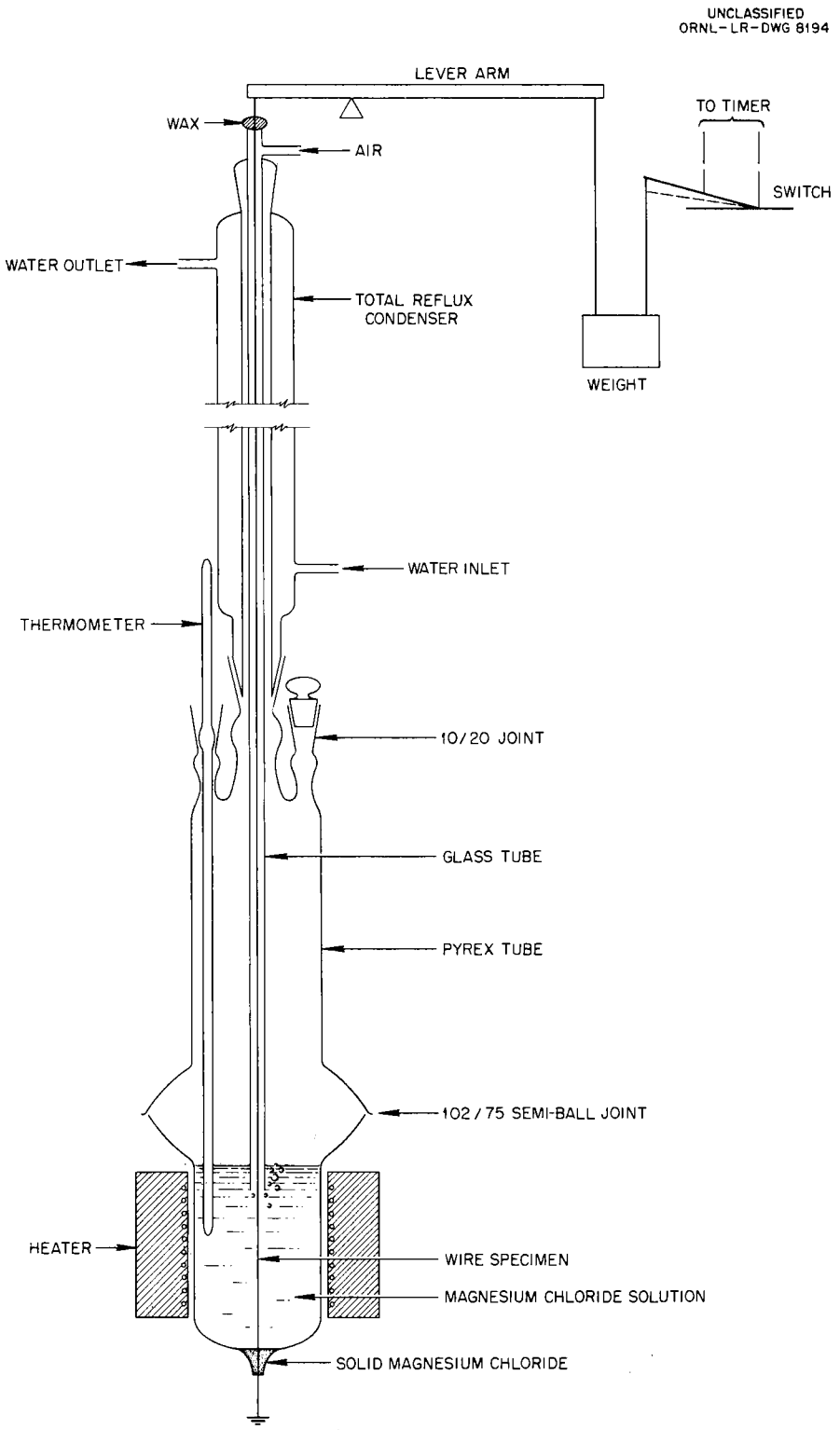

Fig. 60. Stress-Corrosion Cracking Apparatus.

measure of the martensite-forming tendencies of the steels to be investigated.

In preliminary tests on annealed stock type 347 wire, failures occurred in 10 to 16 hr at stresses slightly greater than the handbook yield strength for this material. In the as-received (apparently not fully annealed) condition this wire broke consistently after only 1 to 2 hr of exposure at the same stress level. Examination of the broken specimens revealed many small and a few large circumferential cracks in the vicinity of the break and only slight general corrosion.

Stainless Steel Welds. – The results of dynamic-corrosion tests of 200-, 400-, and 800-hr duration on special flat-plate coupons[8] machined from 1-in. weldments are represented graphically in Fig. 61. The test conditions were as follows: 0.17 *m* uranyl sulfate, 250°C, and 20 fps. All wrought metal specimens were included for comparison. In both holders the weldments involving type 308L welds showed the lowest corrosion resistance, and those involving composition H (an experimental fully austenitic 18% Cr–13% Ni–5% Mn, Cb-stabilized alloy) weld metal compared favorably with wrought type 347 specimens.

Two anomalies appear in these data: (1) type 309SCb in the 800-hr run had extremely poor resistance, and (2) the specimens in holder B, except in two cases, lost considerably more weight after 400 hr than after 800 hr. The same specimens were used in all three tests, and the specimens were electrolytically polished prior to each run. The poor showing of wrought type 309SCb may be due to the presence of about 2% ferrite in the form of stringers. This specimen was practically film-free after the 800-hr run, which indicated that its critical velocity had been reached and that enough time had elapsed for this to be manifested as a

[8] W. J. Leonard and W. O. Harms, *HRP Quar. Prog. Rep. April 30, 1954*, ORNL-1753, p 115.

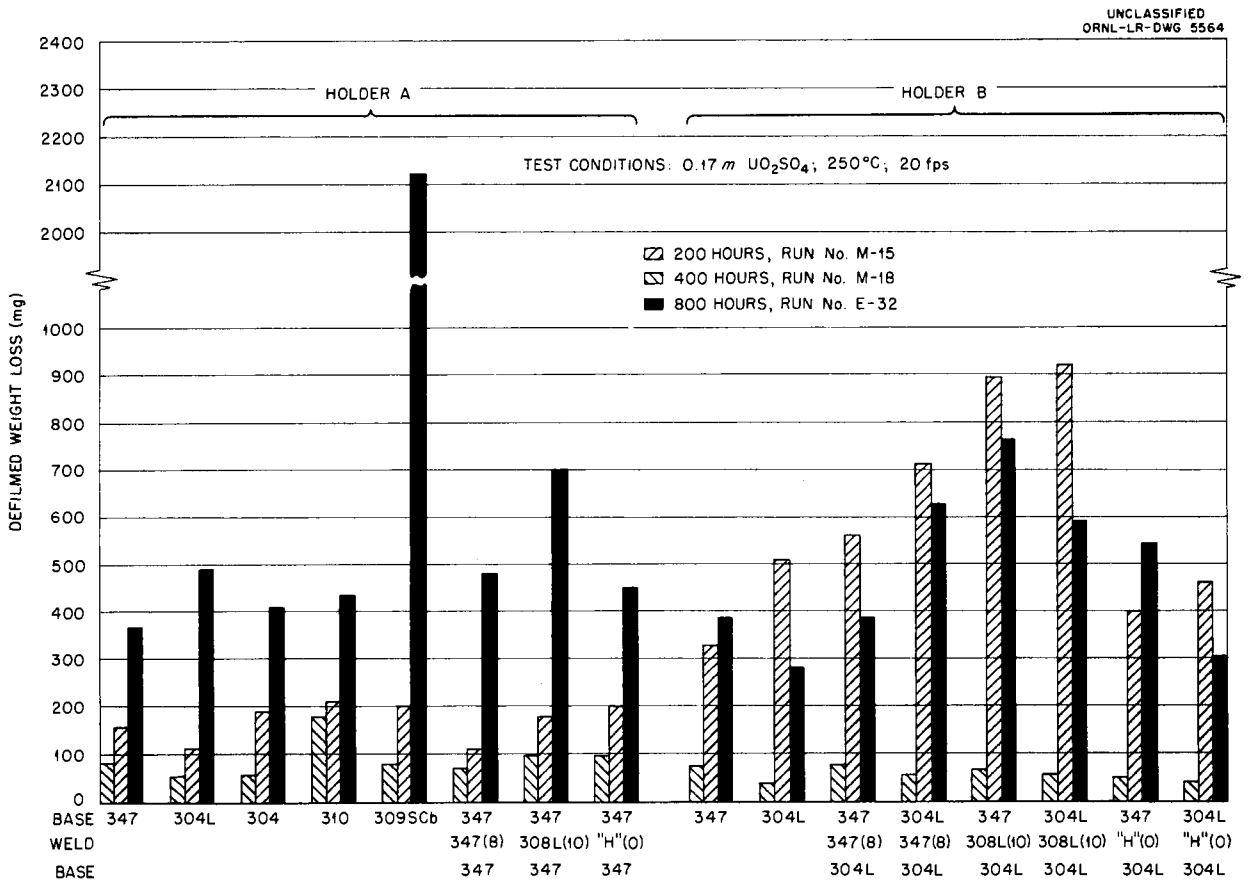

Fig. 61. Dynamic Corrosion of Austenitic Stainless Steel Welds in Uranyl Sulfate.

substantial weight loss. The inconsistency in holder B may be due to the bypass line in the 400-hr run becoming partially plugged, which results in a mean solution velocity somewhat higher than the design value of 20 fps. If these data are excluded, it is seen that a reasonable correlation exists between similar specimens in the two holders.

Wrought Stainless Steels. – Dynamic-corrosion pin-type specimens of types 304L and 347 stainless steels have been swaged and machined and are being heat-treated to give 20 specimens each with ASTM grain sizes of 2, 4, 6, and 8. These specimens will be submitted to the HRP Dynamic Corrosion Group for a systematic study of the effect of grain size on corrosion resistance.

Sigma-phase alloys of compositions 45% Cr–55% Fe and 5% Ni–45% Cr–50% Fe have been prepared for corrosion testing. Iron, chromium, and nickel metals of 99.98, 99.95, and 99.92% purities, respectively, were arc-melted in a purified argon atmosphere. The alloys were remelted several times to ensure homogeneity and hot-rolled at 1200°C to a minimum thickness of 0.210 in. These were heat-treated for 237 hr at 790°C to promote sigma formation. The iron-chromium-nickel alloy lost its magnetism after this treatment and is believed to be fully sigmatized. The iron-chromium alloy, on the other hand, retained some magnetism even after an additional 63-hr heat treatment, indicating the presence of some untransformed ferrite.

A knowledge of the corrosion behavior of sigma phase was considered desirable since certain type 300 stainless steels develop this brittle phase during welding or as the result of heat treatment during fabrication.

Zirconium and Titanium Metals and Alloys

Effect of Hydrogen on Properties of Zirconium and Its Alloys. – An apparatus has been designed and constructed for admitting known quantities of gas to metal specimens at a given temperature. The immediate purpose for this apparatus is to study the effects of alloying elements and surface condition on the rate of absorption of hydrogen by zirconium and its alloys.

The system is capable of a steady vacuum of the order of 10^{-7} mm Hg at room temperature; this is necessary for accurate pressure-volume calculations and to ensure against contamination of the purified hydrogen. Oil-pumped tank hydrogen gas is purified by drying and passing it through titanium turnings and zirconium powder at 700°C,

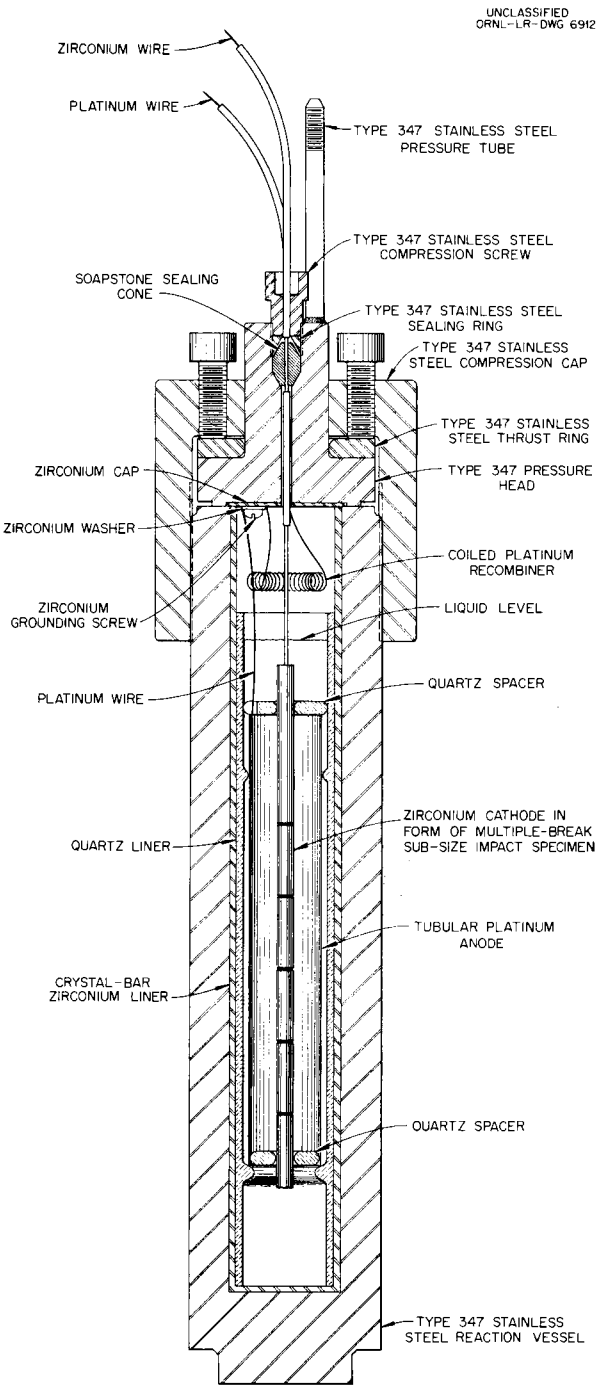

Fig. 62. Electrolytic Cell for Hydrogen Embrittlement Studies.

and then it is absorbed by titanium turnings at 400°C. When hydrogen is needed for an experiment, it is generated by heating the titanium hydride to 700°C. High-purity hydrogen is necessary for this type of research because other gaseous impurities considerably alter both the quantity of hydrogen absorbed and the properties of the metal itself. Specimens of the slow-bend or impact types are suspended from a quartz hook in a quartz reaction tube, and hydrogen is admitted to this system through a liquid-nitrogen-cooled trap from a gas buret.

The Effect of Oxide Films on the Rate of Hydrogen Absorption. – Experiments designed to evaluate the possibility of hydrogen embrittlement of zirconium and zirconium-alloy reactor components, as the result of exposure to radiolytic gas, have been under consideration during this period. The first phase of this work is concerned with the cathodic treatment of zirconium specimens in sulfuric acid at temperatures up to 300°C, since in this way the role of oxide films as diffusion barriers to the passage of hydrogen atoms can be studied. A sketch of the apparatus is shown in Fig. 62. The reaction vessel is a zirconium-lined type 347 stainless steel autoclave containing a tubular platinum anode surrounding a zirconium cathode which is machined in the form of a multiple-break subsize impact specimen. A coil of platinum wire heated approximately 50°C higher than the balance of the system is to serve as catalytic recombiner for the hydrogen and oxygen in the gas phase. The effects of cathodic treatments under several sets of conditions will be evaluated by impact testing, hydrogen analyses, and metallography. The complete apparatus has been constructed and is now being assembled.

HIGH-TEMPERATURE METALLURGY

DYNAMIC CORROSION

G. M. Adamson A. Taboada
V. P. Treciokas

Sodium Corrosion

Hastelloy B. – Two Hastelloy B loops were operated at 1500°F with molten sodium. Loop No. 165 operated for 1000 hr, and the sodium was drained while the loop was at temperature. In the cold leg of this loop what appeared to be very fine metallic crystals were seen adhering to the wall. The second loop, No. 166, plugged after 1010 hr. Upon sectioning, a plug consisting of a mass of fine dendritic nickel crystals was found in the hot leg. These crystals undoubtedly formed in the cold leg and were washed into the hot leg either separately or as a ball. The tubing in these loops was known to be covered by an oxide deposit, but no cleaning step had been used. Both these loops showed rough surfaces with intergranular penetrations to a depth of 2 mils. This attack seems to be a function of the original surface and is found in both the hot and cold legs.

Two additional Hastelloy B loops were then cleaned with dry hydrogen and operated at 1500°F with sodium. Loop No. 188 circulated for 500 hr and loop No. 189 for 1000 hr. In both loops deposits of magnetic crystals were found in the lower cold leg (Fig. 63) and in the hot horizontal section. The metallographic examination of loop No. 188 showed a rough surface with pits and subsurface voids to a depth of 2 mils.

Nickel. – The susceptibility of Hastelloy B to mass-transfer nickel in sodium prompted the operation with sodium of three loops constructed from "A" nickel. Two of the loops were dry-hydrogen

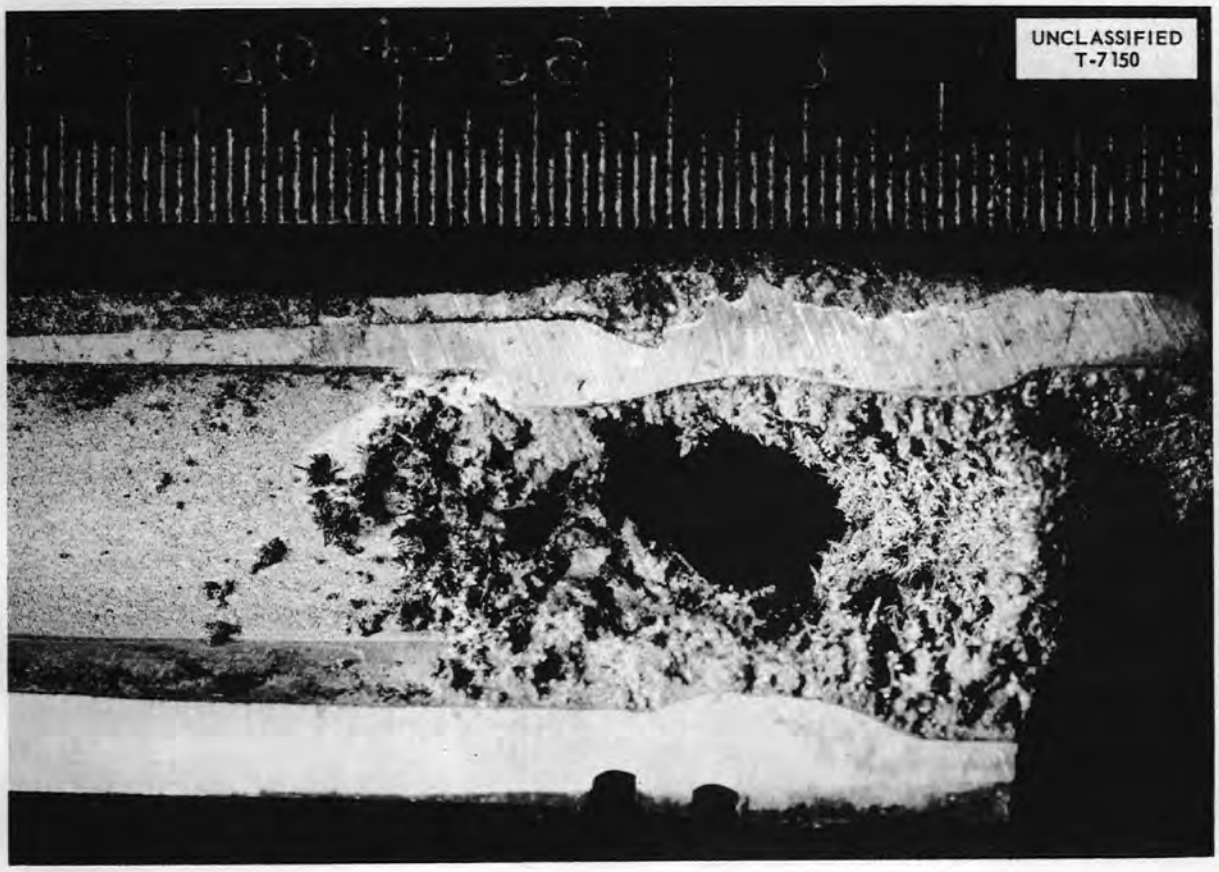

Fig. 63. Deposit in Cold Leg of Hastelloy B Thermal Loop After Circulating Sodium for 1000 hr at 1500°F.

cleaned prior to operation, whereas the third was operated in the as-fabricated condition. Dendritic, magnetic crystals were found in the cold legs of all three loops after operation periods of 500 or 1000 hr at 1500° F.

GENERAL CORROSION

E. E. Hoffman W. H. Cook
C. F. Leitten, Jr.

Single-Crystal MgO Specimens in Static Lithium and Lead

Single-crystal specimens of MgO were static tested at 1500° F for 100 hr in lithium and lead in Globiron containers. These corrosion data supplement those previously reported for single-crystal MgO in other media.[1]

Two MgO specimens, nominally 0.10 × 0.23 × 0.24 in., cleaved from a piece of synthetic MgO crystal, were supplied by the Ceramic Laboratory of the Metallurgy Division. The specimen tested in lithium had a weight loss of 66.4%, and it took on the shape of the Globiron container in the regions of contact. There was no attack on the MgO specimen tested in the lead.

Dissimilar-Metal Mass-Transfer Study on the Zirconium–Type 304 Stainless Steel–Sodium System

The problem of dissimilar-metal mass transfer of zirconium to type 304 stainless steel in sodium has been studied in the temperature range 1000 to 1500° F. Table 6 indicates the conditions of these tests.

In all three tests a seesaw furnace was used with a speed of 1 cpm. The heat-exchange medium was sodium, and the duration of test was 100 hr. The test containers were made of type 304 stainless steel. Zirconium specimens were retained in the hot zone of the stainless steel tubes by partially crimping the capsule wall. Each specimen of zirconium was carefully cleaned and weighed both before and after testing in order to obtain weight-change data. Upon completion of a test, each capsule was sectioned, and samples of each section were submitted for metallographic and spectrographic analyses. The container was sampled in six locations ranging from the hot-zone end to the cold-zone end.

It appeared that no thermal-gradient mass transfer occurred in any of the tests since there was no deposit of zirconium found in the cold zones. Figure 64*a* is a photomicrograph of the cold-zone section of the No. 3 test (hot zone–1500° F). No deposit was found on the surface of the type 304 stainless steel container. This photomicrograph is representative of the cold-zone sections in the other tests.

Upon metallographic examination a layer of fine particles was observed in the hot-zone section of every test. X-ray examination of the surface of a specimen, sectioned from the hot zone of the 1500° F test container, showed no trace of zirconium or zirconium compounds. Figure 64*b* is a photomicrograph of the hot-zone section of the 1500° F test. In this zone the precipitate reached a maximum thickness of 2 mils. This layer is very similar to the layers observed in previous investigations on type 304 stainless steel samples carburized in the presence of sodium.

Spectrographic analysis revealed only a slight trace of zirconium in the hot-zone section of the No. 2 test. Test No. 3 revealed an increase in zirconium content; but again this amount could be considered negligible, for it was of the order of 10^{-3}%. It was noted in this test (hot zone–1500° F) that a slightly larger concentration of zirconium appeared in the cold zone than in the hot zone.

In all cases the zirconium samples, when tested, were found to have gained weight. X-ray analysis revealed a layer of zirconium oxide on the samples.

[1] E. E. Hoffman *et al.*, *ANP Quar. Prog. Rep. Sept. 10, 1954*, ORNL-1771, p 94.

TABLE 6. TEMPERATURE CONDITIONS OF ZIRCONIUM–TYPE 304 STAINLESS STEEL–SODIUM SEESAW TESTS

Test No.	Hot Zone (°F)	Cold Zone (°F)	Temperature Gradient (°F)
1	1000	531	469
2	1200	700	500
3	1500	1030	479

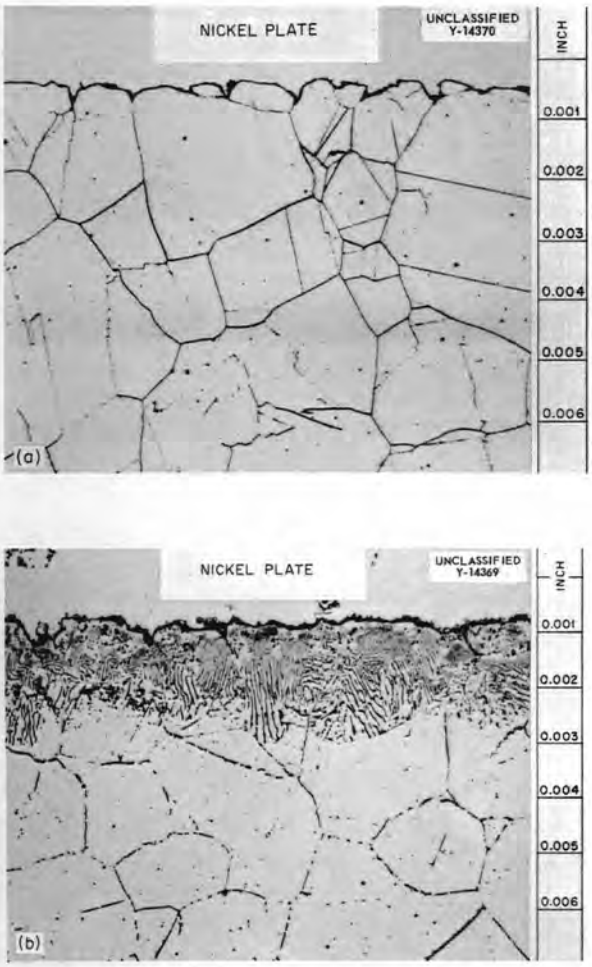

Fig. 64. Sections of a Type 304 Stainless Steel Container After Seesawing for 100 hr at 1500°F. (*a*) Cold zone; 500X; reduced 37%. (*b*) Hot zone; 500X; reduced 42%. Note the layer at the surface of the hot-zone specimen. Etchant: 10% oxalic acid.

The weight changes were as follows:

Test No.	Weight Change (g)
1	+0.0041
2	+0.0089
3	+0.0150

The original weight of the samples was 17 g. Judging from the above data, it is apparent that under the conditions of these tests zirconium exhibits negligible amounts of dissimilar-metal mass transfer to type 304 stainless steel.

Magnesium-Lithium Alloys in Water

An 80% Mg–20% Li alloy which has been proposed as a possible shielding material has been corrosion-tested in water at various temperatures. Specimens of this material were carefully cleaned just prior to testing in order to remove surface films, chiefly Li_3N, which formed on exposure to air. A cleaned specimen was found to gain 0.088 mg/cm^2 if left standing in the atmosphere for 6 hr. Table 7 gives the weight loss of the specimens following tests at various temperatures. One specimen was tested for various lengths of time in 100°C water and was found to lose 0.292 mg/cm^2 in the first 2 min of the test. This was 90% of the weight lost in the 15-min test. This decrease in rate may be attributed to the depletion of lithium atoms on the surface since no protective film could be detected. Pure magnesium tested in water at 100°C for 15 min showed a weight loss of 0.09 mg/cm^2.

TABLE 7. CORROSION OF 80% Mg–20% Li ALLOY IN WATER

Temperature of Water (°C)	Time (min)	Weight Loss (mg/cm^2)
30	15	−0.243
50	15	−0.271
80	15	−0.309
100	15	−0.326

MECHANICAL TESTING

R. B. Oliver D. A. Douglas, Jr.
J. H. DeVan J. W. Woods

Increased attention is being directed toward finding new alloys with better corrosion resistance and high-temperature strength. Therefore, the mechanical testing facilities were expanded during the past year to provide additional equipment for the stress-rupture testing of promising alloys in service environments. Six new lever-arm stress-rupture machines (Fig. 65) were constructed for testing in liquid metals, and four direct-loading or dead-load type units (Fig. 66) for testing in argon, hydrogen, or air. Eight new tube-burst units (Fig. 67) were also added for the study of multiaxial stress systems.

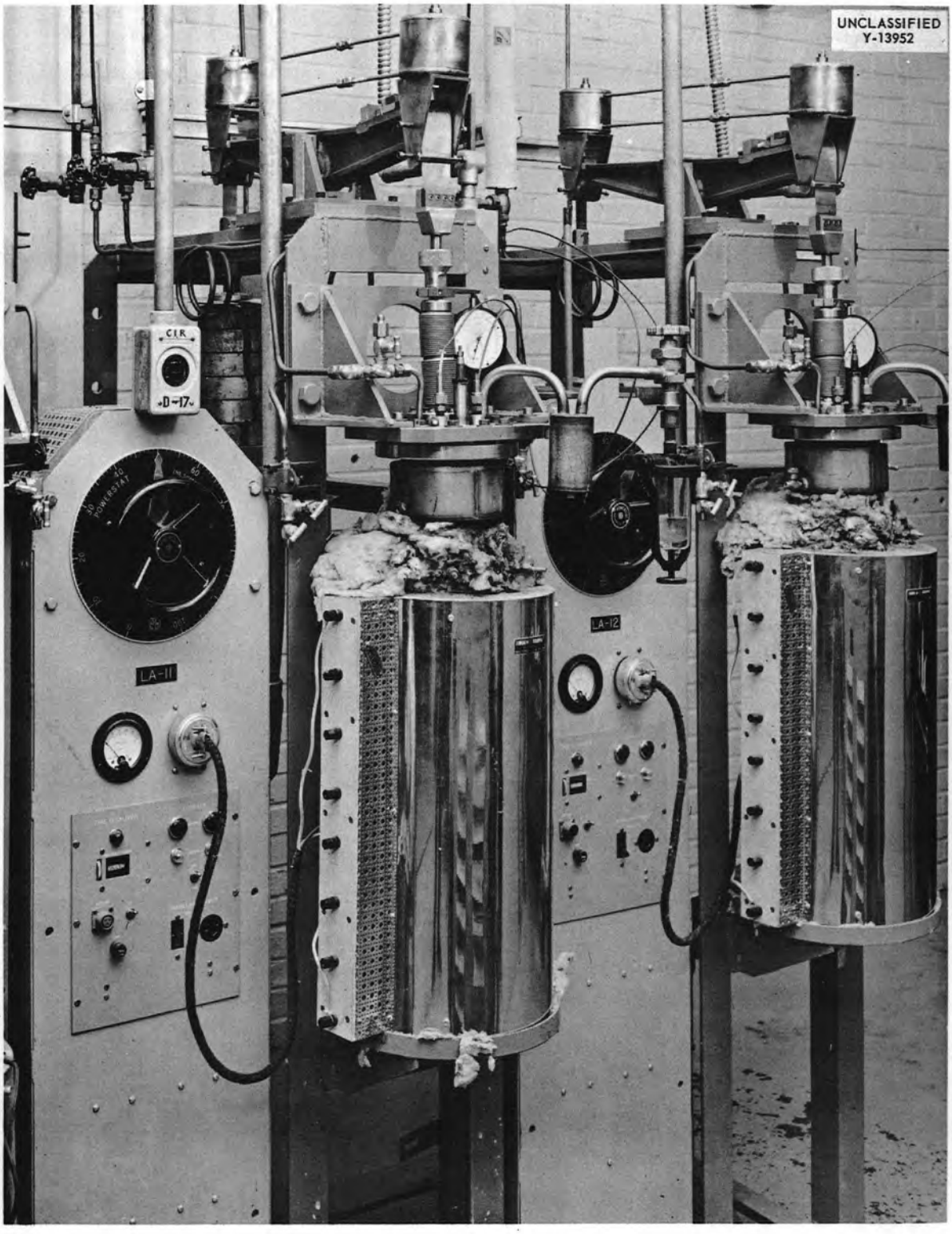

Fig. 65. Lever-Arm-Type Stress-Rupture Machines.

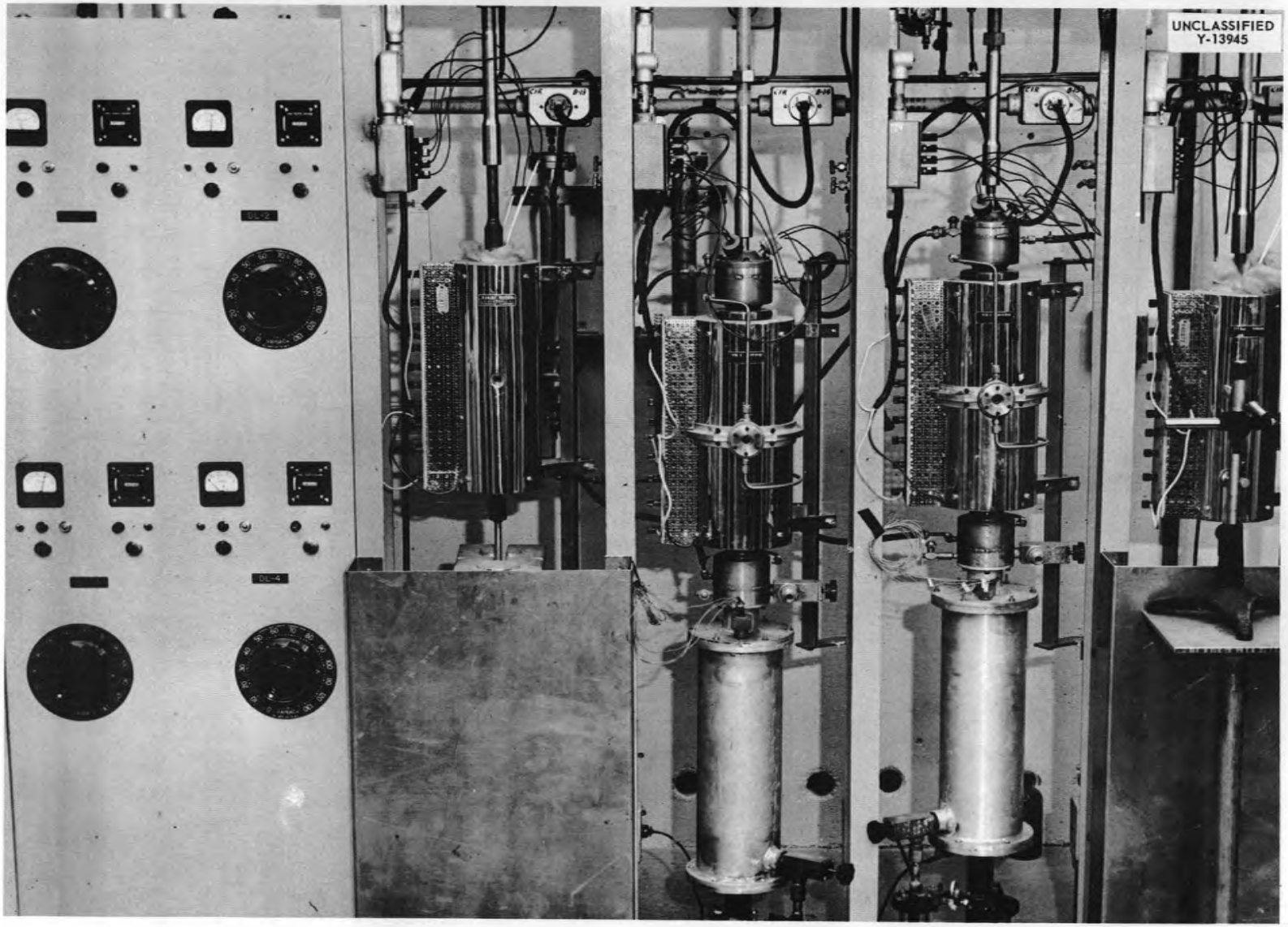

Fig. 66. Dead-Load-Type Stress-Rupture Machines.

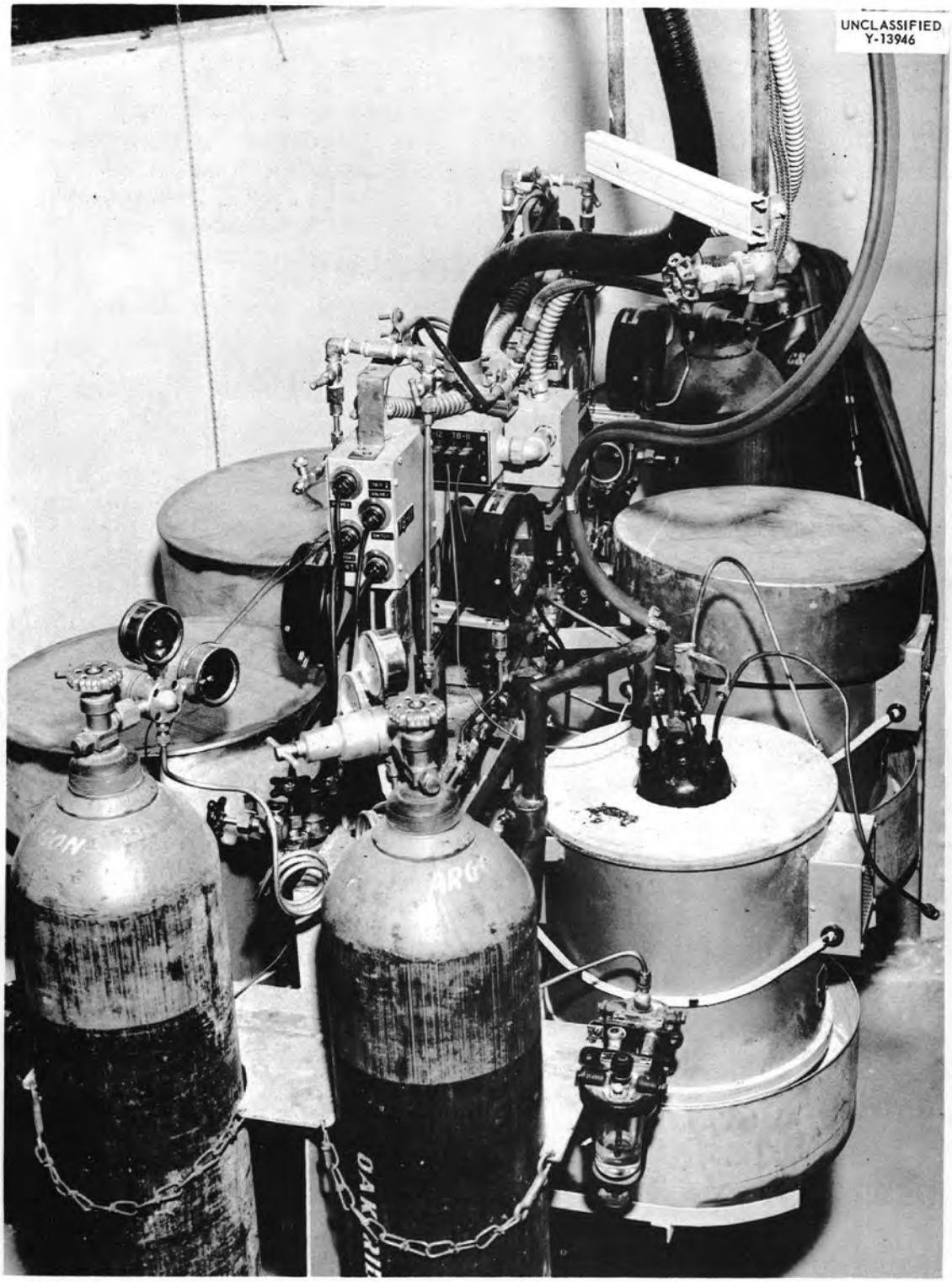

Fig. 67. Tube-Burst Test Unit.

During the previous six months the testing program was interrupted in order to establish a new laboratory in which the new and the old equipment could be located. It is expected, however, that this loss in testing time will be readily offset by the more expedient arrangement of machines and associated temperature control equipment and by the increased testing capacity.

Hastelloy B was considered to be a promising structural material, and a program was recently begun to evaluate its high-temperature strength. A series of tests on solution-annealed material has been completed in an argon atmosphere at 1500 and 1650°F. The rupture strength of Hastelloy B for a given rupture life at these temperatures was found to be substantially greater than that of Inconel or of type 316 stainless steel. This can be seen in Fig. 68, which shows the rupture strengths of these alloys in argon at 1500°F.

Tests run in hydrogen on Hastelloy B and on a sister alloy, Hastelloy C, follow very closely the pattern of similar tests in argon. Limited data have also been obtained in air with quite interesting and, so far, unexplained results. A substantial decrease in the creep rate was observed to lead to much longer rupture life in air than in argon. Further testing of Hastelloy B will be conducted at 1300 and 1800°F.

The program to obtain design data for Inconel under reactor conditions is continuing; and, although several long-term tests are still in progress, sufficient results have been obtained to allow formulation of a series of design curves corresponding to tests made at 1300, 1500, and 1650°F and in argon and fused-salt environments. In Figs. 69–78, curves are plotted showing the times to 0.5, 1, 2, 5, 10% elongations and the times to rupture for various stresses.

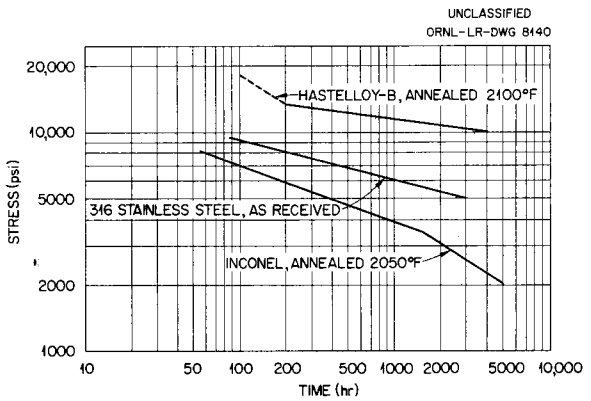

Fig. 68. Stress-Rupture Curves for Hastelloy B, Type 316 Stainless Steel, and Inconel.

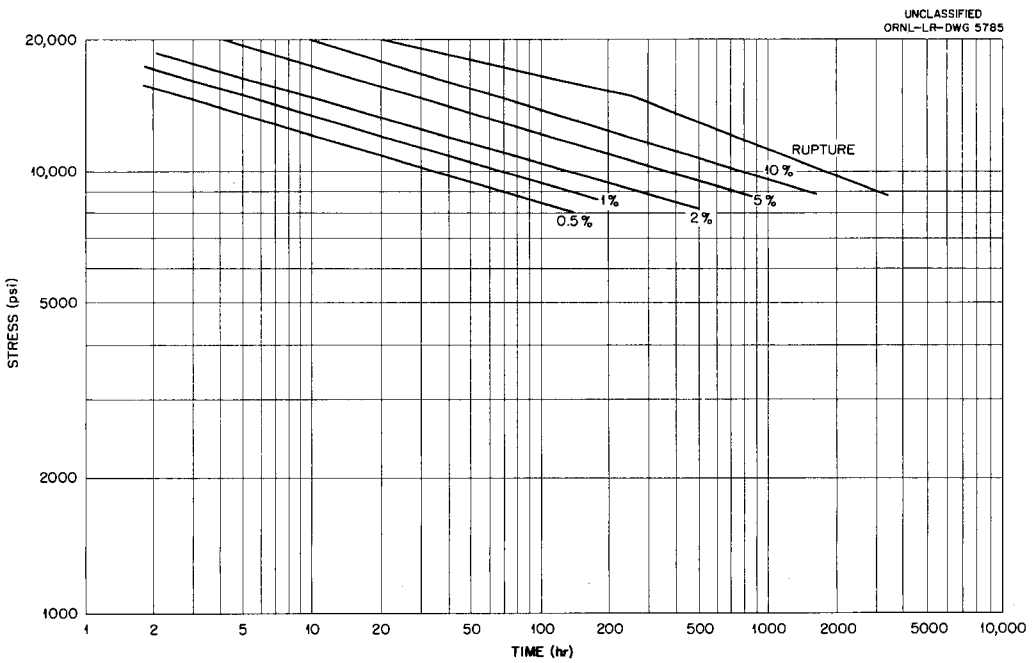

Fig. 69. Design Curves for As-Received Inconel Sheet Tested in Argon at 1300°F.

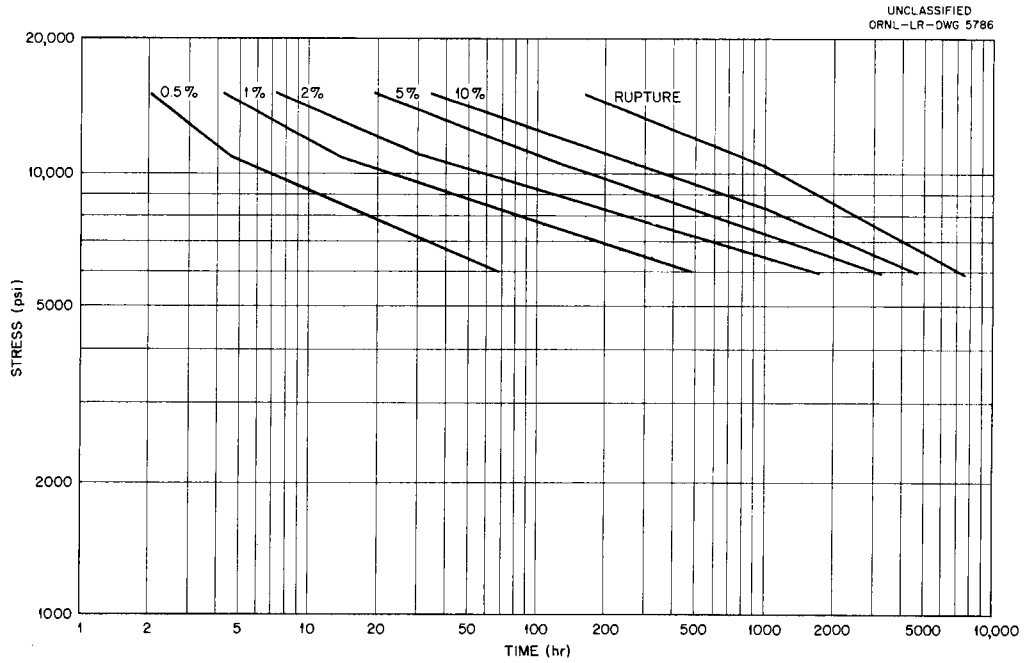

Fig 70. Design Curves for As-Received Inconel Sheet Tested in Fused Salt at 1300°F.

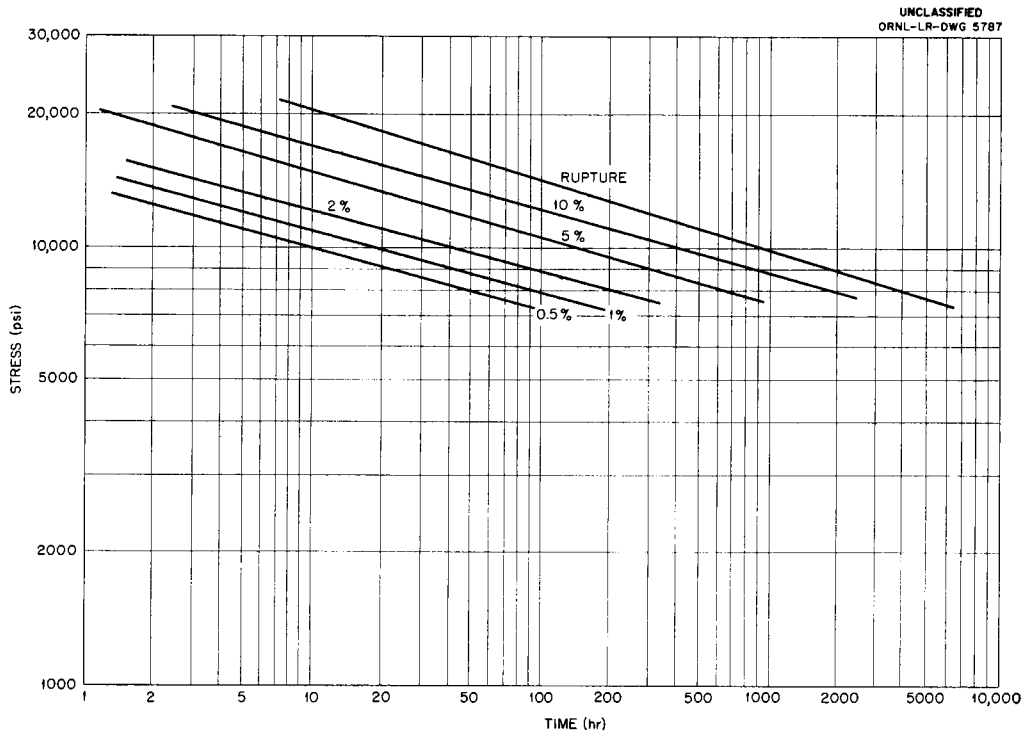

Fig. 71. Design Curves for Inconel Sheet Annealed at 2050°F and Tested in Argon at 1300°F.

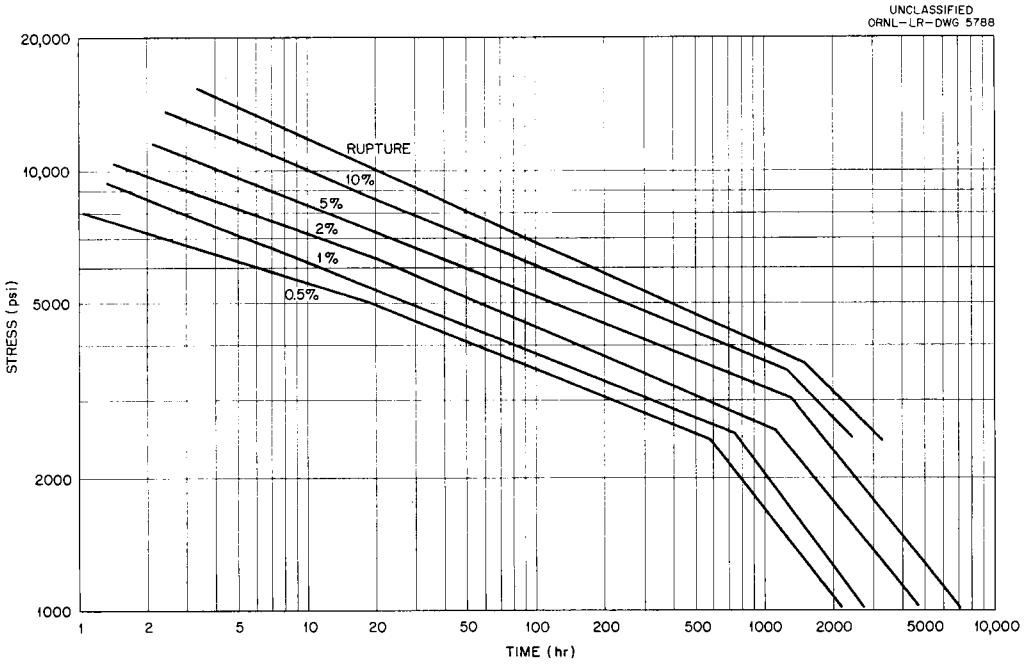

Fig. 72. Design Curves for As-Received Inconel Sheet Tested in Argon at 1500°F.

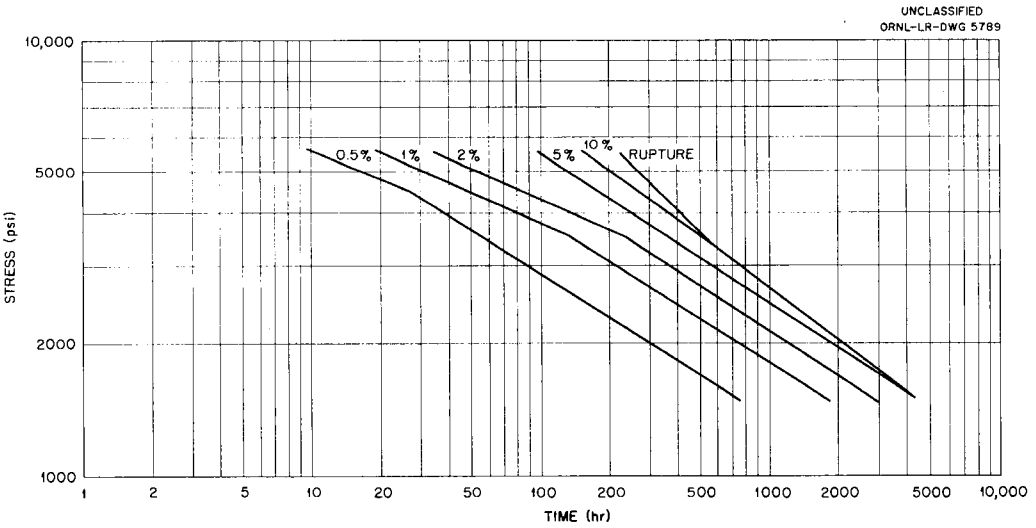

Fig. 73. Design Curves for As-Received Inconel Sheet Tested in Fused Salt at 1500°F.

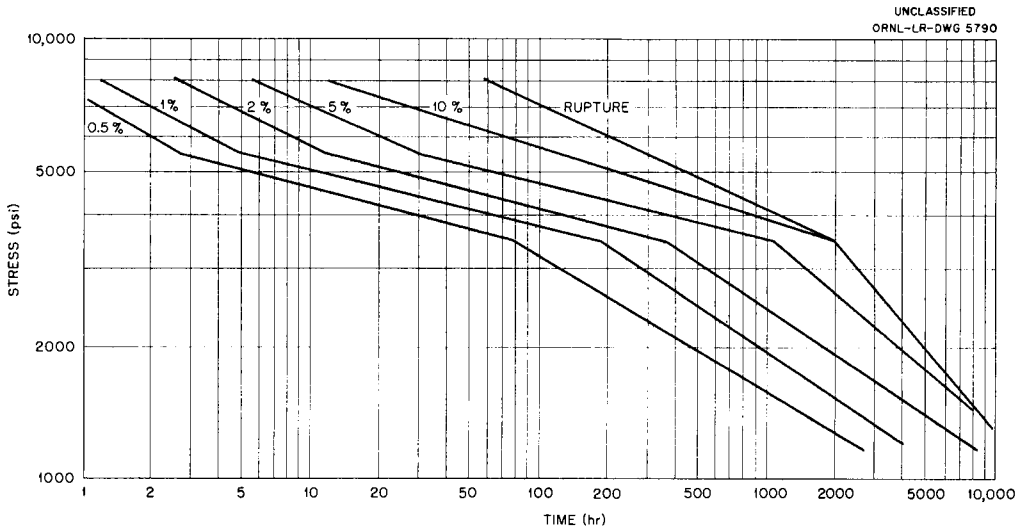

Fig. 74. Design Curves for Inconel Sheet Annealed at 2050°F and Tested in Argon at 1500°F.

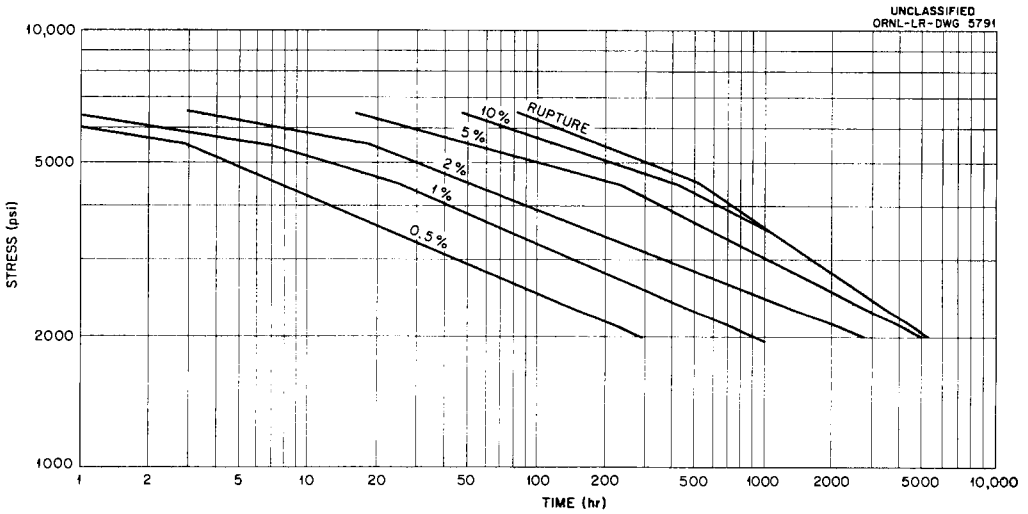

Fig. 75. Design Curves for Inconel Sheet Annealed at 2050°F and Tested in Fused Salt at 1500°F.

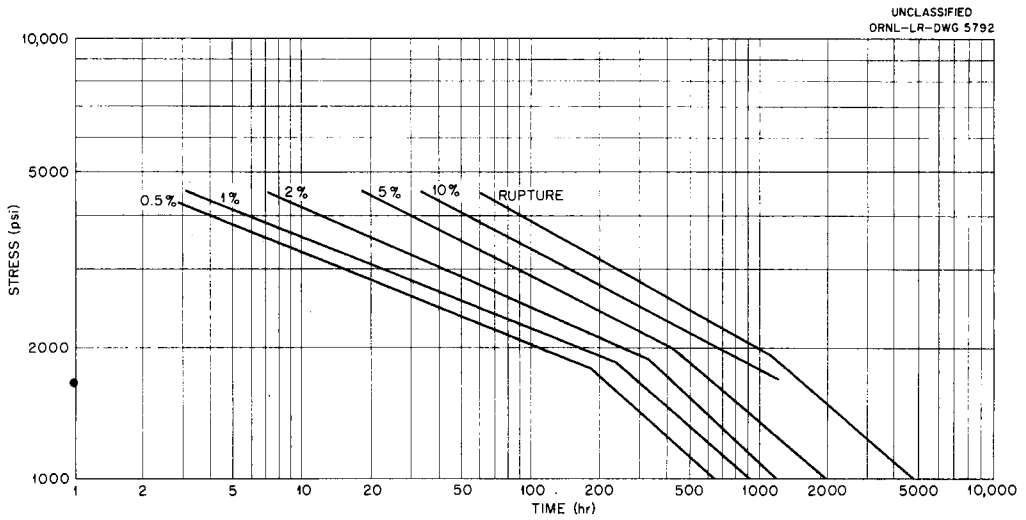

Fig. 76. Design Curves for As-Received Inconel Sheet Tested in Argon at 1650°F.

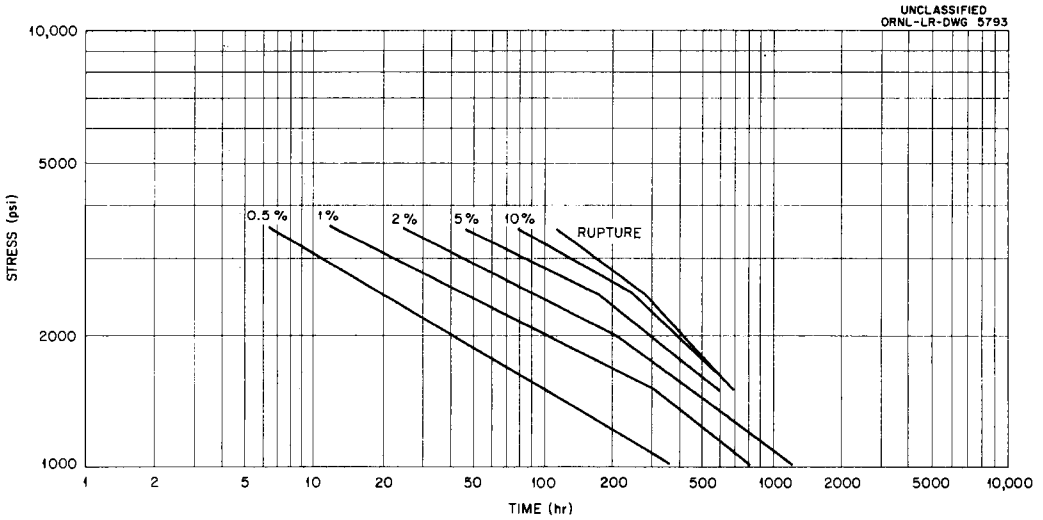

Fig. 77. Design Curves for As-Received Inconel Sheet Tested in Fused Salt at 1650°F.

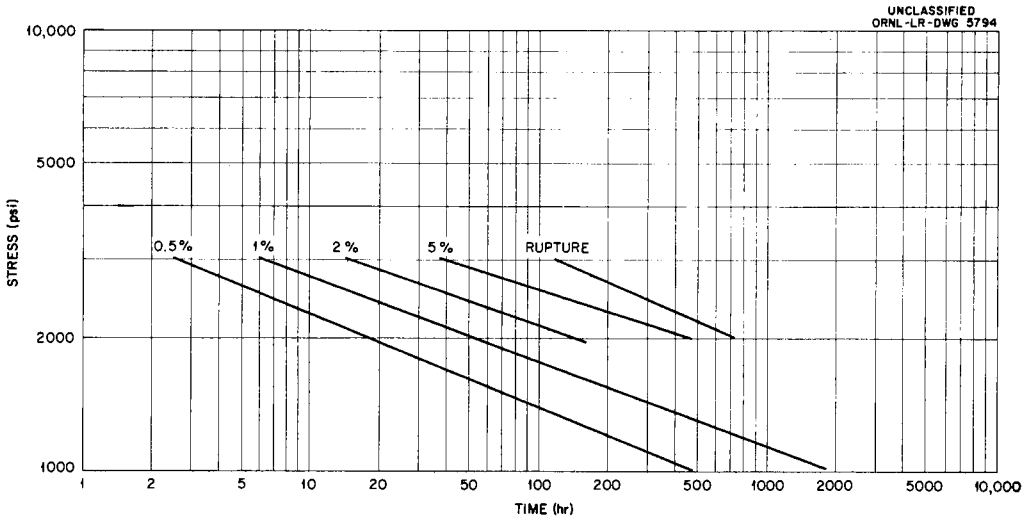

Fig. 78. Design Curves for Inconel Sheet Annealed at 2050°F and Tested in Fused Salt at 1650°F.

WELDING AND BRAZING

P. Patriarca K. W. Reber
R. E. Clausing G. M. Slaughter
Metallurgy Division

J. M. Cisar
Aircraft Reactor Engineering Division

R. L. Heestand
Pratt & Whitney Aircraft

Brazing Alloy Development

The resistance of brazing alloys to high-temperature oxidation is a primary factor to consider in the choice of these materials for use in the fabrication of high-temperature radiators. An evaluation program is, therefore, being conducted to determine the oxidation resistance of 28 potential high-temperature brazing alloys. Inconel T-joints were prepared with these materials, and small samples of these joints were subjected to static air at 1500 and 1700°F for varying times. The results of the tests, as determined by metallographic examination in the as-polished condition, are presented in Table 8. Some of the information found in this table has appeared in a previous semiannual report[2] but is presented again here in a more complete form to permit a comprehensive and detailed evaluation.

The void formation along the braze-metal, Inconel interface, which was noted on the samples brazed with the General Electric 62, General Electric 81, and 73.5% Ni–16.5% Cr–10.0% Si alloys and which was previously thought to result from internal oxidation, is now believed to be associated with a diffusion phenomenon. Check samples which were tested in a vacuum under identical conditions of time and temperature contained voids at a similar location along the interface. Although the nature of the void formation is not completely understood at this time, it has been noted that the quantity of one constituent appears to increase with increasing time at test temperature and with increasing temperature of the test. The identification of this constituent, which is probably a complex intermetallic compound, is to be attempted by x-ray techniques.

As a result of this investigation, it is evident that a majority of the nickel and nickel-chromium base alloys are suitable for service in an oxidizing atmosphere at 1500°F and that several are suitable at 1700°F. Photomicrographs of oxidized Inconel joints brazed with two of the alloys are shown in Figs. 79 and 80. Figure 79 illustrates the excellent resistance to attack of the General Electric 81 alloy after 500 hr at 1500°F. This alloy has been used for the fabrication of units containing austenitic stainless steel or Inconel fin materials; whereas the Coast Metals 52 alloy shown in Fig.

[2] P. Patriarca *et. al.*, *Met. Semiann. Prog. Rep. April 10, 1954*, ORNL-1727, p 62.

TABLE 8. OXIDATION RESISTANCE OF DRY-HYDROGEN-BRAZED INCONEL T-JOINTS

Brazing Alloy	Composition (wt %)	Brazing Temperature (°F)	Oxidation in Static Air*				
			At 1500°F			At 1700°F	
			For 200 hr	For 500 hr	For 1300 hr	For 200 hr	For 500 hr
Commercial Alloys							
Nicrobraz	70 Ni–14 Cr–6 Fe–5 B–4 Si–1 C	2150	Slight	Slight	Slight	Slight	Slight
Low-melting Nicrobraz	80 Ni–5 Cr–6 Fe–3 B–5 Si–1 C	1950	Slight	Slight	Slight	Slight	Slight
Coast Metals 50	93 Ni–3.5 Si–2.5 B–1 Fe	2050	Slight	Slight	Slight	Slight	Slight
Coast Metals 51	92 Ni–4.5 Si–3 B–0.5 Fe	1870	Slight	Slight	Slight	Slight	Slight
Coast Metals 52	89 Ni–5 Si–4 B–2 Fe	1840	Slight	Slight	Slight	Slight	Slight
Coast Metals 53	81 Ni–4 Si–4 B–8 Cr–3 Fe	1950	Slight	Slight	Slight	Slight	Slight
Coast Metals NP	50 Ni–12 Si–2.8 Fe–4 Mo–4.5 P–1 Mn–0.5 Cr	2050	Slight	Slight	Slight	Slight	Moderate
Mond Nickel Co. alloy	64 Ag–33 Pd–3 Mn	2150	Severe	Severe	Severe	Complete	
Copper	100 Cu	2050	Complete			Complete	
Experimental Nickel-Base Alloys							
General Electric 62	69 Ni–20 Cr–11 Si	2150	Slight	Slight	Slight	Slight	Moderate
General Electric 81	66 Ni–19 Cr–10 Si–4 Fe–1 Mn	2150	Slight	Slight	Slight	Slight	Moderate
Ni-Cr-Si	73.5 Ni–16.5 Cr–10 Si	2150	Slight	Slight	Slight	Slight	Moderate
Ni-Si	88 Ni–12 Si	2200	Slight	Slight	Slight	Slight	Slight
Ni-Ge	75 Ni–25 Ge	2150	Slight	Slight	Slight	Moderate	Severe
Ni-Ge-Cr	65 Ni–25 Ge–10 Cr	2130	Slight	Slight	Slight	Slight	Moderate
Electroless Ni-P	88 Ni–12 P	1740	Slight	Slight	Slight	Above melting point of alloy	
Ni-P-Cr	80 Ni–10 P–10 Cr	1830	Slight	Slight	Slight	Above solidus of alloy	
Ni-Mo-Ge	50 Ni–25 Mo–25 Ge	2150	Slight	Slight	Slight	Moderate	Severe
Ni-Sn	68 Ni–32 Sn	2150	Slight	Moderate	Severe	Severe	Complete
Ni-Mn	40 Ni–60 Mn	1950	Complete			Complete	
Ni-Mn-Cr	35 Ni–55 Mn–10 Cr	2050	Severe	Severe	Complete	Severe	Complete
Experimental Precious-Metal-Base Alloys							
Pd-Ni	60 Pd–40 Ni	2300	Very slight	Slight	Moderate	Very slight	Slight
Pd-Ni-Si	60 Pd–37 Ni–3 Si	2150	Very slight	Slight	Moderate	Slight	Moderate
Pd-Al	92 Pd–8 Al	2020	Very slight	Very slight	Very slight	Very slight	Slight
Pd-Ge	90 Pd–10 Ge	2050	Very slight	Slight	Severe	Complete	
Au-Ni	82 Au–18 Ni	1830	Very slight	Very slight	Slight	Moderate	Moderate
Au-Co	90 Au–10 Co	1830	Very slight	Very slight	Moderate	Slight	Severe
Au-Cu	80 Au–20 Cu	1740	Moderate	Complete		Complete	

*Very slight, less than 1 mil penetration; slight, 1 to 2 mils of penetration; moderate, 2 to 5 mils of penetration; severe, greater than 5 mils of penetration; complete, fillet completely destroyed.

80 is of interest in the fabrication of high-conductivity fin assemblies. Only minor oxidation is evident on the Coast Metals 52 brazed joint after it was subjected to the oxidizing atmosphere for the same time and temperature. The resistance of the precious-metal alloys to attack is also very good, but their application in radiator fabrication is not considered to be promising. Their poor compatibility with liquid-metal environments makes their use extremely risky since severe tube-wall dilution during brazing, or solid-state diffusion in service, may produce a high concentration of the precious metal near the circulating liquid.

Cyclic oxidation tests are now being conducted to determine the effect of thermal fluctuations upon the adherence of protective oxide films. Preliminary results indicate that the extent of attack upon most of the alloys has not been appreciably increased, but a more complete analysis is required before definite conclusions can be reached.

Corrosion tests have indicated that brazing alloys of the nickel-chromium-germanium and nickel-chromium-germanium-silicon types may be useful. In order to conduct further research on these alloys

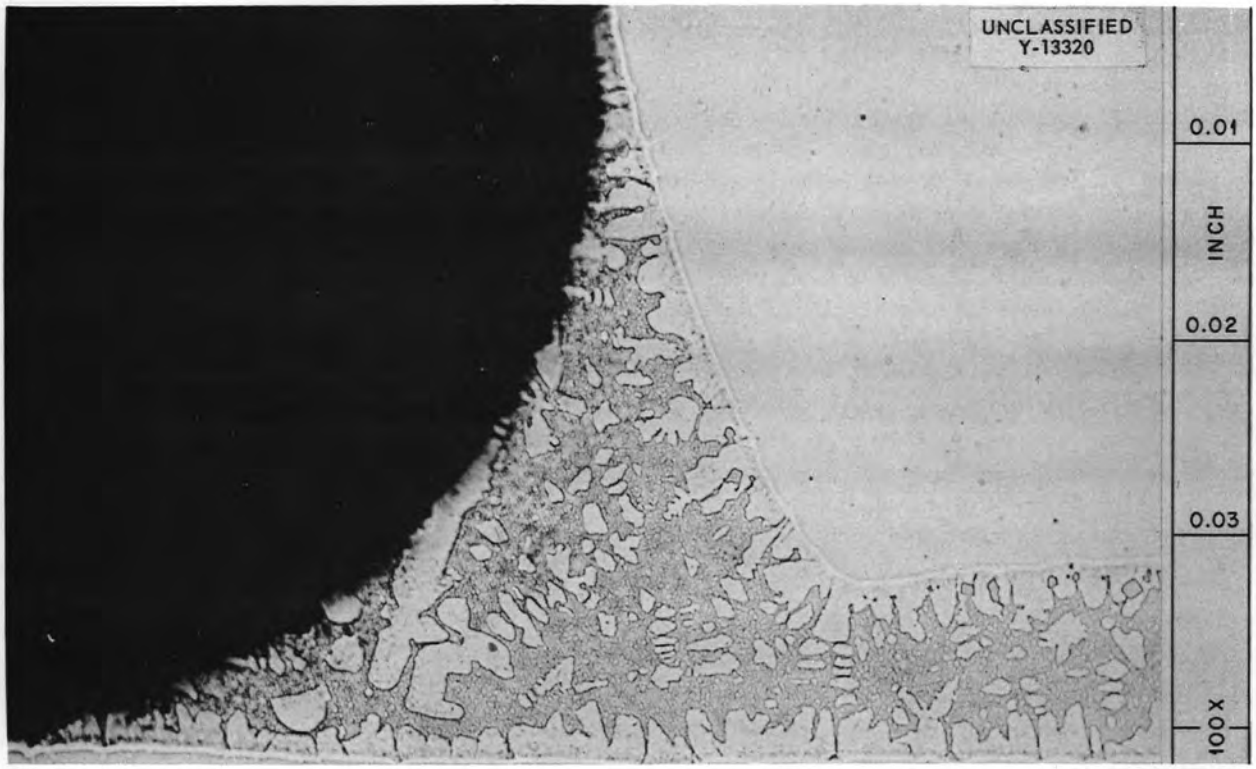

Fig. 79. An Inconel T-Joint Brazed with General Electric 81 Brazing Alloy and Tested in Static Air for 500 hr at 1500°F. Negligible attack is evident. Etchant: electrolytic oxalic acid. 100X.

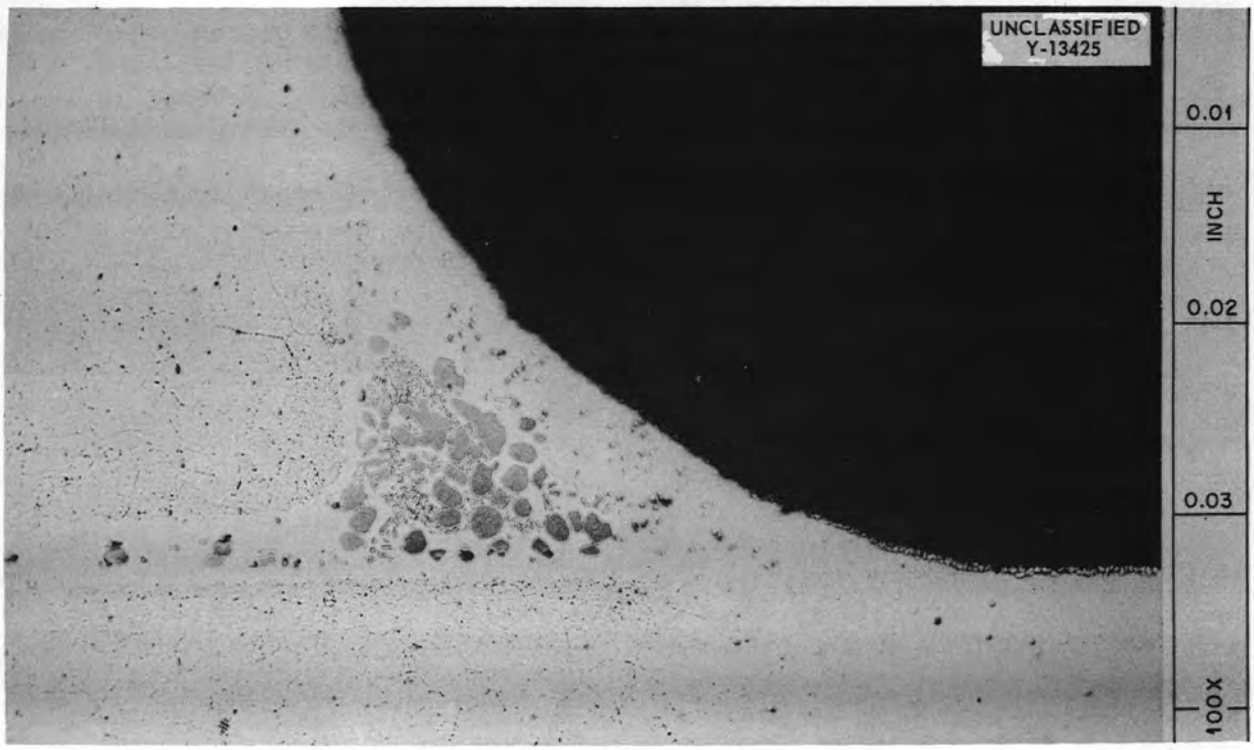

Fig. 80. Inconel T-Joint Brazed with Coast Metals 52 Brazing Alloy and Tested in Static Air for 500 hr at 1500°F. Only very slight oxidation can be seen. Etchant: electrolytic oxalic acid. 100X.

and to provide enough material for tests on heat-exchanger components, a 1-lb quantity of each alloy was arc-melted, as was a similar quantity of the 75% Ni–25% Ge binary alloy. Several techniques have been investigated to reduce these arc-melted ingots to the more desirable powder form, but no suitable laboratory method has been obtained. Grinding with a mortar and pestle or ball-milling has not been satisfactory since the alloy possesses sufficient inherent ductility to prevent easy powdering. Experiments whereby the alloy was induction-melted in a quartz tube and the molten metal was then permitted to drop from a small hole into water have not been promising. Therefore, a commercial manufacturer of brazing-alloy powders was contacted, and 50-g samples were submitted for experimentation with the company's powder-making equipment. Another possibility for succeeding lies in the construction and installation of a small atomizing machine or in the use of larger atomizers available in industry.

The production of brazing-alloy powders from sintered mixtures of elemental powders is now under development, and preliminary experiments have indicated that this technique may be very promising. The elemental powders are carefully mixed and sintered in dry hydrogen for several hours at a temperature very near to that required to fuse the lowest melting-point eutectic in the system. This sintered material may then be crushed easily to provide a fine powder suitable for preplacement on heat-exchanger or radiator components. Experiments are now being conducted to determine the optimum time and temperature conditions that will result in sufficient diffusion without seriously impairing the friability of the compact. The possibilities of applying this presintering method to other alloy systems of interest are likewise being studied.

High-Conductivity Fin-Radiator Fabrication

The fabrication of a radiator with type 430 stainless-steel-clad copper high-conductivity fins has been described in a previous report.[3] The tube-to-fin section was brazed with Coast Metals 52 alloy, and the tube-to-header welding was performed with the semiautomatic inert-arc welding equipment available in the Welding Laboratory. The welded tube-to-header joints were back-brazed as a precautionary measure against the formation of leaks during service.

An analysis of this radiator indicated that critical control must be maintained over the quantity of brazing alloy placed on each tube-to-fin joint. The amount of alloy required must be sufficient to protect the exposed copper on the punched lips of the high-conductivity fins. Not only does this protection ensure that the copper serves its intended purpose in the fin, but it also minimizes the tendency of Hastelloy B tubing to severely oxidize if it is incorporated into radiators as a replacement for Inconel (see section: "Hastelloy B Radiator Fabrication"). The presence of an excess of braze metal, over that required for the protection of the copper, may result in "puddling," which consists in the excess metal merely concentrating on the bottom fins. This condition is undesirable because the air passages between these fins may be sealed and because localized distortion is often evident.

The use of extruded brazing-alloy wires has been extensively investigated as a means of obtaining controlled quantities, but the lack of a suitable binder makes their use somewhat unattractive at the present. An acrylic binder material produces wires that are relatively easy to handle when freshly extruded, but they become embrittled upon aging for a few hours at room temperature. Thus, the assembling of large complicated radiators is seriously hampered by crumbling and by the subsequent movement of the brazing alloy from the desired tube-to-fin location. Another binder material, Castolite, produces wires that are extremely ductile and weak at room temperature, and, therefore, meticulous care must be exercised when the wires are handled.

A dry-powder method of brazing-alloy preplacement has been developed which provides a promising means of obtaining controlled amounts of alloy on each tube-to-fin joint. A stainless steel template containing holes that have been precision drilled is placed over a sheared fin so that each hole is centered over a punched lip. Since the drilled hole is larger than the lip, the template fits securely against the flat portions of the fin. The dry powder is applied, and the excess is removed. After careful removal of the template, the powder is secured to the fin with Nicrobraz cement and allowed to dry. A photograph of a 36-hole fin with brazing alloy prepiaced by this technique is shown in Fig. 81.

[3] P. Patriarca *et al.*, *Met. Semiann. Prog. Rep. Oct. 10, 1954*, ORNL-1875, p 116.

UNCLASSIFIED
Y-14294

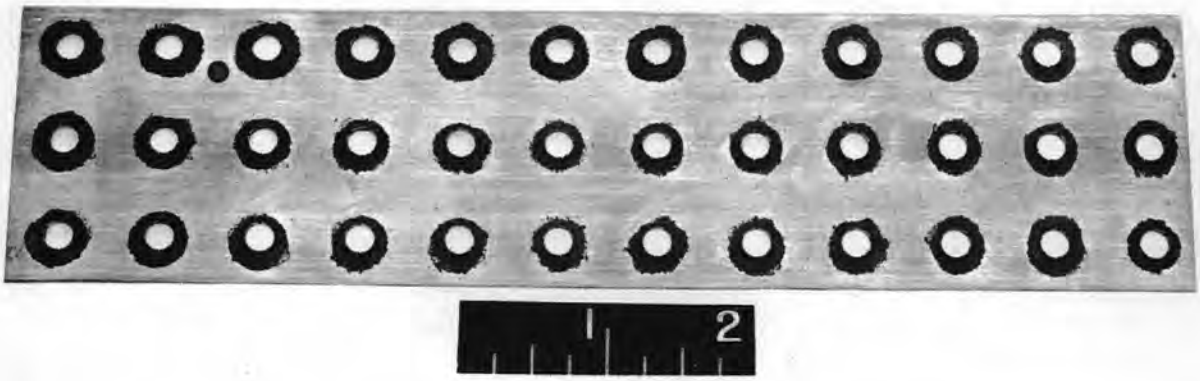

Fig. 81. Radiator High-Conductivity Fin with Brazing Alloy Preplaced by Dry-Powder Technique.

The edge protection of exposed copper on the sheared fin edges is extremely desirable in order to minimize its oxidation and in order to overcome the severe fin distortion resulting from the volume changes occurring during the formation of the oxide. An aluminizing process has been developed in which edge protection is obtained by the formation of a highly oxidation-resistant copper-aluminum alloy. A procedure has also been devised to permit the aluminizing of large numbers of type 310 stainless-steel-clad copper fins. This procedure, which requires that all fins be precision-sheared to exact size, is presented below.

After degreasing in polychlorethylene or another suitable organic solvent, the fins are stacked in groups of approximately 200 and securely clamped with $\frac{1}{4}$-in.-thick stainless steel end plates. The exposed copper edges are then sprayed with three coats of Kestron acrylic spray. This seals the cracks between fins and prevents the flow of an aluminum-bearing slurry onto the stainless steel cladding. A coat of slurry, consisting of 100 cc of acrylic resin to 40 g of atomized aluminum powder (325 mesh), is then applied evenly to the fin edges. After sufficient drying, the clamped fins are heated in helium at 750°F for $2\frac{1}{2}$ hr to accelerate the formation of the oxidation-resistant aluminum bronze. A high helium flow rate (80 ft^3/hr) should be maintained for the first hour, and this can be reduced to 40 ft^3/hr for the remaining heat treatment. After cooling, the excess aluminum can be easily removed from the fin edges with the aid of a brass-wire brush. These fins can then be punched by the conventional techniques.

Test specimens of fins edge-protected by this method have been metallographically examined after 100, 200, 500, and 1000 hr in air at 1500°F. Figure 82, a photomacrograph of such a fin after 1000 hr at temperature, exhibits the excellent protection afforded by this technique. The depth of oxide penetration into an unprotected fin is shown on the same print for comparison purposes. The small voids near the aluminized edge of the protected fins are attributed to the migration of copper into the aluminum-rich surface metal. Cyclic oxidation tests on these aluminized fins are also being conducted to evaluate their stability. After alternately heating to 1500°F and cooling with air to room temperature 70 times in 200 hr, no adverse effects are evident.

In preparation for the subsequent assembling, welding, and brazing of two radiators for the heat-exchanger program, the stainless-steel-clad copper high-conductivity fins have been sheared to the desired final dimensions. They were degreased,

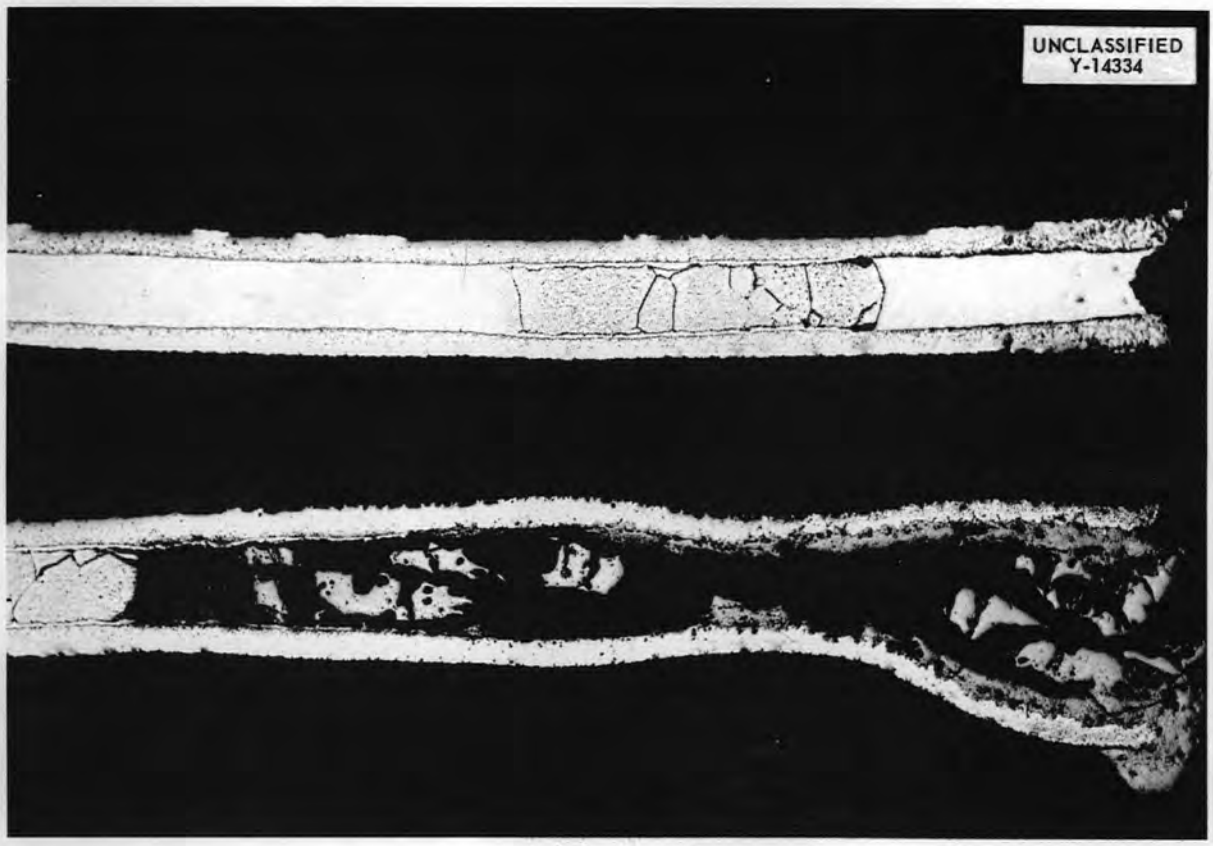

Fig. 82. Type 310 Stainless-Steel-Clad Copper High-Conductivity Fins After Oxidation for 1000 hr at 1500°F. Top fin illustrates the excellent edge protection afforded by the aluminizing treatment. Bottom fin illustrates the severe attack on the unprotected fin.

inspected for surface imperfections, and aluminum-bronze edge-protected by the procedure described above.

After punching, these fins will be assembled on the tubes by utilizing the dry-powder preplacement technique. By using a $\frac{1}{16}$-in. template containing holes of 0.246-in. diameter, the minimum quantity of brazing alloy per joint is provided that will permit good coverage of the exposed copper on the punched fin lips. A modification in the procedure reduces the tendency of alloy to accumulate in excess, which is undesirable and which results from normal variations in the quantity deposited. Two thin sheets of Inconel are placed tightly together at 4-in. intervals along the 12 in. of stacked fins. The capillary joint between these two Inconel sheets acts as a sump to remove any excess brazing alloy that is present. This modification should be easily applied to the radiators since $\frac{1}{16}$-in. Inconel sheets are to be placed at these 4-in. intervals for structural support. A discussion of the fabrication procedures used during welding and brazing of these radiators should be available in the next semiannual report.

The use of the 6% aluminum-bronze high-conductivity fin material has been hampered by the difficulties encountered when brazing these fins to Inconel tubes. The aluminum oxide film present on these fins prevents wetting by the conventional alloys. An electroplate of nickel on the fin did not act as an adequate diffusion barrier to permit wetting by the alloys. A chromium electroplate served as a diffusion barrier, but it is extremely difficult to wet in the hydrogen dew-points readily available in large-scale brazing operations. However, an electroplate of iron on the aluminum bronze was obtained, and tube-to-fin joints brazed with Coast Metals 52 alloy have exhibited excellent

Fig. 83. Iron-Plated Aluminum Bronze High-Conductivity Fins After Brazing with Coast Metals 52. It can be seen that good wettability of the fins was obtained.

wettability, as is shown in Fig. 83. Joints brazed in this manner have shown excellent resistance to oxidation after 100 hr at 1500°F, which indicates that the iron pickup during brazing has not appreciably reduced the oxidation resistance of the nickel-silicon-boron alloy. The excess iron from the fins can be removed after brazing by a suitable pickling operation, or it can be removed early in service as a result of the formation of a non-tenacious iron oxide.

Cermet-to-Metal Brazing

A study of cermet-to-Inconel brazing is being conducted in an attempt to develop suitable techniques for the production of such joints.

Preliminary tests have consisted in determining the wettability of certain cermets with copper and alloys such as gold-nickel, and nickel-phosphorus. Although the nickel binder is easily bonded, it appears that wetting of the nonmetallic portion may be much more difficult. Also of prime importance in the successful production of these joints is the problem of unequal thermal expansions of the two materials. The cermets of immediate interest have thermal coefficients of expansion ranging from 4.0×10^{-6} to 5.7×10^{-6} in./in./°F as compared with 10.2×10^{-6} in./in./°F for Inconel in the range 1000 to 1400°F. The best solution to this problem seems to depend on the combined use of a ductile brazing alloy and a ductile pad of metal between the cermet and Inconel.

A technique now under investigation, which may be useful because both the nonmetallic and metallic portions of the cermet are wet, consists in depositing a 0.0001-in. layer of Electroless nickel–phosphorus on the material. This deposit is then plated with a 0.005-in. copper plate. The unit is joined to Inconel by heating above the melting point of both the nickel-phosphorus and the copper. A joint possessing fair mechanical properties is produced. The phosphorus apparently aids in wetting the cermet and then diffuses into the surrounding

metal sufficiently to permit some ductility. Physical tests on this type of joint will be conducted, and screening tests on other alloys will be performed in an attempt to obtain more satisfactory brazing materials for this application. Methods for bonding ceramics, such as the manganese-molybdenum technique and the titanium hydride technique, will also be investigated.

Fabrication of Hastelloy B Reactor Components

Influence of High-Temperature Aging Upon Microstructures and Physical Properties. – It has been observed that when Hastelloy B is used at temperatures ranging from 1000 to 1700°F, copious quantities of precipitated phases are formed throughout the microstructure. Preliminary observations also indicated that the degree of precipitation in weld deposits and weld heat-affected zones might be noticeably different from that found in wrought structures. An investigation has therefore been initiated to determine the function of several variables upon the type and quantity of precipitate which will be examined metallographically. An attempt is also being made to correlate the physical properties of this material with the observed microstructures.

The variables being investigated in this study include aging temperature, time at aging temperature, prior thermal history, degree of residual cold formation, base-metal composition, original microstructure, and aging environment. Figure 84 reveals the relatively homogeneous microstructure of a section of $^3/_{16}$-in. Hastelloy B plate after a solution heat treatment of 2 hr at 2150°F. Figure 85, a photomicrograph of a similar sample after aging for 1500 hr at 1500°F, illustrates the typical appearance of the precipitate formed at this temperature after extended aging. Figure 86, a high-magnification photomicrograph of the same sample, shows the diverse nature of the precipitated phases. The grain boundaries are clearly outlined by the more massive particles. Aging at 1300°F for prolonged periods produces the characteristic microstructure shown in Fig. 87. The marked difference in structures obtained at these two temperatures would be expected to produce appreciable variations in physical properties. Hot-tensile specimens have been subjected to long-time aging treatments and are now under test to confirm this prediction and others based upon this metallographic evaluation.

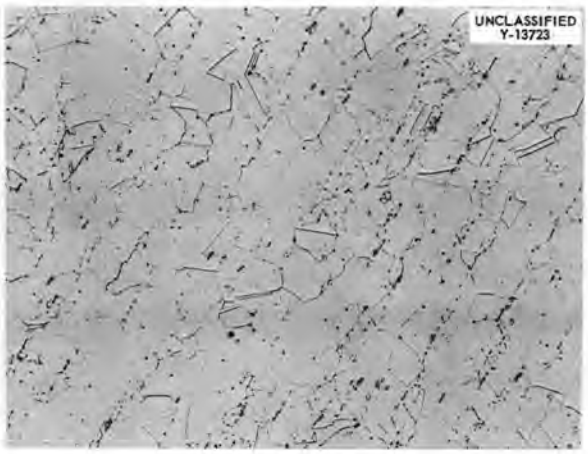

Fig. 84. Hastelloy B, $^3/_{16}$-in. Plate, After Solution Heat Treatment of 2 hr at 2150°F. Note the relatively homogeneous microstructure. Etchant: chrome regia. 150X. Reduced 30.5%.

The quantity of precipitate formed was found to increase proportionally with increasing time at temperature, within the limits of this investigation. A 1950°F "overaging" heat treatment recommended by the Haynes Stellite Company noticeably reduced the rate of precipitation after short-time aging, with the effect still somewhat evident up to 1500 hr.

Residual cold work in Hastelloy B produces a striking effect upon the rate or precipitation during aging, as evidenced by the excessive quantities of precipitate shown in Fig. 88, a photomicrograph of a specimen containing 20% cold deformation and held for 100 hr at 1200°F. Evidence indicates that the induced stresses produced during water quenching from above 1950°F may increase the precipitation rate. The influence of base-metal composition is now being studied, and aging treatments will be performed on specimens of selected chemical analysis. Extreme variations in microstructure are prevalent in welded joints, as would be expected, since they are susceptible both to segregation in the fusion zone and to stresses from the welding process. The original microstructure, as developed by fabrication techniques or thermal treatments, has a decided effect upon the aging process, but each individual case should be evaluated separately. Except under corrosive or oxidizing conditions, the environment does not appear to be important.

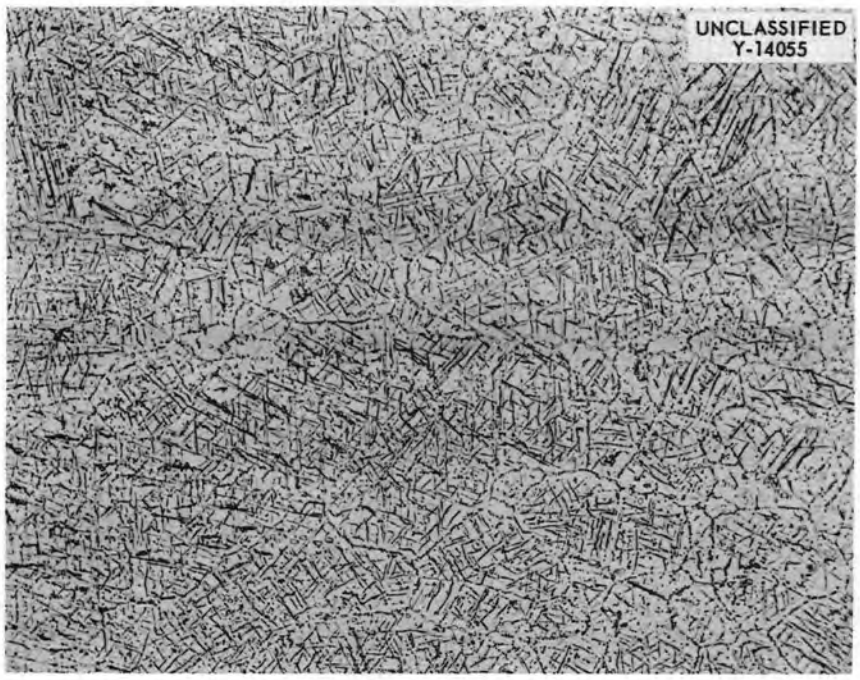

Fig. 85. Hastelloy B, Sample Similar to That in Fig. 84, After Aging 1500 hr at 1500°F. Etchant: chrome regia. 150X.

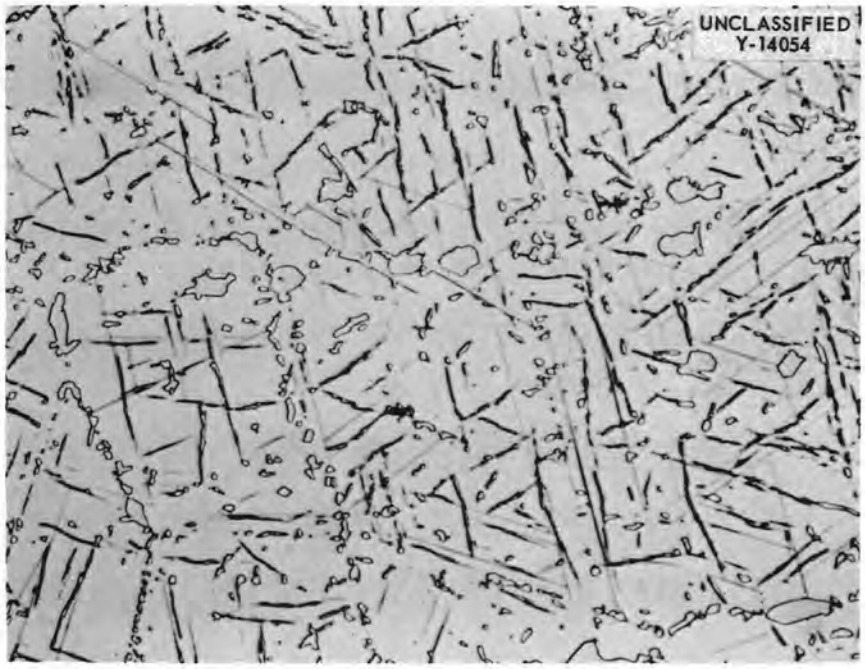

Fig. 86. Hastelloy B, Same Sample as Fig. 85, at Higher Magnification. Note the several types of precipitate present and, particularly, note the more massive particles which outline the grain boundaries. Etchant: chrome regia. 750X.

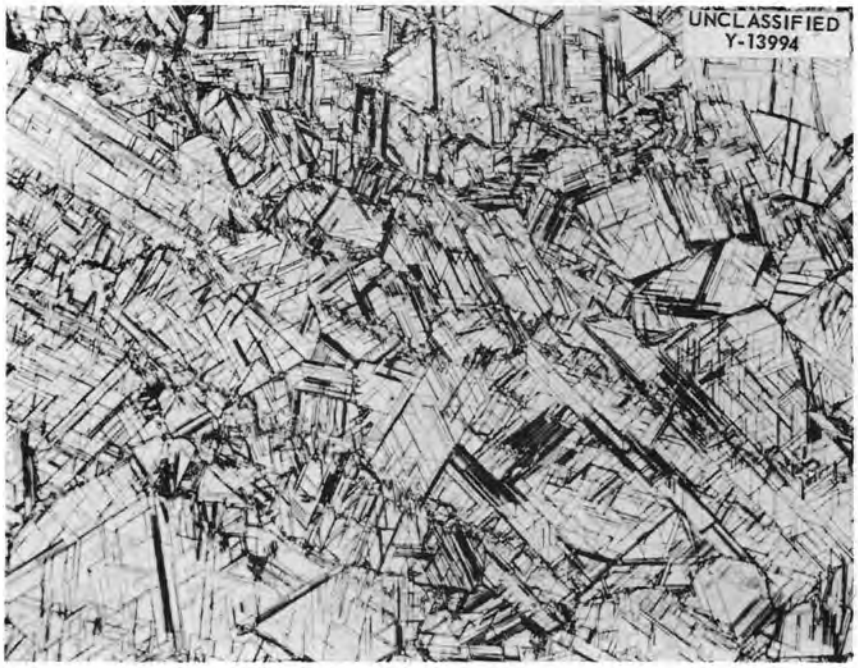

Fig. 87. Hastelloy B Aged at 1300°F for Prolonged Period. Note the Characteristic precipitate which developed. Etchant: chrome regia. 150X.

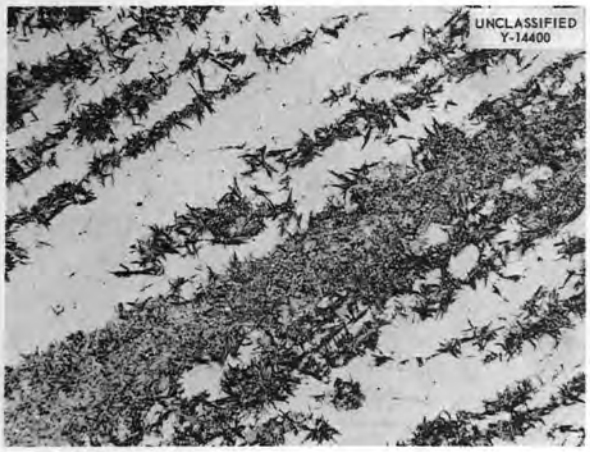

Fig. 88. Precipitation Occurring in Hastelloy B When 20% Cold Reduced and Subsequently Aged 100 hr at 1200°F. Etchant: chrome regia. 150X. Reduced 30.5%.

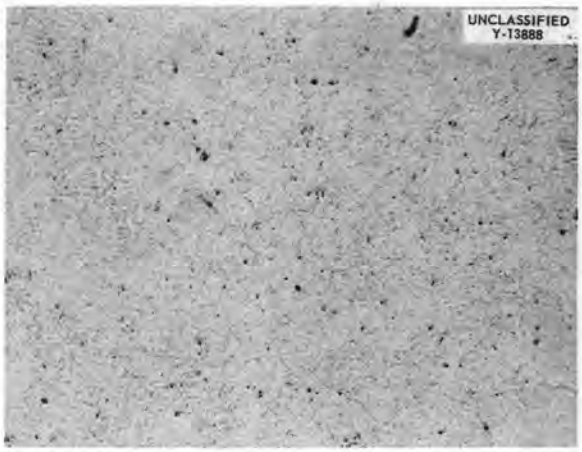

Fig. 89. Hastelloy B, Showing the Structure Obtained by the Experimental Spheroidizing Heat Treatment. Etchant: chrome regia. 150X. Reduced 30.5%.

Early experiments indicated the desirability of a heat treatment which would result in an improvement of certain physical properties such as room- and elevated-temperature ductilities. A stabilized microstructure is also desirable for structural reasons. Since a spheroidized structure should be beneficial from both standpoints, a heat treatment has been developed which produces it. This structure, which is shown in Fig. 89 at a magnification of 150 diameters and in Fig. 90 at a magnifi-

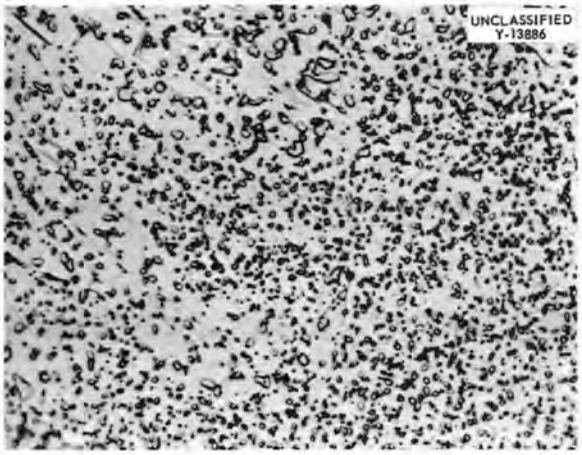

Fig. 90. Hastelloy B, Showing the Structure Obtained by the Experimental Spheroidizing Heat Treatment. Etchant: chrome regia. 2000X. Reduced 31%.

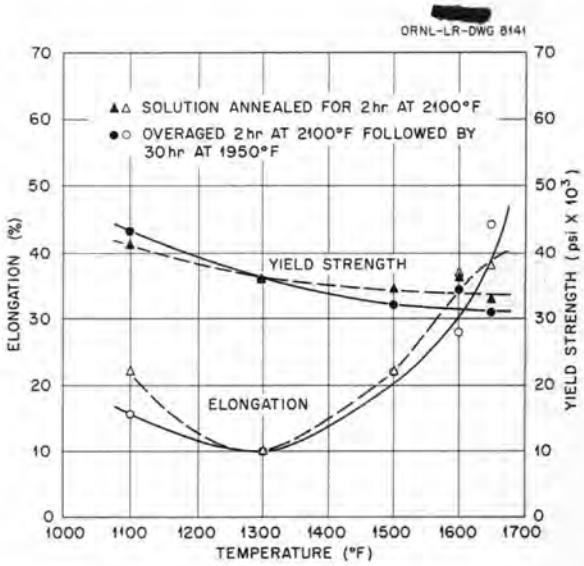

Fig. 91. Yield Strength and Elongation of Aged Hastelloy B Specimens as a Function of Temperature.

cation of 200 diameters, can be obtained by a heat treatment (aging of a 20% cold-reduced specimen at 1200°F for 200 hr followed by spheroidization at 1540°F for 150 hr) which is not deemed practical for structural components. However, physical-test specimens containing this microstructure are being prepared to evaluate its suitability. If the results are promising, further work will be aimed at a more practical means of production.

As a part of the correlation of mechanical properties with microstructure, hot-tensile tests have been completed on wrought specimens aged for 100 hr at five different temperatures. The yield strength and elongation were determined for specimens in the solution-annealed and "overaged" conditions and are shown in Fig. 91. It can be seen that a minimum elongation exists at 1300°F; whereas the yield strength does not appear to be so seriously affected. Long-time aging of hot-tensile specimens is now under progress, and the testing of them should permit a more complete analysis of the precipitation effects which would occur in Hastelloy B during service at these elevated temperatures.

Guided-bend tests have also been performed on specimens, which were $\frac{1}{8} \times \frac{1}{2} \times 1\frac{3}{8}$ in., machined from $\frac{3}{16}$-in.-thick wrought Hastelloy B plate. A similar group of specimens is being cut from inert-arc butt-welded $\frac{3}{16}$-in. plate in such a manner that the weld metal will constitute the center $\frac{1}{4}$ in. of the bend specimen. The parent material specimens, which were initially solution-annealed at 2150°F and quenched, were aged at 1500°F in a vacuum for periods up to 300 hr. Another group of specimens was heat-treated in hydrogen at 2150°F for $\frac{1}{2}$ hr followed by 30 hr at 1950°F prior to aging in vacuum at 1500°F.

The specimens were then loaded as a simple beam at a rate of approximately 1 in./min. The load-elongation curves indicated the maximum deflection at fracture. The deflections were translated into bend angles, as related to the specimen and the bending-jig geometry, and are presented in Table 9. It may be seen that the room-temperature ductility of Hastelloy B aged at a temperature of 1500°F is markedly reduced after a period of exposure of less than 50 hr. If the material is given a stabilizing heat treatment, however, this reduction in ductility is prolonged for a period of between 100 and 200 hr.

An apparatus for the hot-bend testing of wrought specimens and weld-metal specimens is now under construction. The determination of aging rates by hardness measurements is also proposed as a means of supplementing the data accumulated by these other methods.

TABLE 9. EFFECT OF AGING TIME ON ROOM-TEMPERATURE BEND DUCTILITY OF WROUGHT HASTELLOY B

Time at 1500°F (hr)	Bend Angle Before Fracture	
	Specimen Initially As-Received[a]	Specimen Initially Heat-Treated[b]
0	Greater than 135 deg[c] – no fracture	Greater than 135 deg – no fracture
25	Greater than 135 deg – fissuring evident	Greater than 135 deg – no fracture
50	92 deg – complete fracture	Greater than 135 deg – no fracture
75	90 deg – complete fracture	Greater than 135 deg – no fracture
100	84 deg – complete fracture	Greater than 135 deg – no fracture
200	80 deg – complete fracture	90 deg – complete fracture
223	76 deg – complete fracture	82 deg – complete fracture
300	80 deg – complete fracture	75 deg – complete fracture

[a]Solution-annealed at 2150°F.
[b]Solution-annealed at 2150°F for ½ hr, plus 30 hr at 1950°F, followed by water quench.
[c]Maximum bend angle available with apparatus.

Hastelloy B Radiator Fabrication. – Several Hastelloy B radiator components have been fabricated to determine the feasibility of using this material in applications involving thermal shock and high-temperature oxidation. It was thought that the characteristic aging of Hastelloy B with its accompanying loss in ductility might result in fissures in the tubes or tube-to-header joints when they were subjected to simulated cyclic service. Table 10 presents a case history of test radiators that have been built to date for the purpose of evaluating these assemblies under several different conditions. Figure 92 is a photograph of two typical components, one before welding of the split headers, and one after completion. It will be noted in the table that radiator No. 1 differed from the other radiators in that only a single row of five tubes was used. This test was discontinued at 350 hr since the stress distribution on the tubes was not comparable to that on a full-scale radiator.

Radiators Nos. 2 and 3 differed in that No. 2 had several water quenches from 1500°F to simulate a more severely stressed condition. Radiator No. 3 was carefully examined visually after alternately heating to 1500°F and cooling with air ten times. As can be seen from Fig. 93, the fin distortion is not severe enough to cause a material increase in air-pressure drop through the core. The testing temperature of 1200°F was chosen for radiator No. 5 since microstructural studies indicated that aging proceeded very rapidly at this temperature.

All specimens tested at 1500°F or lower, as noted in Table 10, ran the full 500-hr testing period without failures resulting from excessive oxidation or cracking. Specimens were leak-tested periodically by means of a helium leak detector to determine soundness.

From Table 10 it is noted that radiator No. 4 was terminated after 69 hr at 1650°F because leaks developed due to severe accelerated oxidation. Figure 92 shows the completed specimens before testing; whereas Fig. 94 shows the terminated test specimen. Since the severe localized attack suggested the influence of a self-fluxing oxide, a series of experiments was conducted to investigate the effect of several oxides on the susceptibility of Hastelloy B to this phenomenon. The specimens in Table 11 were prepared and were tested under conditions of high-temperature oxidation for varying lengths of time.

Very serious accelerated oxidation occurred with both Hastelloy B and Hastelloy C in contact with copper oxide. Figure 95 shows a specimen of Hastelloy B in contact with copper oxide for 24 hr at 1650°F in air, as compared with an uncontaminated control specimen of Hastelloy B tested under

TABLE 10. HISTORY OF HASTELLOY B TEST RADIATORS

	Radiator No.				
	1	2	3	4	5
Number of tubes	5	10	10	10	10
Type of fin cladding	310	310	Inconel	Inconel	310
Braze alloy	CM52	CM52	CM52	CM52	CM52
Temperature, °F	1500	1500	1500	1650	1200
Time, hr	350	500	511	69	500
Atmosphere	Air				
Number of cycles	8	27	265	8	191
Type of quench	Water	Water	Air	Air	Air
Failure	None	None	None	Oxidized	None

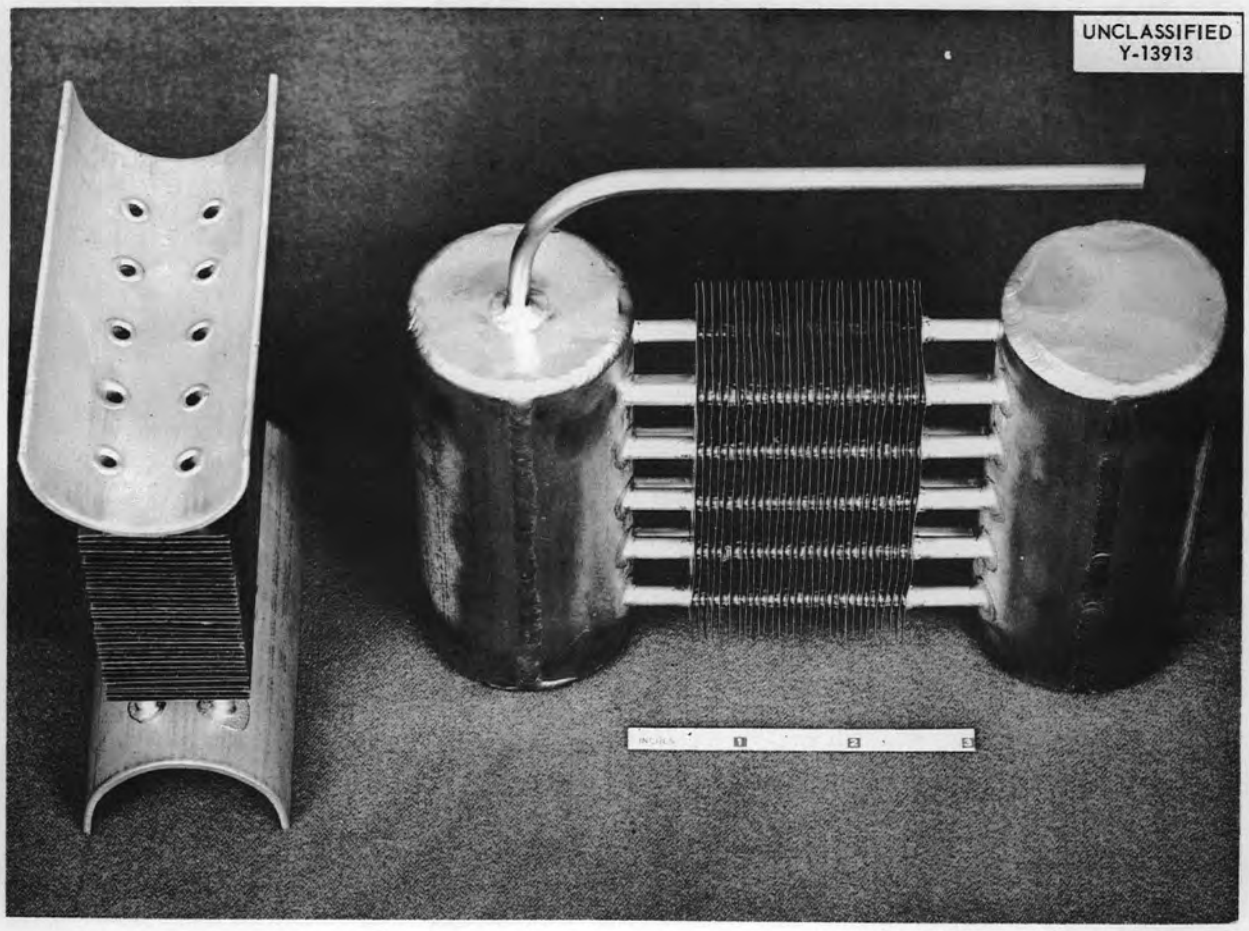

Fig. 92. Hastelloy B Radiator. (*a*) Before welding of split headers. (*b*) Completed.

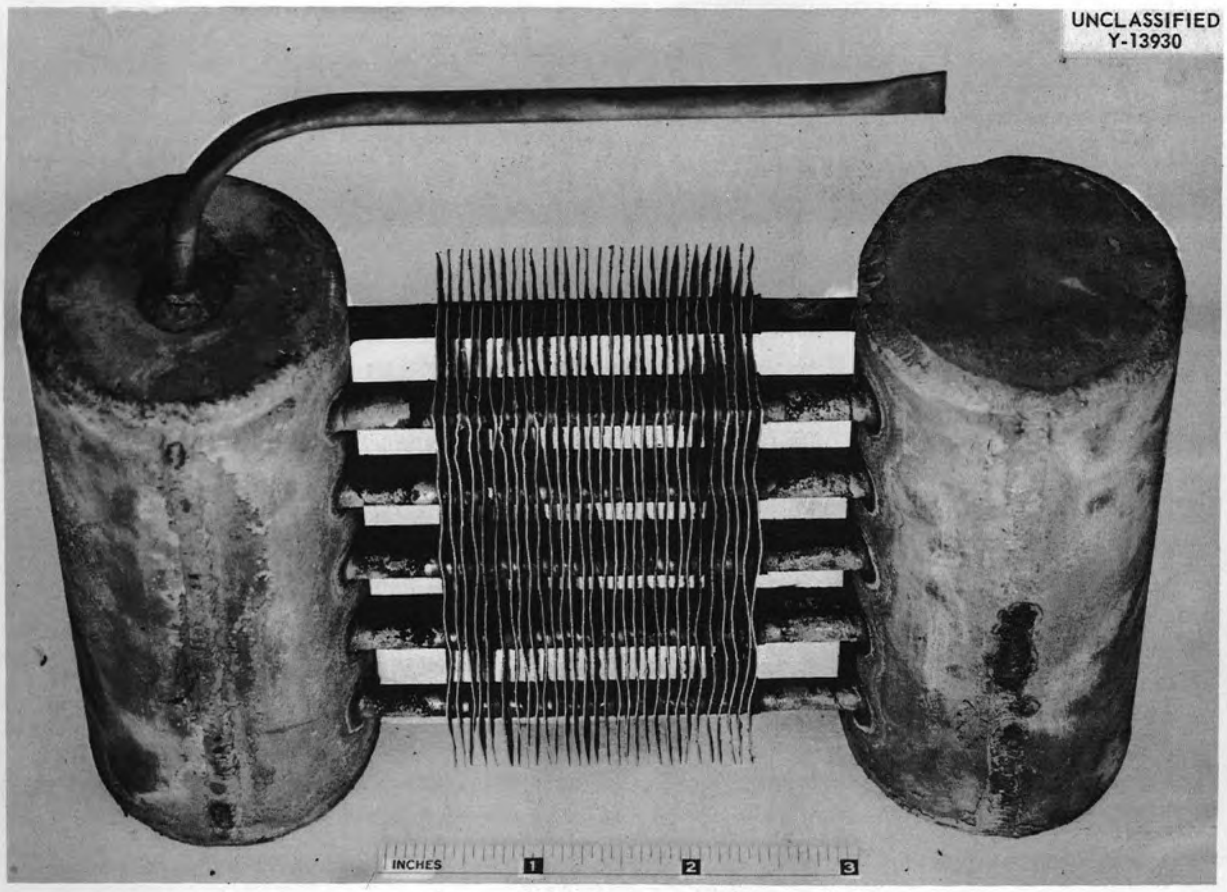

Fig. 93. Hastelloy B Radiator No. 3 After Cooling with Air 10 Times from 1500° F. Mild fin distortion is apparent.

TABLE 11. EFFECTS OF VARIOUS OXIDES ON THE OXIDATION OF HASTELLOY B AND HASTELLOY C

Type of Specimen	Time (hr)	Temperature (°F)	Result
Hastelloy B + Al_2O_3	24	1650	None
	100	1500	None
Hastelloy B + CuO	24	1650	Pitting to 40 mils
	100	1500	Pitting to 15 mils
Hastelloy C + CuO	24	1650	Pitting to 40 mils
	100	1500	
Hastelloy B + SiO_2	24	1650	None
	100	1500	None
Hastelloy B + FeO	24	1650	None
	100	1500	None
Hastelloy B + type 316 stainless steel	24	1650	None
	100	1500	None

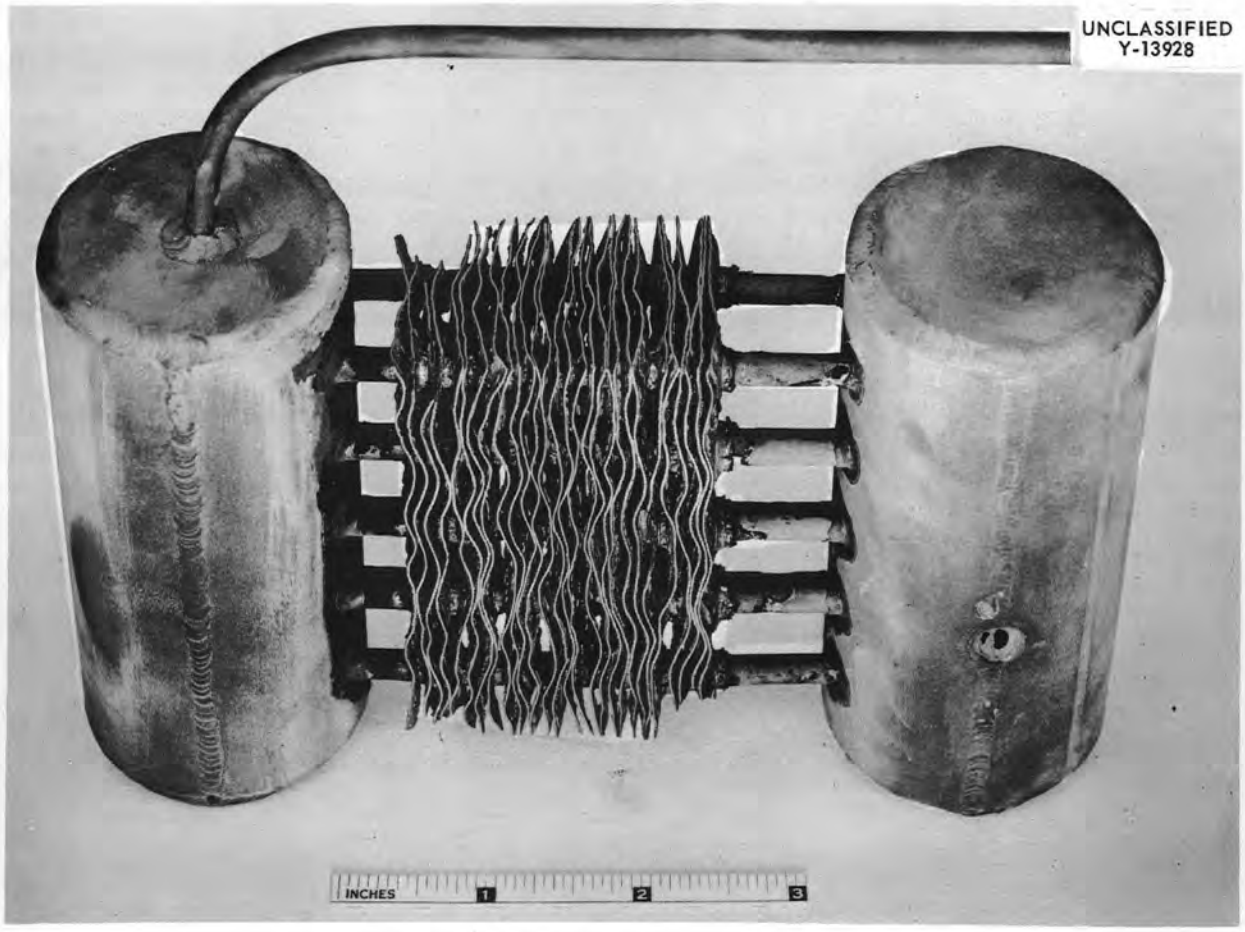

Fig. 94. Hastelloy B Radiator No. 4 After 69 hr at 1650°F.

the same conditions. It will be noted that although pitting occurred only in the area where the copper oxide was placed (this area has been brushed clean of scale) the entire surface of the specimen has a different scaling characteristic. Because this was not observed on specimens treated similarly and tested at 1500°F, testing was carried out at intermediate temperatures to determine the flow point of the composite oxide. The oxide was found to have a flow point of around 1525°F.

Since the fins in radiator No. 4 were also adversely affected, it is suspected that a volatile oxide, MoO_3, condensed on the fins near the headers, with a consequent acceleration in the rate of oxidation. Figure 96 indicates that, although the fins close to the headers were completely oxidized, the others were only distorted and were not oxidized. However, it is thought that high-velocity air may carry the volatile oxide away, reducing the possibility of deleterious affects on the fins.

These experiments illustrated that complete protection of the exposed copper on the lips of the punched high-conductivity fins is of extreme importance and that brazing techniques should be developed to ensure complete coverage by the brazing alloy.

Welding of Hastelloy B. – The fabrication of heavy-wall vessels from Hastelloy B presents welding problems of an entirely different nature from those encountered in the tube-to-header welding of this material. As a means of evaluating the weldability of the material and of determining suitable procedures for its fabrication, a heavy-plate-welding investigation is under way in which

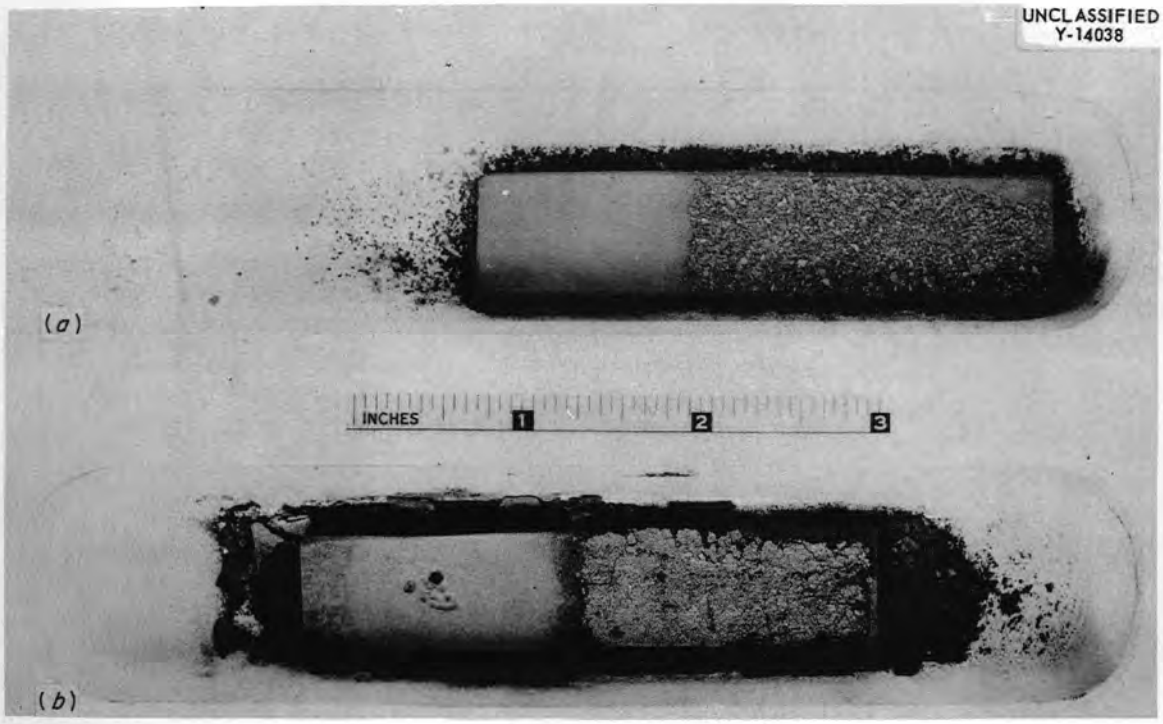

Fig. 95. High-Temperature Oxidation of Hastelloy. (*a*) Hastelloy B oxidized at 1650°F. Note characteristic scale. (*b*) Hastelloy B + CuO oxidized at 1650°F. Note pitting and change in scale characteristics.

the metallic arc and semiautomatic inert-arc-welding processes are being used.

The metallic-arc welds were made on as-received $\frac{3}{8} \times 3 \times 6$ in. plates with the use of a 90-deg included-angle bevel with a $\frac{1}{16}$-in. land and a $\frac{1}{16}$-in. spacing between plates in all cases except plate No. 4. Welds were made with both $\frac{1}{8}$- and $\frac{5}{32}$-in. Hastelloy B electrodes. All plates were tack-welded to a strongback to simulate a severely restrained condition.

Tests on the plate, listed in Table 12, consisted of 180-deg guided-root and face bends in the as-welded and aged conditions. Tensile specimens were also cut from plate No. 3 for testing in the as-welded and aged conditions. All aged specimens were treated at 1500°F for 200 hr.

It will be noted that the bend results presented in Table 12 are somewhat inconsistent. The specimen failures that occurred in plate No. 1 may be attributed to incomplete fusion in the root pass. Plate No. 2 was welded much in the same manner as plate No. 1, but particular care was taken in the deposition of the root pass. All bend tests on this plate were made in the as-welded condition, and no failures were observed.

Plate No. 3 was fabricated to determine the affect of aging upon the bend-test results. From Fig. 97, a photograph of several tensile test specimens and guided bend-test specimens, it can be seen that Nos. 4 and 5 are typical as-welded face and as-welded root bends, while Nos. 6 and 7 are aged face and aged root bends, respectively, from plate No. 3. An as-welded tensile specimen and a welded-and-aged tensile specimen were also prepared from plate No. 3. Figure 97 indicates that No. 1, the as-welded specimen, exhibited good ductility in the parent material, with fracturing occurring in the weld. The aged specimen, No. 2,

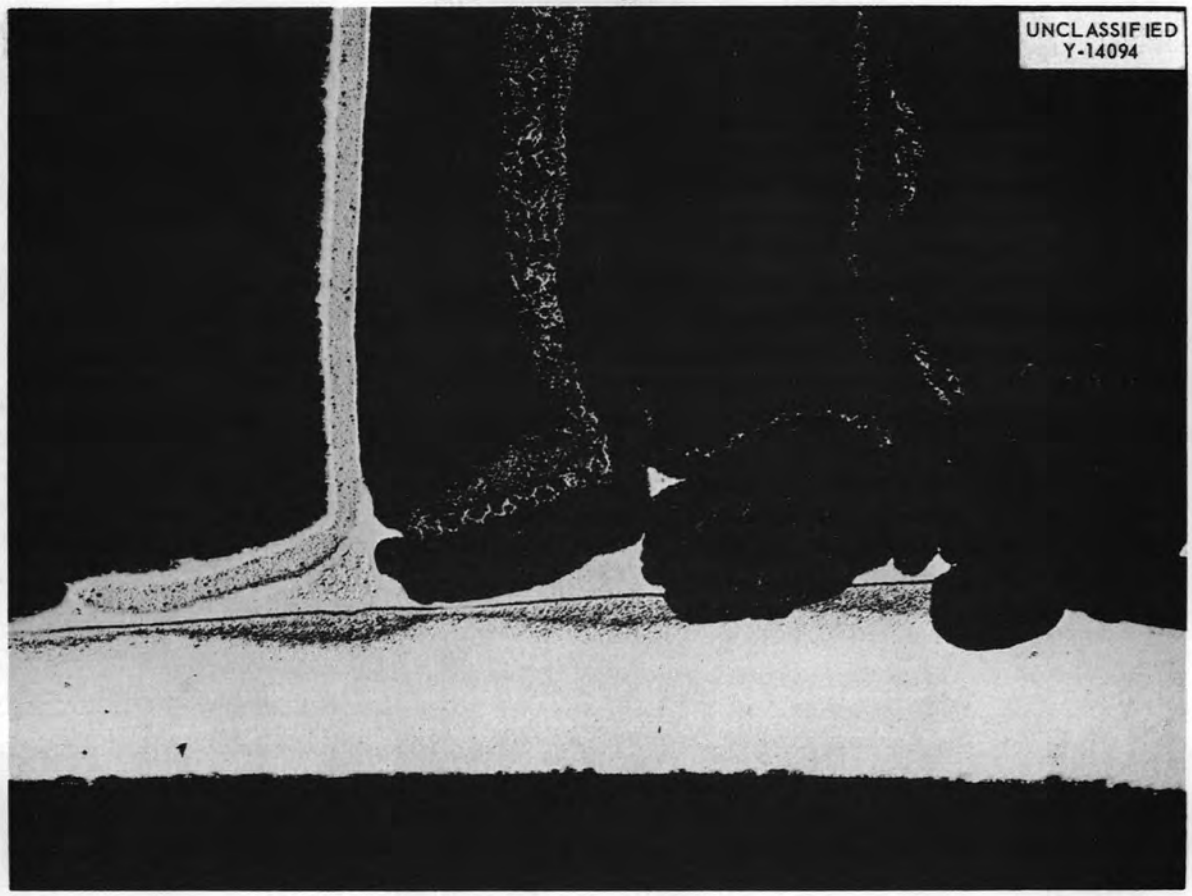

Fig. 96. Tube-to-Fin Section of Hastelloy B Radiator No. 4 Exhibiting Extreme Oxidation of Fins Nearest to Headers.

TABLE 12. DATA ON WELDED HASTELLOY B PLATES

Plate No.	Current (amp)	Wire (in.)	Number of Passes	Bevel	Bend Tests	
					Number of Tests	Number of Failures
1	80	1/8	8	Single	3 root	2 root
					3 face	None
2	90	1/8	7	Single	2 root	None
					1 face	None
3	100	5/32	5	Single	1 root	None
					1 face	None
					1 root aged	Failed
					1 face aged	Failed
4A	95	1/8	7	Double	2	None
4B	100	5/32	7		2	1

also showed good ductility in the parent material, but in this case fracturing also occurred in the zone.

One-half of plate No. 4 was prepared with a $\frac{1}{8}$-in.-dia coated electrode; whereas the remaining half was welded with a $\frac{5}{32}$-in.-dia coated electrode. A radiographic inspection showed that all welds were sound. Two bends from the fillet prepared with the $\frac{1}{8}$-in. rod exhibited good ductility, while one bend from the fillet prepared with the $\frac{5}{32}$-in. rod fractured during testing. Inspection of the fracture showed no apparent flaws.

The inconsistencies in the bend-test data could possibly be attributed to the inhomogeneous yielding observed in the weld zone. The root-bend specimen No. 5 in Fig. 97 shows the extent to which this was present. Specimen No. 3 in Fig. 97 was machined from a double-beveled specimen to determine the effect of bending axially with the weld. Some parting was noticed along the fusion line, but there was no fracture. It is evident that yielding in this longitudinal test is more homogeneous than in the transverse bend test.

Several experimental weld beads have been prepared with the semiautomatic Aircomatic machine available in the Welding Laboratory. These welds were deposited on $\frac{1}{2}$-in. Hastelloy B plate with 0.060-in. Hastelloy B wire as the filler metal. In this process the filler wire is continuously fed from a coiled spool. Conditions have been established which produce good bead-on-plate welds, as determined by visual observation. These con-

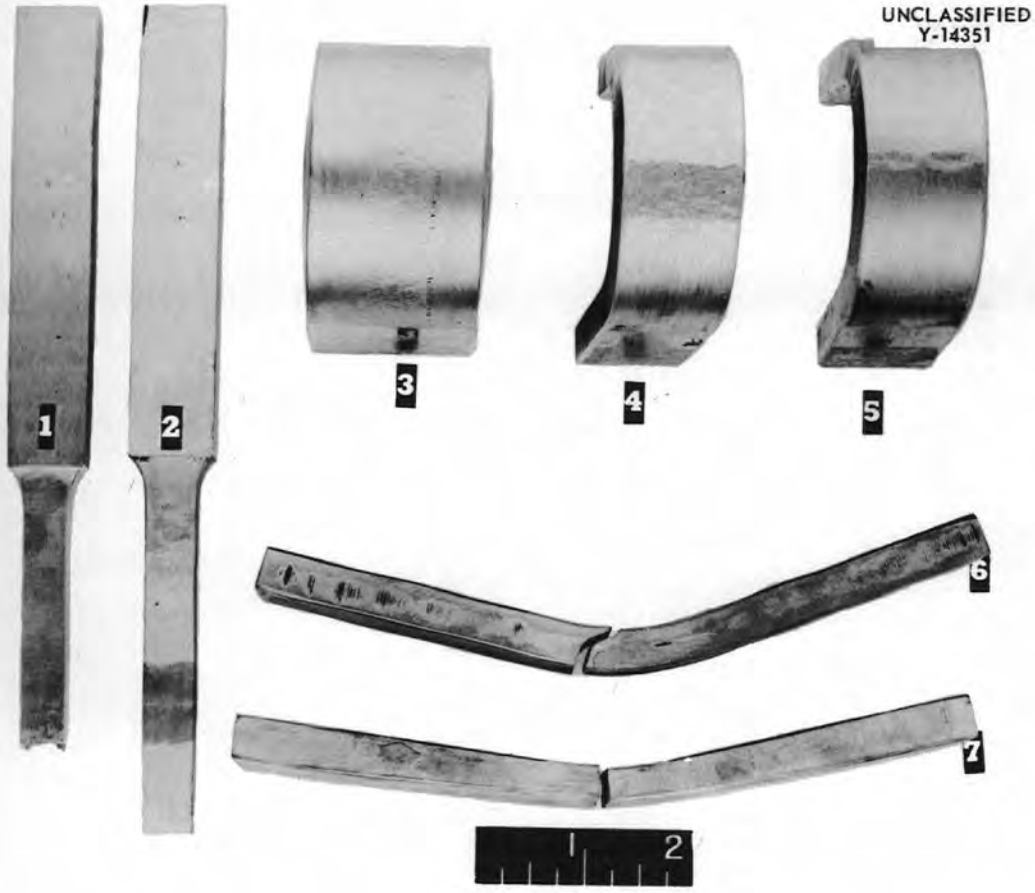

Fig. 97. Bend Test and Tensile Specimens of Metallic-Arc-Welded Hastelloy B. (1) As-welded (broken in weld zone). (2) Welded and aged (broken in parent material). (3) As-welded (bent along axis of welding). (4) As-welded face bend. (5) As-welded root bend. (6) Welded and aged face bend (broken along fusion zone). (7) Welded and aged root bend (broken through center of root).

ditions are listed below to give an indication of the rapid travel speed and deposition rate which can be obtained by this process:

1. arc current, 325 amp,
2. welding travel speed, 325 in./min,
3. rate of wire feed, 200 in./min,
4. argon consumption, 40 ft^3/hr.

Metallographic examination of these welds indicated that porosity would not be a major problem when welding with this equipment. However, further experiments will be conducted to evaluate the physical properties of these welds in order to compare them with the properties of welds made by the conventional manual inert-arc process.

ORR Project

Procedure Specifications and Operators' Qualification Test Specifications have been prepared for the inert-gas arc welding of several aluminum alloys of interest to the ORR Project. These specifications were prepared in accordance with Section IX of the ASME Boiler and Pressure Vessel Code: Non-Ferrous Section. These specifications and their corresponding applications are listed below:

PS-3 and QTS-3	61ST6 to 61ST6 and 63ST6 to 63ST6 with 43S filler wire
PS-4 and QTS-4	61ST6 to 54S with 43S filler wire
PS-5 and QTS-5	54S to 54S with 54S filler wire
PS-6 and QTS-6	3S to 54S with 54S filler wire
PS-7 and QTS-7	3S to 61ST6 with 43S filler wire

PHYSICAL CHEMISTRY OF CORROSION

G. P. Smith

Mass Transfer in Liquid Lead

J. V. Cathcart

It was the purpose of this investigation to survey the mass-transfer properties in liquid lead of a variety of metals and alloys with the aim of obtaining an insight into the roles of various important alloying materials in fixing the resistance to mass transfer of given alloys. Thus, pure metals, such as chromium, columbium, and nickel, and alloys having practical structural importance were tested. Work on this project has now been terminated.

All tests were performed in small quartz thermal-convection loops. The test specimens were fastened in the hot and cold legs of the loops. In all cases a temperature gradient of about 300°C was maintained across the loops, with the hot-leg temperature being 800 to 810°C. Details of the construction and operation of the loops, as well as details of the experimental results, may be found in earlier reports.[4]

The only new material tested during the past quarter was type 310 stainless steel. A loop containing this alloy plugged after 65 hr of operation with hot- and cold-leg temperatures of 805 and 500°C, respectively. A transverse section of the hot-leg specimen is shown in Fig. 98.

The results of this research project are summarized in Fig. 99. The numbers at the end of the bars in the chart represent the length of time for each test. Except as noted on the chart, every loop was operated until it plugged.

The pure metals tested, as a rule, showed rather poor resistance to mass transfer (see chart); exceptions were molybdenum and columbium. These two metals were the only materials studied which experienced virtually no mass transfer or corrosion under the test conditions. At the other extreme, nickel was found to be highly subject to mass transfer; the nickel loops plugged in about 2 hr. Loops containing chromium and iron plugged in about 100 and 250 hr, respectively, and thus can be considered as being intermediate between molybdenum and columbium on one hand and nickel on the other, as regards resistance to mass transfer.

The alloys studied could be conveniently grouped on the basis of whether their resistance to mass transfer was about the same as or greater than the average of their pure-metal components. Examples of the former category are furnished by the 300-series stainless steels, Inconel, and Nichrome V. On the other hand, loops containing the 400-series stainless steels, and alloys such as 45% Cr–55% Co, Hastelloy B, etc., required much longer times before they plugged than would have been predicted on the basis of the data for their pure-metal components. The results obtained with the 45% Cr–55% Co alloy were particularly striking; more than 750 hr was required before a loop containing this material plugged. Plugging

[4] J. V. Cathcart, *ANP Quar. Prog. Reps. Dec. 10, 1952*, ORNL-1439, p 148; *Sept. 10, 1954*, ORNL-1771, p 100; *Dec. 10, 1954*, ORNL-1816, p 88.

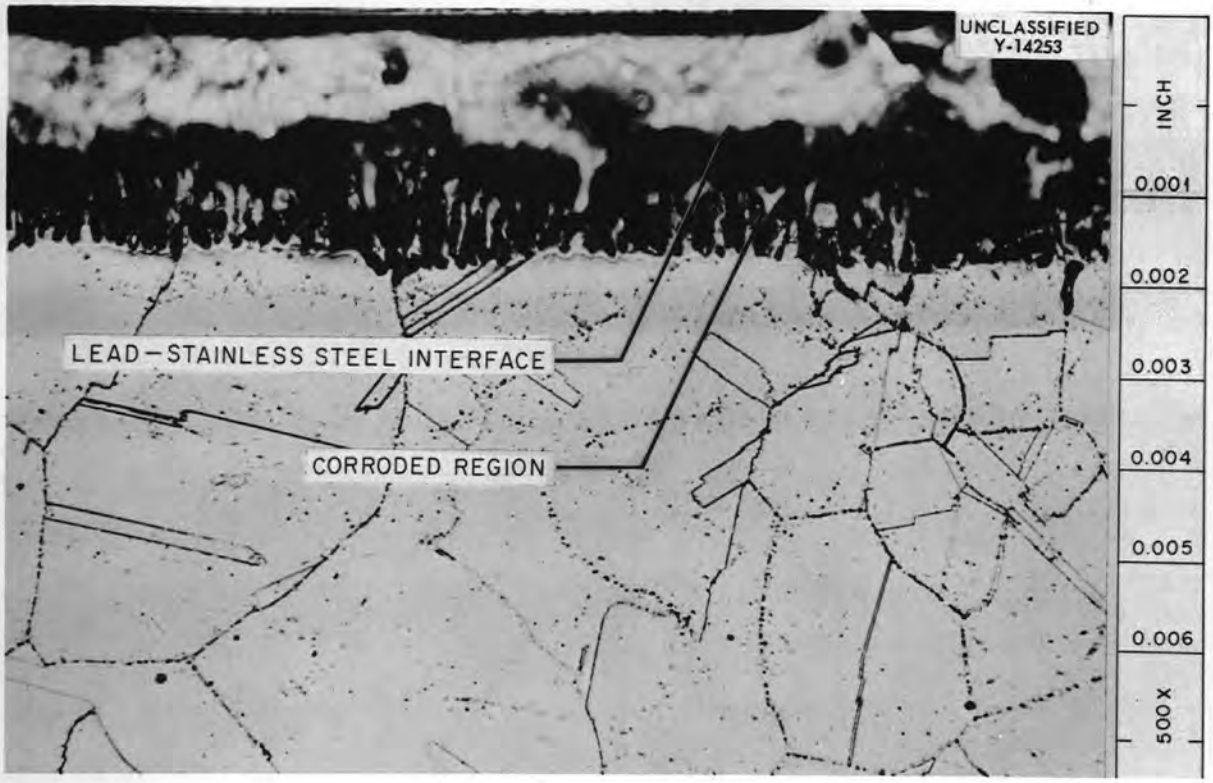

Fig. 98. Transverse Section of Hot-Leg Specimen of Type 310 Stainless Steel Loop No. 1. 500X. Reduced 5%.

times of 100 and 80 hr were recorded for comparable chromium and cobalt loops, respectively.

A survey of the phase diagrams of the alloys tested showed that those alloys having a greater-than-expected resistance to mass transfer either contain a phase which is an intermetallic compound or else have a composition that is relatively close to one that would produce an intermetallic compound. Conversely, in the case of other alloys either no intermetallic compounds exist or the compositions are far removed from those of possible compounds. On the basis of the data available a reasonable conclusion is that the alloys containing an intermetallic compound will, in general, possess a higher resistance to mass transfer than will those in which compound formation is not possible. The only exception to this rule, as regards the alloys tested, was the 50% Cr–50% Fe alloy. This composition corresponds closely to the theoretical composition for the sigma-phase region in the iron-chromium diagram, and it was thought that this alloy would possess a relatively great resistance to mass transfer. However, the average plugging time for two such loops was 39 hr. No completely satisfactory explanation for the apparent anomaly has been found; but it was thought that on account of the extreme friability of the test specimens these very short plugging times might have been due to a mechanical failure of the specimens.[5]

A topical report covering this research project is in preparation.

Mass Transfer and Corrosion in Fused Hydroxides

M. E. Steidlitz W. H. Bridges

Hydroxide Corrosion. – During the past year, work on the mass transfer of nickel in sodium hydroxide[6] has indicated the possibility of finding

[5] J. V. Cathcart, *ANP Quar. Prog. Rep. Dec. 10, 1954*, ORNL-1816, p 91.

[6] W. H. Bridges, *Met. Semiann. Prog. Rep. April 10, 1954*, ORNL-1727, p 52.

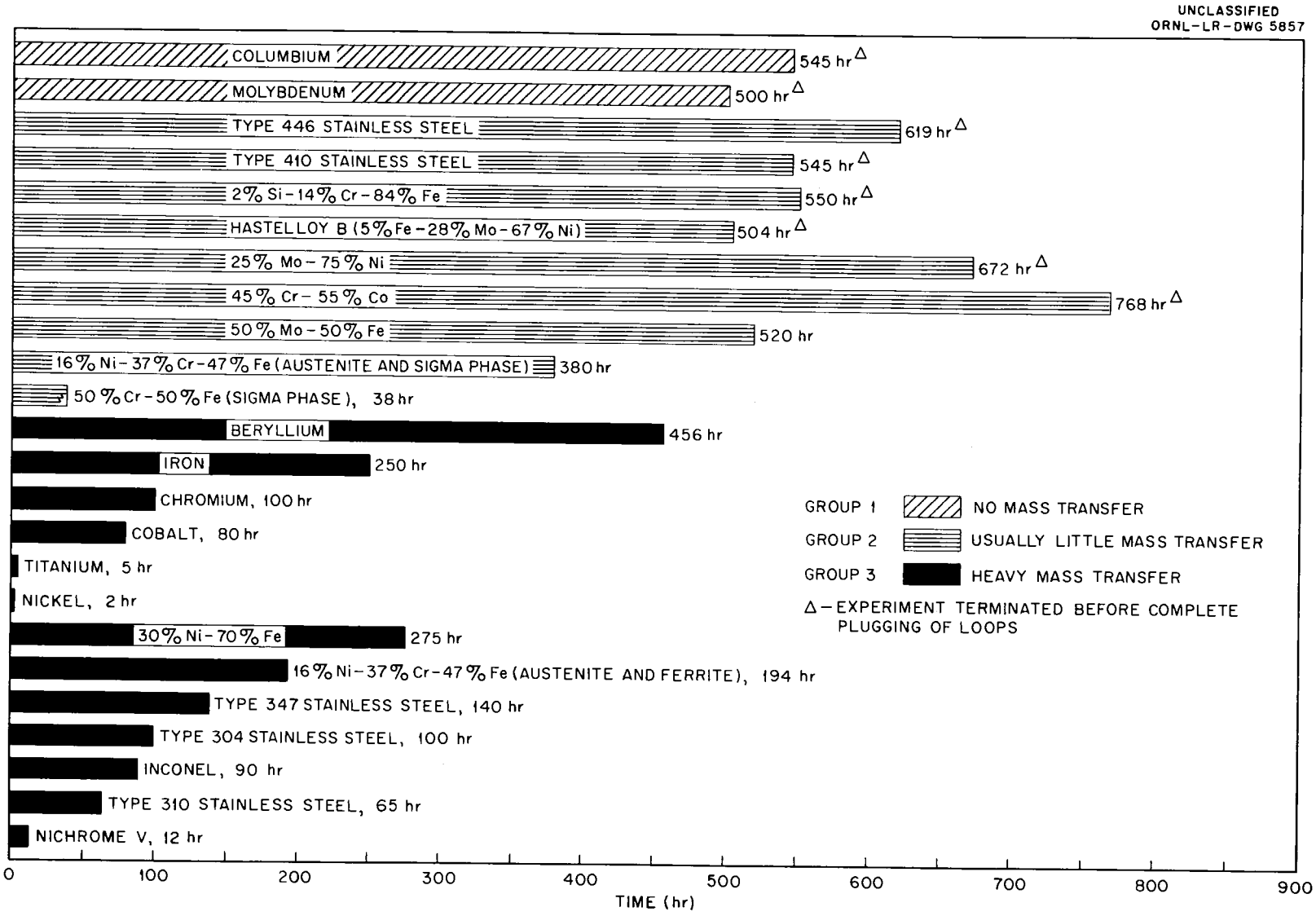

Fig. 99. Mass Transfer in Liquid Lead.

limiting top temperatures and temperature gradients at which mass transfer will not occur. In order to investigate this more thoroughly and in order to extend the work to other potential container materials, a new corrosion test apparatus has been constructed.

The new system, Fig. 100, is essentially a multicontainer duplicate of the single model used in the earlier work. Five steel pots are connected through appropriate valving to vacuum, purified helium, and purified-hydrogen lines and to a bubbler which connects to the exhaust line extending up into a hood.

Sodium hydroxide is contained in a bucket made of the material under study. This bucket is hung from the cold finger, which is also made of the test material. The pot, heated by an external furnace, heats the bucket and hydroxide; while an air jet, blown down the inside of the tubular cold finger, provides the thermal gradient. The hydroxide is circulated by thermal-convection currents established between the bucket and cold finger. Temperatures are measured on the bucket and inside the cold finger. A thermocouple outside the pot controls the furnace.

Spectrophotometry of Fused Hydroxides

C. R. Boston

It has been previously pointed out[7] that the application of spectrophotometric techniques should provide information concerning the fundamental nature of fused salts. In continuation of this approach to the problem, construction of the previously described high-temperature spectrophotometer[7] has been completed. Approximate absorption spectra have been measured for fused sodium hydroxide at various temperatures up to 700°C in air, with sodium hydroxide at 350°C being used as reference. Limitations of the instrument restricted the measurements to the wavelength range, 400 to 650 mμ only.

The experimental procedure briefly consisted in placing the periclase cell containing sodium hydroxide in the light path and in measuring, at a given temperature, the photocell response at various wave lengths relative to the response at 600 mμ, which is the wavelength of maximum response at 350°C. Repeating this procedure at various temperatures gave a series of curves all of which intersected at 600 mμ and which by their general form gave some indication of how the absorption was changing with temperature.

With increasing temperature a rapid increase in absorption appears at the shorter wavelengths; but at 700°C, although the absorption at 440 mμ is increasing as usual, the absorption at 400 mμ reverses its trend and drops markedly. This results in a sharp absorption peak at 440 mμ. The long-wavelength end of the spectrum does not appear to be significantly influenced by temperature change. These preliminary measurements are approximate and will serve mainly as a guide in designing future apparatus and experiments.

Improvements in experimental design are now in progress. These include the fabrication of a deeper cell to prevent the hydroxide from creeping out, as is frequently the case with the present cell. In addition, auxiliary apparatus will be constructed to permit maintaining a controlled atmosphere over the melt.

Fused Hydroxides as Acid-Base Analog Systems

G. P. Smith

In the preceding semiannual progress report[8] it was shown that fused hydroxides are thermodynamically capable of undergoing self-decomposition in several ways. Two of these ways are equilibria I and II shown below, which are interrelated by a cross-equilibrium, III:

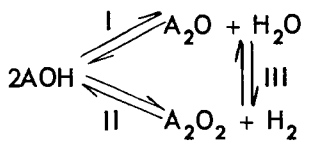

In a very qualitative way these equilibria may be compared with two of the self-decomposition equilibria known for water:

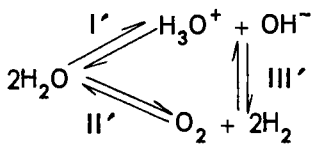

Self-decomposition equilibrium I′ is the well-known acid-base equilibrium of aqueous chemistry. Self-decomposition equilibrium II′, though seldom considered in low-temperature aqueous chemistry, is

[7] C. R. Boston *et al.*, *Met. Semiann. Prog. Rep. Oct. 10, 1954*, ORNL-1875, p 152.

[8] C. R. Boston, G. P. Smith, *et al.*, *Met. Semiann. Prog. Rep. Oct. 10, 1954*, ORNL-1875, p 147.

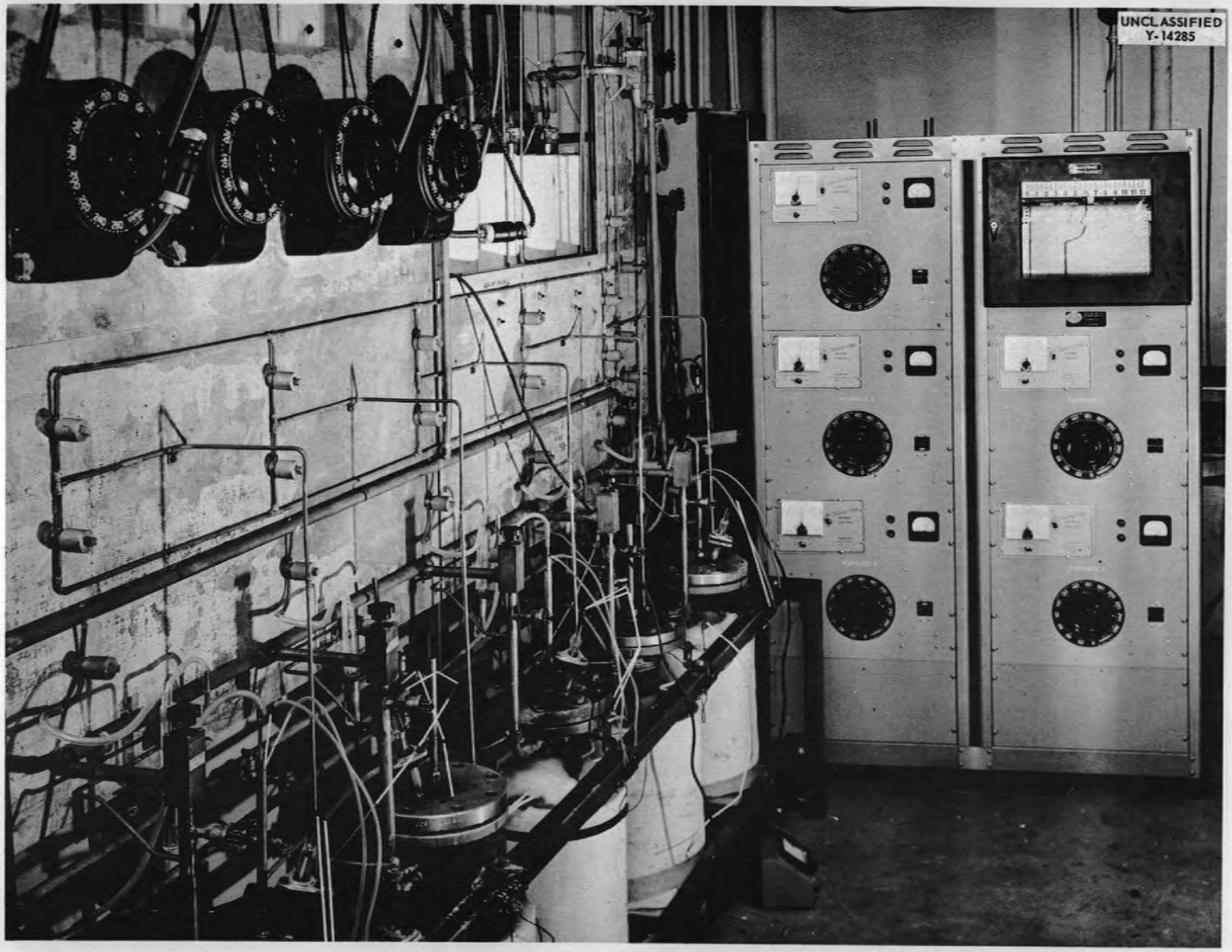

Fig. 100. Fused-Hydroxide Corrosion-Testing Apparatus.

of considerable importance at elevated temperatures.

It is evident that equilibria I and I′, II and II′, and III and III′ bear at least a superficial resemblance to one another. Thus, it might be expected that equilibrium I for fused hydroxides controls a class of reactions in these media in the same way that equilibrium I′ controls acid-base reactions in water. It is the contention of the writer that this is the case. In this progress report self-decomposition equilibrium I will be examined in quantitative detail with the aid of thermodynamics. Then, it will be shown in a qualitative way how the results may be used to develop an acid-base analog theory of reactions. The reason for developing such a theory lies in the expectation that it will greatly assist in systematizing a part of hydroxide chemistry in the same way that acid-base analog theories have systematized the chemistry of a wide variety of other solvent media.

In the remainder of this report only self-decomposition equilibrium I will be considered. The results which are obtained remain valid whether or not other self-decomposition equilibria exist.

Law of Mass Action for Self-Decomposition. – Previously,[8] expressions concerning the law of mass action were obtained for the self-decomposition of hydroxides, but they were limited to a consideration of the activities of electrically neutral thermodynamic species. It will be instructive to derive a similar expression by postulating that a fused hydroxide is essentially ionic in nature. This approach cannot be said to be more correct than the other but only that it is more useful. The evidence that supports the ionization postulate will be treated in a later report.

Consider an alkali-metal hydroxide, AOH, which undergoes the self-decomposition reaction:

$$2AOH = A_2O + H_2O$$

The standard free energy change $\Delta F°$ of this reaction defines an equilibrium constant K_d, which will be referred to as the self-decomposition constant, by means of the reaction isotherm,

$$\Delta F° = -RT \ln K_d \ .$$

Furthermore,

$$K_d = \frac{a_{A_2O} a_{H_2O}}{a^2_{AOH}} \ ,$$

where the activity terms must be referred to the same standard states as those chosen in obtaining $\Delta F°$, which will be taken here as the conventional free-energy standard states rather than the conventional solution-theory standard states. By using the ionic-activity definitions given by Temkin's rules,[9] there is obtained

$$K_d = \frac{a^2_A a_O a_{H_2O}}{a^2_A a^2_{OH}} = \frac{a_O a_{H_2O}}{a^2_{OH}} \ ,$$

where a_A, a_O, and a_{OH} are the activities of the A^+, O^{--}, and OH^- ions.

A set of concentration terms may be defined as follows. Given a melt composed of the following numbers of k species of cations per unit volume: N_1^+, N_2^+, ..., N_k^+; the following numbers of l species of anions per unit volume: N_1^-, N_2^-, ..., N_l^-; and the following numbers of m species of neutral molecules per unit volume: $N_1°$, $N_2°$, ..., $N_m°$, then

$$N_i^+ = \frac{n_i^+}{\sum_1^k n_j^+ + \sum_1^m n_j°} \ ,$$

$$N_i^- = \frac{n_i^-}{\sum_1^l n_j^- + \sum_1^m n_j°} \ ,$$

and

$$N_i° = \frac{n_i°}{\sum_1^k n_j^+ + \sum_1^l n_j^- + \sum_1^m n_j°} \ .$$

It will be noted that for the limiting case of no ions the concentration terms $N_i°$ become mole fractions; and for the limiting case of no neutral molecules the concentration terms N_i^+ and N_i^- reduce to Temkin's definitions of ionic fractions.

Using these definitions, there is obtained

$$K_d = \frac{\gamma_O N_O \gamma_{H_2O} N_{H_2O}}{\gamma^2_{OH} N^2_{OH}} \ ,$$

where the γ's are activity coefficients.

Assume that the extent of self-decomposition is

[9] M. Temkin, *Acta Physicochimica U.R.S.S.* **20**, 411 (1945).

small. Both N_{OH} and γ_{OH} approximate unity, the latter because of our choice of standard states. Thus $\gamma_{OH}^2 N_{OH}$ approximates unity. Furthermore,

$$N_O \cong \frac{n_O}{n_{OH}}$$

and

$$N_{H_2O} \cong \frac{n_{H_2O}}{2n_{OH}}$$

since $n_{OH} >> n_O + n_{H_2O}$ and $n_A \cong n_{OH}$. By the definition of decomposition pressure previously given,[8] $n_O = n_{H_2O}$; therefore, $N_O = 2N_{H_2O}$. Thus,

$$K_d = \gamma_O \gamma_{H_2O} 2N_{H_2O}^2 = 2\frac{\gamma_O}{\gamma_{H_2O}} a_{H_2O}^2$$

It is assumed that water vapor at these temperatures and up to 1 atm pressure behaves as an ideal gas, $a_{H_2O} = p_{H_2O}/p^\circ_{H_2O}$. But by the choice of standard states specified above $p^\circ_{H_2O} = 1$. Therefore,

$$K_d = 2\frac{\gamma_O}{\gamma_{H_2O}} p_{H_2O}^2 \quad (1)$$

Equation 1 holds for the pure hydroxide. If there is an excess of either water or oxide ions,

$$K_d = a_O p_{H_2O} \quad (2)$$

or

$$K_d = \gamma_O N_O p_{H_2O} .$$

Thermodynamics of Water in Fused NaOH. – Fused sodium hydroxide and liquid water (under suitable pressure) are miscible in all proportions. At temperatures a little below the melting point of sodium hydroxide, the single-phase region is still extensive. Data for the partial pressure of water over this system are available for temperatures up to 350°C.[10] Although for our own purposes these data are inadequate, they are worth examining.

Figure 101 is a plot of the vapor pressures of water at 350°C as a function of composition computed in two ways. Curve A was obtained for

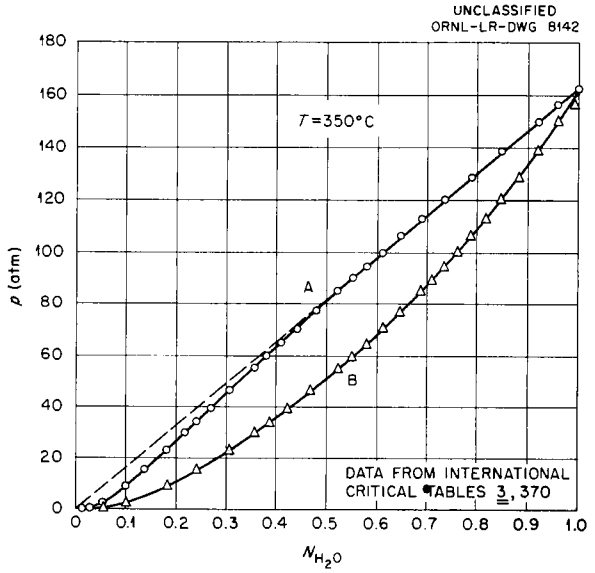

Fig. 101. Vapor Pressure of Water Over Sodium Hydroxide–Water Solutions at 350°C as a Function of the Concentration of Water in the Melt. Curve A, assuming complete ionization. Curve B, assuming no ionization.

N_{H_2O} computed according to the definition given in the preceding section. Curve B was obtained by computing N_{H_2O} as a mole fraction, assuming NaOH to exist as molecules. The dotted line corresponds to Raoult's law in the form $p = p^*N$, where p^* is the vapor pressure of liquid water. Curve A very closely approximates this law for $1 \geqq N \geqq 0.5$; whereas curve B does not even asymptotically approach it. The concentration definition used for curve B will not be considered further.

Figure 102 is a plot of p/p^* vs N for four temperatures. All the curves approximate Raoult's law for large values of N and show negative deviations for small values of N. These deviations decrease by a large factor in the 150°C range illustrated.

The existence of a negative deviation is not surprising. Water and NaOH form two congruently melting and four incongruently melting compounds. Although this compound formation is assisted by hydrogen bonding, which is probably unimportant at 350°C, ion-dipole attraction may be expected to be appreciable. There is no reason to suppose that the deviations would become positive even at relatively high temperatures.

[10] *International Critical Tables*, vol 3, p 370, McGraw-Hill, New York, 1928.

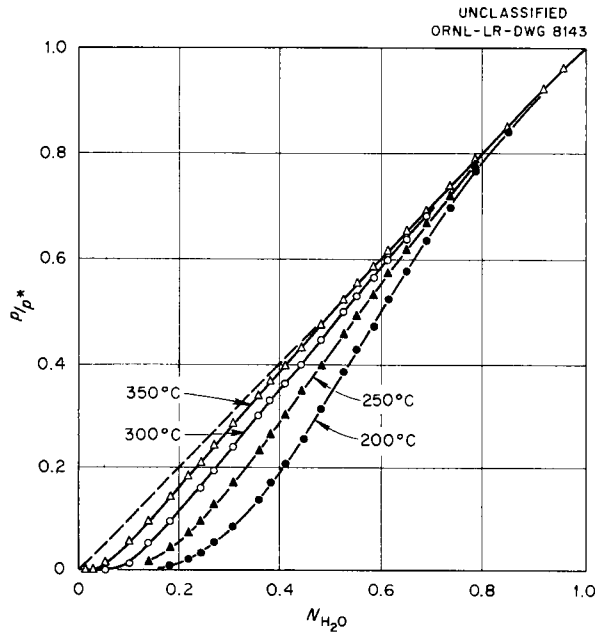

Fig. 102. Ratio of the Vapor Pressure of Water Over Sodium Hydroxide–Water Solutions to the Vapor Pressure of Liquid Water at the Same Temperature as a Function of the Concentration of Water in the Melt.

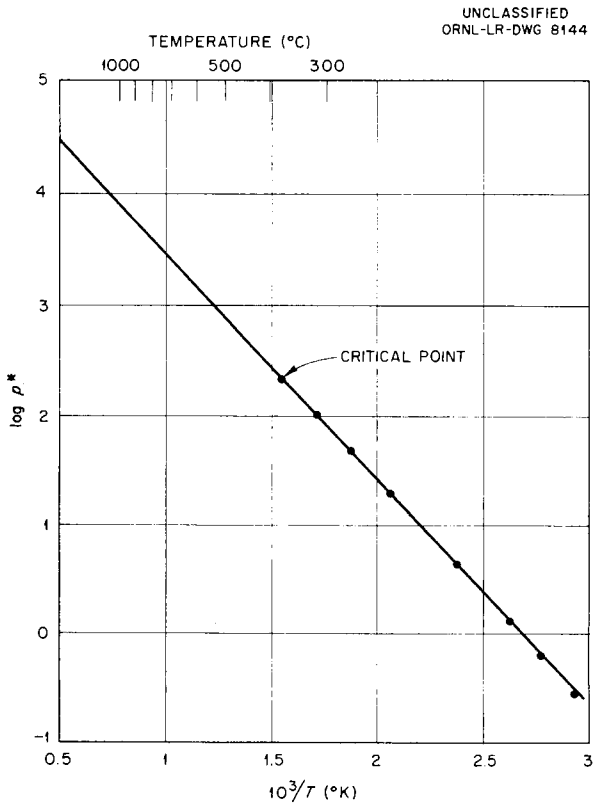

Fig. 103. Extrapolation of the Vapor Pressure of Liquid Water Above the Critical Point. These values are suitable for computing limiting activity coefficients.

If the system obeyed Raoult's law, the activity coefficient of water would be given by the expression $\gamma = p^*/p^\circ$ or (since we have chosen $p^\circ = 1$) by $\gamma = p^*$. As significant positive deviations are not expected, this becomes a limiting value for the real system, that is, $\gamma \leqq p^*$. The range of N over which equality holds will increase with increasing T.

Although the critical temperature for water is 374°C, a meaningful extrapolation to higher temperatures may be obtained on a log p^* vs $1/T$ plot,[11] as shown in Fig. 103. The line selected for extrapolation may be represented as

$$\log \gamma_{max} = \log p^* = 5.52 - \frac{2.05 \times 10^3}{T} .$$

Thus, γ_{max} is of the order of 10^2 at the melting point of sodium hydroxide, of the order of 10^3 at 500 to 600°C, and of the order of 10^4 at 1000°C.

[11] J. H. Hildebrand and R. L. Scott, chap. XV in *Solubility of Nonelectrolytes*, 3d ed., Reinhold, New York, 1950.

In order to examine the activity coefficients for dilute solutions of water in NaOH, the data in Fig. 102 are given on a log-log plot in Fig. 104. The iso-γ lines, irrespective of the choice of standard state, are parallel to the diagonals shown. The values assigned to these lines in Fig. 104, designated γ^*, are such that $\gamma = \gamma^* p^*/p^\circ$. Therefore for our choice of standard states, $\gamma = \gamma^* p^*$ and for the Hildebrand standard states, $\gamma = \gamma^*$.

For Fig. 104 the last one or two points on each curve are probably not reliable. Nevertheless, the curves have at best just reached an inflection point; and since they must eventually at least asymptotically approach an iso-γ line, it is evident that γ^* at 350°C is at least 10^{-1} and possibly less than 10^{-2}. Hence, the Henry's-law constant is at least as small as 1.6 and possibly as small as 0.1.

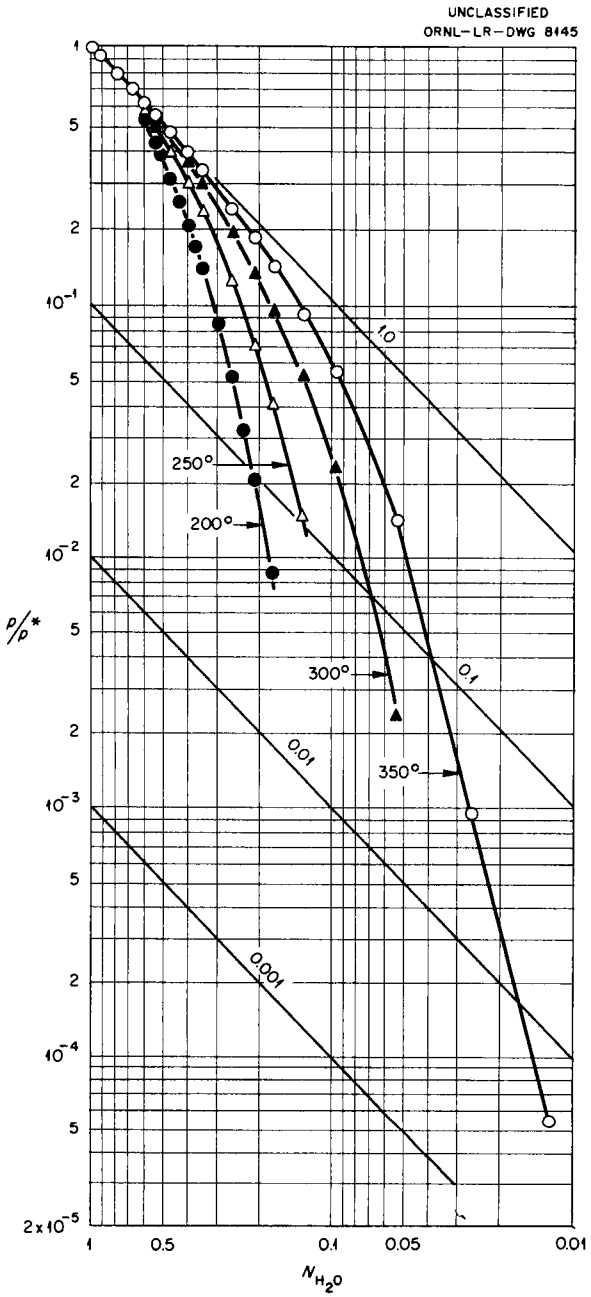

Fig. 104. Data from Fig. 102 Plotted So As to Obtain the Hildebrand Activity Coefficients, γ^*.

It is evident that these data cannot be quantitatively extrapolated to very small water concentrations. This will be possible only when data are obtained which extend appreciably beyond the inflection point.

Variations of K_d with Composition. – In the derivation of expressions for K_d, given above, it will be noted that, because of the assumption of ionization, the activity coefficients explicitly involving cations canceled. Qualitatively, this is because the cations do not enter into the self-decomposition reaction, which may be written as the ionic reaction,

$$2OH^- = H_2O + O^{--}$$

The effect of the cations is to control the value of K_d by their relative polarization of the various species in the above equation. The quantitative aspects of this behavior will be considered in the next two sections.

It should be pointed out first that fused alkali-metal carbonates and sulfates, when acting as reaction media, form acid-base systems which are closely analogous to fused alkali-metal hydroxides. The corresponding anionic self-decomposition equilibria are the following:

$$CO_3^{--} = CO_2 + O^{--}$$

and

$$SO_4^{--} = SO_3 + O^{--}$$

This fact will be useful in that more information is available concerning reactions in fused carbonates and sulfates than there is concerning reactions in fused hydroxides.

Two expressions will be derived. First, for a reaction medium (whether hydroxide, carbonate, or sulfate) containing a single nonreactive cationic species, it will be shown that there exists a linear empiric relation between the ionic potential of the cation and the self-decomposition constant, K_d, for the medium. Second, for a reaction medium which contains two or more nonreactive cationic species, a thermodynamic formula will be derived which relates the self-decomposition constant, K_d, of the medium to its cationic composition. These two expressions can be combined in principle to give a complete, phenomenological description of the role of nonreactive cations in acid-base analog reactions in the media under consideration.

Empiric Relations for K_d. – In 1951 Cartledge[12] gave simple empiric relations relating the heats of oxysalt formation to the ionic potentials of the

[12] G. H. Cartledge, *J. Phys. & Colloid Chem.* **55**, 248 (1951).

cations based on their corrected univalent radii. However, his relations are not quite what we need. In 1952 Ramberg[13] found that an arbitrary parameter exists for each of the alkali and alkaline-earth metals which, when plotted against the heats of oxysalt formation per two equivalents, gives a straight line for each kind of oxysalt. The writer has used Ramberg's work as a starting point to obtain the empiric relations shown in Fig. 105.

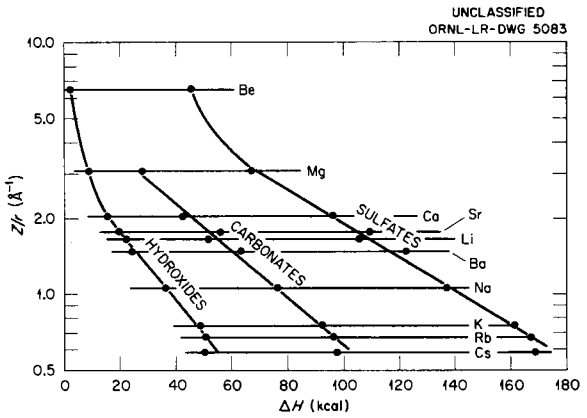

Fig. 105. Heats of Decomposition for Oxysalts as Functions of the Cationic Potentials.

In Fig. 105 the ΔH values that are plotted are for the following self-decomposition reactions:

$$2MOH = H_2O + M_2O$$

$$M_2CO_3 = CO_2 + M_2O$$

$$M_2SO_4 = SO_3 + M_2O$$

where M is an alkali metal, and

$$M'(OH)_2 = H_2O + M'O$$

$$M'CO_3 = CO_2 + M'O$$

$$M'SO_4 = SO_3 + M'O$$

where M′ is an alkaline-earth metal. Reactants and products are in their standard states. Thus, for example, in the case of the hydroxide curve the enthalpy change for reactions involving the same number of anions is what is being compared, so that the only variable along the hydroxide curve is the kind of cation. The numerical values are taken from the data of Rossini *et al.*[14] and are for 25°C. Along the vertical axis are plotted values of the ionic potential (Z/r) on a logarithmic scale, where Z is the charge on the cation and r is its ionic radius as given by Pauling.[15]

The values of all the metals except cesium and beryllium, and magnesium for the hydroxide curve, may be represented fairly well by straight lines.

Figure 106 is a similar plot for ΔF rather than ΔH. The values are from the same source, except for the sodium hydroxide value which was computed by Smith and Boston. There is, of course, much less ΔF data than ΔH data. However, it is evident that the straight-line relations are still preserved and that the slopes of the ΔF vs Z/r functions are the same as those of the ΔH vs Z/r functions. Reliable data at elevated temperatures are too scarce to be plotted like the data in Figs. 105 and 106. However, data for the sulfates of calcium, barium, and potassium were plotted for a series of high temperatures and were found to form straight lines as closely at these temperatures as they do at 25°C.

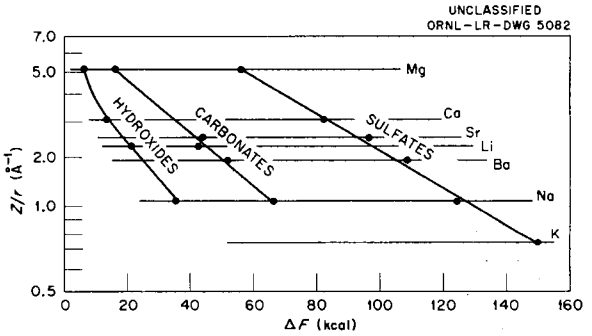

Fig. 106. Free Energies of Decomposition for Oxysalts As Functions of the Cationic Potentials.

Because of the relation between the curves in Figs. 105 and 106, it is reasonable to assume that over the straight-line portions of the curves the entropy terms are constants which are independent of the cations. If this result is combined with the reaction isotherm, it can be said that the straight-

[13] H. Ramberg, *J. Chem. Phys.* **20**, 1532 (1952).

[14] F. D. Rossini *et al.*, *Selected Values of Chemical Thermodynamic Properties*, Natl. Bur. Standards (U.S.) Circ. 500, Washington, D. C., 1952.

[15] L. Pauling, *Nature of the Chemical Bond*, 2d ed., Cornell University Press, Ithaca, 1940.

line portions of the curves in Fig. 105 are represented by equations of the form

$$\log K_d = a \log \frac{Z}{r} + b ,$$

where K_d is the self-decomposition equilibrium constant, and a and b are constants which are characteristic of the anions only.

The values for the beryllium compounds deviate from the straight-line relations in such a way as to lead to a greater stability than would be expected. This effect is, perhaps, associated with the extra resonance energy which is to be expected from the very high polarizing ability of an ion of such large ionic potential.

Dependence of K_d on Cationic Composition. – A thermodynamic relation will now be derived which gives K_d as a function of composition for media containing two or more kinds of cations. First, the notation to be used to express concentrations will be presented, and then the derivation will be outlined in terms of an isothermal-isobaric cycle of four component processes.

Consider a melt composed of n_1 moles of $(X_1)OH$, n_2 moles of $(X_2)OH$, ..., n_1' moles of $(Y_1)(OH)_2$, ..., such that the total number of gram-atoms of OH from all hydroxides is n_{OH}, where the X_i are alkali metals and the Y_i are alkaline-earth metals. This melt will be represented by the expression $n_{OH}AOH$.

The electrical equivalent fraction $\bar{N}_i$ of X_i^+ ions is by definition equal to the number of charges in the melt due to X_i^+ divided by the total number of positive charges on all ions in the melt. Therefore, by applying the requirement of electrical neutrality, it is found that

$$n_i = n_{OH}\bar{N}_i ,$$

and for the Y_i^{++} ions

$$n_i' = \frac{n_{OH}}{2} \bar{N}_i' .$$

Process 1:

$$2AOH \longrightarrow A_2O + H_2O$$

A quantity of melt containing 2 gram-atoms of OH is converted into 1 mole of water in its standard state and a solution of oxides containing 1 gram-atom of oxygen. The free-energy change accompanying this process defines, in terms of the reaction isotherm, an equilibrium constant which is the self-decomposition constant K_d of the melt AOH.

$$\Delta F_1 = -RT \ln K_d .$$

Process 2:

$$A_2O + H_2O \longrightarrow \Sigma \bar{N}_i (X_i)_2O + \Sigma \bar{N}_i' (Y_i)O + H_2O$$

The final product of process 1 is separated into component oxides, each in its standard state:

$$\Delta F_2 = \Sigma \bar{N}_i \, \Delta F^\circ_{(X_i)_2O} + \Sigma \bar{N}_i' \, \Delta F^\circ_{(Y_i)O} - \Sigma \bar{N}_i \, \bar{F}_{(X_i)_2O} - \Sigma \bar{N}_i' \, \bar{F}_{(Y_i)O} ,$$

where $\Delta F^\circ_{(X_i)_2O}$ represents the standard free energy of formation of $(X_i)_2O$, and $\bar{F}_{(X_i)_2O}$ represents the partial molal free energy of $(X_i)_2O$ in the solution of oxides, A_2O. By combining terms in the above equation and applying the definition of activity, there is obtained

$$\Delta F_2 = RT \left[\Sigma \bar{N}_i \ln a_{(X_i)_2O} + \Sigma \bar{N}_i' \ln a_{(Y_i)O} \right]$$

where $a_{(X_i)_2O}$ is the activity of $(X_i)_2O$ in the solution of oxides, A_2O.

Process 3:

$$\Sigma \bar{N}_i (X_i)_2O + \Sigma \bar{N}_i' (Y_i)O + H_2O \longrightarrow \Sigma 2\bar{N}_i (X_i)OH + \Sigma \bar{N}_i' (Y_i)(OH)_2$$

The final products of process 2 are reacted individually with the water to yield the corresponding hydroxides in their standard reference states. For the free-energy change for this process, there is obtained, upon collection of like terms,

$$\Delta F_3 = \Sigma \bar{N}_i \left[2\Delta F^\circ_{(X_i)OH} - \Delta F^\circ_{(X_i)_2O} - \Delta F^\circ_{H_2O} \right] + \Sigma \bar{N}_i' \left[\Delta F^\circ_{(Y_i)(OH)} - \Delta F^\circ_{(Y_i)O} - \Delta F^\circ_{H_2O} \right] .$$

The quantities in parentheses define, by means of the reaction isotherm, two sets of equilibrium constants, K_i and K_i', which are the same as the self-decomposition constants of the constituent hydroxides, $(X_i)OH$ and $(Y_i)(OH)_2$, respectively. Thus,

$$\Delta F_3 = RT(\Sigma \bar{N}_i \ln K_i + \Sigma \bar{N}_i' \ln K_i') .$$

Process 4:

$$\Sigma 2\bar{N}_i\,(X_i)OH + \Sigma\bar{N}_i'\,(Y_i)(OH)_2 \longrightarrow 2AOH$$

The final products of process 3 are mixed to form the solution with which we started.

$$\Delta F_4 = \Sigma 2\bar{N}_i\bar{F}_{(X_i)OH} + \Sigma\bar{N}_i'\bar{F}_{(Y_i)(OH)_2} - \Sigma 2\bar{N}_i\Delta F^\circ_{(X_i)OH} - \Sigma\bar{N}_i'\Delta F^\circ_{(Y_i)(OH)_2}\ .$$

Proceeding as for Process 2,

$$\Delta F_4 = -RT\left[\Sigma\bar{N}_i \ln a^2_{(X_i)OH} + \Sigma\bar{N}_i' \ln a_{(Y_i)(OH)_2}\right],$$

where $a_{(X_i)OH}$ is the activity of $(X_i)OH$ in the solution of hydroxides, AOH.

The sum of the free-energy changes for the steps of the isothermal cycle must vanish. Whence, $-\Delta F = \Delta F_2 + \Delta F_3 + \Delta F_4$. By writing these terms out, changing the logarithm base to 10, dividing through by RT, and collecting some of the like terms,

$$(1)\quad \log K_d = \Sigma\bar{N}_i \log K_i + \Sigma\bar{N}_i' \log K_i' + \Sigma\bar{N}_i \log\frac{a_{(X_i)_2O}}{a^2_{(X_i)OH}} + \bar{N}_i' \log\frac{a_{(Y_i)O}}{a_{(Y_i)(OH)_2}}\ ,$$

where the activity terms are *not* the activities of the various constituents in a hydroxide melt in equilibrium with its self-decomposition products; they are activities of oxides in a solution containing nothing but oxides, and activities of hydroxides in a solution containing nothing but hydroxides. Equation 1 is a thermodynamically exact formula.

Now let it be assumed that the solutions consist of ions and apply Temkin's rules[9] to the activity terms. Equation 1 reduces to

$$(2)\quad \log K_d = \Sigma\bar{N}_i \log K_i + \Sigma\bar{N}_i' \log K_i' + \Sigma\bar{N}_i \log\frac{\gamma^2_{X_i}\gamma_O}{\underline{\gamma}^2_{X_i}\underline{\gamma}^2_{OH}} + \Sigma\bar{N}_i' \log\frac{\gamma_{Y_i}\gamma_O}{\underline{\gamma}_{Y_i}\underline{\gamma}^2_{OH}}\ ,$$

where the γ's are ionic activity coefficients. In particular, γ_{X_i}, γ_{Y_i}, and γ_O are the activity coefficients of X_i^+, Y_i^{++}, and O^{--}, respectively, in a solution of oxides only; and $\underline{\gamma}_{X_i}$, $\underline{\gamma}_{Y_i}$, and γ_{OH} are the activity coefficients of X_i^+, Y_i^{++}, and OH^- in a solution of hydroxides only.

A simplification in notation may be introduced if the subscripts for the alkaline-earth metals are changed from $Y_1, Y_2, \ldots, Y_n$ to $Y_{m+1}, Y_{m+2}, \ldots, Y_{m+n}$, where m is the number of kinds of alkali metals and n is the number of kinds of alkaline-earth metals. Thus

$$(3)\quad \log K_d = \Sigma\bar{N}_i \log K_i + \Sigma\bar{N}_i \log\frac{\gamma_i^{2/\nu}\gamma_O}{\underline{\gamma}_i^{2/\nu}\gamma_{OH^-}}\ ,$$

where the summation is from unity to $m + n$, and ν is the charge on the cation.

Two models of an ideal mixture of electrolytes have been proposed as approximations to reality, one model by Temkin[9] and one by Herasymenko.[16] If Temkin's model is a good approximation, then the activity coefficients in Eq. 3 will approximate unity to the same degree. If Herasymenko's model is a good approximation, then the above activity coefficients will by no means approximate unity or even constants. A considerable volume of computations published since 1945 not only overwhelmingly supports Temkin's model as the better of the two but indicates that Temkin's model is a satisfactory first approximation for a surprising variety of fused electrolytes. Therefore, the equation

$$(4)\qquad \log K_d = \Sigma N_i \log K_i$$

will be taken as a first approximation. Furthermore, note that Eq. 4 should be a better approximation than the model of an ideal solution on which it is based, inasmuch as the activity coefficients in Eq. 2 occur as ratios of similar terms which probably tend to cancel.

Acid-Base Analog Concepts. – A partisan debate is currently in progress over what is the "best" definition of the terms "acid" and "base." Consider, for example, Luder and Zuffanti's[17] comparison of the Lewis definition with Einstein's

[16] P. Herasymenko, *Trans. Faraday Soc.* **34**, 1245 (1938).

[17] W. F. Luder and S. Zuffanti, *The Electronic Theory of Acids and Bases*, Wiley, New York, 1946.

theory of relativity, and Bell's[18] reply. This debate has obscured the leading part which acid-base analog theory has played in developing a systematic chemistry of such diverse solvent media as anhydrous hydrogen cyanide, liquid sulfur dioxide, and selenium(IV) oxychloride.

The acid-base concepts and definitions which will be used here were chosen because they are useful in treating fused hydroxides and other oxysalt systems. Nothing more is claimed for them.

In terms of the solvent-system concept first introduced by Franklin[19] for liquid ammonia and subsequently applied by Jander[20] to a variety of liquids, it is clear that the reaction

$$(1) \qquad 2OH^- = H_2O + O^{--}$$

fulfills the formal requirements for a water-like acid-base equilibrium and, hence, that the fused alkali-metal hydroxides may be properly considered as acid-base solvent systems.

The self-decomposition of a fused hydroxide is a proton donor-acceptor equilibrium. Hence, the protonic-solvent theory is applicable and leads to the following analysis. Half the hydroxyl ions in Eq. 1 are proton donors and, hence, are defined to be acids. They may be regarded, in a formal way, as dissociating into protons and oxide ions, as in Eq. 2. The protons,

$$(2) \qquad OH^- \rightleftharpoons H^+ + O^{--}$$

$$(3) \qquad H^+ + OH^- \rightleftharpoons H_2O$$

$$(4) \qquad OH^- + OH^- \rightleftharpoons H_2O + O^{--}$$

Acid I Base II Acid II Base I

having an exceptional polarization potential, react almost completely with the solvent, Eq. 3, represented by the other half of the hydroxyl ions in Eq. 1. Water, the product of this reaction, thus may be regarded as a solvated proton (onium species) in fused-hydroxide solution. Using the protonic-solvent theory, the quantitative extent of reaction is regarded as being controlled by the relative proton affinities of the two bases involved in any acid-base equilibrium.

[18] R. P. Bell, *Quart. Revs. (London)* 1, 113 (1947).

[19] E. C. Franklin, *The Nitrogen System of Compounds*, Reinhold, New York, 1935.

[20] G. Jander, *Die Chemie in wasserähnlichen Lösungsmitteln*, Springer, Berlin, 1949.

At least three types of protonic-solvolytic reactions might be expected. First, the hydride ion provides a special case:

$$(5) \qquad H^- + OH^- \rightleftharpoons O^{--} + H_2$$

Second,

$$(6) \qquad OH^- + HB \longrightarrow B^- + H_2O$$

where B^- is taken as a generalized representation of an anionic species.

Third,

$$(7) \qquad OH^- + B^- \longrightarrow BH + O^{--}$$

The second type of solvolytic reaction requires that the hydroxyl ion be a stronger proton acceptor than the B^- ion. There are, of course, many examples of this, such as the obvious reaction,

$$(8) \qquad OH^- + HCl \longrightarrow Cl^- + H_2O$$

In fused hydroxides this type of reaction is solvolytic, not neutralization. Equation 8 represents an obvious reaction because of the exceedingly weak base-character of the chloride ion. There should, however, be a series of such reactions involving bases with proton affinities lying between those of Cl^- and OH^-, such as HPO_4^{--} and HCO_3^-.

The third type of solvolytic reaction, Eq. 7, requires that the B^- ion be a stronger base than the O^{--} ion. At best, there will be very few instances of this.

Neutralization reactions in fused hydroxides, which can be treated by the protonic theory, are also of three types. One type is the reaction of water with the oxide ion,

$$(9) \qquad H_2O + O^{--} \longrightarrow 2OH^-$$

where the water may come from the dissociation of another compound.

The second type is the reaction of water with an ion which is a stronger base than the hydroxyl ion but a weaker base than the oxide ion. This is essentially the reverse of Eq. 6; thus,

$$(10) \qquad H_2O + B^- \longrightarrow BH + OH^-$$

The third is the reverse of Eq. 7; thus,

$$(11) \qquad O^{--} + HB \longrightarrow B^- + OH^-$$

There are a great many reactions in fused hydroxides which involve the self-dissociation equilibrium but which cannot be usefully treated in terms of the protonic-solvent theory. Consider, for example, the familiar reaction,

$$(12) \qquad CO_2 + 2OH^- \longrightarrow CO_3^{--} + H_2O$$

The application of the Bronsted theory here requires a rather complex, formal treatment. The actual proton exchange is between the bases, OH^- and O^{--}. The weaker base, OH^-, serves as the proton acceptor, and the stronger base, O^{--}, serves as the proton donor. This is the reverse of the neutralization reaction given in Eq. 9 and would not be predicted by the protonic-solvent theory. This seeming contradiction may be resolved in a formal way, but it is much more useful to apply the following straightforward approach. In Eq. 12 the greater oxide-ion affinity of carbon dioxide compared with water determines the direction of the reaction.

Lux,[21] and Flood and Forland[22] have advanced a definition of acids and bases which was designed to treat the special problems encountered in nonprotonic fused-oxide systems. According to them, a base is an oxide-ion donor, and an acid is an oxide-ion acceptor; thus,

$$(13) \qquad \text{Base} \rightleftharpoons \text{Acid} + O^{--}$$

Under this definition the conventional classification of slags as acidic or basic is preserved.

The detailed application of this concept by its originators involves some awkwardness. For example, they regard alkali-metal cations as acid analogs in fused alkali-metal oxysalts. The analysis which was presented earlier in this report shows, however, that such cations do not behave in a way analogous to acids but rather play the special role of determining the self-dissociation constant of the medium. As long as the oxidic concept is used in a qualitative way, the awkwardnesses are not so apparent. Therefore, we will reserve a critical review for a future report in which the treatment will be more quantitative than is given here.

This acid-base concept has not been applied to solvent systems, but by a small extension this may be done. Consider two competing equilibria of the above type.

$$(14) \qquad \begin{array}{ccccccc} & & AO & \rightleftharpoons & A^{++} & + & O^{--} \\ O^{--} & + & B^{++} & \rightleftharpoons & BO & & \\ \hline AO & + & B^{++} & \rightleftharpoons & BO & + & A^{++} \\ \text{Base I} & & \text{Acid II} & & \text{Base II} & & \text{Acid I} \end{array}$$

The acid-base equilibrium shown by Eq. 14 may be considered to be controlled by a balance between the oxide-ion affinities of the reactant acid and the product acid in a way analogous to the balance between the proton affinities of the bases in protonic solvents.

The self-dissociation of hydroxyl ions according to Eq. 1 completely fulfills the requirements of the Lux definition, Eq. 13. It may at first seem improper to assign to two hydroxyl ions the role of a single base. Although this is not permissible in the Bronsted definition, it is a natural consequence of the Lux definition. The process of joining two ortho-oxyanions by eliminating an oxygen ion and forming an oxygen bridge, such as occurs in pyro-anions, is one of the types of reactions to which the Lux definition applies. For example,

$$(15) \qquad 2PO_4^{---} \rightleftharpoons P_2O_7^{4-} + O^{--}$$

Thus, water, H-O-H, may be regarded as a pyro-analog compound of hydrogen, and the hydroxyl ion as the ortho-oxyanion of hydrogen. Because of acid-base relations involving pyro-ions, such as shown in Eq. 15, two hydroxyl ions will always be taken together to serve as a Lux base-analog.

The solvolytic reactions involving the oxides and oxysalt solutes can be roughly classified according to the ionization energy of the atom other than oxygen in the oxide. This method of classification is possible, because the ionization energy of an atom is related to its oxide-ion affinity. It is convenient to divide the elements into four groups according to ionization energy.

First, oxides and oxysalts of atoms having high ionization energy should react with the fused hydroxides to give a change in coordination. For example,

$$(16) \qquad SO_3 + 2OH^- \rightleftharpoons SO_4^{--} + HOH$$

See also Eq. 12.

Second, oxides and oxysalts of atoms of medium

[21] H. Lux, *Z. Elektrochem.* **45**, 303 (1939).

[22] H. Flood and T. Förland, *Acta Chem. Scand.* **1**, 592, 781, 790 (1947).

ionization energy should react with fused hydroxides either to form or to depolymerize polyanionic acids. For example,

$$(17) \quad P_2O_7^{4-} + 2OH^- \rightleftharpoons 2PO_4^{---} + HOH$$

probably will take place. The possible reactions of this type are numerous because of the substantial variety of polyanions. For example, consider the stepwise depolymerization of silicon-oxygen compounds, beginning with the three-dimensional network in silicon dioxide, passing through the two-dimensional net polyanions, through the one-dimensional chain (and ring) polyanions, the pyroanion, and finally ending with the orthosilicate anion.

This second type of solvolytic reaction should tend toward depolymerization and, for some parent atoms, toward formation of the ortho-oxyanion because of the relatively high basic character of the hydroxyl ion. However, the ortho-oxyanion is not always the most stable form. It has been shown[23] that the higher borates are depolymerized down to the pyroborate, not the orthoborate, by an excess of fused NaOH. Available evidence[24] indicates that the pyrosilicate–sodium hydroxide reaction does not by any means go all the way to the orthosilicate but that the following equilibrium is established:

$$(18) \quad 2SiO_4^{4-} + H_2O \rightleftharpoons Si_2O_7^{6-} + 2OH^-$$

This represents an acidic-buffer equilibrium in fused NaOH.

Third, ions derived from atoms of low ionization energy should react to form oxides. In some studies to be reported later, G. F. Petersen and the writer have found many examples of this type of reaction. For example,

$$(19) \quad NiCl_2 + 2OH^- \longrightarrow NiO_{ppt} + H_2O + 2Cl^-$$

The resultant oxide may undergo further reaction to form a soluble anion. For example,

$$(20) \quad NiO_{ppt} + 2OH^- \longrightarrow NiO_{2\,soln}^{--} + H_2O$$

(The anionic formula shown refers to the substance which precipitates from solution on cooling, Na_2NiO_2.)

Fourth, oxides of atoms which have very low ionization energy should not undergo solvolysis at all. The behavior of such cations (derived from alkali and alkaline-earth metals) has already been described.

The simplest neutralization reaction is, of course, the reaction of the oxide ion with water. This could be considered as either protonic or oxidic. In a very striking experiment performed by Agar and Bowden,[25] sodium oxide was titrated in fused sodium hydroxide with gaseous water; the polarization of an oxygen electrode was used as an indicator. Another type of oxidic neutralization is

$$(21) \quad AO + H_2O \longrightarrow A^{++} + 2OH^-$$

where the acid analog, A^{++}, must have a stronger oxide-ion affinity than water has. The orthoborate ion, BO_3^{---}, in fused sodium hydroxide should be such a substance. The reaction between an acid analog and the oxide ion is a pseudo neutralization in which no solvent is produced. This reaction includes all those considered in the original Lux theory.

Film Formation on Metals

J. V. Cathcart

The investigation of the oxidation characteristics of sodium has been continued. Sodium is a metal which according to the "cracking theory of oxidation"[26] should exhibit a linear oxidation rate. This study was initiated because preliminary experiments indicated that sodium, contrary to the theory, actually forms a highly protective oxide film in dry oxygen. Subsequent work has verified these early findings. The research has been continued in an effort to clarify the oxidation mechanism that is operative for sodium and to relate it to the more thoroughly investigated oxidation mechanisms of copper, aluminum, etc.

On the basis of the results obtained with sodium, it was concluded that a fundamental error existed in the currently accepted oxidation model for metals obeying a linear rate law and that it was

[23] G. W. Morey and H. E. Merwin, *J. Am. Chem. Soc.* **58**, 2252 (1936). These authors report that the orthoborate was formed, but the composition which they give is clearly that of the pyroborate.

[24] J. D'Ans and J. Löffler, *Ber. deut. chem. Ges.* **63B**, 1446 (1930).

[25] J. N. Agar and F. P. Bowden, *Proc. Roy. Soc. (London)* **A169**, 220 (1938).

[26] U. R. Evans, *Metallic Corrosion, Passivity, and Protection*, p 102, Longmans, Green, New York, 1946.

desirable to investigate carefully the oxidation of some metal which does follow a linear rate equation. Columbium was regarded as especially suitable for this purpose. Below approximately 400°C it obeys a parabolic rate law; while above this temperature its oxidation rate is linear. At 400°C the initial stages of oxidation appear also to follow a parabolic rate, but, after several hours of oxidation, the rate increases and becomes almost linear.[27] Thus, a careful investigation of the structure and composition of the oxide films formed at or near 400°C should provide valuable information as to the conditions which lead to a linear oxidation rate.

An added incentive for the study of the oxidation properties of columbium is the fact that this metal possesses very desirable high-temperature structural properties. Its use has been largely limited by its excessive oxidation rate at high temperatures. Moreover, the accumulation of more information concerning its oxidation mechanism was considered desirable in the belief that a means could be devised to overcome its tendency to oxidize excessively.

Sodium Oxidation. – The oxidation rate of sodium was followed by measuring the change in pressure in a closed reaction chamber as the reaction proceeded. A sensitive differential manometer, utilizing Octoil-S diffusion-pump oil as the manometric fluid, served as the pressure-sensing device.

The apparatus used is shown in Fig. 107. Although its principle of operation was the same as that of the apparatus used earlier in the work,[28] several improvements have been made. The sodium reservoir consisted of a glass bulb closed at one end with a thin-walled break-off tip. The reservoir was filled under vacuum through a side arm with sodium which had been purified by repeated vacuum distillations at a pressure of 10^{-6} to 10^{-7} mm Hg. After the removal of the sidearm, the reservoir was attached to a tube below the oxidation bulb, as shown in the drawing. A small furnace was built which could be placed around the entire apparatus. The sodium reservoir and the manometer protruded from suitable holes. The entire apparatus could thus be baked out under a vacuum before any sodium was admitted to the system. Care was taken to load the manometer by the vacuum distillation of Octoil-S from a separate bulb into the manometer arms. This procedure ensured that the manometric fluid would not act as a source of appreciable gas.

After a bakeout period of 16 to 20 hr, the system was allowed to cool to room temperature, and the breakoff tip above the sodium reservoir was crushed. The sodium was then distilled into the tube below the oxidation bulb and the sodium reservoir pulled off. Finally, the sodium was distilled into the oxidation bulb and allowed to condense on the walls. Both these final distillations were made under a pressure of approximately 2×10^{-7} mm Hg. As the last step before the admission of oxygen, the tube below the oxygen bulb was sealed off, as were the vacuum leads to the two reference bulbs.

A 50-cc flask served as an oxygen reservoir. Prior to being attached to the oxidation apparatus, it was filled with carefully purified oxygen to a pressure such that, when the gas was allowed to expand into the reference and oxidation bulbs, the resultant pressure was 200 mm Hg. The purification of the oxygen was accomplished by passing it over hot copper oxide (to remove hydrogen) and Ascarite (to remove carbon dioxide) and finally drying it over $Mg(ClO_4)_2$ and in a liquid-nitrogen trap.

The tube leading from the oxygen reservoir to the breakoff tip was made of 2-mm capillary tubing. By thus minimizing the volume above the reservoir, it was possible in the low-temperature runs to immerse the reservoir in a cold bath and precool the oxygen to the desired reaction temperature.

When the breakoff tip above the oxygen reservoir was smashed, the oxygen passed through the T-connection above the manometer and simultaneously filled the reference and oxidation bulbs to identical pressures. The intersection of the tubes of the T was then collapsed as quickly as possible with a hand torch. The three arms of the manometer were thus separated, and any change in pressure in the oxidation bulb due to the reaction of sodium and oxygen was reflected in a change in the relative heights of the oil columns of the manometer.

The use of the above described T-connection instead of a stopcock had two advantages. First, it prevented all possibility of a leak occurring in the system. More important, this arrangement, by

[27] H. Inouye, *The Scaling of Columbium in Air*, ORNL-1565 (Sept. 24, 1953).

[28] J. V. Cathcart, *Met. Semiann. Prog. Rep. Oct. 10, 1953*, ORNL-1625, p 33.

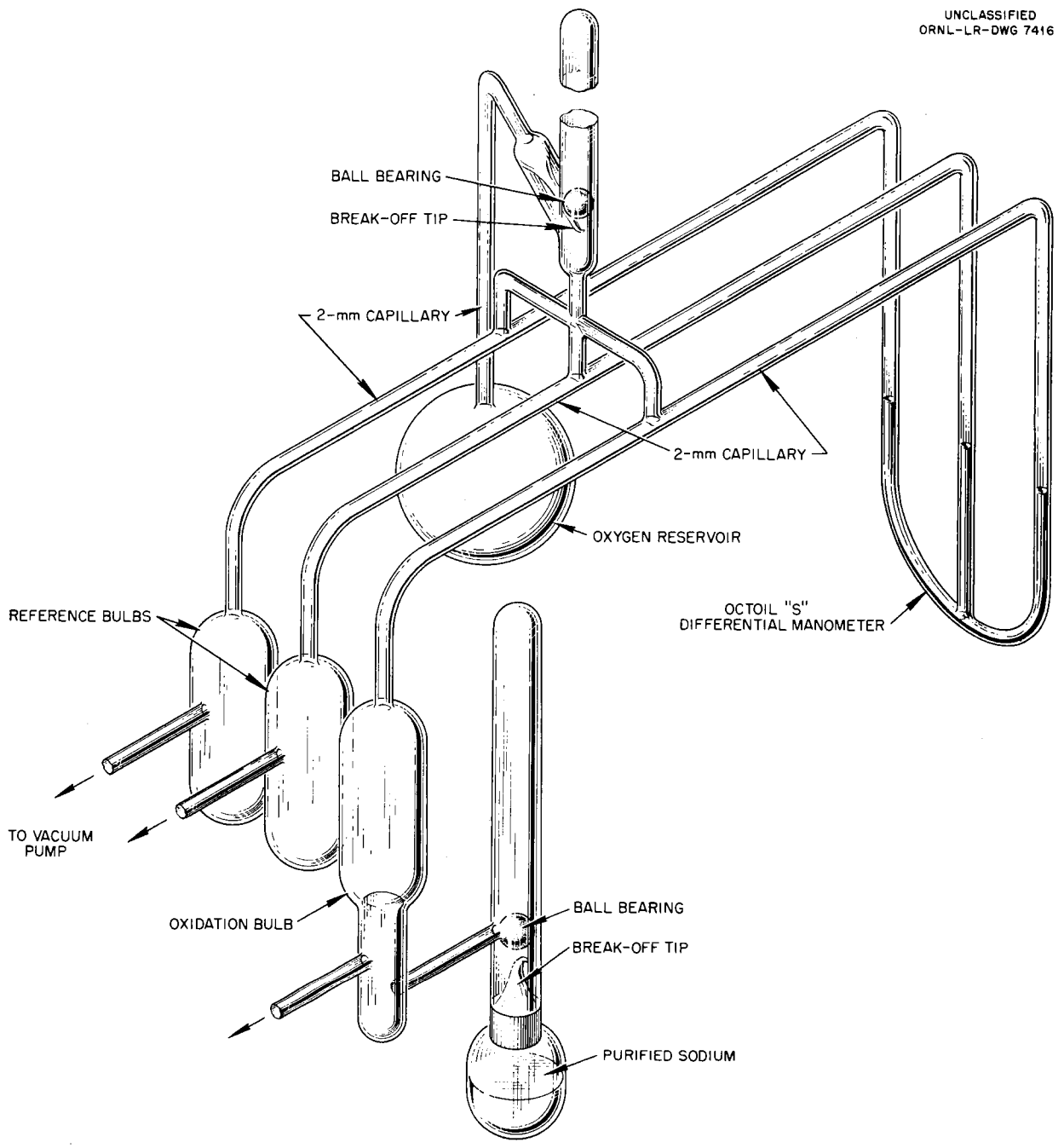

Fig. 107. Apparatus for Measuring the Oxidation Rate of Sodium at Low Temperatures.

dispensing altogether with stopcocks, eliminated the danger of the contamination of the sodium surface by stopcock-grease vapors and permitted the bakeout of the entire system during the initial stages of evacuation. It was felt that these considerations were sufficiently important to forego the greater conveniences of a stopcock.

During the period covered by this report, oxidation measurements were made at 35 and −79°C, and a series of measurements at −20°C is now in progress. At 35°C an apparatus identical with that shown in Fig. 107 was used, except that

only one reference bulb was found necessary. For reasons to be described below, however, the second reference bulb proved very helpful for experiments at the two low temperatures.

A bath consisting of powdered dry ice mixed with a 50-50 vol % solution of carbon tetrachloride and chloroform was used to attain the proper temperature for the oxidation measurements at –79°C. The density of the carbon tetrachloride and chloroform mixture was approximately the same as that of dry ice. The combination produced a slurry of uniform consistency in which there was little tendency for the dry-ice particles to segregate.

At –79°C sodium oxidized at a very slow rate. The maximum pressure changes which occurred in the system because of the oxidation were 0.2 to 0.3 mm Hg. For this reason it was necessary to pay particularly careful attention to factors which could cause spurious pressure readings. One obvious source of error was a temperature difference between the reference and oxidation bulbs. This difficulty was overcome by utilizing a relatively thin slurry in the cold bath and stirring it very vigorously. A less easily corrected source of trouble stemmed from the fact that, of necessity, the reference and oxidation bulbs were maintained at dry-ice temperature while the manometer and connecting tubes were at room temperature. A simple gas-law calculation will show that in such a system any change in the temperature of either the cold bath or the manometer in general produced a difference in pressure between the oxidation bulb and the reference bulb. A special case, which is an exception to this rule, is found when the volumes of gas at the two temperatures are identical on both sides of the manometer. The magnitude of the pressure difference is dependent both on the ratio of the volumes of gas held at the two temperature extremes and on the difference in temperature. Thus, this effect was of no great importance for experiments at temperatures close to room temperature, but became significant at –79°C.

It was impossible to maintain exactly equal volumes on both sides of the manometer, and the attainment of precise temperature control in the cold bath at –79°C was almost as difficult. The equilibrium temperature of any dry-ice bath is determined by the sublimation point of carbon dioxide; however, the constancy of the sublimation temperature is dependent upon the constancy of the partial pressure of carbon dioxide above the bath. Thus, unless the bath is contained in a closed vessel, variations in temperature will occur in the bath on account of changes in the partial pressure of carbon dioxide above it. In addition, the fact that the heat of solution of carbon dioxide in carbon tetrachloride and chloroform is negative caused the temperature of the bath to fall below the equilibrium sublimation temperature when the cold mixture was first prepared. Since the bath was contained in a Dewar flask, the lowered temperature tended to persist for long periods of time unless a heater was immersed in the bath.

For these reasons, it was decided that precise temperature control of the apparatus at –79°C was impracticable. However, it was essential that some reference point be established for the bath so that the apparatus could be brought back to the initial conditions of the experiment after, for example, each renewal of the dry-ice charge in the bath. The addition of a second reference bulb proved satisfactory for this purpose. The two reference bulbs represented a "differential gas thermometer." It was observed that within about 10 min after the start of an experiment a small difference in the heights of the oil in the reference arms of the manometer was usually established. This difference remained constant as long as the temperature of the bath and the room temperature were unchanged. When deviations in this difference were observed, it was possible to make slight alterations in the bath temperature (for example, by removing part of the cover of the Dewar flask and so decreasing the partial pressure of carbon dioxide above the bath) and thus re-establish the desired pressure difference in the reference bulbs.

It was recognized that the constancy of the pressure difference between the two reference bulbs did not necessarily indicate a corresponding constancy in the cold-bath temperature. Frequently, the adjustments in the bath temperature (necessary to maintain the above pressure difference) represented a counterbalance to changes in room temperature. The resultant small changes in the bath temperature, of course, meant a change in the temperature at which oxidation occurred; but since the oxidation rate of sodium is not a sensitive function of temperature at –79°C, this

alteration of the experimental conditions was not considered significant. In any event, as may be seen in Fig. 108, the use of the technique described above produced excellent agreement among the data for three separate experiments at −79°C.

The data from oxidation measurements at 35 and −79°C along with the results previously obtained at 25 and 48°C are shown in Fig. 108. The oxide-film thickness is plotted against the time of oxidation on a log-log scale. The various curves represent the composite of the data from three or more experiments.

The fact that the curves were not linear showed that the data did not fit any of the conventional rate equations of the form

$$x^n = kt \ , \qquad n = 1, 2, 3 \ ,$$

where x is the thickness of the oxide film after time t and k is the rate constant. The data were also tested against the inverse logarithmic equation

$$\frac{1}{x} = A - B \ln t \ ,$$

where x and t are the same as above and A and B are constants. This equation, proposed by Mott and Cabrera,[29] also failed to give a satisfactory fit even for the data taken at −79°C. It was concluded that the mechanism of oxidation of sodium under the chosen experimental conditions is different from the ones proposed in any of the current oxidation theories. That the rate-determining step in the oxidation does involve a diffusional process is indicated by the decrease in the oxidation rate at all the temperatures investigated.

Perhaps the most striking feature of the experimental results was the slowness with which oxidation occurred. Very roughly, 1 unit of the ordinate scale is equivalent to 10 Å of film thickness. Thus after 1000 min of oxidation at −79°C, the thickness of the oxide film was only about 30 Å; whereas at 48°C, it was 500 Å.

The very small amount of oxide formed illustrates the highly protective character of sodium

[29] N. Cabrera and N. F. Mott, *Repts. Progr. in Phys.* 12, 163 (1948–1949).

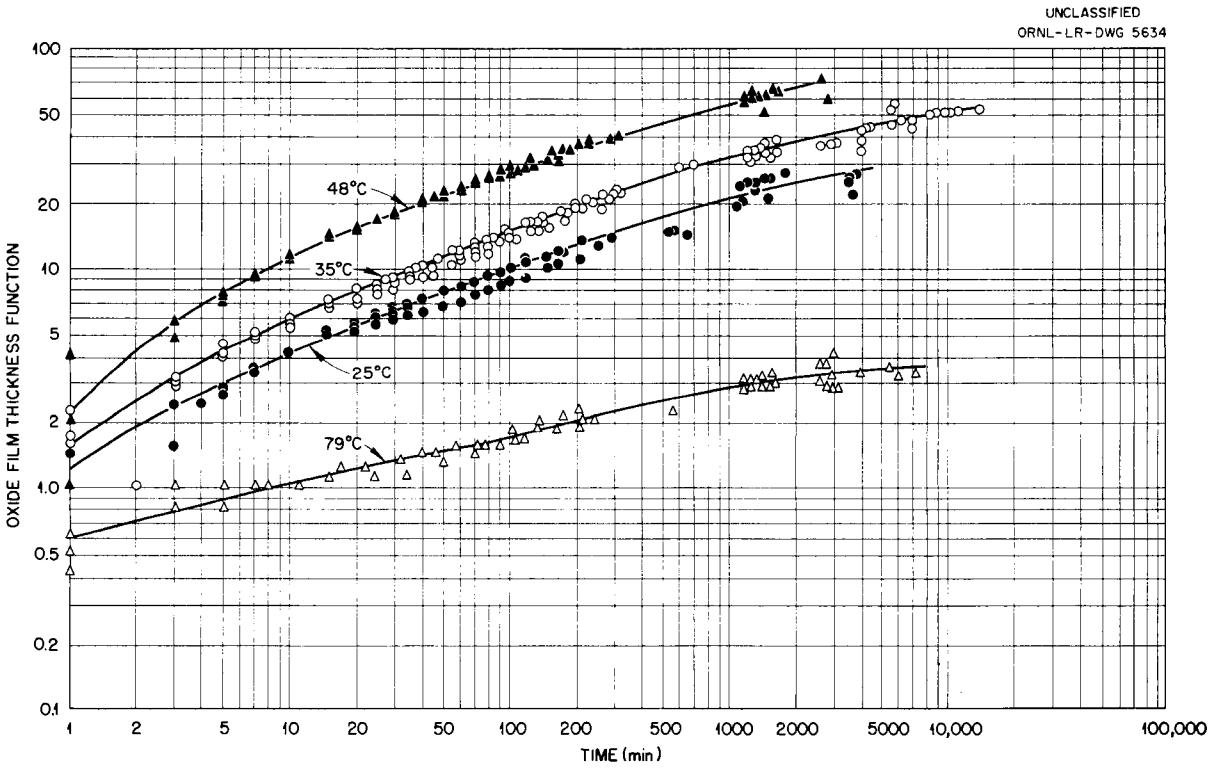

Fig. 108. Film Thickness of Sodium Oxide as a Function of Time for a Series of Temperatures.

oxide films in carefully dried oxygen. The frequently accepted idea that sodium obeys a linear oxidation rate must be discarded. In addition, the results suggest that the oxidation mechanism for sodium and possibly, also, that for the other alkali and alkaline-earth metals need not be regarded as being of a special nature but may be very similar to the oxidation mechanism for the heavier metals, such as copper and aluminum. As further details of the oxidation characteristics of sodium and other "ultra light" metals become available, a theory of oxidation may possibly be devised that is applicable to at least the low-temperature oxidation of all metals.

Oxidation of Columbium. – The work on columbium is in the preliminary stage. It is planned to measure the rate of oxidation of columbium at several temperatures in the neighborhood of 400°C and then to correlate the rate and oxide thickness with the structure and porosity of the oxide. In this manner it should be possible to establish the conditions which exist in the film both when a parabolic rate law is obeyed and when the rate becomes linear.

An experiment, in which highly purified oxygen was used, was performed to obtain a check on the oxidation rate of columbium at 400°C. Qualitative verification was obtained of the phenomenon, reported by Inouye,[27] of the transition of the oxidation rate from a parabolic rate equation to a linear relation. The initial stages of oxidation produced oxide films which exhibited interferences (colors). As the reaction proceeded, however, the specimens became coated with a white, opaque oxide film whose surface was rough. The appearance of the white oxide seemed to coincide approximately with the transition from the initial parabolic rate equation to a linear rate. X-ray examination of these specimens is now in progress.

PACKAGE POWER REACTOR PROGRAM

J. E. Cunningham

Development work is well advanced on the stainless steel–uranium dioxide fuel component proposed for service in the Army Package Power Reactor. Material and dimensional specifications covering the flat-plate-type component are essentially complete. Sufficient fabrication technology is available so that the construction of full-scale, enriched fuel elements for irradiation test purposes can proceed.

A cooperative program was initiated between WAPD and ORNL to test an experimental stainless steel fuel assembly in core 1 of the STR. The test element will be exposed for 400 hr of full power operation under the combined hydraulic, thermal, pressure, and irradiation conditions present. Such performance information is needed to aid in the development of a cheap, reliable plate-type fuel component for relatively long-time service in the APPR.

The design data on the composite fuel plates contained in the test element are summarized in Table 13.

The status on construction of the test element, as well as the progress on other phases of the program, is described in the following sections.

FISHTAILING IN APPR FUEL PLATES

R. C. Waugh

Some progress has been made since the last report in developing techniques to constrain the degree of fishtailing; that is, the extrusion of core material between the frame and cover plates at the leading and trailing ends of the plate during hot rolling. The two primary factors studied were the direction of rolling and the amount of reduction during the initial hot passes.

Results of the study are summarized in Table 14. A comparison between plates 130 and 131 shows that reversing the direction of rolling after each hot pass reduced the total amount of fishtailing by 39%. It is also apparent that the bulk of the fishtailing occurred during the first 40% pass. The definite advantage of using lighter initial passes, in addition to reversing the direction of rolling after each hot pass, is shown by comparison between plates 131 and 335. It is apparent, therefore, that fishtailing may be minimized by reversing the direction of rolling after each hot pass and by using light initial hot passes.

APPR COMPONENT ASSEMBLING BY BRAZING

R. J. Beaver

APPR assemblies with 18 flat composite stainless steel plates containing normal UO_2 have been satisfactorily brazed within dimensional tolerances. A modification of the brazing cycle established for solid stainless steel assemblies was necessary as a result of severe warpage of the composite plates when subjected to the fast heating and cooling cycle. Present practice is

TABLE 13. GENERAL DESIGN DATA ON STR TEST PLATES

Total number of fuel plates required	12
Plate (clad-core-clad) thickness, mils	7.6–14.8–7.6
Core mixture composition, wt %	17.92 UO_2–0.19 B_4C–81.89 SS
Enriched UO_2 content per plate, g	13.077
U^{235} enrichment level, %	93.14
U^{235} content per plate, g	10.716
U^{235} distribution per plate, g/cm^2	0.040
B_4C content per plate, g	0.138
Natural boron content per plate, g	0.108
Stainless steel content per plate, g	187.402

TABLE 14. DATA FROM TESTS DESIGNED TO DETERMINE EFFECT OF ROLLING ON FISHTAILING IN THE CORE SECTION

Plate No.	Initial Reductions (%/pass)	Initial Core Thickness (in.)	Final Core Reduction (%)	Rolling Direction	Average Fishtail at Leading End (in.)	Average Fishtail at Trailing End (in.)	Total Fishtailing Average Value (in.)
130	40, 40, 40, 40	0.275	73	Single	0.630	0.110	0.740
131	40, 40, 40, 40	0.275	73	Reversed after each pass	0.370	0.080	0.450
335	10, 10, 25, 25, 25	0.150	90	Reversed after each pass	0.074	0.062	0.136

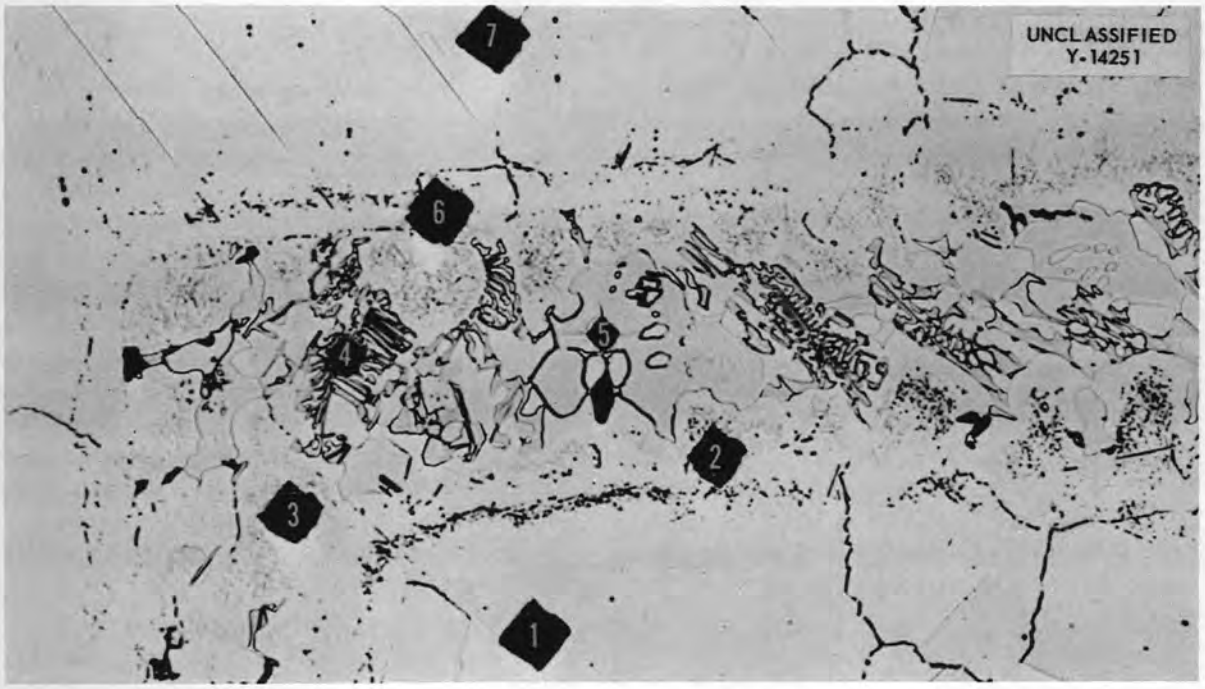

Fig. 109. Microstructure of Joint Brazed with Coast Metals NP Alloy in Assembly No. 28. Vickers hardness values (VHN) for 100-g load: (1) 143, (2) 202, (3) 189, (4) 764, (5) 732, (6) 176, (7) 146. Etchant: 10% oxalic acid. 250X.

to initiate the heating cycle at 350°C, heat to 1140°C at a rate of approximately 200°C/hr, braze, and furnace cool. Coast Metals NP alloy (49.5% Ni–27% Fe–11.0% Si–7.6% Mo–3.7% P) is presently being used as the braze metal. Braze metal is applied dry with an eye dropper of 0.030 in. ID. After presetting, the alloy powder is glued in place with Nicrobraz cement.

The physical testing of brazed joints, prepared with Coast Metals NP brazing alloy and type 304L stainless steel, has been initiated. Several composite bars pulled at room temperature gave an average ultimate strength value of 28,800 psi in tension.

The microstructure of a typical brazed joint, taken from fuel assembly No. 28, is shown in Fig. 109. Illustrated also are the diamond hardness indentation marks obtained on running a hardness traverse across the brazed-joint section. The hardness data reported in Fig. 109 reveal

that the brazed structure contains extremely brittle phases in an apparently ductile matrix.

PREPARATION OF COMPONENT FOR IRRADIATION TESTING IN THE STR

A subassembly, composed of stainless-steel-clad, enriched UO_2-bearing fuel plates, was prepared for irradiation testing in Mark I core of the STR. The subassembly consisted of two fuel unit sections; each contained six parallel flat plates brazed to 50-mil-thick grooved stainless steel side plates which were spaced 134 mils apart. The units were mechanically joined together end-for-end by means of a common alignment comb and were housed in a rectangular stainless steel seam-welded tube. Figure 110 illustrates the fuel test sections and tube prior to encasement. After insertion the units were spaced to allow for thermal expansion and pinned rigidly to the housing at each end.

The plates were $21\frac{7}{8}$ in. long and $2\frac{1}{4}$ in. wide. The 30-mil plate thickness consisted of 14.8 mils of fuel-bearing core and 7.6 mils of stainless steel cladding. The fuel-bearing sections of the composite plates were $20\frac{15}{16}$ in. long and 2 in. wide. The type of stainless steel employed in the construction of the fuel sections was AISI grade 304L throughout, except for the alloy steel in the core, which was a modified 304 grade containing 2.37% silicon.

The core was prepared by a powder-metallurgy process which consisted in cold pressing at 33 tsi, sintering at 1150°C, and coining to size. The cores consisted of 17.92 UO_2, 0.19 B_4C, and 81.89 wt % prealloyed steel. Particle sizes of the powders used in the makeup of the core section prior to cold pressing were:

Material	Particle Size (μ)
UO_2	44 to 88
B_4C	<44
Modified 304 stainless	< 149

The UO_2 was prepared by sintering the product resulting from a steam autoclave treatment of enriched-metal turnings at 1700°C. The B_4C powder was obtained by grinding to the desired size the metallurgical grade supplied by the Norton Company. The modified 304 stainless steel powder consisted of irregular particle shapes, as supplied by Vanadium-Alloys Steel Co.

Twenty-four billets were prepared by punching solid-type 304L stainless plates, inserting the coined core in the frame, and tack-welding type 304L stainless cover plates to the frame. Prior to assembling, the mating surfaces were wire-brushed. The billets were rolled in air but were protected from excessive scaling by preheating and reheating in a hydrogen atmosphere. Total hot reduction ranged between 86.7 and 88.0%. Cold reduction varied between 18.1 and 25.3%.

Fig. 110. STR Irradiation Test Element with Enclosure Box.

Following hot rolling, the plates were cleaned in 5% HF–15% HNO_3–80% H_2O solution. The plates were annealed-flattened at 1150°C.

All plates were autoclave corrosion tested at WAPD. The test consisted in an exposure to 360°C static water at 2800 psi for 72 hr. The plates were inspected radiographically for homogeneity. Twelve were selected for brazing into assemblies and were carefully machined to size. One of the remaining plates was sectioned and then submitted for chemical analysis, which supplements the radiographic inspection for homogeneity. The results revealed a maximum deviation of 1.2% about the 15.77% U_t average in the plate core. The average deviation was 0.76%.

Several assemblies composed of plates containing normal UO_2 were brazed to ensure that dimensional specifications could be met. The first was a mockup of the enriched unit, with the exception that it contained only three plates. This unit was tested by WAPD in their "D" loop for dimensional changes and corrosion resistance under dynamic STR water conditions. The assembly proved to be dimensionally stable during a two-week testing period. In order to maintain plate spacings within 5% of nominal, ten plate assemblies were brazed, from which the six plate sections were obtained. Three assemblies, one composed of plates containing normal UO_2 and two composed of the enriched plates, were brazed into assemblies which met the required tolerances.

The brazing procedure was similar to that used for APPR assemblies. Coast Metals NP alloy was used as the braze metal, and all assemblies were slowly heated to 1150°C, brazed, and furnace-cooled.

A detailed evaluation of 278 brazements from the units assembled and brazed in exactly the same manner as the enriched units revealed well-brazed joints. The lateral spread of braze metal from the side plate was confined to a distance of $\frac{1}{16}$ in. A typical joint is shown in Fig. 111.

After the enriched test units were snugly fit into the stainless steel housing, the completed subassembly was shipped to WAPD, where it underwent a series of tests. It successfully withstood a three-day autoclave corrosion test in 680°F static water pressurized at 2800 psi, and a one-week test in the Bettis mockup. The subassembly was placed in the STR on March 7, 1955. It is estimated that there will be approximately 8% burnup of U^{235} atoms during this test.

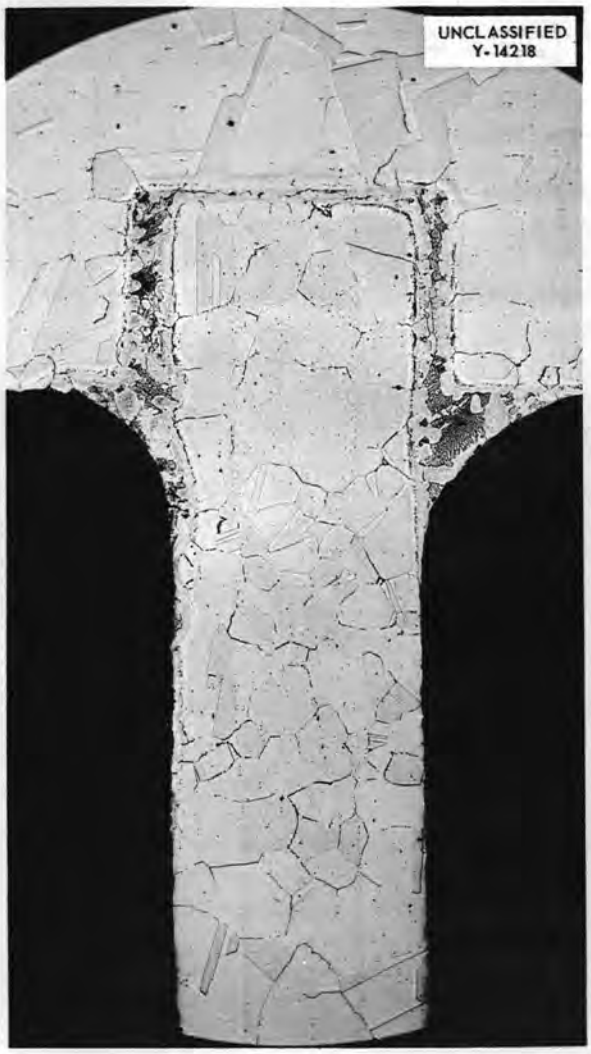

Fig. 111. Cross Section of a Typical Joint Brazed with Coast Metals NP Alloy. Etchant: 10% oxalic acid.

PREPARATION OF TEST COMPONENT FOR IRRADIATION TESTING IN THE MTR

A test element, composed of composite stainless steel plates containing UO_2 and B_4C, was designed for the purpose of obtaining the radiation-damage effect of 58% burnup of U^{235} atoms on fuel plates containing various particle sizes of UO_2. The design of the element closely approximated the design of the APPR assembly and consisted of 19 flat composite-fuel plates, 20 mils thick, spaced 115 mils apart and brazed to grooved stainless steel side plates. The stainless steel

assembly was housed in an aluminum box (the outer dimensions matching the outer dimensions of the MTR fuel section) for insertion directly into the MTR core. The test was designed to irradiate plates of two fuel concentrations. One type contained 17.92 wt % UO_2; the other contained 25.81 wt % UO_2. Particle sizes of UO_2 to be tested ranged in increments from 7 to 105 μ.

Two problems were encountered during construction of the test components which resulted in re-evaluation of the experiment. Radiographic inspection of cores containing the various UO_2 particle sizes revealed severe inhomogeneity in the majority of the plates fabricated. In addition, it was found that during brazing of dummy units the 20-mil plates sagged, resulting in out-of-tolerance plate spacings. The program was revised, and plans were made to test two elements in the MTR. Both elements basically are similar to the above-described unit, with the exception that the composite fuel plates are 30 mils thick. The first element is designed to contain plates with UO_2 concentrations of 18.6, 22.2, and 27.0 wt %, respectively. A 44- to 88-μ UO_2 particle-size range is to be used in conjunction with B_4C in a prealloyed, modified type 304 stainless steel matrix. The primary purpose of this test is to obtain the effect of radiation damage on UO_2 of a 44- to 88-μ particle range as correlated with increasing burnup of total atoms. The test is designed for a 40% burnup of U^{235} atoms of the 18.6 wt % UO_2 core. After fabrication of this element and development of techniques for processing homogeneous cores containing UO_2 in increments from 7 to 105 μ, a second unit will be prepared in order to obtain information for optimization of the fuel-bearing core makeup in the APPR.

CERAMICS RESEARCH

J. M. Warde
J. R. Johnson
C. E. Curtis
L. M. Doney
S. D. Fulkerson
R. L. Hamner
P. Haydon
A. J. Taylor
G. D. White

PRODUCTION OF LARGE PARTICLES OF UO_2 FROM UO_3 HYDRATES

For numerous applications in solid fuel elements, large-grained UO_2 is required. It has been shown that excessive radiation damage occurs to metal matrix materials in sandwich fuel elements where the UO_2 grains are smaller than approximately 40 μ. Previous techniques to obtain larger particles were based on sintering fine-grained UO_2 at about 2000°C and crushing to size. In addition to low efficiency these methods have other undesirable features. There is a container problem, since the UO_2 is reactive at 2000°C with most materials. Some losses are encountered.

A technique has been developed which eliminates some of these difficulties. In earlier ORNL work it was noted that large crystals of UO_3 hydrate could be grown in an autoclave by mixing a small amount of uranyl nitrate with fine-particle UO_3. It was also known that UO_2 could be made by reducing UO_3 in hydrogen. A trial, combining these two processes, showed that large particles of UO_2 could be made by reducing large crystals of UO_3 in H_2. Some of the various forms and sizes are illustrated in Figs. 112–117.

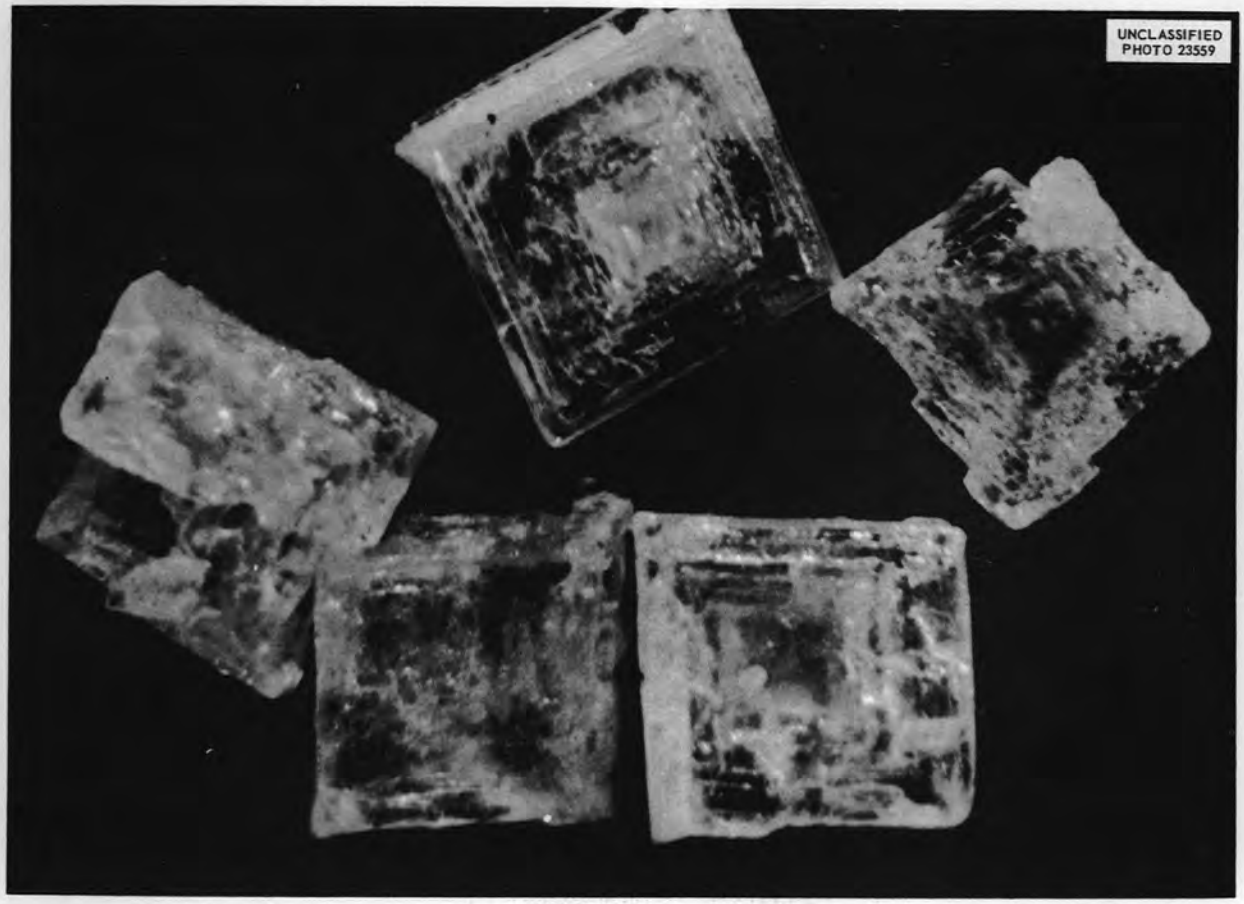

Fig. 112. Some of the Various Forms and Sizes of Large UO_2 Particles Made by Reducing Large UO_3 Crystals with Hydrogen.

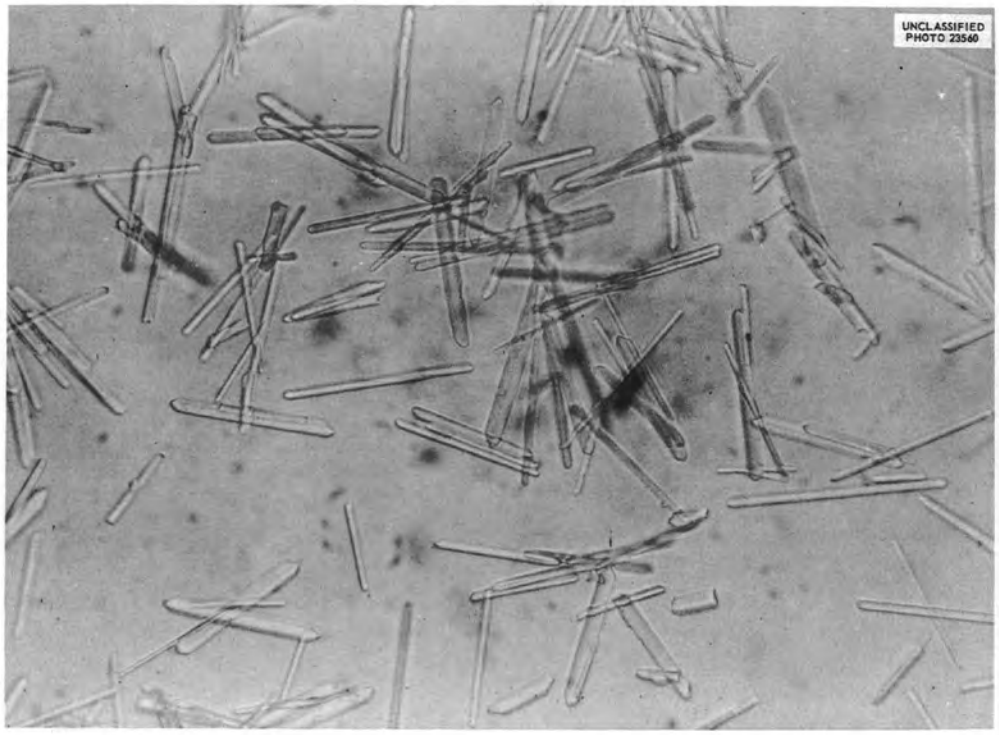

Fig. 113. Some of the Various Forms and Sizes of Large UO_2 Particles Made by Reducing Large UO_3 Crystals with Hydrogen.

Fig. 114. Some of the Various Forms and Sizes of Large UO_2 Particles Made by Reducing Large UO_3 Crystals with Hydrogen.

Fig. 115. Some of the Various Forms and Sizes of Large UO_2 Particles Made by Reducing Large UO_3 Crystals with Hydrogen.

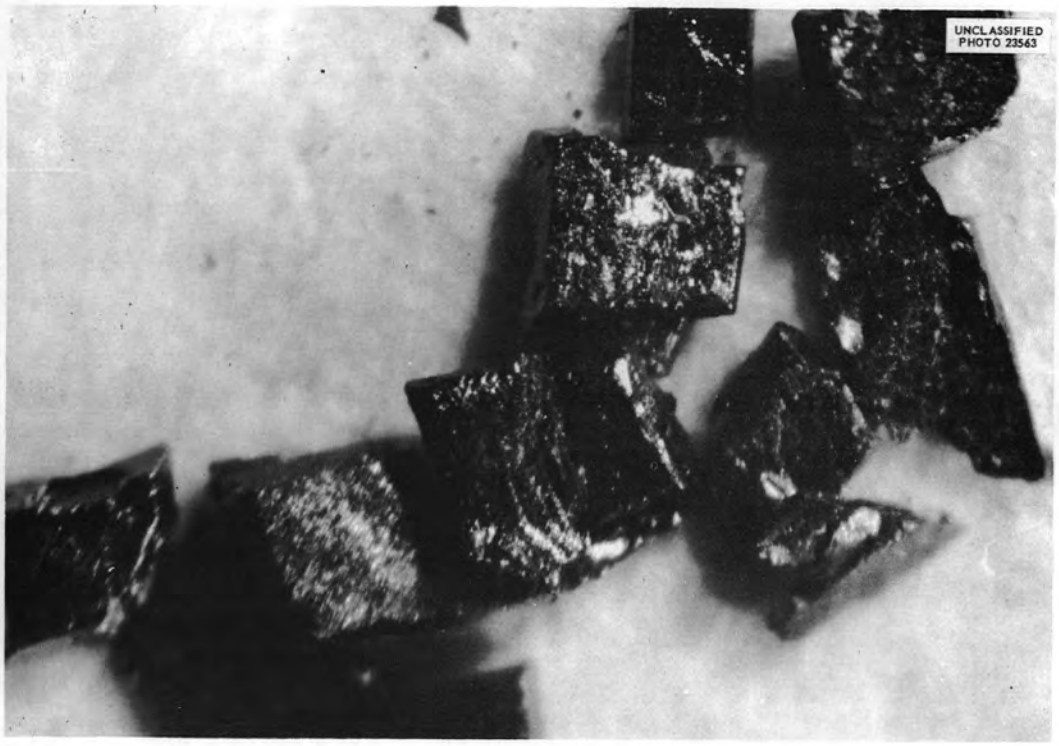

Fig. 116. Some of the Various Forms and Sizes of Large UO_2 Particles Made by Reducing Large UO_3 Crystals with Hydrogen.

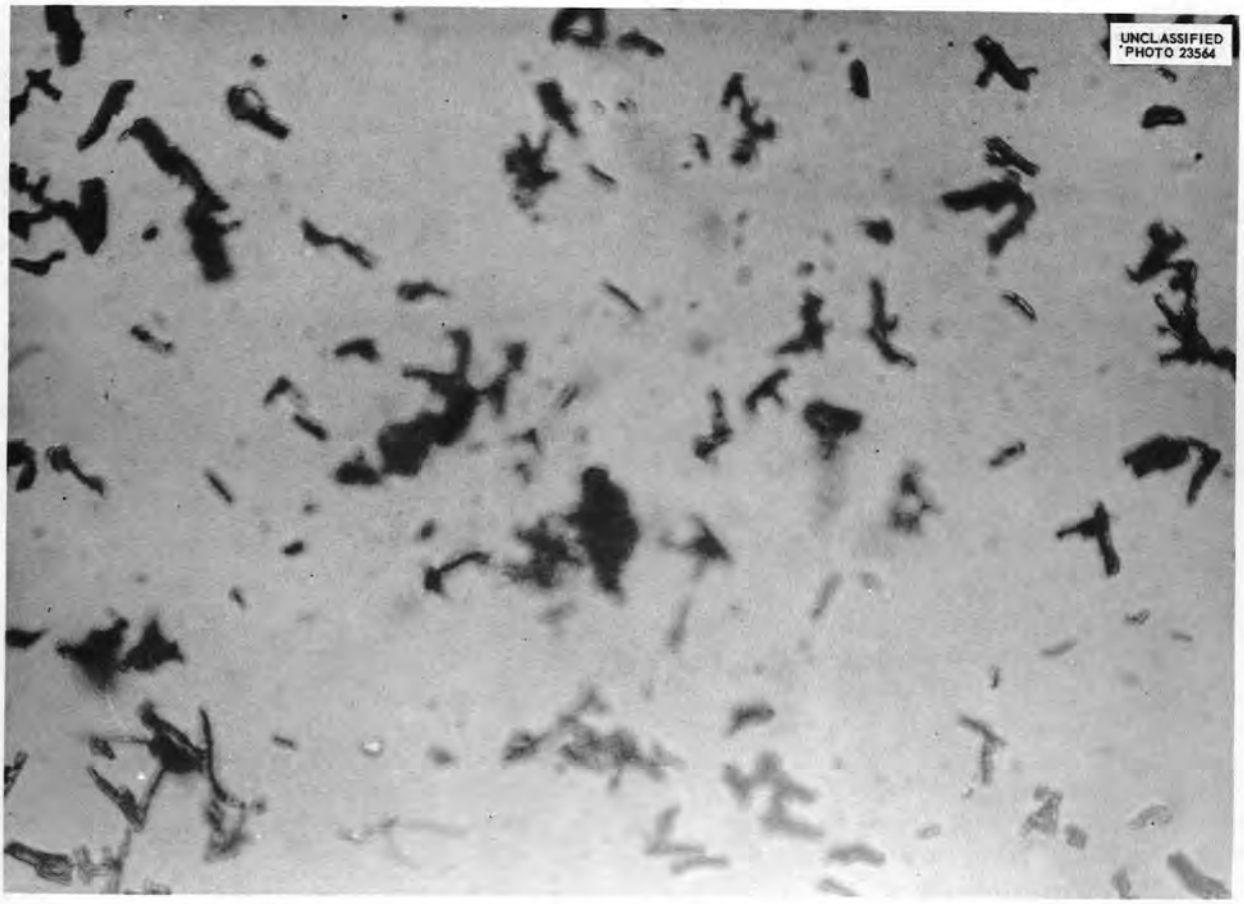

Fig. 117. Some of the Various Forms and Sizes of Large UO_2 Particles Made by Reducing Large UO_3 Crystals with Hydrogen.

From work in which undesirable, large crystals of UO_3 had been grown in fuel-slurry experiments,[1,2] sufficient information was obtained to grow crystals successfully. According to this information, $UO_3 \cdot H_2O$ crystallizes in three forms: needles, plates, and bipyramids. For fuel-element work, the bipyramids would probably be preferred because each of the other two forms has one very small dimension. Information indicated that the bipyramids are more likely to be formed when needles or plates of $UO_3 \cdot xH_2O$, or calcined $UO_2(NO_3)_2$ are digested in dilute solutions of uranyl ion.

Although the work is in its preliminary stages, large crystals of $UO_3 \cdot H_2O$ have been grown. The crystals were grown in an autoclave at 250°C from a slurry consisting of five parts $UO_3 \cdot H_2O$ needles to one part $UO_2(NO_3)_2 \cdot 6H_2O$. These proportions were arbitrarily chosen, and the experiments have indicated that this uranyl-ion concentration is higher than necessary. To date, the variables investigated in these experiments have been the time of heating in the autoclave and the amount of water present. Time of heating seems to have least effect when the moisture content is such that the crystals come from the autoclave with no covering water, but it is of greater importance when the crystals are under liquid at the end of a run. In the latter case time seems to control the proportion of needles converted to large crystals, but it seems to have little effect on the final size of the large crystals.

[1] F. R. Bruce *et al.*, *HRP Quar. Prog. Rep. July 1, 1952*, ORNL-1318, pp 77, 79; R. N. Lyon *et al.*, *HRP Quar. Prog. Rep. July 1, 1952*, ORNL-1318, p 90.

[2] J. O. Blomeke, *HRP Quar. Prog. Rep. Oct. 1, 1952*, ORNL-1424, p 32; R. N. Lyon *et al.*, *HRP Quar. Prog. Rep. Oct. 1, 1952*, ORNL-1424, p 39.

The bulk of the large crystals (approximately 75%) will not pass through a No. 50 screen (297 μ). The crystals produced in the uranyl nitrate experiments have, with one exception, had the shape of a truncated four-sided pyramid and give the appearance of being sheaves of large plates built up into crystals. Classification of these crystals is incomplete at the moment.

The exception noted above was the occurrence of large needles of $UO_3 \cdot H_2O$ found in a long-period experiment (70 hr). These needles ranged up to approximately 1 cm in length and 1 mm in diameter. Such large needles, if they can be grown in quantity, may be of interest to the fuel-element program in that they break down into blocky particles rather than platy particles.

In another experiment greenish-colored bipyramids were grown from uranyl acetate hydrolyzed in the autoclave at 250°C for 19 hr. These crystals were not so loose and clean as those that were grown from the seeded uranyl nitrate solutions. However, since the crystals were definite bipyramids, uranyl acetate will be investigated further.

In this process the material losses can be carefully controlled and kept to a minimum. The temperatures of both the autoclave treatment and the hydrogen reduction are relatively low, eliminating reaction problems. The efficiency of the process is of the order of 90%, so that very little autoclave reprocessing of the UO_3 is required.

UO_2 VOLATILIZATION IN FIRING

A fired BeO ceramic with a porosity of 6% and containing 16% UO_2 lost about 20% of its UO_2 after 66 hr at 1400°C in static air. In the search for a method for protecting the UO_2 from oxygen at high temperatures, two approaches are being investigated: (1) development of a stable compound of UO_2 with various oxides of favorable properties and (2) production of a protective ceramic coating. Although these approaches have previously been studied, there is still much that can be done.

BeO SLIP CASTING

A method has been worked out for slip casting BeO ceramics in the presence of a basic deflocculant; the electrolyte used is tetrasodium pyrophosphate. This process offers advantages in simplicity and mold life over the usual one employing acid deflocculation.

THORIA DENSIFICATION

Densification of ThO_2 by CaO is most effective if the CaO (0.5 wt %) is first calcined at 900°C and then added to the ThO_2. The mixture is pressed into shape and sintered at 1600 or 1800°C. Densities of 94- to 97%-of-theoretical ThO_2 were obtained thus. Higher proportions of CaO (to 2%), additions of the CaO to the calcine itself, and increasing the calcining temperature to 1800°C, all resulted in lower densities.

When the presence of CaO is detrimental, a density of 95% of theoretical can be attained by calcining the ThO_2 to 900°C and by firing the pressed calcine at 1800°C.

CONVERSION AND RADIATION EFFECTS ON ThO_2

Two thorium oxide rods were prepared for irradiation in the LITR by the Solid State Division. They were made in slug form and canned in aluminum jackets. The details of the rods and their exposures are given in Table 15.

There were no significant dimensional changes in the canned rods. The slugs were gripped in a vise, and the aluminum can ends were sawed off. The ThO_2 was observed to have changed from its original white or pink color to what appeared to be a black color. The aluminum jackets were dissolved with hot sodium hydroxide

TABLE 15. EFFECT OF RADIATION ON THORIUM OXIDE RODS

Rod number	1	2*
Weight, g	235.6	660
Density (% of theoretical)	87	96
Size, in.		
Diameter	0.75	1.1
Length	4.5	4.5
Jacket size, in.		
Before		
Diameter	1.441 ± 0.002	1.441 ± 0.002
Length	7.050	6.753
After		
Diameter	1.447 ± 0.003	1.444 ± 0.002
Length	7.009	6.752
nvt**	1.7×10^{20}	2.4×10^{20}

*½ wt % CaO added to ThO_2 in fabrication.
**LITR.

solution at the Chemistry Division laboratories. Photographs of the unjacketed slugs are shown in Figs. 118–121. A single modulus-of-rupture test was made at the Solid State Division on slug No. 1, and the test indicated that the ThO_2 still had a modulus of rupture of at least 2000 psi. Its original strength was about 5000 psi on the basis of determinations made on similar ThO_2 material. Examination of the slugs indicates that there may have been some thermal stresses leading to the breakage observed for slug No. 2. Possible fracture may also have occurred when the slugs were clamped in a vise.

Exact determination of U^{233} in these test slugs is being made by the Chemical Technology Division. These tests indicate that ThO_2 slugs canned in aluminum will remain dimensionally stable under irradiation up to about 2.4×10^{20} nvt where calculated U^{233} conversion is approximately 0.17%. Properly handled slugs no larger than 0.75 to 1.00 in. in diameter will probably suffer no fracture, or, at least if fracture occurs, the pieces will be quite large.

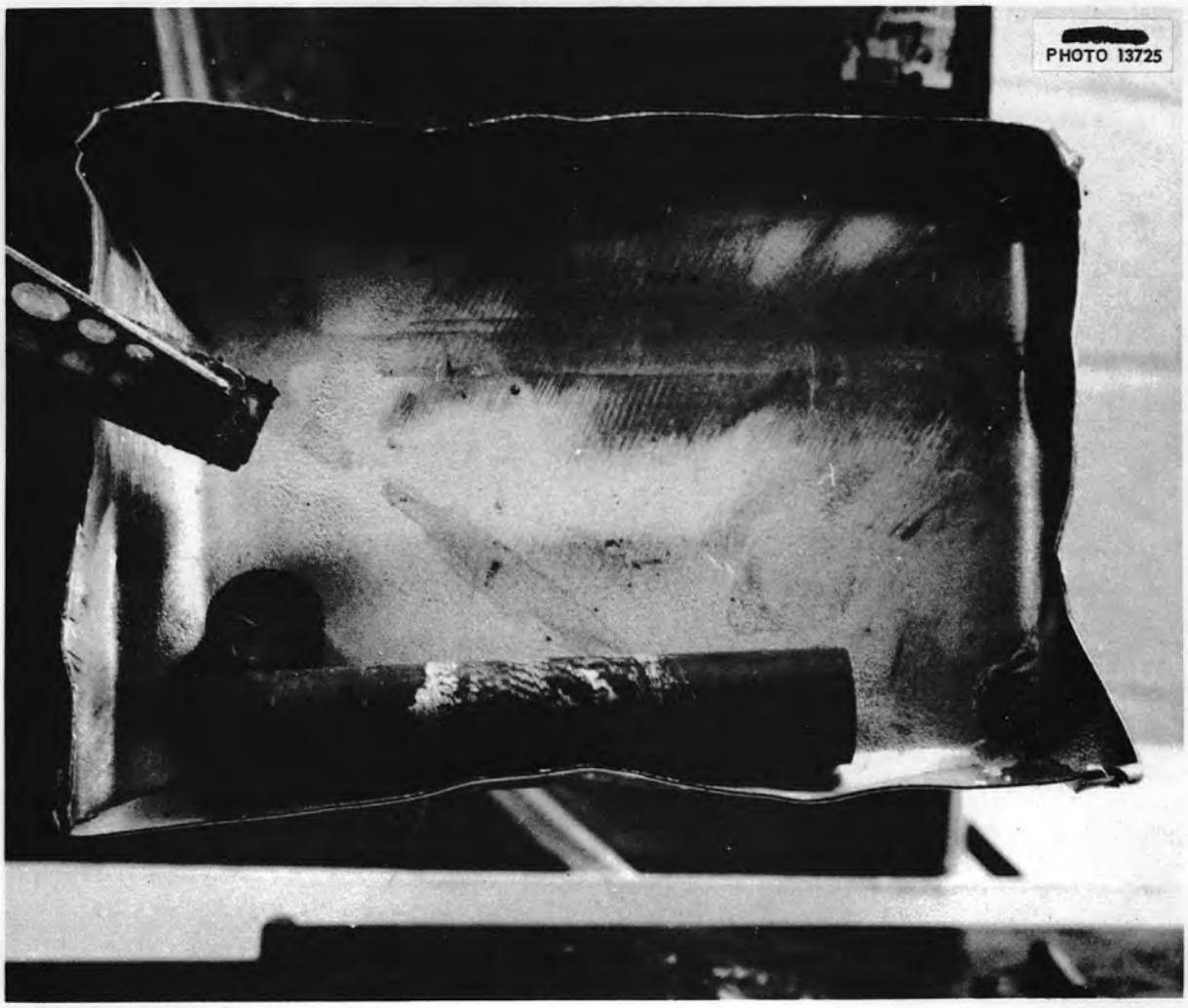

Fig. 118. Irradiated ThO_2 Rod, ¾-in. dia. Small piece broken from end.

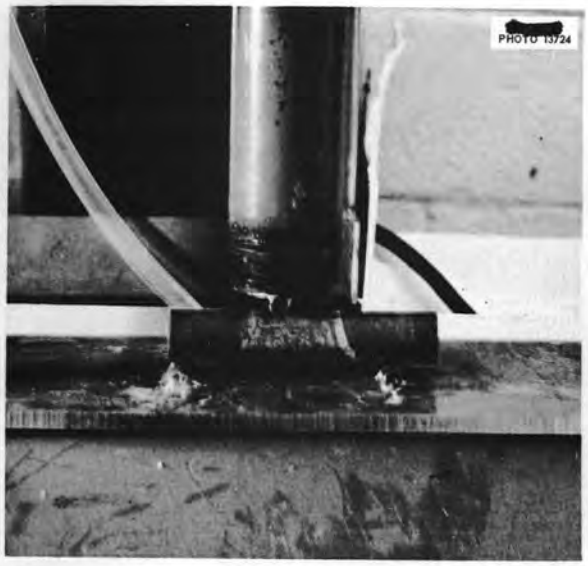

Fig. 119. Modulus of Rupture Test on ¾-in.-dia ThO_2 Rod.

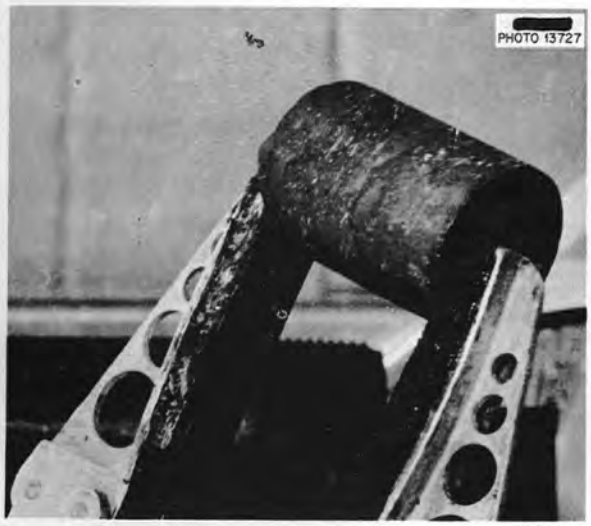

Fig. 120. Broken Piece of Irradiated ThO_2 Rod, 1.1-in. dia, with Surface Cracks.

SiC-Si FUEL ELEMENT

Work continues on the development of an SiC-Si fuel element. A major portion of the effort has been directed toward the development of a satisfactory fuel mix; this was divided into two categories, one in which USi_2 is used as the fuel and the other in which UO_2 is used as the fuel.

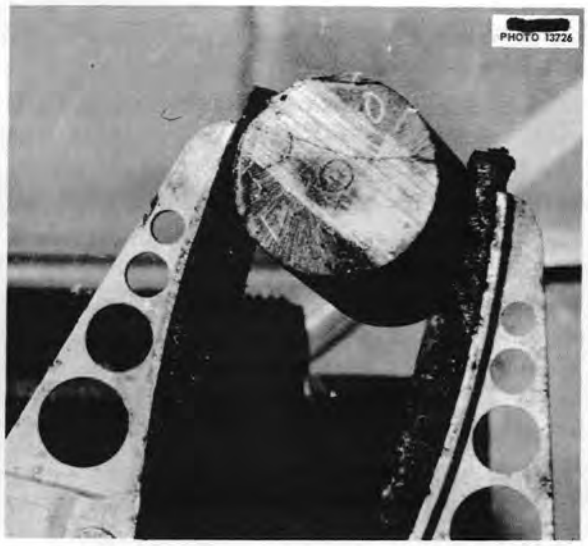

Fig. 121. Irradiated ThO_2 Rod, 1.1-in. dia, with Internal Cracks.

Fuel Mixes Containing USi_2. – First attempts to use USi_2 as fuel in the sandwich-type element met with failure. When incorporated in the sugar-graphite body, the silicide was oxidized by volatiles from the binder during the bakeout operation; and the subsequent volume change transformed the piece into a powdery mass. The oxidation characteristics of the silicide, as shown in Fig. 122 (differential thermal analysis and weight gain curves), necessitated the use of an oxygen-free binder in the body raw materials.

Nitron ($C_{20}H_{16}N_4$) pitch and petroleum pitch were used successfully as binders. With regard to the bakeout operation, the latter was selected as a working material because of its availability and much lower cost. Preliminary experiments, however, showed that the pitch-graphite body was not comparable to the sugar-graphite body in green strength nor in structure of the finished Si-SiC piece.

Sandwiches made of the pitch-graphite body containing −325 mesh USi_2 failed during the siliconizing operation. It is believed that the fine-grained silicide contained in the porous carbon structure oxidized while being lowered into the melt, and the subsequent violent reaction of the fine oxide with the silicon caused the piece to disintegrate. Successively coarser fractions of USi_2 were introduced as fuel. All fractions

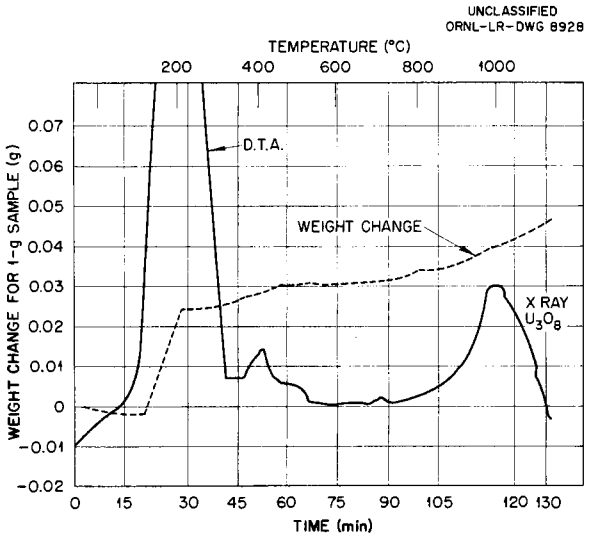

Fig. 122. Oxidation Characteristics of Uranium Disilicide as Obtained by Differential Thermal Analysis and Weight-Change Determinations.

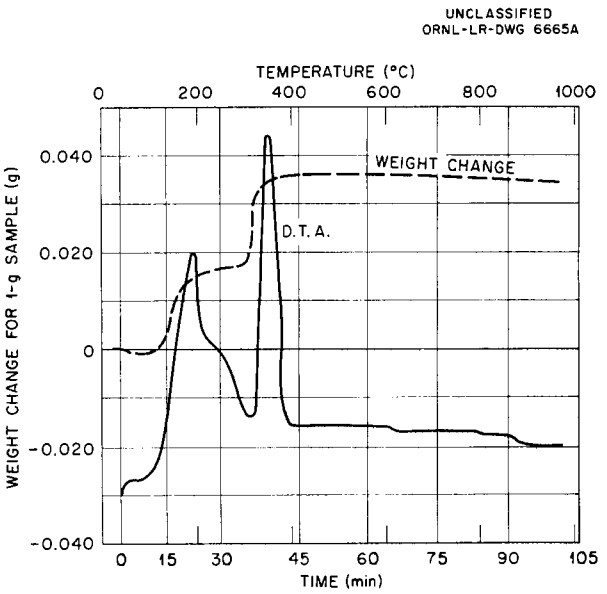

Fig. 123. Differential Thermal Analysis and Weight Change of Steam-Oxidized Uranium Chips.

below −200 mesh proved to be too fine to survive the siliconizing operation.

Sandwiches were completely impregnated without cracking or exploding when −140 +200 mesh USi_2 was used as fuel. Some of the globules of excess silicon were radioactive. These sweated out of the piece after impregnation and cooling, which indicated that part of the fuel was being brought to the surface of the piece. These results emphasized the necessity for having a fuel which would not become molten during the siliconizing operation and migrate to the surface. Efforts were then concentrated on using UO_2 as the fuel and retaining it as UO_2 throughout the process.

Fuel Mixes Containing UO_2. – Experiments were conducted with two different grades of UO_2: (1) UO_2 made by steam oxidation of uranium chips and (2) Norton's fused UO_2 which had been crushed, sintered, and reground to size.

Since prevention of oxidation to U_3O_8 was of vital importance during fabrication and impregnation, differential thermal analysis and weight-gain experiments were run in air to determine the oxidation characteristics of both materials. On comparing Figs. 123 and 124, it is seen that the steam-oxidized material reacts with oxygen more rapidly and at a lower temperature than does the fused grade; however, it was still considered worth while to run experiments with the steam-oxidized UO_2 since this material would be available in the enriched state.

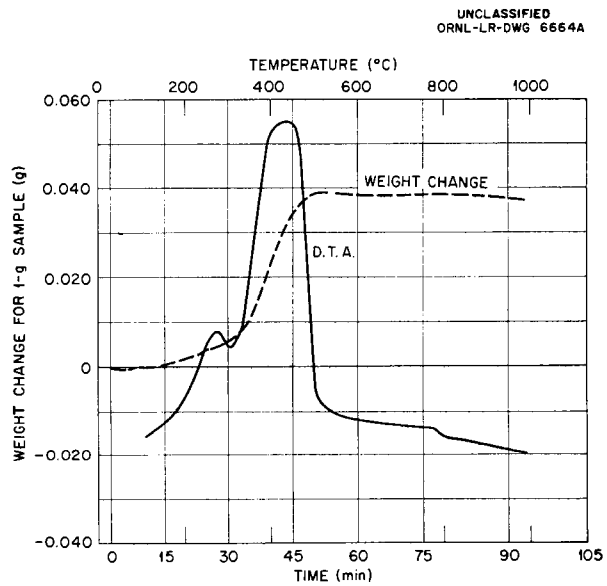

Fig. 124. Differential Thermal Analysis and Weight Change of Norton's Fused UO_2.

When −325 mesh material of both grades was used with the sugar-graphite body, the UO_2 reacted with the silicon; and the piece disrupted during impregnation.

It was believed that the stresses set up, due to differential shrinkage between the shell and the core containing the fuel mix, might be a factor in the exploding and splitting phenomena; hence, comparative studies were made of the two as separate bodies in order to determine their shrinkage characteristics; and adjustments were made accordingly. It was found that the shell material shrank about 5% more than the core material, and a sandwich of the two was sufficiently stressed to cause considerable warpage. Shrinkages were adjusted by adding charcoal to the shell material in order to reduce shrinkage or by increasing the sugar content in order to increase shrinkage. The latter was more satisfactory with regard to impregnation characteristics. Such adjustment prevented warpage of the sandwich, but the explosion phenomenon during the siliconizing process was not alleviated.

A study was then made of the reaction characteristics of the fuel mix as a separate body. The temperature required to start the reaction between the silicon and the fuel mix was higher than that for the straight body, and only a skin reaction resulted. The fuel mix apparently requires a temperature boost to begin and to sustain the reaction. In order to observe the role of the shell material as a booster, open-edged sandwiches, which exposed the fuel material, were siliconized. It was observed that the shell material did provide the temperature boost necessary for the reaction of the core material and that the reaction of the core material, once started and sustained, proceeded violently so as to disintegrate the piece.

The next approach was to prevent or to reduce the reaction between the UO_2 and silicon by increasing the grain size of the UO_2. Fractions of material (up to $-20 +50$ mesh) were introduced as fuel. The steam-oxidized material, being platy and very thin, reacted explosively regardless of grain size. A considerable improvement was noted with the coarser grained fused UO_2, however. Cracking of the sandwich was observed during cooling; but the extent of impregnation was increased, and the reaction was not explosive.

Figure 125 is a polished section illustrating the behavior of a large grain of UO_2 in the siliconizing operation. A reaction area around the grain is noted, but, for the most part, the grain is intact. The UO_2 grain cracked, apparently on cooling, since the cracks are void of silicon. Also,

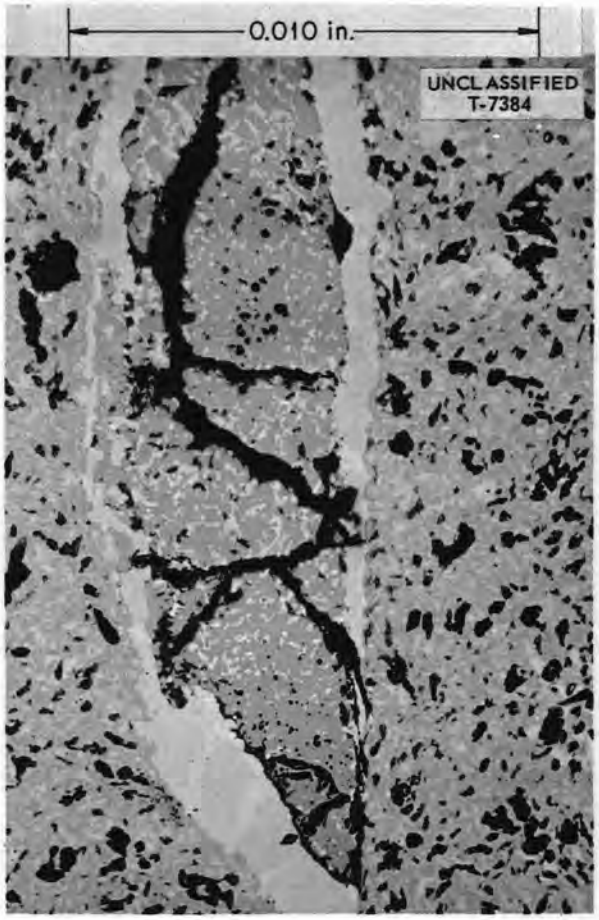

Fig. 125. A 20-mesh UO_2 Particle in Si–SiC. 250X.

metallic flecks appear throughout the grain; these phenomena are possibly due to the grain being an agglomerate with some porosity. Experiments are under way in which single-crystal UO_2 is used as fuel.

The large grain resulted in poor distribution of the fuel, good mixing being difficult to attain because of the large differences in particle size and densities of the raw materials. Another approach along similar lines is now in progress.

Previous results show that the silicon will react only superficially with a dense particle of carbon or graphite. Thus, if fine-grained UO_2, desirable for good fuel distribution, is encased in a hard shell of carbon before introduction into the piece, reaction of the UO_2 with the silicon should be prevented. Preliminary experimentation, concerning this idea, shows promise. The specimens

which were tried have cracked, but distribution of fuel is greatly improved; and the reaction of the UO_2 is apparently prevented since the usual evidence of silicide formation is not noted.

Other Approaches to Fuel Element Development. – Attempts were made to produce an Si-SiC body by refabricating a crushed bulk body that was made in the usual manner. Specimens made of the Si-SiC material were hot-pressed, or cold-pressed and sintered. In both cases a porous beta-SiC structure resulted, the silicon apparently having melted and leaked out of the structure. The addition of excess silicon before sintering produced similar results, and this approach was abandoned.

Another impregnation technique was developed. The specimen is placed on a graphite or carbon block with a graphite box containing a measured amount of silicon resting on top. When the assembly is heated, the silicon melts and reacts with the porous carbon piece below to form Si-SiC. Plans are under way to try this technique, which has the following advantages: (1) the operation can be carried out in an inert atmosphere, and, thus, oxidation of the graphite and fuel is prevented; (2) the use of a measured amount of silicon might prevent or certainly reduce the amount of silicon sweating from the piece on cooling.

Figure 126 shows a furnace that has been designed for this work. The assembly will be pushed into the heating zone of the furnace, and the furnace will then be closed and evacuated. A clean inert gas will be introduced, and the system brought up to temperature. The assembly will be withdrawn immediately after reaction takes place, and the operation repeated with a new assembly.

RARE-EARTH CERAMICS

Two rare-earth oxides, samarium oxide and gadolinium oxide, fabricated into ceramics and sintered at 1300 and 1500°C had the properties given in Table 16.

The 1300 and 1500°C Gd_2O_3 ceramics and the 1300°C Sm_2O_3 ceramics were stable in boiling water; the 1500°C Sm_2O_3 body disintegrated when boiled. The Sm_2O_3 and Gd_2O_3, each in equi-

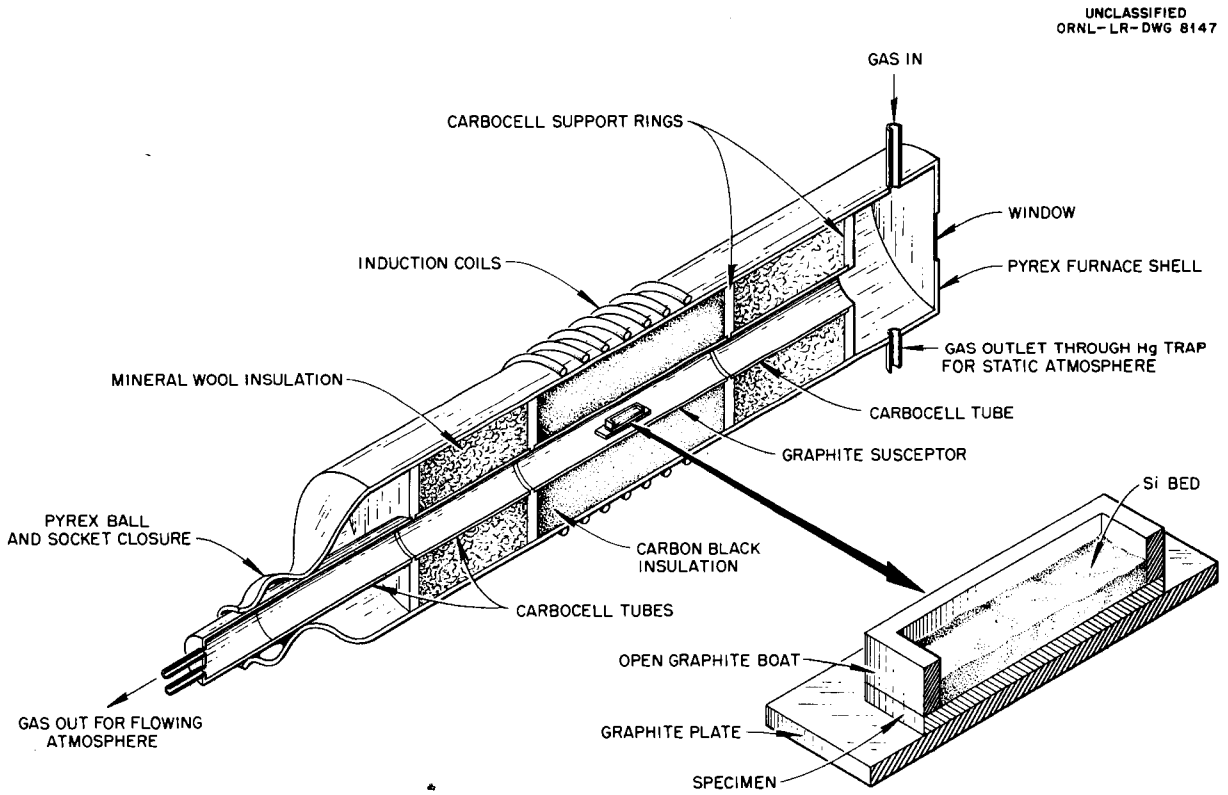

Fig. 126. "Dry Shooting" Furnace for Si–SiC.

TABLE 16. PROPERTIES OF Sm_2O_3 AND Gd_2O_3 CERMETS SINTERED AT TWO DIFFERENT TEMPERATURES

	Sm_2O_3		Gd_2O_3	
Sintering temperature, °C	1300	1500	1300	1500
Density (bulk), g/cc	6.0	7.4	6.97	7.6
Porosity (apparent), %	23.0	4.1	10.4	1.2
Modulus of rupture, psi	1800	2000	2740	2840
Modulus of elasticity, psi	4.4×10^6	26.5	14.5	18.0
Coefficient of linear thermal expansion, in./in./°C		9.9×10^{-6}		10.5
Melting point, °C	2350 ± 20		2350 ± 20	

molecular binary compositions with the following oxides, were fired at 1500°C and reacted as follows:

1. Both formed compounds with Al_2O_3, Fe_2O_3, SiO_2, and SrO; Sm_2O_3 with Al_2O_3 and Fe_2O_3, and Gd_2O_3 with the same two oxides apparently had the perovskite structure similar to barium titanate.
2. The Sm_2O_3 and Gd_2O_3 formed solid solutions with CaO, HfO_2, MgO, ThO_2, and ZrO_2.

X-ray diffraction studies at room temperature were made on the rare-earth oxides: CeO_2, Sm_2O_3, Eu_2O_3, Gd_2O_3, Dy_2O_3, Ho_2O_3, Er_2O_3, Tm_2O_3, Yb_2O_3, and, also, Y_2O_3. The CeO_2 was face-centered cubic with $a_0 = 5.395$; Sm_2O_3 consisted of a cubic and another undetermined phase. All the other rare earths were cubic and of the Tl_2O_3 type, with a_0 decreasing from 10.88 to 10.39 with increasing atomic number. The Y_2O_3 was also cubic, with $a_0 = 10.64$. X-ray diffraction patterns of these oxides after calcination at 1400°C are being obtained.

Sm_2O_3-Gd_2O_3 CERAMIC CONTROL RODS

Control-rod specimens consisting of a mixture of Sm_2O_3 and Gd_2O_3 (see Fig. 127) were made for measurements of their value as reactor poisons. An analysis of the rare-earth mixture is given below:

Sm_2O_3	63.8%
Gd_2O_3	26.3%
Dy_2O_3	4.8%
Nd_2O_3	0.9%
Y_2O_3 and other rare earths	4.2%

These specimens were evaluated in the Critical Experiment Facility, and the data obtained will be reported by that group.

The specimens were made in two forms: rods, and cylinders having holes large enough to accommodate the rods. Precalcined powders were dry-pressed in steel dies at approximately 1000 psi. The mixture when fired to 1400°C sintered to a density of 6.94, making strong ceramic-oxide specimens. These were ground to size: 0.450 ± 0.001 in. OD × 0.750 in. long and 0.790 ± 0.001 in. OD × 0.510 ± 0.001 in. ID × various lengths. Smaller specimens are to be sent to the MTR for radiation-damage tests.

GRAPHITE-HYDROGEN REACTION AND EROSION INVESTIGATION

For some ANP rocket concepts it is proposed to use hydrogen as a propellant which passes through a graphite-UO_2 core at high velocity. Because it was reported that hydrogen reacted seriously with graphite, attempts were made to coat graphite with ZrC. All methods tried so far have resulted in unsatisfactory coatings. An investigation is under way to determine the reaction of graphite with hydrogen at 2300°C.

A static-gas test has been developed wherein a plate of graphite is heated in hydrogen to 2300°C. Little, if any, reaction was noted when the graphite was exposed at 1800°C for 2 min and at 2300°C for 30 sec. Gas analyses are being made of the hydrogen which surrounded the specimen.

HAFNIUM CARBIDE INVESTIGATIONS

Because of a continuing interest in hafnium carbide, a further study of this material has been started. Hafnium carbide is of interest principally because of its hardness and high melting point and secondarily because of its high cross section for neutron absorption.

The method chosen for the synthesis of hafnium carbide was as follows: Hafnium oxide and very fine, pure graphite (1.75 times the amount of carbon

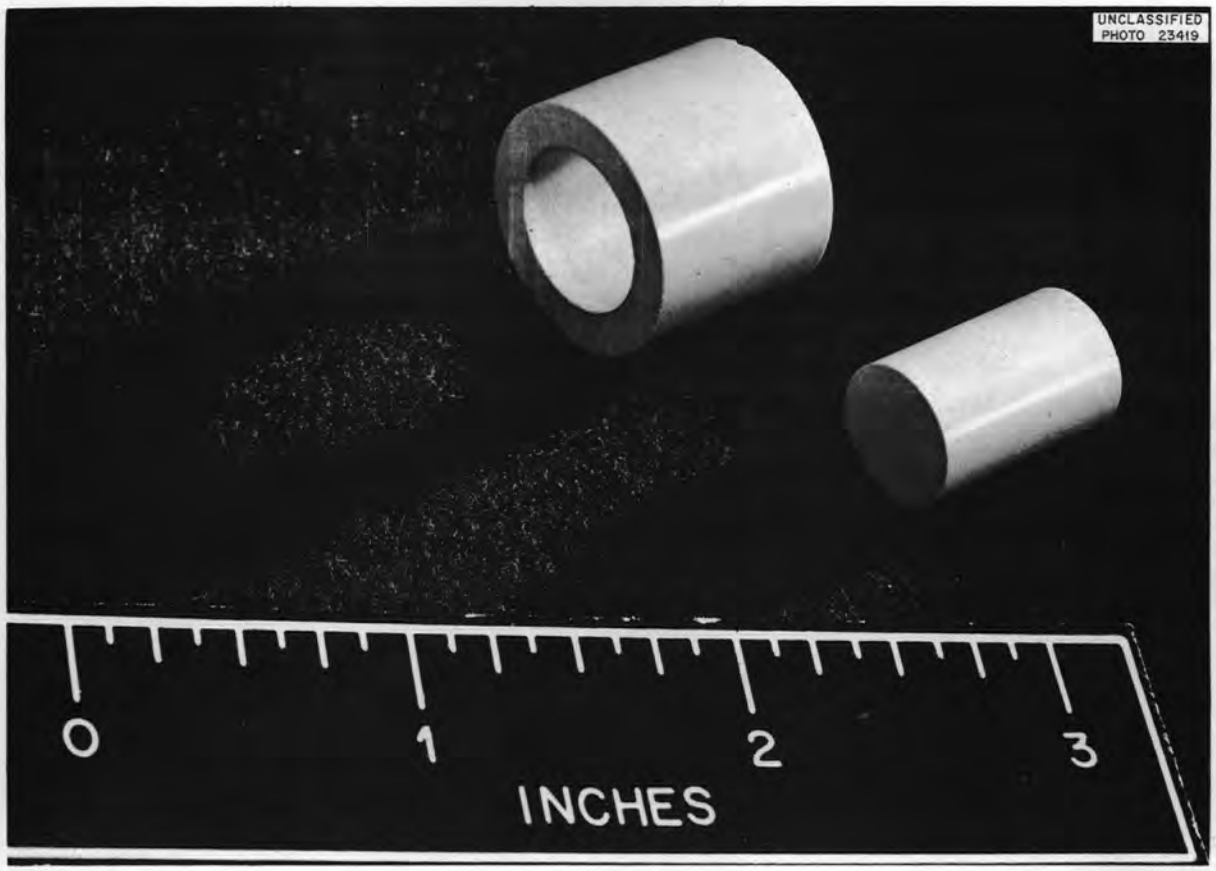

Fig. 127. Ceramic Specimens Consisting of a Mixture of Sm_2O_3 and Gd_2O_3 for Reactor-Poison Evaluation.

required for the reaction $HfO_2 + 2C \longrightarrow HfC + CO_2$) were mixed with 2 wt % of Cere-Amic flour binder. This mixture was dampened slightly, pressed into small bars, and then dried. These bars were fused in a tungsten arc into a metallic-appearing mass, which was very hard and quite brittle.

X-ray examination of this fused product showed that it was predominantly hafnium carbide with very minor amounts of free carbon. A carbon analysis gave 8.3% total carbon, which is just 2% above the theoretical 6.3% carbon of hafnium carbide.

Since any practical utilization of hafnium carbide will require that the fused bars be reduced to a fine powder in an iron ball mill with subsequent leaching with HCl to remove the iron, the solubility of the carbide in 1:10 dilute HCl was determined. This was found to be of the order of 0.25%, or very nearly insoluble.

Hardness measurements were made on the as-fused material. The specimen was polished with diamond-paste abrasive, and microhardness was obtained with a Bergsman Micro-Hardness Tester using a Vickers indenter with a 100-g load. There were much larger crystals of hafnium carbide present in this material than there were in the samples which were used for previously reported hardness values. There was no difficulty in finding a satisfactory field to make the indentations. Because of the size of the crystals and the heavier load used, the data obtained with the present sample are considered to be much more accurate than the earlier values. The values ranged from 1939 to 2305; therefore, the hardness is of the same order as that of boron carbide.

A photomicrograph of the hafnium carbide, Fig. 128, which shows several Vickers indentations, is included in this report. The dark

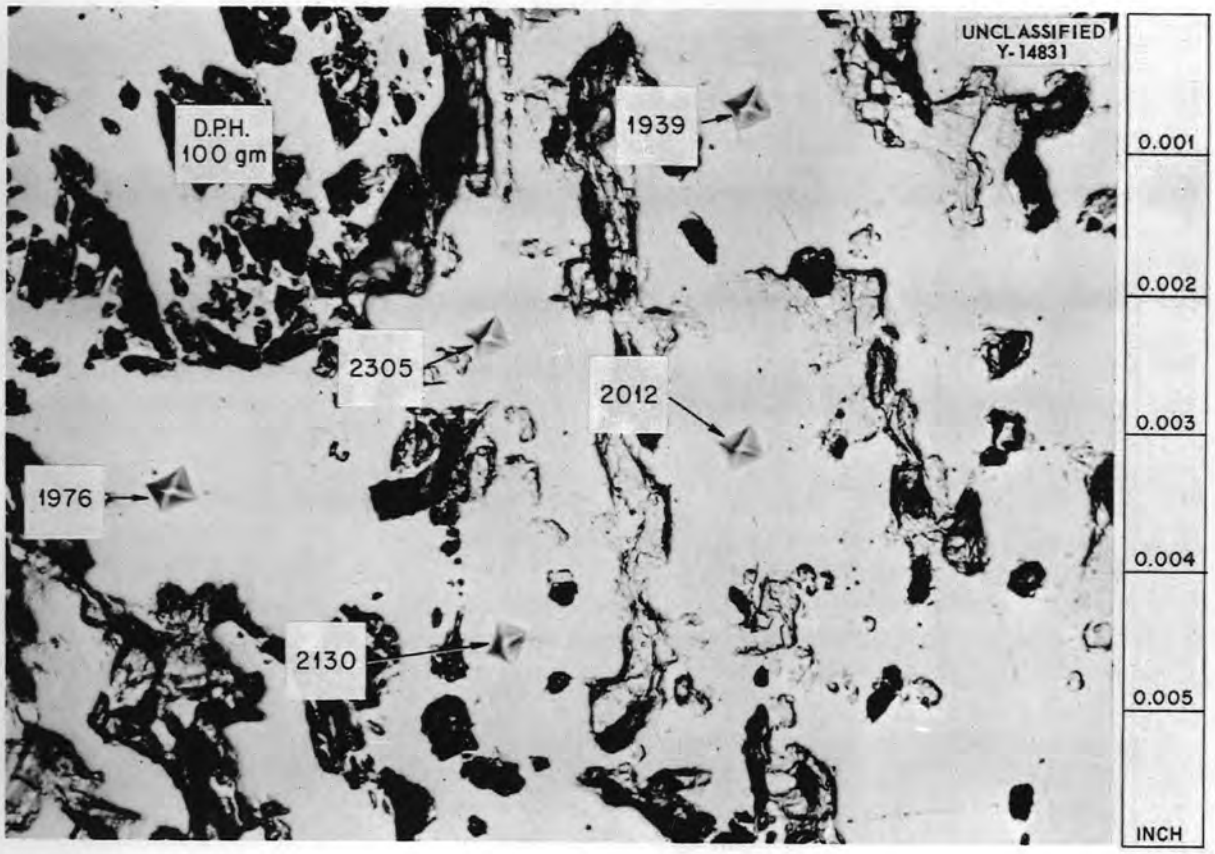

Fig. 128. Hafnium Carbide with Vickers Indentations.

areas are voids or graphite particles, and the light-colored material is the hafnium carbide.

SPECIFIC HEAT MEASUREMENTS

Enthalpy determinations, from three different temperatures to 0°C, were made on gadolinium and samarium oxides in the ice calorimeter. Specific heats or thermal capacities were derived from these data and are given in Table 17.

Similar data on UO_2 sealed in fused silica are being obtained in the same manner.

TABLE 17. SPECIFIC HEATS OF Sm_2O_3 AND Gd_2O_3 FOR THREE DIFFERENT TEMPERATURE RANGES

Material	Temperature (°C)	Enthalpy (cal/g)	Average Specific Heat (cal/g·°C)
Gd_2O_3	400–0	70.45	0.176
	700–0	136.94	0.196
	1000–0	206.14	0.206
Sm_2O_3	400–0	71.62	0.179
	700–0	137.99	0.197
	1000–0	204.66	0.205

HIGH-TEMPERATURE X-RAY STUDIES

A high-temperature attachment for use on an x-ray spectrometer was put into operation. The apparatus shown in Figs. 129 and 130 was designed in such a manner that it could be mounted and dismounted with ease. It consists of a water-cooled, aluminum cylinder with a vacuum-tight lid which fits the open end of the cylinder and a projecting rod (by which the attachment is fitted into the goniometer) on the closed end. The sample holder, tantalum heating element and reflector, aperture for pumping a vacuum, and thermocouple leads are all mounted on the lid.

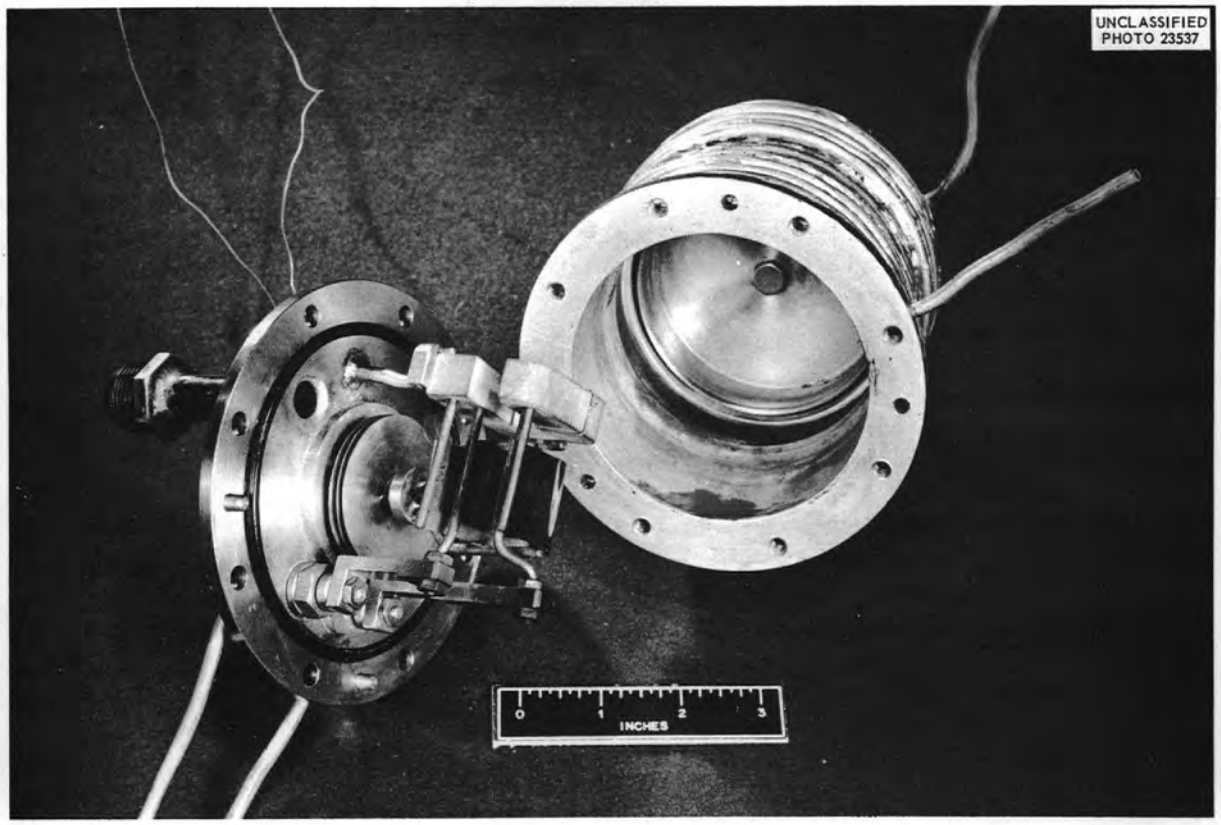

Fig. 129. A High-Temperature Attachment for Use on an X-Ray Spectrometer.

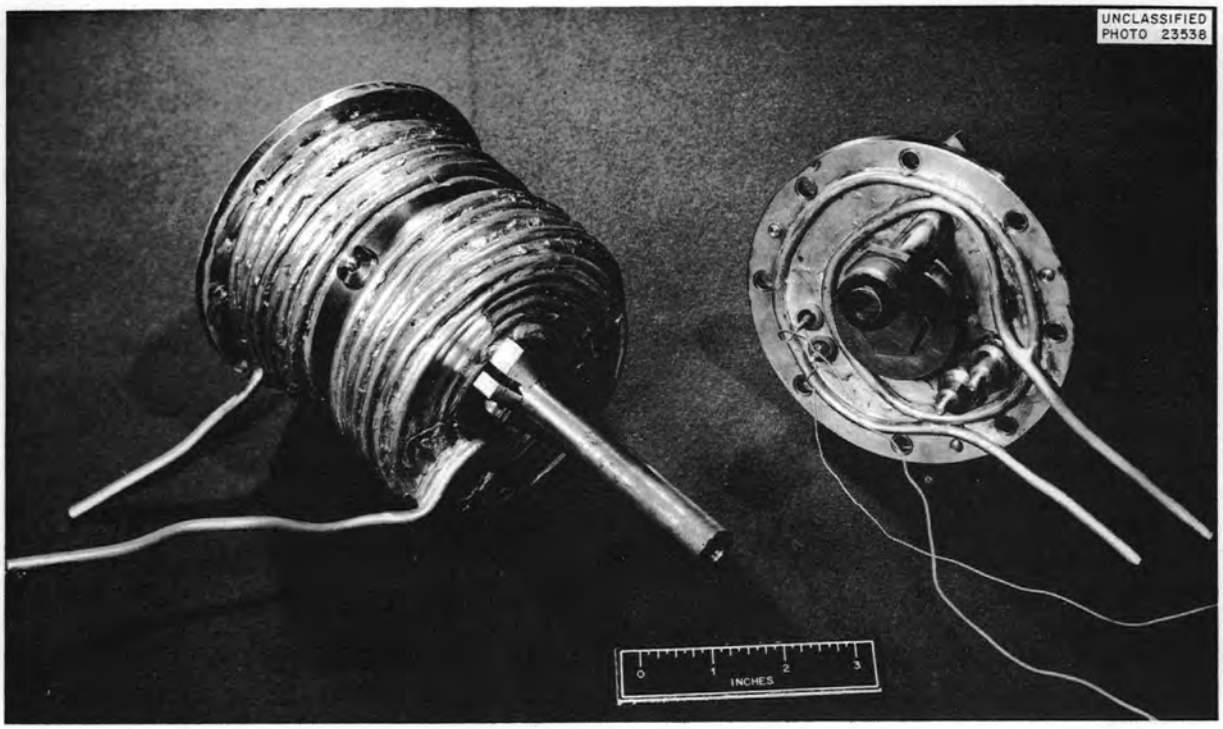

Fig. 130. Another View of the Same Apparatus Shown in Fig. 129.

Around the center of the cylinder is a beryllium window through which the x rays pass. When assembled, the attachment can be pumped down to a vacuum of less than 1 μ by means of a Welch pump and a small diffusion pump.

Initially the attachment was aligned by using a ThO_2 sample. The bracket which holds the sample can be rotated or shifted vertically or horizontally. It is held in position by three radial setscrews. By manipulating these setscrews, the ThO_2 sample was put in a position where one of its stronger x-ray peaks was at the proper angle and had maximum intensity. Thus far, the alignment has remained true even though about 20 samples have been x-rayed.

The thermocouple accuracy was determined by checking the inversion temperature of K_2SO_4. The temperature measurement is accurate within ±5°C.

A sample of Sm_2O_3 was run on the attachment to determine its inversion temperature. X-ray patterns up to 1050°C showed no inversion. The temperature was not raised above 1050°C, because a Chromel-Alumel thermocouple was being used.

A sample of Na_2ZrF_6 has been x-rayed at temperatures up to 600°C. It has been determined by quenching that there are five polymorphs of this compound, and the approximate temperature ranges for the different forms have also been determined by quenching. High-temperature x-ray patterns of this compound are being run in an effort to determine the inversion temperature more accurately. To date, good high-temperature patterns have been gotten on two of the forms. Work is still in progress on this problem.

CERAMIC ASPECTS OF WASTE DISPOSAL

Work continues on developing a method for the safe and economical disposal of high-level radioactive wastes. The possibility of incorporating radioactive isotopes contained in Hope solution into a ceramic body is being investigated. The method studied involves mixing the liquid waste with clay, limestone, soda ash, or other material to form a gel or slurry which is subsequently dried and sintered to produce a mass in which the isotope may be fixed and from which the isotope cannot be leached. If feasible, the heat required in this process is to be obtained from radioactive decay; otherwise, some external heating technique will be considered.

The results of prior investigations in developing an economical low-firing ceramic body have been previously reported.

Fixation of Radioisotopes

Twelve new compositions containing various mixtures of Volunteer Portland Cement Co. shale, limestone, sodium carbonate, phosphate tailings, and fly ash were mixed with Hope solution, and dried portions of each were fired at 1550, 1650, and 1750°F. These were examined, and the best compositions were selected for further tests using Hope solution to which Sr^{90} had been added.

The compositions selected were as follows:

No. 5 – 250 ml of Hope solution, 26,000 counts/min/ml
30 g of Na_2CO_3
30 g of finely ground Chickamauga limestone
200 g of Volunteer Portland Cement Co. shale, – 16 mesh

No. 15 – same as No. 5 except 100-g shale

No. 16 – same as No. 5, with 150 g of shale

No. 9 – same as No. 5, with finely ground phosphate tailing substituted for the shale

These compositions have been dried and will be fired at 1550, 1650, and 1750°F as soon as the exhaust system is connected to the furnaces. After firing, leaching tests will be made to determine whether the fired ceramic bodies retain the Sr^{90}. If the Sr^{90} is retained, other radioisotopes will be tried.

Apparatus has been built and is in operation to determine whether Sr^{90} is released during firing.

Concrete for Retaining Hope Solution

Concrete blocks were obtained from the Volunteer Portland Cement Co. One composition contained limestone and the other quartz aggregate. Two-inch cubes were sawed from blocks of each composition. Six of each composition have been placed in Hope solution, and, for control, another set of each has been immersed in tap water. After soaking for 30 days, the cubes will be dried and sent to the Volunteer Portland Cement Co. for compressive strength tests. These tests should indicate whether concrete deteriorates in Hope solution.

Concrete cylinders each having a hole about 2 in. in diameter and 5 in. deep were also obtained from the Volunteer Portland Cement Co. The

holes in two of them were filled with Hope solution, and after 18 days there was no leakage. After 30 days the cylinders will be sectioned to determine solution penetration.

The holes in similar cylinders have been filled with Hope solution containing Sr^{90}. The cylinders have been placed in buckets of water, and, after 30 days, tests will be made to determine whether there has been migration of Sr^{90} and NO_3^- into the surrounding water. This test is designed to indicate whether radioisotopes from a Hope solution stored in concrete tanks will migrate into ground water.

Waste Disposal Heat Experiment No. 1

In order to determine the feasibility of self-fusion of fission-product waste in formulated clay-flux mixes, a series of heat experiments have been devised. The first experiment was designed to indicate the power generation required in such a mix in order to bring it to 900°C in a well-insulated vessel. The second experiment is to show the effects of boiling the mix in slurry form until it reaches dryness. Any fumes or volatile products emitted as the mix increases in temperature from 100 to 900°C will be sampled and analyzed.

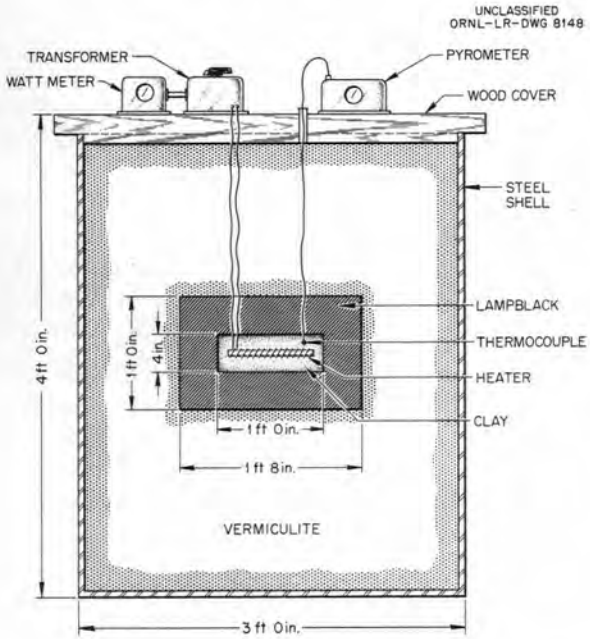

Fig. 131. Apparatus for Self-Fusion of Fission-Product–Clay Mixture.

The apparatus for the first experiment is shown in Figs. 131 and 132. The results are shown in Fig. 133. An electric heater generated 40, 60, and 80 w and brought the highest temperature of

Fig. 132. Another View of Self-Fusion Apparatus.

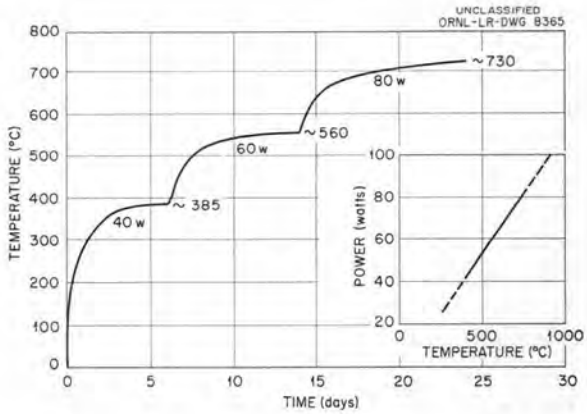

Fig. 133. Time-Temperature Plot for Self-Fusion Experiment No. 1.

the dry clay in the inner container up to 385, 560, and 730°C, respectively, at equilibrium. Because a power lead failed at the heater, the experiment could not be continued on to higher temperatures. However, the data indicate that approximately 100 w would have brought the temperature up to 900°C, and this wattage is approximately what is believed to be required. Under these conditions about 0.01 w/cc would be sufficient for self-fusion of a fission product–clay mix. Present experiments indicate that with this power generation stable mixtures may be feasible.

Viscosity Studies of Selected Clays for Use in Lining Waste-Disposal Pits

In one concept of liquid-waste disposal the use of pits or lagoons lined with a barrier material to prevent or inhibit migration of radioactivity into the ground has been proposed. Clays are of potential interest for this application; and in the studies being carried out at the Ceramic Laboratory, it seemed desirable to know something definite about their relative absolute viscosities and flow characteristics. The MacMichael Viscosimeter was designated for use in obtaining this information. This rotational-type viscometer was calibrated with graded solutions of sucrose in water to determine the instrumental constants for a series of component combinations (suspension wires, cup speed, depth of sample, and temperature) which are intended to cover a wide range of viscosities.

It was planned to measure the viscosity of several compositions in a range of suspension or solution concentrations. The materials under consideration were ball clay and bentonites, and the vehicles were distilled water, Hope carrier solution (acid), and simulated W-8 solution (alkaline).

At the present time partial consistency curves and "apparent" viscosities have been determined for Gleason ball clay, Wyoming bentonite, and Panther Creek bentonite at a concentration of 10 g of solids in 100 cc of vehicle. The Gleason clay has been studied also at concentrations of 20 and 30 g/100 cc.

These consistency curves show that the Hope solution increases the viscosity of Panther Creek bentonite, whereas W-8 solution decreases it. Both solutions lower the viscosity of the Wyoming bentonite very considerably, the W-8 even more effectively than the Hope. The viscosity of the Gleason ball clay is increased quite appreciably by both solutions. The mixtures of 10, 25, and 30 g of Gleason ball clay in 100 cc of distilled water show a consistent increase in apparent viscosity with increasing clay content.

Procedure. – Weighed portions of the clays were mixed with the vehicle in a Hamilton Beach mixer for 15 min and then were allowed to stand for 24 hr in order to reach thermal equilibrium and allow dissipation of air bubbles. Batches of 300 cc were made up so that there would be enough to obtain efficient mixing and to fill the viscometer cup. Just before the sample was placed in the cup, the suspension was gently but thoroughly stirred with a glass rod and rubber policeman.

With the spindle in place and the cup filled to the 4-cm immersion mark with the suspension, the motor was turned on to the lowest speed, 14 to 16 rpm. As soon as the dial deflection reading was noted, the motor speed was increased to 26 rpm; and the deflection was noted again. The same procedure was used at 34 and 43 rpm. Then the same increments were used in descending order. This series of deflection readings plotted against the rpm produced the consistency curves shown in Figs. 134–137. Except where indicated, the disk spindle was used. The cylinder spindle and smaller cup were used when the apparent viscosity was so great as to exceed the safe limit for the No. 26 wire. This wire covered the greatest range of materials under study, as well as the sucrose calibration solutions. The temperatures for the series of determinations varied within the range of 22 to 28°C.

Computations. – Calibration of the MacMichael Viscosimeter[3] consisted in determining the constant of the instrument, K, for the particular combination of wire, bob, and immersion distance at a given temperature:

$$K = \frac{\eta H N}{M^{\circ}} ,$$

where

K = the constant,
η = viscosity, centipoises,
H = depth of submergence of the plunger, cm,
N = revolutions of the cup, rpm,
M° = deflection, MacMichael degrees.

[3] *Instructions for the MacMichael Viscosimeters.*

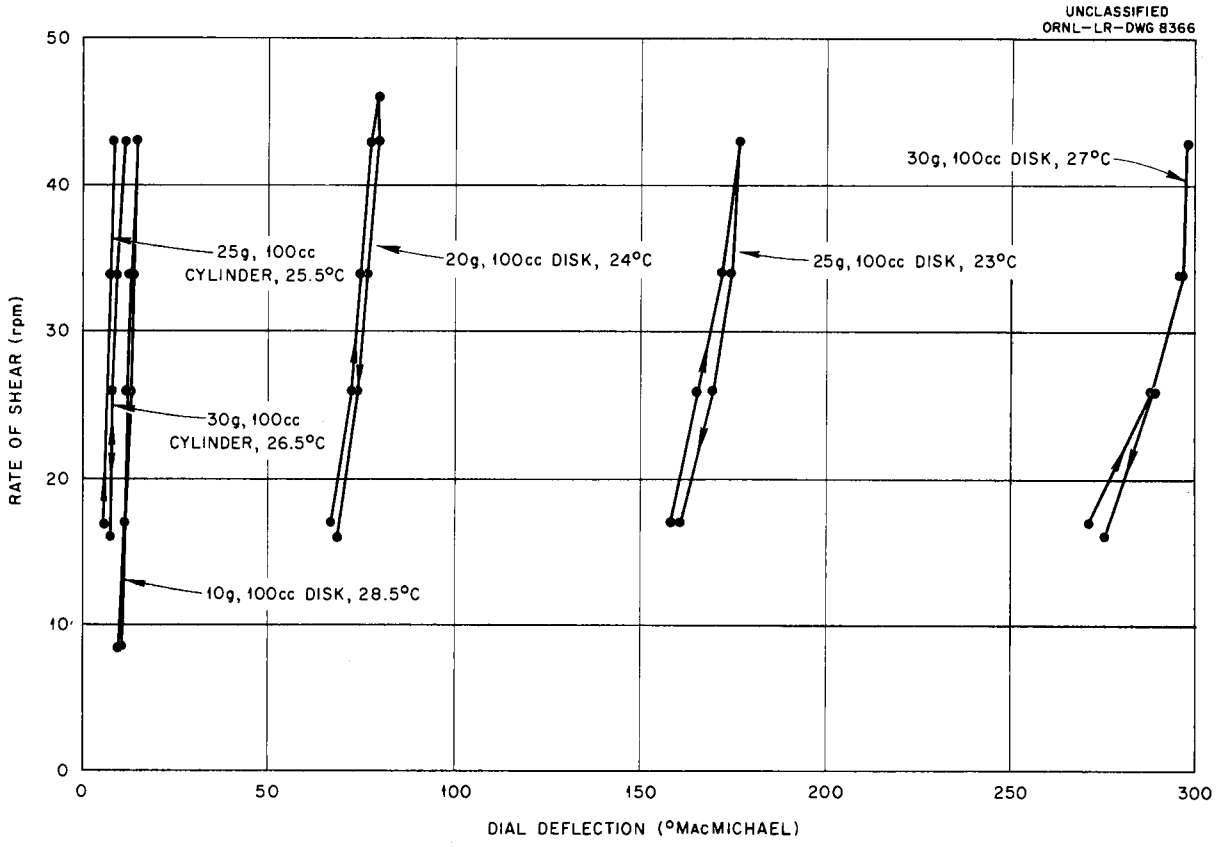

Fig. 134. Consistency Curves for Gleason Clay in Distilled Water.

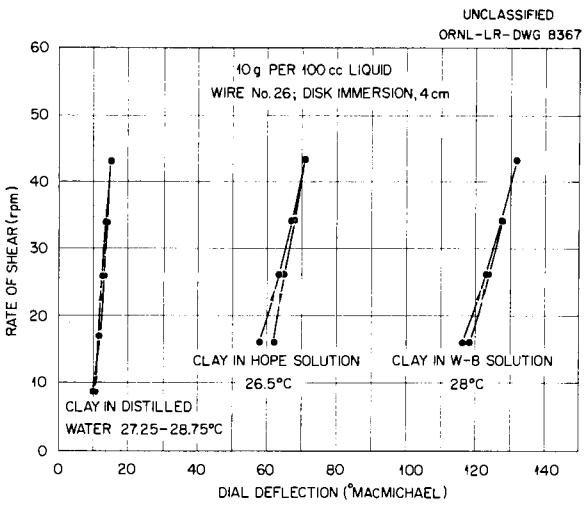

Fig. 135. Consistency Curves for Gleason Clay in Various Media.

After K was determined with the known solutions of sucrose, the unknowns were determined by the formula $\eta = KM^{\circ}/HN$.

The viscosities determined in this way for the clay and bentonites are shown in Table 18 and Fig. 138.

Discussion. – The viscosities of the clay and bentonite mixtures reported here are in reality "apparent" viscosities since the suspensions under study are not Newtonian liquids. They are not liquids whose rate of flow is proportional to the shearing stress; their consistency curves do not progress linearly from the ordinate. Apparent viscosity is an imaginary quantity applied to non-Newtonians.[4] This quantity is obtained experimentally by dividing the shearing stress by the rate of shear and multiplying by the instrumental constant.

[4]H. Green, *Industrial Rheology and Rheological Structures*, p 286, Wiley, New York, 1949.

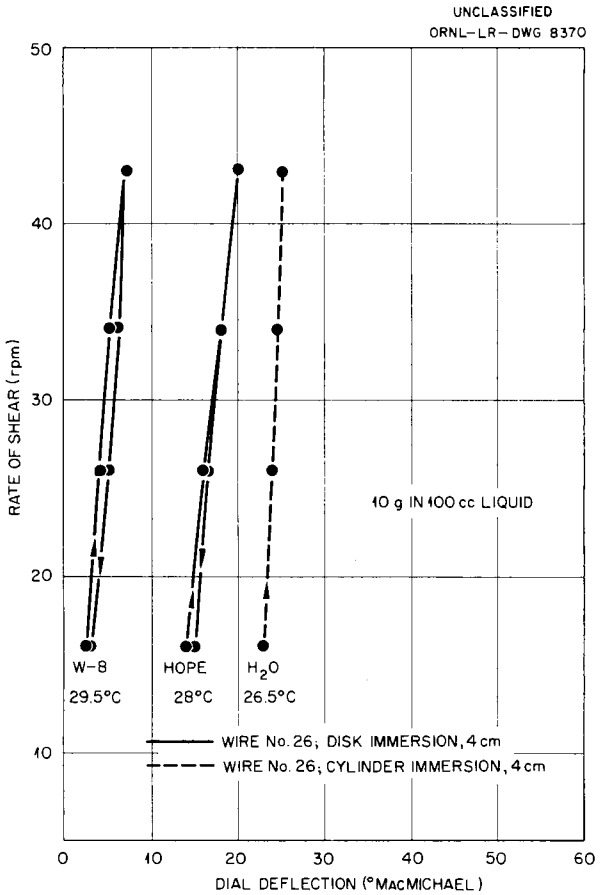

Fig. 136. Consistency Curve for Wyoming Bentonite in Various Media.

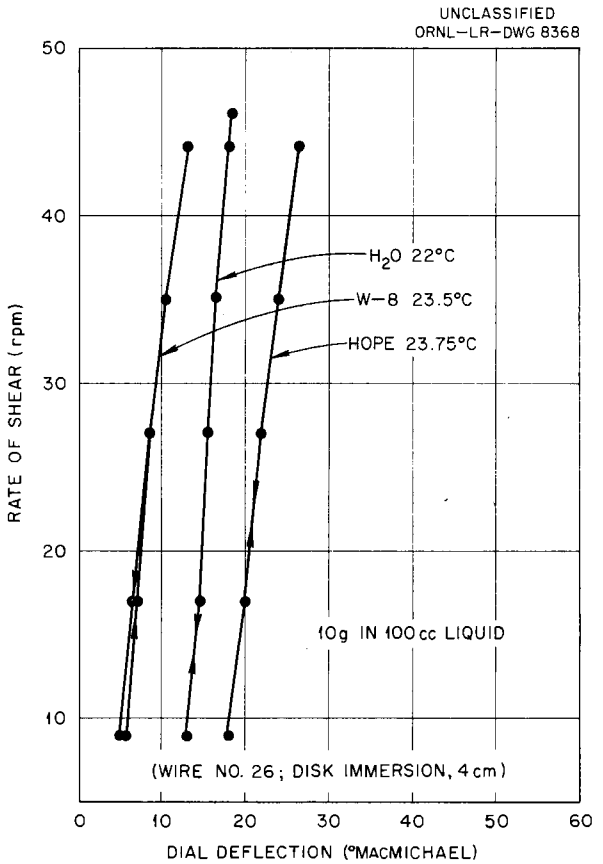

Fig. 137. Consistency Curve for Panther Creek Bentonite in Various Media.

TABLE 18. APPARENT VISCOSITIES OF CLAY AND BENTONITES IN THREE DIFFERENT MEDIA

Sample	Amount of Sample per 100 cc (g)	Apparent Viscosity (centipoises)		
		H_2O	Hope Solution	W-8 Solution
Panther Creek bentonite	10	8.12×10^2	2.36×10^4	2.80×10^2
Wyoming bentonite	10	$1.45 \times 10^{99*}$ (cylinder)	1.27×10^4	3.82×10
Wyoming bentonite	20		5.40×10^{11}	5.18×10^9
Gleason ball clay	10	5.38×10^2	2.16×10^8	1.40×10^{14} (disk) $4.07 \times 10^{26*}$ (cylinder)
Gleason ball clay	25	$3.45 \times 10^{18*}$ (disk) $4.94 \times 10^{32*}$ (cylinder)		
Gleason ball clay	30	$1.56 \times 10^{30*}$ (disk) $6.97 \times 10^{46*}$ (cylinder)		

*Extrapolated values of this order are extremely unreal and are included only to illustrate this fact.

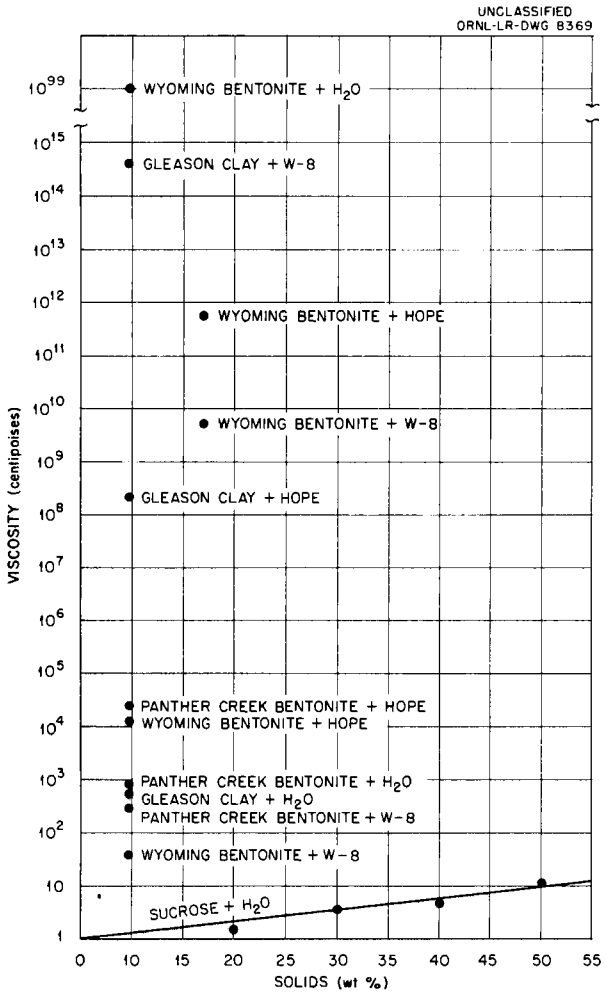

Fig. 138. Apparent Viscosities of Clay and Bentonites in Temperature Range 20–28°C.

If the MacMichael Viscosimeter employed in the above clay and bentonite determinations could obtain speeds of 100 rpm or more, the complete consistency curves which resulted would allow "plastic viscosity" and "yield values"[5] to be determined. However, the partial consistency curves obtained in this study indicate such properties as plastic flow, pseudoplastic flow, dilatant flow, and thixotrophy.[6] The Panther Creek suspensions show strong evidence of being dilatant.

Cylinder- and disk-bob determinations made on the same material do not seem to correlate in any fashion.

Conclusion. – The main objective of this study is to explore the relative effects that the waste-product solutions may have on the various materials being considered for use in the waste-disposal plan. These effects do show up in a comparison of the partial consistency curves obtained and the "apparent" viscosities derived from them. The continuation of these studies is contemplated wherein more concentrated suspensions of the bentonites and perhaps on other materials will be used.

[5] *Ibid.*, p 41.
[6] *Ibid.*, p 80.

METALLOGRAPHIC RESEARCH

R. J. Gray

R. S. Crouse T. M. Kegley
T. K. Roche E. L. Long
E. J. Manthos

TECHNIQUES FOR THE METALLOGRAPHY OF HIGH-PURITY ALUMINUM

T. K. Roche

Numerous specimens of high-purity aluminum have been submitted to the Metallography Section for examination. This work is being done as a part of the effort of the Fundamental Physico-Metallurgical Research Group in their study of the preferred orientation developed in extruded and recrystallized bars of this material.

Until recently the metallography of these specimens consisted entirely in microstructural examination of longitudinal and transverse sections of the bars in an attempt to determine such things as amount of deformed material, degree of recrystallization, and grain size of recrystallized material. Another technique is now being used in conjunction with general microstructural examination, whereby some idea of the preferred orientation developed in these bars is afforded by the use of etch pits.

Because of the softness of aluminum and, hence, its tendency to flow when abraded, the mechanical polishing of aluminum is difficult and time-consuming. A simpler approach to the metallographic preparation of aluminum is more desirable. Electrolytic methods are particularly adaptable to the high-purity material which is relatively free of impure inclusions; these inclusions are either removed or left in relief when this method of preparation is used. As stated previously, the preferred-orientation study deals with high-purity aluminum; therefore, electrolytic methods are being used exclusively for the final preparation of these specimens. Intermediate polishing steps, using rapid-cutting diamond abrasives, precede the final electrolytic preparation. Several electrolytes have been recommended for the electrolytic polishing of aluminum, but the most satisfactory one found to date consists of 15 parts ethyl alcohol to 1 part perchloric acid. When a stainless steel cathode is used and 35 v applied across the cell, polishing is completed in a matter of several minutes, and a mirrorlike surface is left that is free of disturbed material introduced during intermediate mechanical polishing.

Structure delineation of the material in question is not well defined by straight chemical etching following electrolytic polishing because of the many subgrains and deformation bands with low-angled orientation boundaries that are present in the recrystallized and deformed portions of the extruded bars. These low-angled boundaries are best brought out by anodizing the specimens electrolytically and by examination under polarized light. The anodic film is applied to the specimen with the use of an electrolyte (70% orthophosphoric acid, 26.5% ethylene glycol, 2.5% distilled water, and 1% hydrofluoric acid), a stainless steel cathode, and 35 v across the cell. Anodization is completed in approximately 2 min. Etching of higher-angled orientation boundaries in the specimens is concurrent with anodization and affords satisfactory examination under bright-field illumination. Deformed areas can be distinguished from recrystallized areas, a slight amount of detailed structure within each of these types of areas being evident. If a sensitive-tint plate is introduced into the optical system, the microstructure can be viewed in color, and the detailed structure will be more or less apparent, depending upon the optimum thickness of the anodized film.

The polishing and anodizing techniques outlined above have made it possible to determine whether a particular specimen is deformed, recrystallized, or partly recrystallized, but nothing is learned of the orientation developed. As an aid to the Fundamental Physico-Metallurgical Research Group in their x-ray determination of the preferred orientation developed in the aluminum bars, etch pits are being used to show the approximate relative orientations of deformed and recrystallized material. The pits are produced in transverse sections of the bars, after electrolytic polishing, by immersing the specimens in a solution of 80 parts hydrochloric acid, 25 parts nitric acid, 5 parts hydrofluoric acid, and 20 parts water. Pitting requires only a few

seconds at room temperature, but it will take slightly longer if the acid solution is cooled in an ice jacket. Pits produced in the shape of equilateral triangles indicate a near (111) orientation, and pits in the shape of squares indicate a near (100) orientation. Anodizing the specimens after pitting allows the microstructure to be examined under sensitive tint or the deformed and recrystallized areas with their characteristic pits to be observed under bright-field illumination. Etching of the high-angled orientation boundaries concurrent with anodization made this possible. No apparent damage is done to the etch pits in anodizing the specimens.

The following photomicrographs illustrate the techniques described above. Figure 139 shows a longitudinal section from a bar of aluminum extruded at a rate of 615 fpm at 450°F. This specimen has been electropolished, anodized, and photographed with polarized light. The structure is partially recrystallized. Figure 140 illustrates the use of etch pits as an aid in the determination of preferred orientation developed during extrusion. This specimen, electropolished, pitted, anodized, and photographed with bright-field illumination, is a transverse section from a bar extruded at a rate of 0.32 fpm at 850°F. The triangles indicate a near (111) orientation developed in the deformed material, and the squares indicate a near (100) orientation developed in the areas which recrystallized during extrusion. Figure 141 is the same field seen in Fig. 140 with the deformed portion of the specimen, that is, (111) orientation, shown in more detail. These deformation markings are brought out by the use of a sensitive-tint plate.

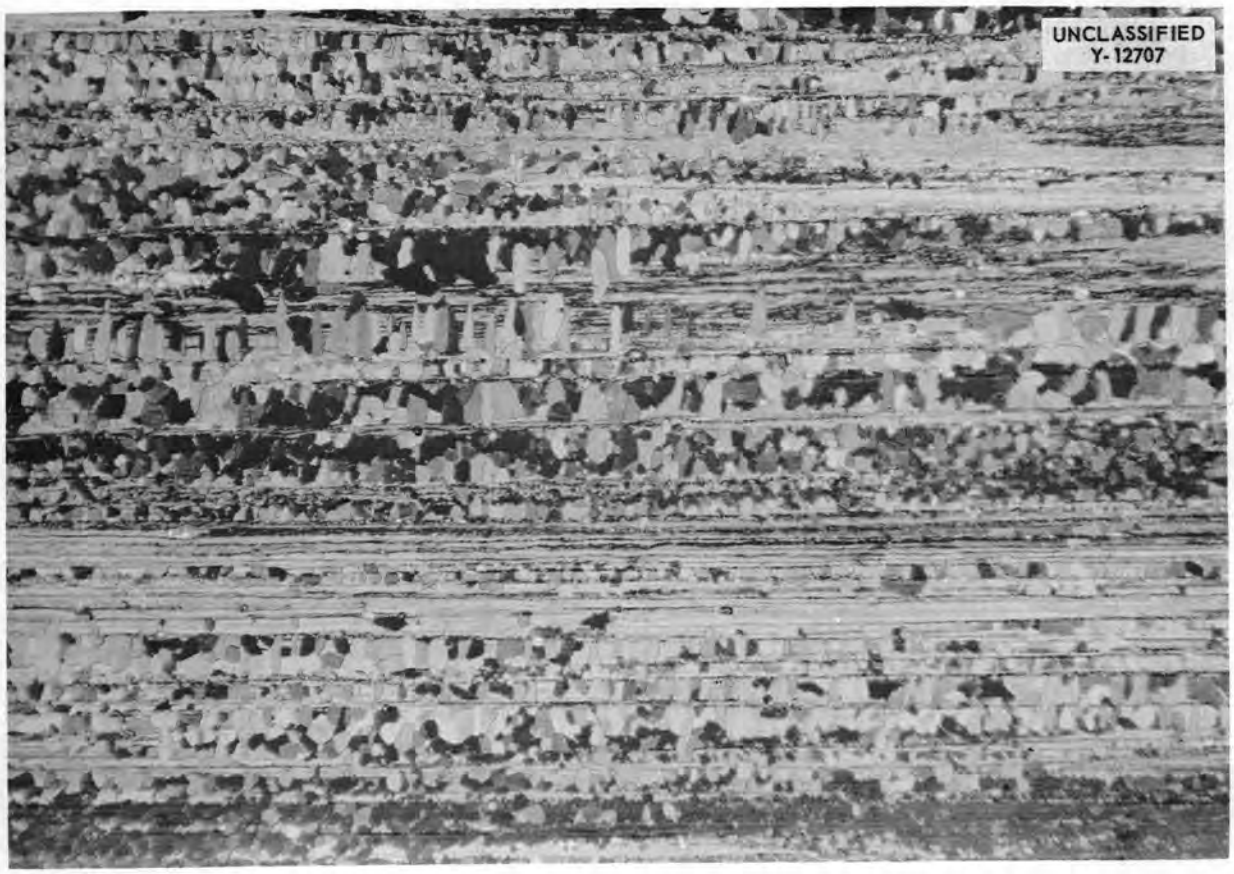

Fig. 139. Longitudinal Section from Aluminum Bar Extruded at 450° F and 615 fpm. Structure is partially recrystallized. Specimen was electropolished, anodized, and photographed with polarized light. 100X.

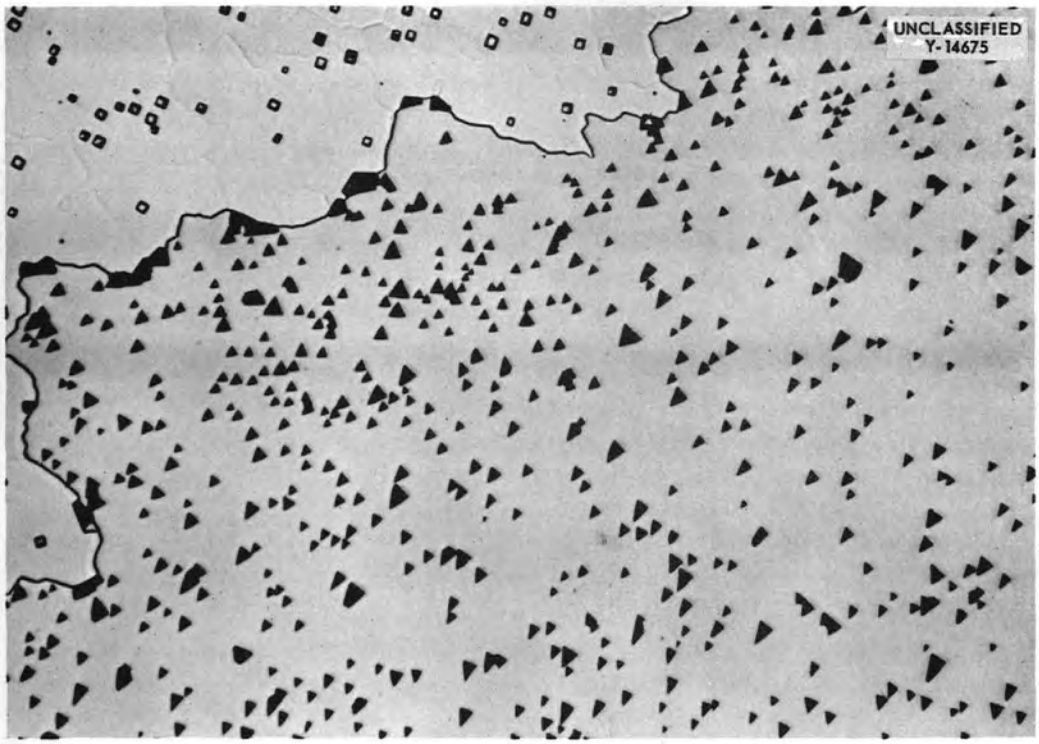

Fig. 140. Transverse Section from Aluminum Bar Extruded at 850° F and 0.32 fpm. Etch pits indicate orientation. Specimen was electropolished, pitted, anodized, and photographed with bright-field illumination. 500X. Reduced 13.5%.

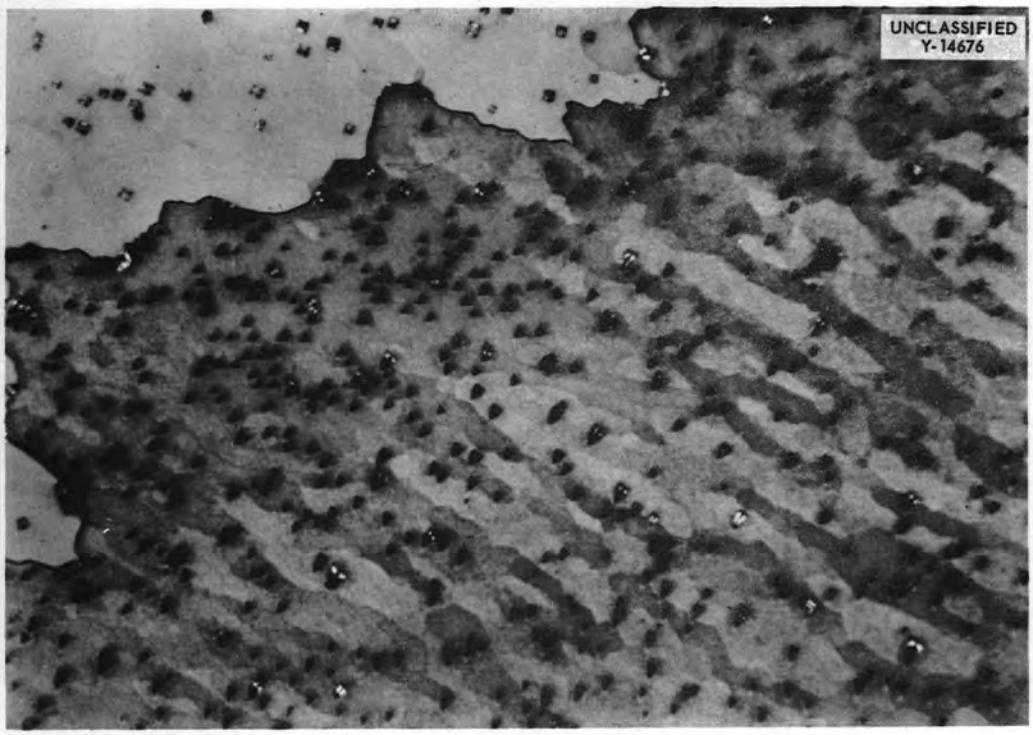

Fig. 141. Same Field as in Fig. 140 But a Sensitive-Tint Plate Was Used in Photographing. Detailed structure in deformed {111} area is brought out. 500X. Reduced 13.5%.

INCLUSIONS IN HIGH-PURITY AND COMMERCIAL-GRADE URANIUM-IRON ALLOYS[1]

R. J. Gray

An AEC cooperative metallography program for the study of uranium inclusions was started approximately one year ago to identify the inclusions present in the commercial-grade uranium, which would, in turn, help in obtaining a commercial-grade uranium of higher purity.

Argonne National Laboratory offered to provide alloys in which their high-purity uranium made by the electrodeposition of uranium crystals from a fused-salt electrolyte was used.

The metallography laboratory at ORNL has been investigating the inclusions present when iron is added. Preliminary castings were made from commercial-grade uranium to determine the desirable iron addition to the scarce high-purity uranium. Three alloys with 12.0, 2.93, and 0.4 wt % iron additions to the commercial-grade uranium were made and were examined metallographically.

The construction diagram for the uranium-iron system is shown in Fig. 142. In the alloys of

[1] A more complete report will appear in "Technical Papers of the Ninth Metallography Technical Information Service Conference."

UNCLASSIFIED
ORNL-LR-DWG 8974

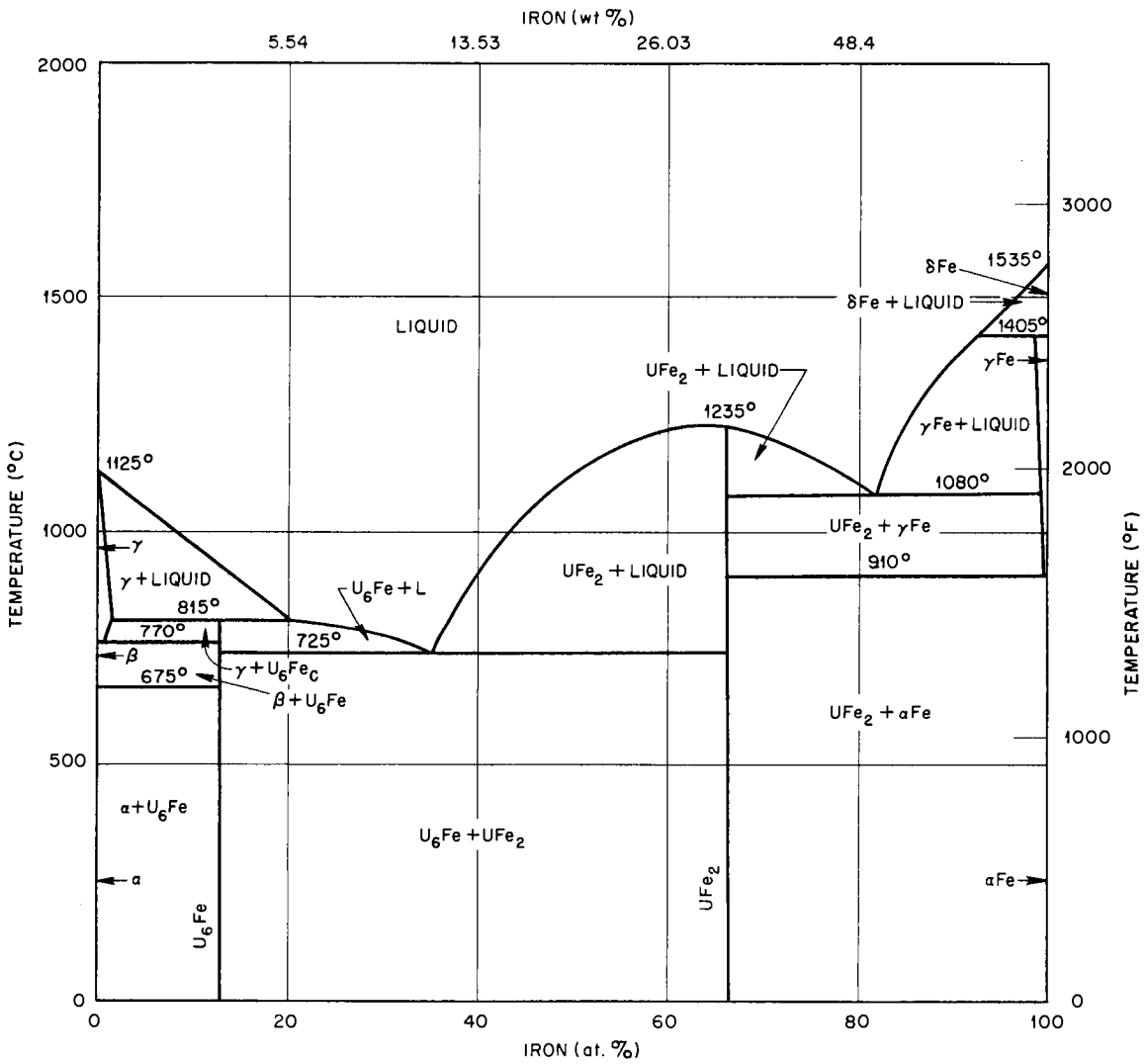

Fig. 142. The Constitution Diagram of the Uranium-Iron System. Reprinted from R. W. Bussard and H. E. Cleaves, "The Binary Alloys of Uranium," *J. Met. and Cer.*, TID-65 1, No. 1, pp 25–53 (1948).

interest there is a compound of U_6Fe which develops peritectically at 815°C. Literature data present a eutectoid somewhat below 1 at. % iron.[2] The microstructures of the alloys with the 2.93 and 0.4 wt % iron additions are shown in Figs. 143, 144, and 145. In Fig. 143 the harder phase, as shown by Vickers hardness impressions, is U_6Fe and the softer dendritic "islands" are $\alpha U + U_6Fe$ hypereutectoid composition. The cubical- and triangular-shaped inclusions are probably uranium carbides. The addition of 0.4 wt % iron to the commercial uranium, shown in Figs. 144 and 145, results in only a small amount of peritectically formed U_6Fe. The matrix is hypereutectoid alpha uranium and U_6Fe. The 1.01 wt % iron addition to high-purity uranium is shown unetched in Fig. 146 and after etching in Fig. 147. The continuous-phase U_6Fe and the matrix of hypereutectoid $\alpha U + U_6Fe$ are clearly defined.

The investigation of the iron additions to high-purity uranium will continue with the preparation of an alloy of approximately 0.06 wt % iron content.

[2] R. W. Bussard and H. E. Cleaves "The Binary Alloys of Uranium," *J. Met. and Cer.*, TID-65 1, No. 1, pp 25–53.

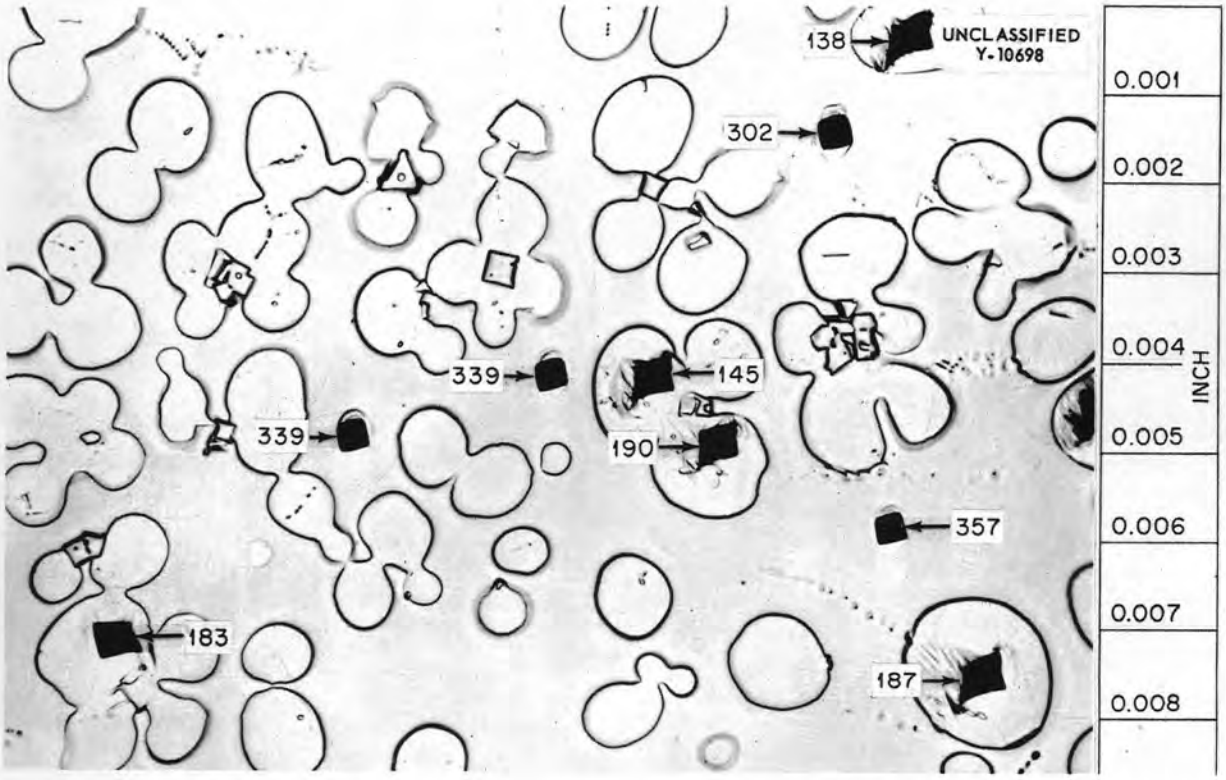

Fig. 143. Commercial Uranium–2.93 wt % Iron Alloy. Harder phase is U_6Fe. The islands are hypereutectoid $\alpha U + U_6Fe$. 500X. Reduced 7%.

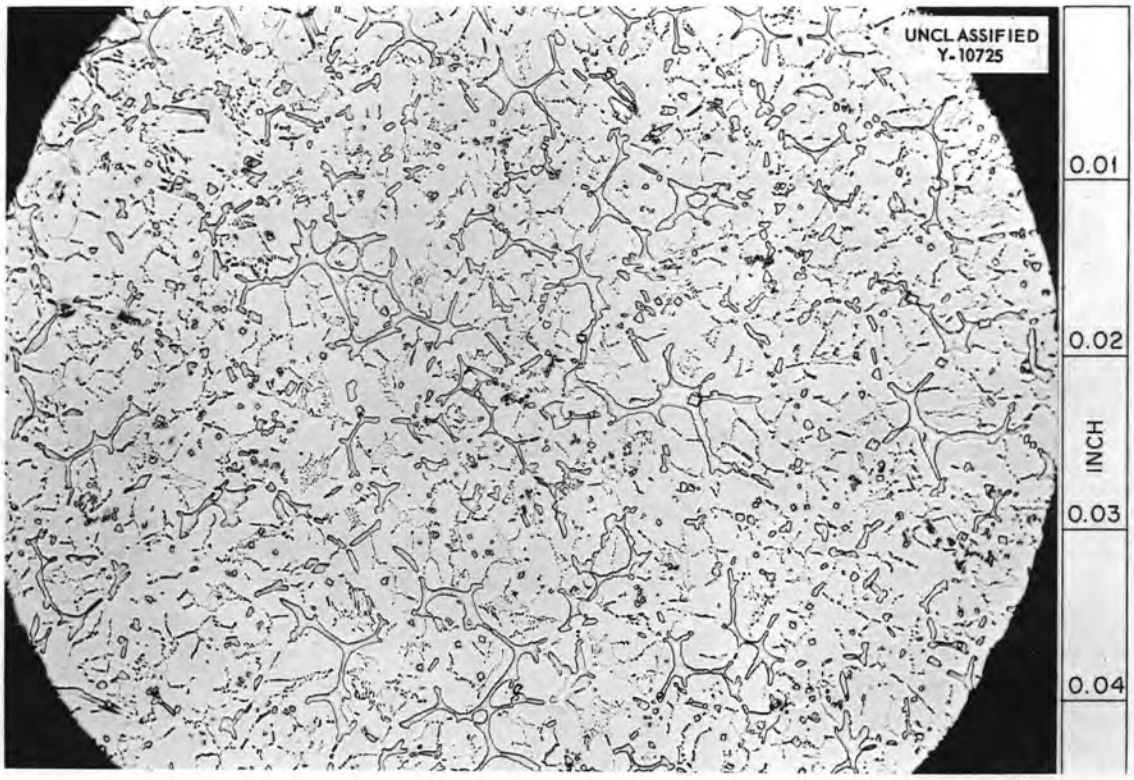

Fig. 144. Commercial Uranium–0.4 wt % Iron Alloy. The discontinuous phase is U_6Fe in a matrix of hypereutectoid $\alpha U + U_6Fe$. 100X. Reduced 10%.

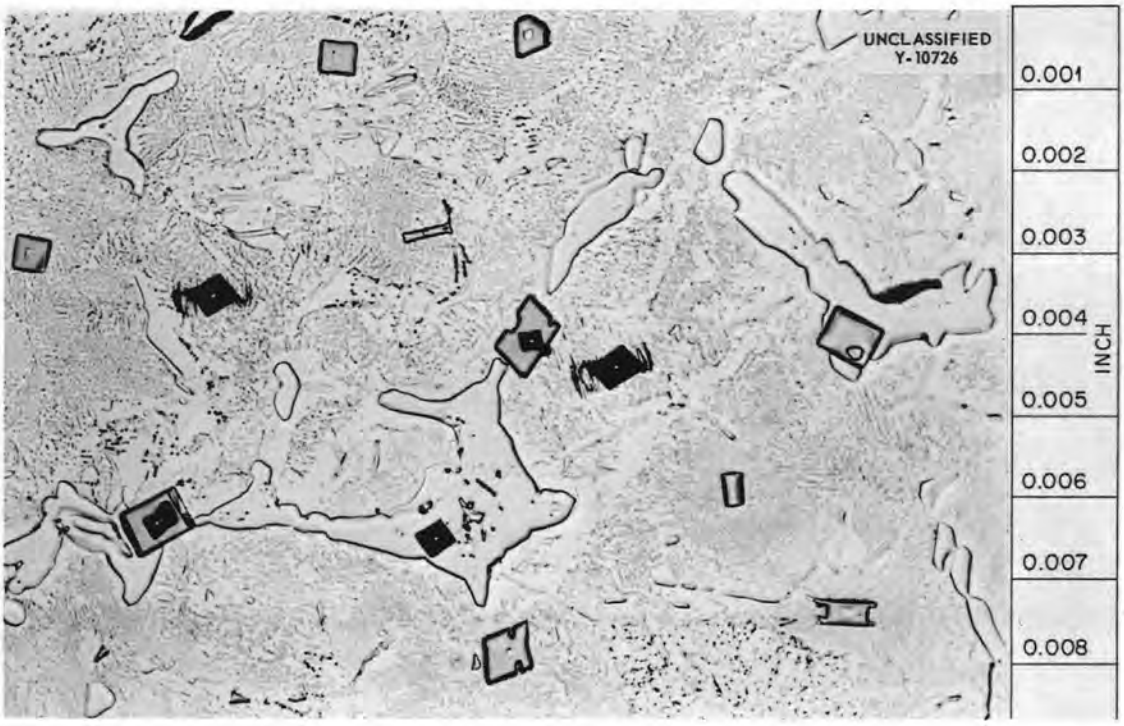

Fig. 145. Same Alloy as in Fig. 144 but Etched to Show the Hypereutectoid Microstructure. Note carbide(?) impurities. 500X. Reduced 13.5%.

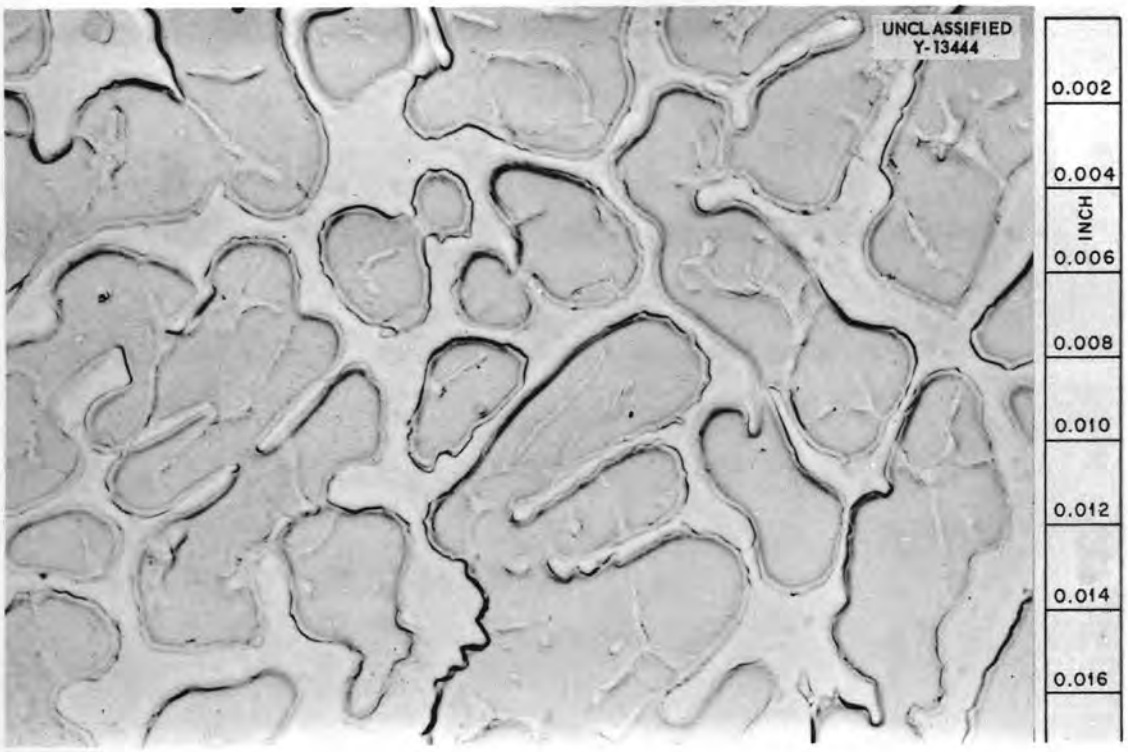

Fig. 146. High-Purity Uranium–1.01 wt % Iron Alloy. Unetched. The white continuous phase is a peritectically formed U_6Fe. 250X. Reduced 12%.

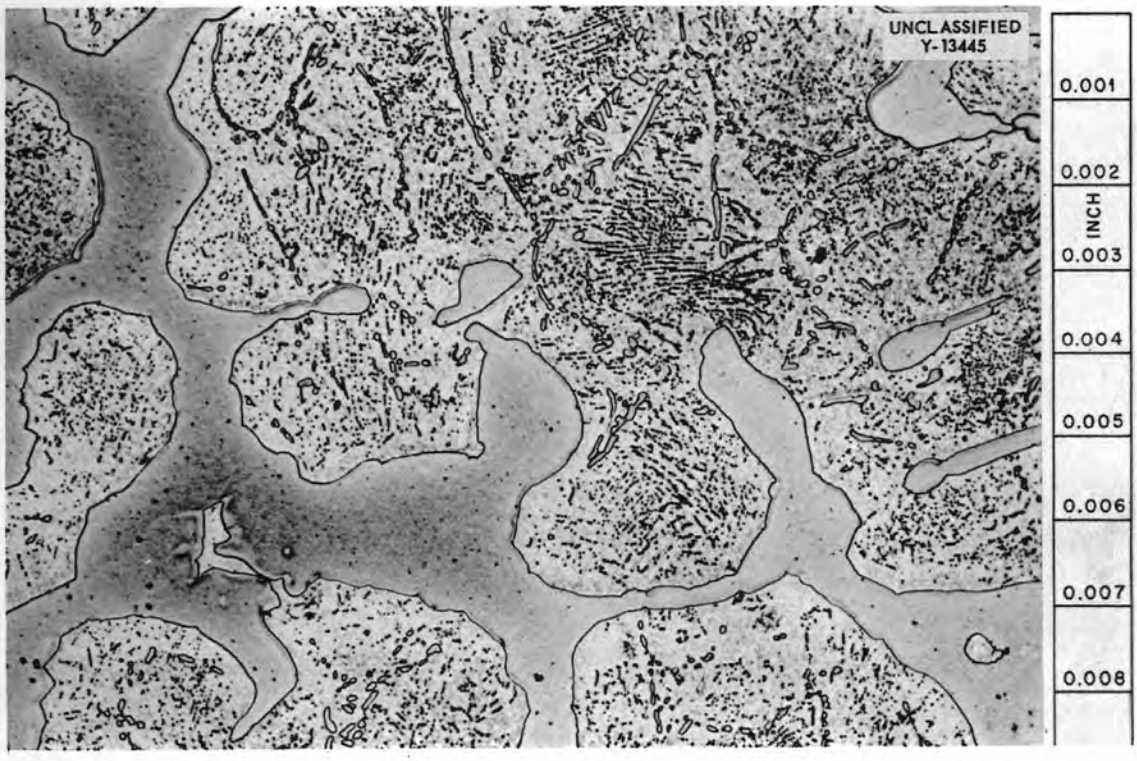

Fig. 147. Same Alloy as in Fig. 146 but Etched. Note the fine hypereutectoid microstructure of $\alpha U + U_6Fe$. Also note the absence of impurities in this microstructure as compared to microstructure in Fig. 145. 500X. Reduced 11%.